Doctoral Dissertation

Measurement of Neutrino Oscillation Parameters with Study of Neutrino Interaction Effects

Soichiro Kuribayashi

High Energy Physics Group
Division of Physics and Astronomy
Graduate School of Science
Kyoto University

Abstract

This thesis reports the measurement of the neutrino oscillation parameters with studies of neutrino interaction effects in the T2K experiment.

The T2K experiment is a long-baseline neutrino oscillation experiment in which the neutrino beam produced at J-PARC is measured with a near detector located 280 m away and a far detector Super-Kamiokande located 295 km away from the neutrino production target. The neutrino oscillation parameters δ_{CP}, θ_{23}, and Δm^2_{32} have been measured with the highest accuracy in the world. In particular, the goal of T2K is to obtain evidence of the CP violation ($\delta_{CP} \neq 0, \pi$) in neutrino oscillations. To achieve this goal, it is important to precisely evaluate systematic uncertainties.

Especially, the uncertainty of the neutrino interaction model is a major source of the systematic errors in the current neutrino oscillation measurements. In the current analysis, these uncertainties are incorporated based on theoretical models and measurements from external experiments, and they are reduced using data from near detector measurements of neutrino interactions. Using the constraints on the systematic errors with the near detector measurements, we compared the MC prediction with the data at the far detector. Finally, assuming the normal mass ordering and using the reactor experiment results for θ_{13}, we obtained $\sin^2\theta_{23} = 0.561^{+0.021}_{-0.032}$, $\Delta m^2_{32} = 2.494^{+0.041}_{-0.058} \times 10^{-3}\mathrm{eV}^2/\mathrm{c}^4$ and $\delta_{CP} = -1.97^{+0.97}_{-0.70}$. For more precise measurements, event selections for the near and far detectors were updated. The new selections for the near detector fit are based on the existence of the photons and protons in the final state. They were adopted in order to get more precise prediction of backgrounds for ν_e events and several neutrino interaction events deeply related to the outgoing proton kinematics at the far detector. As for the far detector analysis, a new selection for multi Cherenkov rings was added to increase the statistics.

In addition, there are several neutrino interaction model candidates in the oscillation analysis since our understanding of the neutrino interactions is not sufficient. Therefore, "choice" of the interaction models was required. This choice can be a potential bias which should be considered as the large systematic errors in the oscillation analysis results. To address this issue, we used simulation data with a set of alternative neutrino interaction models to evaluate the biases for that choice. We compared the analysis results between the nominal models and the alternative models, and then examined the effect of the model changes on the measurement results of the neutrino oscillation parameters. Taking into account the selection updates, we evaluated various interaction models related to events that include protons and pions in the final state. For δ_{CP} and θ_{23}, there is no significant bias. On the other hand, it was found that there is a deviation of approximately 2.7×10^{-5} $\mathrm{eV}^4/\mathrm{c}^2$ for Δm^2_{32}. This bias was considered as a systematic error and the final analysis results were obtained.

As a result of the updated oscillation analysis, we obtained $\sin^2\theta_{23} = 0.561^{+0.019}_{-0.038}$, $|\Delta m^2_{32}| = 2.494^{+0.040}_{-0.057}\mathrm{eV}^2/\mathrm{c}^4$, and $\delta_{CP} = -1.97^{+0.97}_{-0.62}$ with the reactor experiment results for θ_{13}. CP conserving values of δ_{CP} are excluded at 90% confidence level. These results are the world's highest precision for these oscillation parameters.

Acknowledgement

I would like to express my deepest gratitude to the following person who has supported the completion of my Ph.D. thesis.

First, I am profoundly thankful to Prof. Tsuyoshi Nakaya. I revere your attitude and deep insight towards the research and physics. Without your encouragement and support, I could not written the Ph.D. thesis even after I started working in the private company. I would like to appreciate Dr. Tatsuya Kikawa. He was always kind and courteous to me, even though I was an underachiever. Your encouragement kept me going when everything was going wrong and I was feeling down. I also respect your sincere attitude toward the research. I would like to express my appreciation to Prof. Atsuko Ichikawa. I respect your passion and creativity for physics and your imaginative ideas have helped me to carry out my research.

I want to express my gratitude to BANFF people, Ciro Ricco, Laura Munteanu, Tristan Doyle, Joe Walsh and Xu Yong-heng. I could advance my study with your kind technical help to use the BANFF framework. I would like to also appreciate NIWG members, Stephen Dolan and Luke Pickering. I respect your passion for the neutrino interaction and it motivated me more than ever. I would like to thank OA group conveners, Patrick Dunne and Benjamin Quilain. I respect your great leadership and I saw firsthand that it produced excellent results. I am grateful to p-theta members, Yohei Noguchi, Luccile Mellet, Lukas Berns and Kenji Yasutome. Your kind support to advance our fake data study was very helpful for me. I would also like to appreciate Super FGD group members, Tsunayuki Matsubara, Masaki Kawaue, Takuji Arihara, Aoi Eguchi, Mahesh Jakkapu, Davide Sgalberna, Konosuke Iwamoto and Tomohisa Ogawa. I am very happy to have worked with you to construct the new near detectors and I hope the measurement of the Super FGD work!

I want to appreciate my colleages in Kyoto HE group, Tomofumi Abe, Takuji Ikemitsu, Takahiro Odagawa, Masanori Tajima, Masayuki Hatano, and Yuya Mino. It was a great pleasure to spend time with such talented peers as yourselves. I would also like to thank Kyoto HE group members, Prof. Osamu Tajima, Prof. Roger Wendell, Dr. Toshi Sumida, Dr. Junya Suzuki, Dr. Shunsuke Adachi, Dr. Yudai seino, Dr. Hu Jianrun, Masashi Yoshida, Yoshinori Sueno, Bungo Sugashima, Yoshiaki Tsujikawa, Feng Jiahui, Lee Yohan, Takane, Sano, Hironobu Nakata, Nobuyuki Yoshimura, Zhoujun Hu, Shunta Arimoto, Chihiro Kawamoto, Yukimasa Kashino, Soichiro Takeichi, Naoto Onda, Takumi Tsushima, Naoya Matsushita, Yuma Muto, Harumi Sekiguchi and Mana Sasaki. You have made my lab life so much fan!

I would also like to thank my fiancee Shihomi. Your support and love led me to the comple-

tion of my Ph.D. thesis. Finally, I would like to give many thanks to my family, Hiroshi Kuribayashi, Mieko Kuribayashi, Aiko Kuribayashi, Naomi Kuribayashi and Sakura Kuribayashi for supporting my Ph.D. course.

Contents

Part I

Introduction

Chapter 1

Introduction

This chapter describes the physics of neutrinos mainly about neutrino oscillations, we also introduce the outline of this thesis.

1.1 Neutrino

1.1.1 History of Neutrino

The history of neutrino began in the early 20th century and its various fascinating characters have been revealed up to the present. In 1930, neutrino existence hypothesis was first proposed by W. Pauli to explain the continuous energy spectrum of β-rays ($n \to p + \bar{\nu} + e^-$) [1]. The existence of neutrinos was confirmed in 1956. C. L. Cowan and F. Reines detected anti-electron neutrinos from a reactor by observing inverse β decay($\bar{\nu} + p \to n + e^+$) [2]. In 1962, L. M. Lederman, M. Schwartz, and J. Steinberger confirmed the existence of the second flavor of neutrinos, based on the experimental fact that the neutrinos from π^+ decay differ from those from β decay [3]. Furthermore, it was experimentally confirmed that the number of generations of light neutrinos is three by measuring the decay width of the Z^0 bosons by LEP and SLC in 1989 [4]. On the other hand, tau neutrino, which is the third-generation neutrino was directly observed by DONUT in 2000 [5].

Based on the above experimental facts, it was found that neutrinos have three generations corresponding to each charged lepton flavor (e, μ, τ). In addition to these characteristics, neutrinos are considered to be neutral particles with spin 1/2 which interact via the weak interaction in the Standard Model.

1.1.2 Neutrino Oscillation

Neutrino oscillation is a periodic change of the lepton flavor of neutrino during its flight. This phenomenon exists when mass eigenstates and flavor eigenstates are not identical. In the Standard Model, neutrinos are regarded as massless particles. However, the fact that neutrinos have tiny mass was discovered experimentally by the observation of this phenomenon as described later.

Thus, it is known that neutrino have three different eigenstates for mass and flavor, and the relationship between them can be described with a unitary matrix as follows,

$$|\nu_l\rangle = U_{l,i}\,|\nu_i\rangle \;\text{ with} \left\{ \begin{array}{c} l = e, \tau, \mu \\ i = 1, 2, 3 \end{array} \right\} \tag{1.1}$$

where ν_l and ν_i are the flavor and mass eigenstates and, $U_{i,j}$ is a three by three unitary matrix which is called PMNS (Pontecorvo, Maki, Nakagawa, Sakata) matrix [6]. The unitarity matrix U can be parametrized using $\theta_{23}, \theta_{13}, \theta_{12}, \delta$, and written as,

$$\begin{aligned} U_{\text{PMNS}} &= \begin{pmatrix} 1 & 0 & 0 \\ 0 & c_{23} & s_{23} \\ 0 & -s_{23} & c_{23} \end{pmatrix} \begin{pmatrix} c_{13} & 0 & s_{13}e^{-i\delta} \\ 0 & 1 & 0 \\ -s_{13}e^{i\delta} & 0 & c_{13} \end{pmatrix} \begin{pmatrix} c_{12} & s_{12} & 0 \\ -s_{12} & c_{12} & 0 \\ 0 & 0 & 1 \end{pmatrix} \\ &= \begin{pmatrix} c_{12}c_{13} & s_{12}c_{13} & s_{13}e^{-i\delta} \\ -s_{12}c_{23} - c_{12}s_{23}s_{13}e^{i\delta} & c_{12}c_{23} - s_{12}s_{23}s_{13}e^{i\delta} & s_{23}c_{13} \\ s_{12}s_{23} - c_{12}c_{23}s_{13}e^{i\delta} & -c_{12}s_{23} - s_{12}c_{23}s_{13}e^{i\delta} & c_{23}c_{13} \end{pmatrix} \end{aligned} \tag{1.2}$$

where c_{ij} and s_{ij} are $\cos\theta_{ij}$ and $\sin\theta_{ij}$, respectively. The complex phase δ is called the Dirac CP phase (δ_{CP}) since the PMNS matrix yields CP symmetry breaking when δ_{CP} is not equal to 0 or π. If neutrinos are Majorana particles, two additional Majorana CP phases appear [7]. Unlike to the Dirac CP phase, they do not change the (anti) neutrino oscillation probabilities and only turn up in the lepton number violating processes such as $0\nu\beta\beta$ decay and neutrino-antineutrino oscillation.

When we consider the time variation of the neutrino's mass eigenstates, assuming that they are the plane waves, we can find that :

$$|\nu_i, t\rangle = |\nu_i, 0\rangle\, e^{-i(E_i t - p_i x)} \tag{1.3}$$

where E_i and p_i are the energy and momentum for each mass eigenstate respectively. Furthermore, since the flavor eigenstates $|\nu_l, t\rangle$ can be written as a superposition of the mass eigenstates $|\nu_i, t\rangle$, the time variation of them are described as,

$$\begin{aligned} |\nu_l, t\rangle = \sum_i U_{l,i}\,|\nu_i, t\rangle = \sum_i U_{l,i}\,|\nu_i, 0\rangle\, e^{-i(E_i t - p_i x)} &= \sum_{i,l''} U_{l,i}U_{i,l''}\,|\nu_{l''}, 0\rangle\, e^{-i(E_i t - p_i x)} \\ &= \sum_{i,l''} \{U_{l,i}e^{-i(E_i t - p_i x)}U^*_{l'',i}\}\,\left|\nu_{l'',0}\right\rangle \end{aligned} \tag{1.4}$$

where we use $U^\dagger = U^{-1}$ due to its unitarity. Thus, the transition amplitudes of the flavor

eigenstates $U_{l',l}(t)$ are written as,

$$U_{l',l}(t) = \langle \nu_{l'}, 0 | \nu_l, t \rangle = \langle \nu_{l'}, 0 | \sum_{i,l''} \{ U_{l,i} e^{-i(E_i t - p_i x)} U^*_{l'',i} \} | \nu_{l''}, 0 \rangle = \sum_i U_{l,i} e^{-i(E_i t - p_i x)} U^*_{l',i}. \quad (1.5)$$

Therefore, oscillation probability is given as follows,

$$P_{l,l'}(t) = |U_{l',l}(\mathrm{t})|^2 = |\sum_i U_{l,i} e^{-i(E_i t - p_i x)} U^*_{l',i}|^2. \quad (1.6)$$

Assuming the relativistic limit, approximation formula is given as

$$E_i t - p_i L \simeq E(t - L) + m_i^2 \frac{L}{2E} = m_i^2 \frac{L}{2E} \quad (1.7)$$

where E and L ($= t$ in natural units) are the energy and traveling distance of the neutrinos, respectively. Using this approximation, oscillation probability can be written as follows,

$$\begin{aligned}
P(\nu_\alpha \to \nu_\beta) &\simeq \sum_i U_{\alpha i} e^{-i m_i^2 \frac{L}{2E}} U^*_{j\alpha} \sum_j U^*_{\alpha j} e^{i m_j^2 \frac{L}{2E}} U_{\beta j} \\
&= \sum_i U_{\alpha i} U^*_{i\beta} U^*_{i\alpha} U_{\beta i} + \sum_{i>j} 2\mathrm{Re}(U_{\alpha i} U^*_{i\beta} U^*_{j\alpha} U_{\beta j} e^{-i m_i^2 \frac{L}{2E}}) \\
&= \delta_{\alpha\beta} - 4 \sum_{i>j} \mathrm{Re}(U_{\alpha i} U_{\beta i} U_{\alpha j} U_{\beta j}) \sin^2 \left(\frac{\Delta m^2_{ij} L}{4E} \right) \\
&+ 2 \sum_{i>j} \mathrm{Im}(U_{\alpha i} U_{\beta i} U_{\alpha j} U_{\beta j}) \sin^2 \left(\frac{\Delta m_{ij} L}{2E} \right) \\
&= \delta_{\alpha\beta} - 4 \sum_{i>j} \mathrm{Re}(U_{\alpha i} U_{\beta i} U_{\alpha j} U_{\beta j}) \sin^2 \left(\frac{1.27 \Delta m^2_{ij}([\mathrm{eV}]^2) L[\mathrm{km}]}{4E[\mathrm{GeV}]} \right) \\
&+ 2 \sum_{i>j} \mathrm{Im}(U_{\alpha i} U_{\beta i} U_{\alpha j} U_{\beta j}) \sin^2 \left(\frac{1.27 \Delta m^2_{ij}([\mathrm{eV}]^2) L[\mathrm{km}]}{2E[\mathrm{GeV}]} \right). \quad (1.8)
\end{aligned}$$

While this is the neutrino oscillation probability in vacuum, actual measurement needs to consider neutrino oscillation probability in matter. Especially, in the current long baseline neutrino oscillation experiments with accelerator neutrinos, two oscillation probabilities are measured mainly :

$$
\begin{aligned}
P(\nu_\mu \to \nu_e) &\simeq 4c_{13}^2 s_{13}^2 s_{23}^2 \sin^2\phi_{31} \qquad (1.9)\\
&+ 8c_{13}^2 s_{12}s_{13}s_{23}(c_{12}c_{23}\cos\delta_{\rm CP} - s_{12}s_{13}s_{23})\cos\Phi_{32}\sin\Phi_{31}\sin\Phi_{23}\\
&- 8c_{13}^2 c_{12}c_{23}s_{12}s_{13}s_{23}\sin\delta_{\rm CP}\sin^2\Phi_{32}\sin^2\Phi_{31}\sin^2\Phi_{21}\\
&- 2c_{13}^2 s_{12}^2 s_{23}^2 \frac{aL}{E}(1-2s_{13}^2)\cos\Phi_{32}\sin\Phi_{31}\\
&+ 8c_{13}^2 s_{13}^2 s_{23}^2 \frac{a}{\Delta m_{31}^2}(1-2s_{13}^2)\sin^2\Phi_{31}\\
P(\nu_\mu \to \nu_\mu) &\simeq 1 - 4c_{13}^2 s_{13}^2 (c_{12}^2 c_{23}^2 + s_{12}^2 s_{13}^2 s_{23}^2)\sin^2\Phi_{32} \qquad (1.10)
\end{aligned}
$$

where $a = 2\sqrt{2}G_F n_e E$, $\Phi_{ij} = \frac{\Delta m_{ij}^2 L}{4E}$, G_F is the Fermi constant and n_e is the electron density in the matter. Here the main terms are written down using $\Delta m_{21}^2 \ll \Delta m_{32}^2$ and the first line of Eq.1.9 is the dominant term. As shown in these Eq.1.9 and 1.10, these probabilities can be described as a function of fixed distance L and energy E. Therefore, oscillation parameters θ_{ij} and Δm_{ij} can be measured through the observation of these oscillations.

The oscillation probability for the anti-neutrinos is obtained just by inverting the sign of δ_{CP} and a. Thus, third line of Eq.1.9 causes the differences between the probability of $\nu_\mu \to \nu_e$ and $\bar{\nu}_\mu \to \bar{\nu}_e$ when $\sin\delta_{CP} \neq 0$ and this term is called CP violating term. Using this character δ_{CP} is measured.

Fourth and fifth lines of Eq.1.9 describe matter effect terms. These terms appear due to the interaction with matter when the neutrinos travel through a dense substance such as earth and sun [8], [9]. Tau neutrinos and muon neutrinos can interact with the matter only through the neutral current, while electron neutrinos can interact through both of neutral and charged currents. Thus, Hamiltonian during the flight of electron neutrinos is slightly different from the other neutrinos' and it changes the oscillation probability. This property can be used to measure the sign of the mass-squared difference and several experiments determine that of Δm_{12}^2 with solar neutrino oscillations. On the other hand, the sign of Δm_{13}^2 has not yet been determined.

1.2 Current Knowledge of Neutrino Oscillations

1.2.1 Measurements of the Neutrino Oscillations

The solar neutrino problem was the first indication of the neutrino oscillations. In 1968, the Homestake experiment measured the neutrino flux from the nuclear fusion in sun and found the neutrino flux rate was 1/3 of expected value from the standard solar model [10]. After that, Kamiokande [11], GALLEX (GALLium EXperiment) [12], GNO (Gallium Neutrino Observatory) [13] and SAGE (Soviet American Gallium Experiment) [14] also observed this deficit. For a long time, this issue had been an open question. However, in 1998, neutrino oscillations were experimentally discovered by the measurement of atmospheric neutrino at Super-Kamiokande [15]. Figure 1.1 shows that the number of detected ν_μ was greatly reduced by the neutrino oscillations. Neutrinos had been thought to be massless spin 1/2 particle called Weyl particles

in the Standard Model. However, this discovery proved that neutrinos are massive and now considered to be Majorana or Dirac particles.

After this discovery, several experiments have measured the oscillation parameters precisely using various kinds of neutrino sources which include not only natural ones but also artificial ones, such as reactors and accelerators. The current status of the measurements of each oscillation parameter will be described briefly and the latest results are summarized in Tab.1.1.

$\theta_{23}, \Delta m^2_{32}$

Measurements of these parameters started with the atmospheric neutrinos in the Super-Kamiokande [16]. Ice-Cube [17] experiment is also performing the measurement with the atmospheric neutrinos. Nowadays, accelerator neutrino experiments including the T2K and NoνA experiments measure them with muon neutrino disappearance.

θ_{13}

Whether this parameter is zero or not had been an open question for many years. In 2011, the T2K experiment indicated this value is not equal to 0 with the measurement of electron neutrino appearance [18]. Nowadays, short baseline reactor neutrino experiments Daya Bay [19], RENO [20] and Double Chooz [21] are world-leading measurements of this parameter.

$\theta_{12}, \Delta m^2_{12}$

These parameters have been measured by solar neutrino experiments such as Homestake [10], Kamiokande [11], Super-Kamiokande [22], SNO [23], and Borexino [24] with electron neutrino disappearance. In addition, KamLAND [25] measures the values with anti-electron neutrino disappearance of reactor neutrinos.

δ_{CP}

The oscillation parameters except for δ_{CP} were measured with about 5% precision. Nevertheless δ_{CP} is still difficult to measure precisely. Currently, this value is being measured mainly by accelerator neutrino experiments such as T2K, Super-Kamiokande[22] and NoνA [26].

1.2.2 Physics behind Neutrino Oscillations

Neutrino oscillations themselves are physics beyond the Standard Model, and its discovery is an interesting topic in modern physics. Nowadays, a number of experiments measure the oscillation parameters and have revealed several things. However, there are still open questions behind them.

Leptogenesis via CP Violation in Neutrino Oscillation

To explain the matter-antimatter asymmetry in Universe, Sakharov Conditions [29] are required as follows,

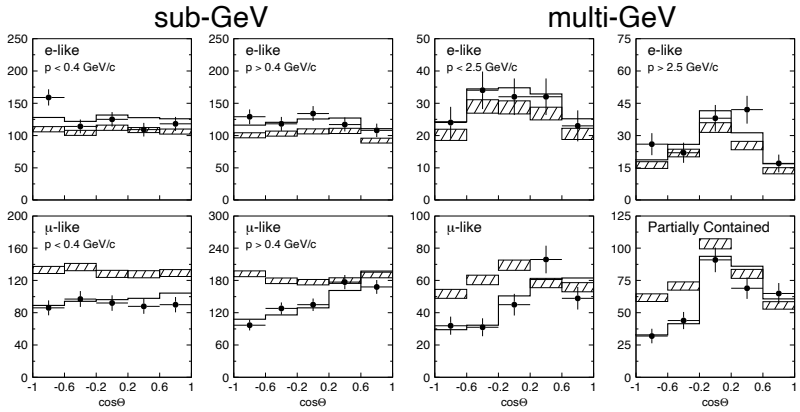

Figure 1.1: Zenith angle distributions of charged leptons from the interactions of the atmospheric neutrinos measured by SK. The hatched region describes the no-oscillation case, and the bold line corresponds to the case assuming neutrino oscillation. The distributions are consistent with the case assuming neutrino oscillation [15].

- Violation of baryon number
- Violation of both C-symmetry and CP-symmetry
- Interactions out of thermal equilibrium

The violation of the CP symmetry in quarks has already been discovered by the decays of K mesons [30], and also confirmed by B mesons at BaBar [31] and Belle [32]. That CP violation is described as the Dirac CP phase in the CKM matrix. However, the size of the CP violation in the CKM matrix alone is not sufficient to explain the matter-antimatter asymmetry in Universe [33]. To resolve this deficit, a theory was proposed to explain it by the CP symmetry breaking in leptons through sphaleron process [34]. This idea is called leptogenesis. The leptogenesis requires the CP violation in the lepton sector and the discovery of the CP violation in neutrino mixing matrix is important to reveal the mystery of cosmic generation.

Mixing Angle

Theoretical description of the PMNS matrix is very similar to the Cabibbo Kobayashi Maskawa (CKM) matrix [35, 36], which describes the mixing of quarks. However, the mixing angles of the PMNS matrix is much larger than those of the CKM matrix. To explain its difference, several physics theories are proposed. Especially, θ_{23} is close to the maximum angle ($\pi/4$) according to the latest measurement. If it is the maximum mixing, there could be unknown physics behind

Table 1.1: Summary of the results of the latest oscillation measurement [27, 28]. NO and IO are normal and inverted orderings of neutrino mass, respectively. What these orderings are will be explained in Sec. 1.2.2.

Parameter	Ordering	Best-fit $\pm 1\sigma$	3σ range
$\Delta m^2_{32}/10^{-3}\mathrm{eV}^2$	IO	$-2.498^{+0.028}_{-0.029}$	-2.584 - -2.413
$\Delta m^2_{31}/10^{-3}\mathrm{eV}^2$	NO	$2.515^{+0.028}_{-0.028}$	$+2.431$ - $+2.599$
$\Delta m^2_{21}/10^{-5}\mathrm{eV}^2$	NO, IO	$7.42^{+0.21}_{-0.20}$	6.82 - 8.04
$\sin^2\theta_{12}$	NO	$0.304^{+0.013}_{-0.012}$	0.269 - 0.343
	IO	$0.304^{+0.012}_{-0.012}$	0.269 - 0.343
$\sin^2\theta_{23}$	NO	$0.573^{+0.018}_{-0.023}$	0.405 - 0.620
	IO	$0.578^{+0.017}_{-0.021}$	0.410 - 0.623
$\sin^2\theta_{13}$	NO	$0.02220^{+0.00068}_{-0.00062}$	0.02034 - 0.02430
	IO	$0.02238^{+0.00064}_{-0.00062}$	0.02053 - 0.002434
$\delta_{CP}[^o]$	NO	194^{+52}_{-25}	105 - 405
	IO	287^{+27}_{-32}	192 - 361

it. Thus, the precise measurement of these mixing angles is very important to validate these theories.

Neutrino Mass Ordering

With the measurement of neutrino oscillations in vacuum, it is possible to obtain the absolute value of the differences in mass squared of the neutrino mass eigenstates, while it is impossible to determine if they are positive or negative values. The sign of Δm^2_{12} was determined by the measurements of solar neutrinos using matter effect. However, the other sign has not yet been determined, and whether the ordering is normal ordering ($m^2_3 > m^2_2 > m^2_1$) or inverted ordering ($m_2 > m_1 > m_3$) is still unknown as shown in Fig. 1.2. Neutrino masses themselves cannot be explained by the Standard Model, and various models are being proposed to describe them. Some of these models predict the normal or inverted ordering, and the determination of the mass ordering is important for the validations [37].

1.3 Introduction of T2K experiment

The Tokai to Kamioka (T2K) experiment is aiming to measure the neutrino oscillation parameters using accelerator neutrinos. Figure 1.3 shows the overview of the T2K experiment. In the T2K experiment, a neutrino beam is produced at the Japan Proton Accelerator Research Complex (J-PARC) in Tokai. The neutrino beam is measured at the near detector located 280 m from the neutrino beam production point and a far detector (Super-Kamiokande) located 295 km away from the beam production point.

The current main goal of the T2K experiment is to search for CP violation through the measurement of δ_{CP}. The measurement precision of δ_{CP} is dominated by the statistical un-

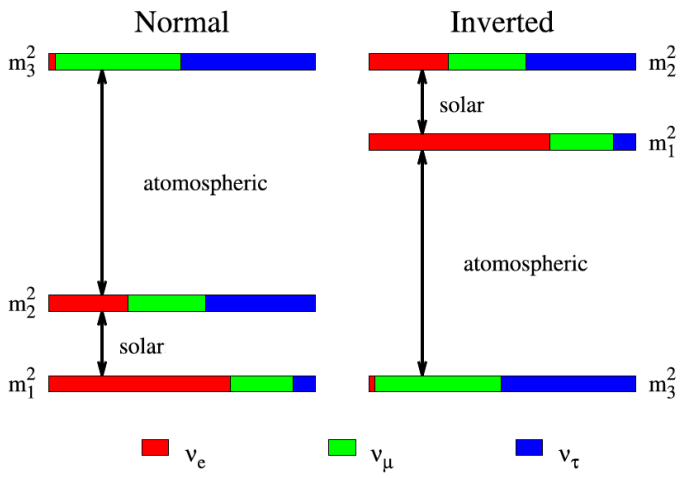

Figure 1.2: Concept of normal (left) and inverted (right) ordering of neutrino mass. The absolute difference in the mass squared of each mass eigenstate is known from measurements of neutrino oscillations. However, the magnitude of m_1, m_2 and m_3 is not known. Taken from [38]

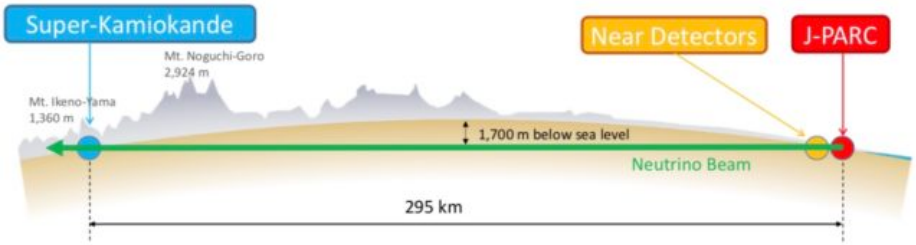

Figure 1.3: Overview of the T2K experiment.

certainty since neutrino rarely interacts with matters. However, understanding of systematic uncertainties is essential for the accurate measurements of the neutrino oscillation parameters. Furthermore, systematic uncertainty will be more important when we get more statistics in the next generation experiments, such as Hyper-Kamiokande [39]. Table 1.2 shows the systematics uncertainty for each sample at the Super-Kamiokande. The systematic uncertainty is dominated by that for the cross section of the neutrino interactions as shown in the second and third rows of the table. The total systematic uncertainty in the T2K oscillation analysis is summarized in the bottom row of this table.

Table 1.2: The systematic uncertainties on the number of the events at the Super-Kamiokande for each sample in T2K. The detail of these samples will be described in Sec. 4.5.3. Taken from [40].

	1-Ring μ		1-Ring e		
Error source	ν mode	$\bar{\nu}$ mode	ν mode	$\bar{\nu}$ mode	ν mode CC1π
Beam	4.3%	4.1%	4.4%	4.2%	4.4%
Cross section (constrained by near detectors)	4.7%	4.0%	4.8%	4.1%	4.1%
Cross section (all)	5.6%	4.4%	8.4%	6.2%	5.6%
Beam + Cross section (constrained by near detectors)	3.3%	3.3%	3.3%	3.1%	4.0%
Beam + Cross section (all)	4.4%	2.9%	7.7%	5.7%	5.6%
Super-Kamiokande detector sytematics	3.3%	2.9%	4.1%	4.3%	16.6%
Total	5.5%	4.4%	8.8%	7.3%	17.8%

1.4 Problems toward the Precise Measurement of the Oscillation Parameters

Precise measurement of oscillation parameters, especially δ_{CP} is very important for our progress in physics. However, there are still large systematic uncertainties which is driven from the uncertainties of the neutrino interaction models in the T2K experiment as described in the previous section.

The uncertainty of neutrino-nucleus interaction models is a main source of the systematic uncertainty because the prediction of event rates and spectrum at each detector are calculated based on the models. Figure 1.4 shows the neutrino flux prediction for each neutrino-nucleus interaction mode in the T2K experiment. Although Charged Current Quasi Elastic (CCQE) Interaction ($\nu_l + n \rightarrow l^- + p$) is dominated, the other various neutrino interaction modes contaminate significantly. It requires us to combine a variety of neutrino-nucleus interaction models. Even though many theoretical works have been performed to understand them, there are still large systematic uncertainties of the interaction models due to its complexities.

To constrain these uncertainties, T2K performs the fit comparing the data and MC prediction at the near detectors (near detector fit). Many improvements of the near detector fit, such as new modelings and new sample selections were achieved to be more sensitive to the nuclear effects in the latest analysis. This nuclear effect is one of the key aspects in understanding the interaction models, as described in Sec 3.3. Furthermore, in order to see more of the nuclear effects, new proton kinematics parameters are also being implemented for the future analysis. On the other hand, it is still difficult with the near detector fit and the current modeling to cover the potential systematics error sources which stem from the "choice" of the neutrino interaction models. The evaluation of the such errors will be a key to the accurate measurement of neutrino oscillation.

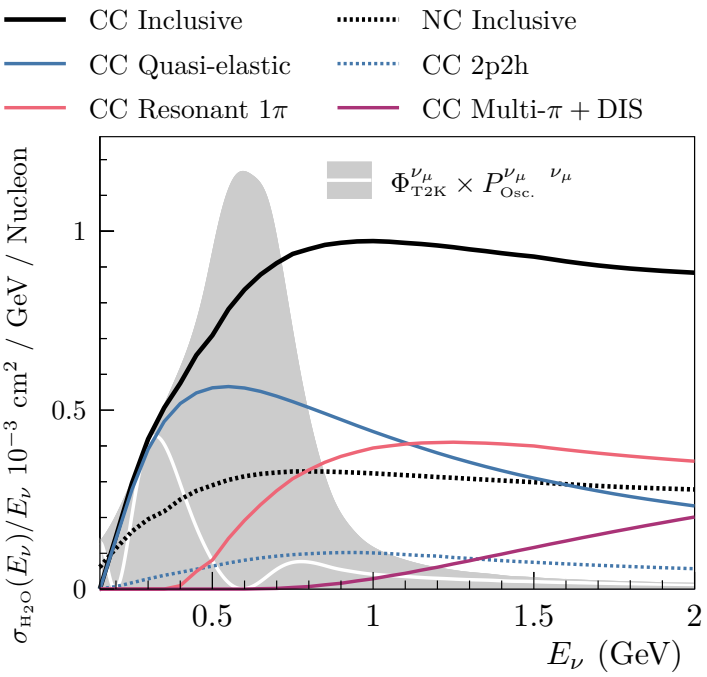

Figure 1.4: This figure shows the predictions for the contributions to sum of the Charged Current (CC) and Neutral Current (NC) inclusive cross section for muon neutrinos interacting as a function of neutrino energy. CCQE interaction (blue line) is a dominant mode in the T2K energy region while CC 2p2h (blue dotted line), CC Resonant 1π (red line), and CC Multi-π and DIS (magenta line) interactions exist. The detail of these interactions will be described in Sec. 3.2. Taken from [41].

1.5 Outline of This Thesis

This thesis describes the results of the oscillation analysis in the T2K experiment in which we used the neutrino beam data collected from Jan. 2010 to Feb. 2020. First, Chapter 2 describes an overview of the T2K experiment. Chapter 3 explains in detail the neutrino interaction model which is an important part in the measurement of the oscillation parameters.

From Chapter 4 to Chapter 7, the details of T2K oscillation analysis are described focusing on the uncertainty of neutrino interaction model and near detector fit. Chapter 4 introduces the overview of how the T2K experiment measures the oscillation parameters and the results of the original analysis. In Chapter 5, we describe how the near detector fit is improved for the updated analysis. Chapter 6 introduces the evaluation of potential systematics error from the neutrino interaction modeling in our oscillation analysis. Chapter 7 presents the results of our latest oscillation analysis. Prospects mainly about the improvement of our analysis and near detectors are discussed in Chapter 8. Finally, this thesis is concluded in Chapter 9.

Part II

Measurement of Neutrino Oscillation Parameters

Chapter 2

T2K Experiment

Tokai to Kamioka (T2K) experiment is a long-baseline neutrino oscillation measurement [42]. As described in the previous chapter, in the T2K experiment, a high-intensity neutrino beam is generated at the Japan Proton Accelerator Research Complex (J-PARC) in Tokai. The neutrino beam is measured at the near detectors placed at the J-PARC and a far detector (Super-Kamiokande) placed 295 km away from the neutrino beam source. We will describe the overview of each component in this section. The overview of the analysis flow will be described later in the Chapter 4.

2.1 Neutrino Beam (J-PARC)

2.1.1 Overview of Neutrino Beamline

The T2K neutrino beam is produced by the J-PARC accelerators, which consist of LINear ACcelerator (LINAC), Rapid Cycling Synchrotron (RCS), and Main Ring (MR), as shown in Fig. 2.1. LINAC accelerates an H^- ions up to 400 MeV and converts them to protons at injection to RCS with charge stripping foils. At RCS, these protons are accelerated up to 3 GeV with a 25 Hz cycle and then injected into the MR synchrotron. MR accelerates them up to 30 GeV and transports them as eight bunches to Target Station (TS) every 2.48 seconds. Each bunch of the proton beam has about 58 ns width and they are separated by about 580 ns. In TS, these protons strike a carbon target, and outgoing charged pions and kaons are focused by the three electromagnetic horns [43]. These hadrons decay mainly into muons and neutrinos in a 96 m-long decay volume as follows,

$$\pi^+ \to \mu^+ \nu_\mu \tag{2.1}$$

$$\pi^- \to \mu^- \bar{\nu}_\mu. \tag{2.2}$$

The sign of these hadrons, positive or negative, can be selected by the polarity of the horn currents. Therefore, either neutrino or anti-neutrino also can be chosen. We call the former

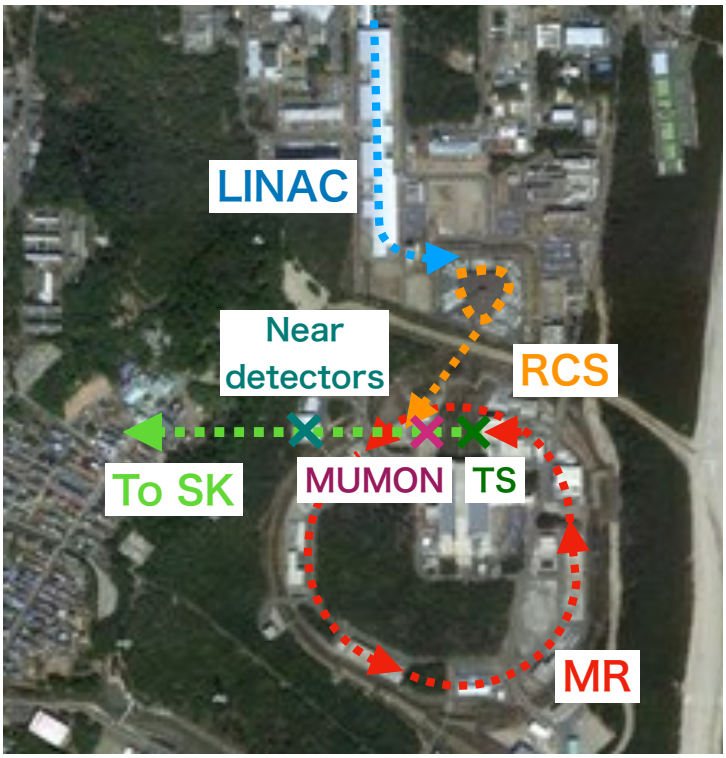

Figure 2.1: An aerial photograph of the J-PARC accelerators.

neutrino mode and the latter anti-neutrino mode. The remaining particles except for neutrinos and muons are absorbed by a beam dump at the end of the decay volume. These muons above 5 GeV are profiled by a muon monitor (MUMON)[44, 45] downstream of the beam dump and the neutrino beam profiles is measured by INGRID which will be described later.

2.1.2 Off-Axis Method

Neutrino beam is generated by the two-body decay of hadrons, thus neutrino energy beam spectrum has a broad distribution. To make it narrow, off-axis method is adopted in T2K experiment [46]. Figure 2.2 shows the layout of overall T2K experiment. Super-Kamiokande detector and one of near detectors are placed 2.5° off-axis with respect to the beamline direction.

The neutrino beam in T2K is mainly produced by the two-body decay of charged π particles. Thus, the neutrino energy E_ν is given as,

$$E_\nu = \frac{m_\pi^2 - m_\mu^2}{2(E_\pi - p_\pi \cos\theta_\nu)} \tag{2.3}$$

where E_π, m_π and p_π are energy, mass and momentum of charged π particles respectively. θ_ν is the decay angle between directions of the neutrino and the charged π particle. As shown in Fig. 2.3, neutrino energy increases linearly in response to p_π when θ_ν is equal to 0. On the other hand, when θ_ν has a non-zero value, E_ν does not exceed certain value even for large p_π. Figure

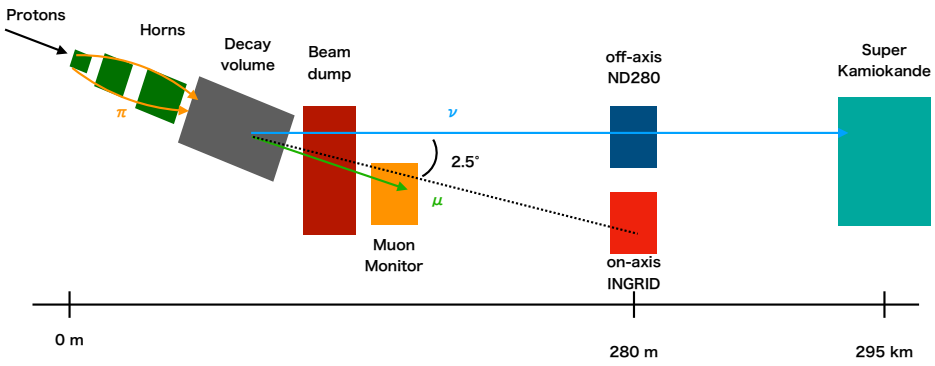

Figure 2.2: An arrangement of the main apparatus in T2K experiment.

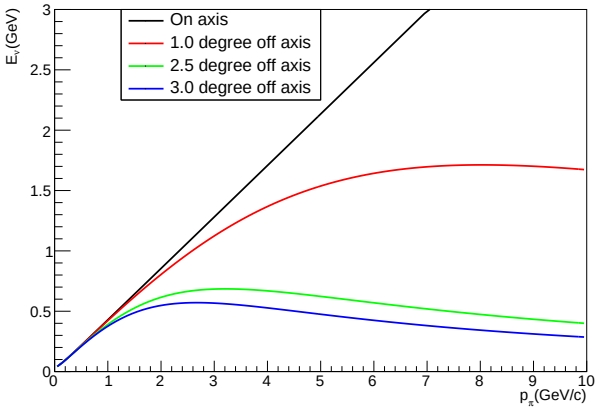

Figure 2.3: Comparison plots of neutrino energy as a function of pion momentum for each neutrino beam direction.

2.4 shows the neutrino energy spectrum for each off-axis angle and oscillation probabilities in T2K. As shown in the bottom plot, energy spectrum gets narrow when off-axis angle compared to on-axis. T2K adopted 2.5° to set the energy spectrum peak 0.6 GeV where the oscillation probabilities are maximized at Super-Kamiokande as shown in top and middle plots.

2.2 Near Detectors

T2K experiment has two kinds of near detectors to measure the neutrinos before oscillations and they are placed at 280 m downstream from the neutrino beam target. One detector is called INGRID located on-axis and the other one is called ND280 located off-axis.

2.2.1 INGRID (On-axis detector)

INGRID, an on-axis detector is designed to measure the neutrino beam profile and stability. This detector consists of 14 identical modules arranged in a 10 m×10 m cross-shape as shown

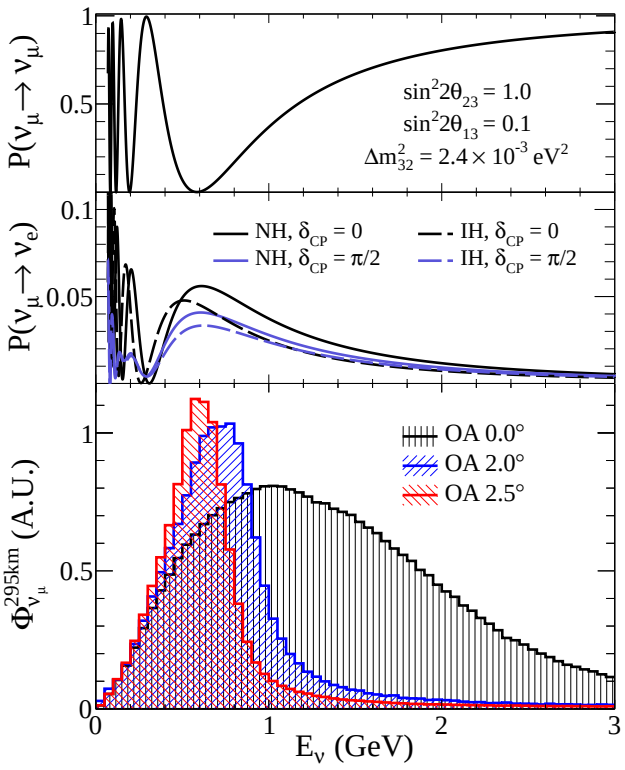

Figure 2.4: The oscillation probability at T2K (top) and the neutrino beam flux for different angles (bottom).

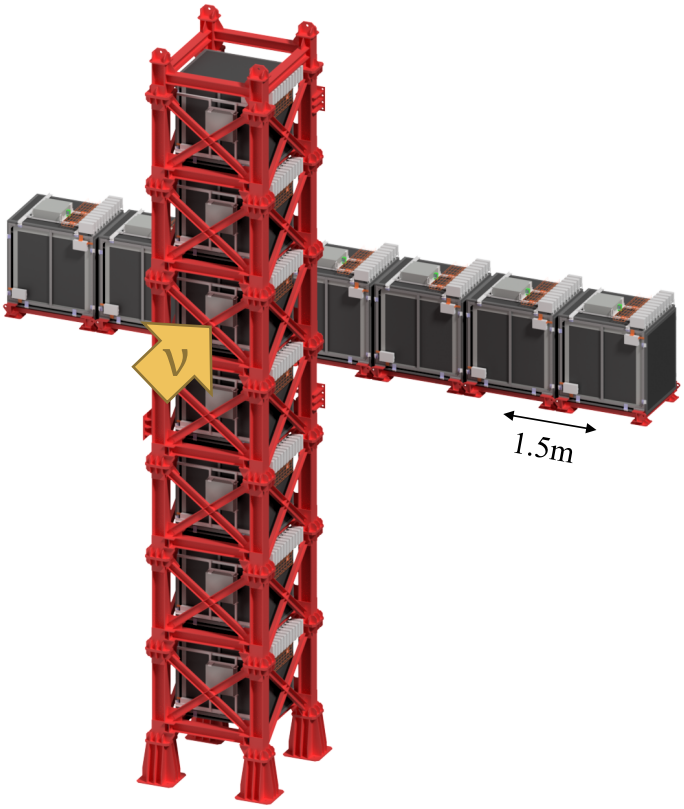

Figure 2.5: Overview of the INGRID detector.

in Fig. 2.5. Each of these modules has a sandwich structure consisting of nine layers of iron and eleven layers of scintillator plates, and its total weight is about 7 tons. Using these modules, INGRID can measure the beam direction with a precision better than 1 mrad which is the requirements in the T2K experiment. Figure 2.6 shows one example of a neutrino beam profile measured by INGRID. The event rate for each module is fitted by Gaussian distribution, from which we can obtain the center values as the peak positions and beam widths from the Gaussian 1σ values.

2.2.2 ND280 (Off-axis detector)

ND280, off-axis near detector is designed to constrain the neutrino flux and neutrino interaction models in our analysis by measuring the neutrino beam flux and neutrino-nucleus cross section before oscillations. This detector is a complex detector as shown in Fig. 2.7 and surrounded by a dipole magnet which was used for the UA1 experiment [47]. This UA1 magnet can provide a magnet field of 0.2 T and allows us to measure the sign and momentum of charged particles precisely.

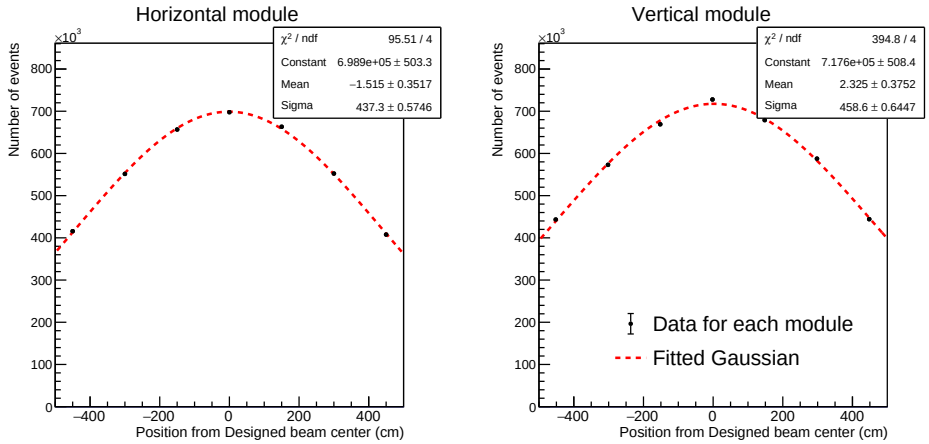

Figure 2.6: Neutrino beam profile in the neutrino mode beam measured by INGRID (example of the T2K run10 period). Black points show the data and the red dotted line shows the beam profile which is determined by the Gaussian fit to the data.

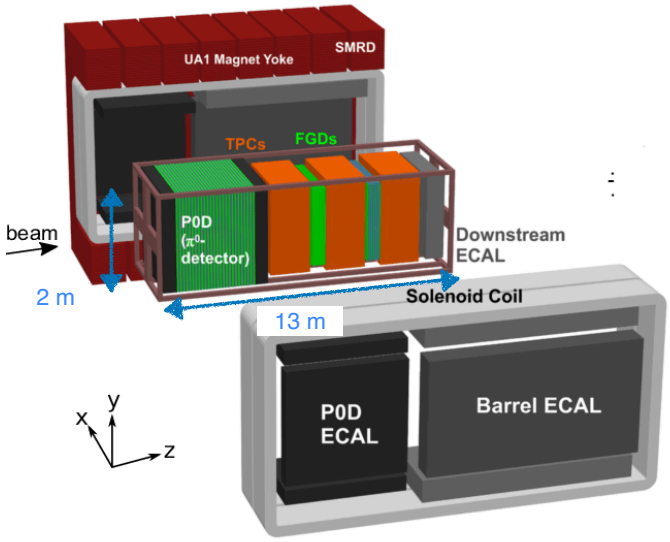

Figure 2.7: Overview of the ND280

Fine Grained Detector (FGD)

FGD [48] is dedicated to measuring the vertex and tracks of neutrino interactions. There are two FGDs and each detector has a slightly different detector structure. The upstream one is called FGD1 and consists of 15 layers of rod-shaped scintillators. The vertical and horizontal layers of the scintillators are arranged alternately in a plane perpendicular to the beam direction. Each scintillator has WaveLength Shifting (WLS) fibers through a hole in its center to read out scintillation light by MPPCs(Multi Pixel Photon Counters) which are placed at one edge of the fibers.

The downstream one is FGD2 and it has a similar structure but contains seven alternating scintillator modules interleaved with six passive water modules. This water target allows us to measure the neutrino interaction cross-section on water which is the same target as the far detector. The outer dimensions of each FGD are 230 cm (width) $\times$ 240 cm (height) $\times$ 36.5 cm (depth in beam direction), and the target mass is 1.1 t.

Time Projection Chamber (TPC)

There are three TPCs [49] in the tracking region to reconstruct 3D track the charged particles from P0D and two FGDs. These detectors with the magnetic field are capable of performing the measurements of sign, momentum, and identification of the particles through the curvatures and energy deposits of the tracks.

Figure 2.8 shows a simplified drawing of the TPC design. The TPC adopted a double box design, where the walls of the inner box act as the field cage and those of the outer box do at ground potential by CO_2 acting as an insulator between them. The inner box is filled with a gas mixture, $Ar : CF_4 : C_4H_{10}$ $(95 : 3 : 2)$. The inner box panel surfaces form a copper strip pattern and produce a uniform electric field to drift the ionization electron from the central cathode towards micromegas [50] in the readout planes. The micromegas is used for gass-amplified read out of the ionizing electrons.

The TPCs perform the particle identification (PID) by using a truncated mean of measurements of energy loss of charged particles [49]. Figure 2.9 shows the distribution of the deposited energy as a function of momentum. The PID in the TPC uses "pull" which is determined by the energy deposit along the track for the calculation of probability of each particle type.

The pull for each particle type α is given as,

$$Pull_\alpha = \frac{\left(\frac{dE}{dx}\right)_{\text{means}} - \left(\frac{dE}{dx}\right)_{MC,\alpha}}{\sigma} \tag{2.4}$$

where $(dE/dx)_{\text{means}}$ is the measured energy loss per length and $(dE/dx)_{\text{MC},\alpha}$ is expected energy loss per length for given particles α. σ is the resolution of the energy deposit. Using this pull, the likelihood for PID of particle α in the TPC can be defined as,

$$L_\alpha = \frac{e^{-Pull_\alpha^2}}{\sum_i e^{-Pull_i^2}}. \tag{2.5}$$

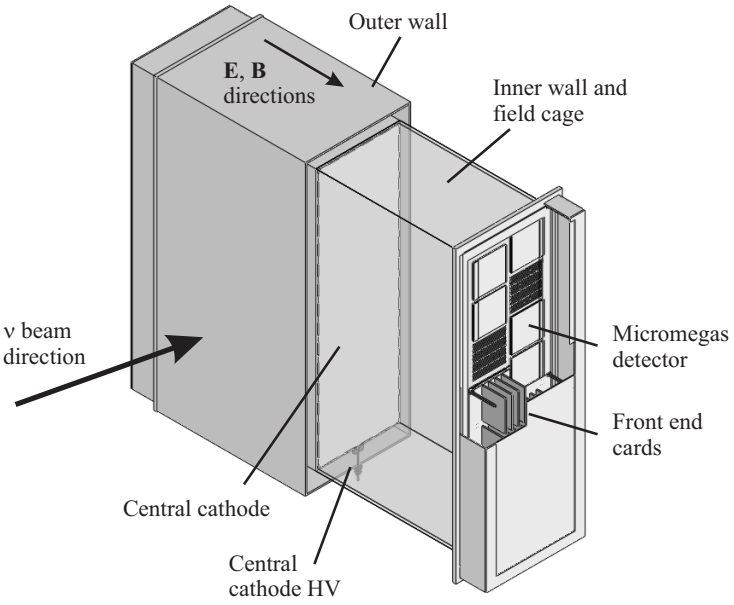

Figure 2.8: A simplified diagram of the TPC design. Taken from [49].

where the dominator is sum of the pulls of the charged particles which should be considered. The resolution of energy deposit is $7.8 \pm 0.2\%$ for minimum ionizing particles, better than the requirements in the T2K experiment. This resolution with this pull method allows us to distinguish a muon from an electron with a misidentification rate of 0.2% where its momentum is below 1 GeV/c.

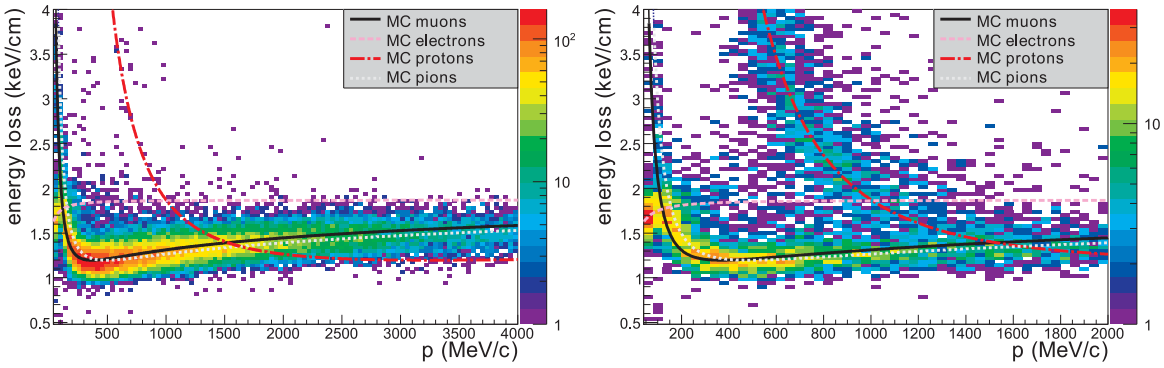

Figure 2.9: Energy deposit per unit length as a function of momentum for negative (left) and positive (right) particles in the TPCs. Taken from [49].

Other Detectors in ND280

There are Pi-zero Detector (P0D), Elector Magenetic CALorimeter (ECAL) and Side Muon Range Detector (SMRD) in addition to FGDs and TPCs in ND280. P0D is dedicated to measure the neutral pions which can be the background in electron neutrinos measurement at Super-Kamiokande. This detector is located at the most upstream of the beam and is composed of layers of scintillator alternated with water bugs. ECAL is located in the outermost layer and downstream. This detector can capture the electromagnetic showers of electrons and gamma rays produced by neutrino interaction. SMRD consists of scintillator planes which are placed in the air gaps between iron plates of UA1 magnet. This detector can track muons which escape the inner detectors at high angle. It also provides a cosmic trigger signal and veto for particles coming from outside.

2.3 Far Detector (Super-Kamiokande)

Super-Kamiokande (SK) is a 50 kt water Cherenkov detector and serves as the far detector in T2K experiment. It is composed of two main volumes which are called inner detector (ID) and outer detector (OD) respectively as shown in Fig. 2.10 and they are separated optically by Tyvek sheets. The ID consists of 11129 inner PMTs with a 50 cm aperture, which surrounds the water, and the OD does of 1885 outer PMTs with a 20 cm aperture installed to veto external backgrounds. The inner PMTs which cover 40% of the detector's total inner surface area can detect neutrinos by the Cherenkov radiation of charged particles from the neutrino interactions on water. The Cherenkov light forms a ring-shaped pattern which is useful for the extraction of kinematic information of the neutrino. The shape of Cherenkov light from a muon is a clear ring, while that from an electron is fuzzy due to its electromagnetic shower as shown in Fig. 2.11. This character makes it possible to determine whether the light is from a muon neutrino or an electron neutrino.

2.4 T2K Data Taking

Figure 2.12 shows history of the MR proton beam power and the protons on target (POT). The beam power has reached maximum of 515 kW and it will be upgraded to 1.3 MW in the near future. The data w/ 3.6×10^{21} POT are used for the current oscillation analysis.

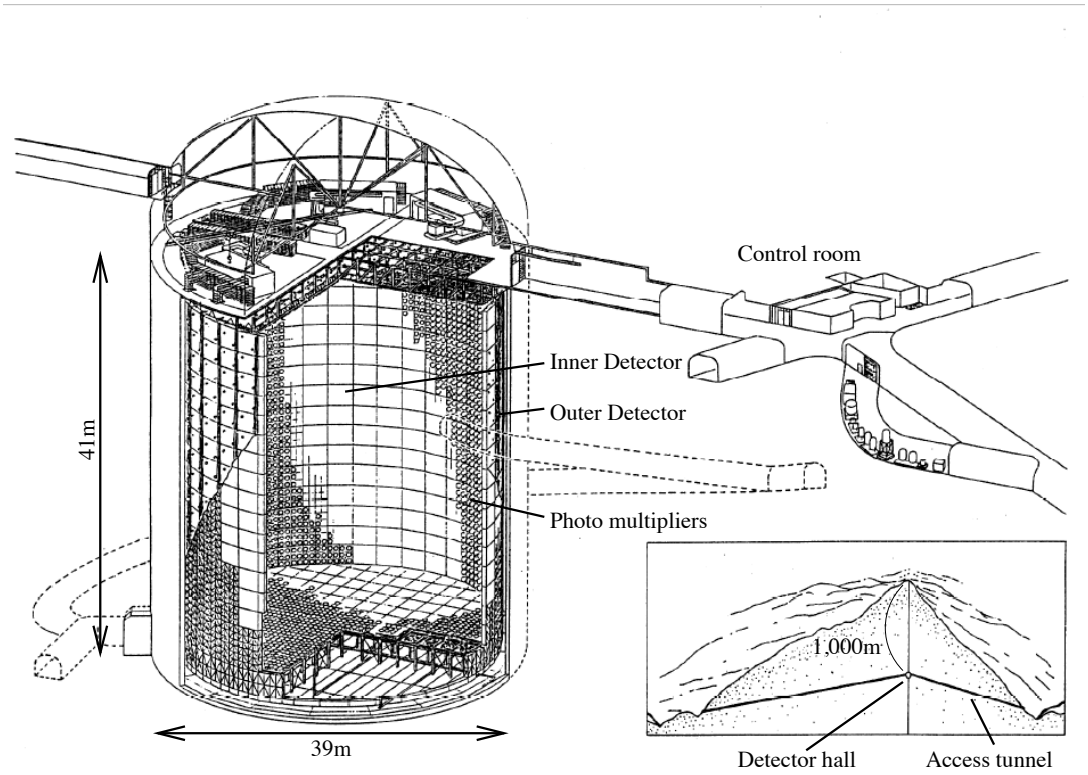

Figure 2.10: A schematics view of the SK [51].

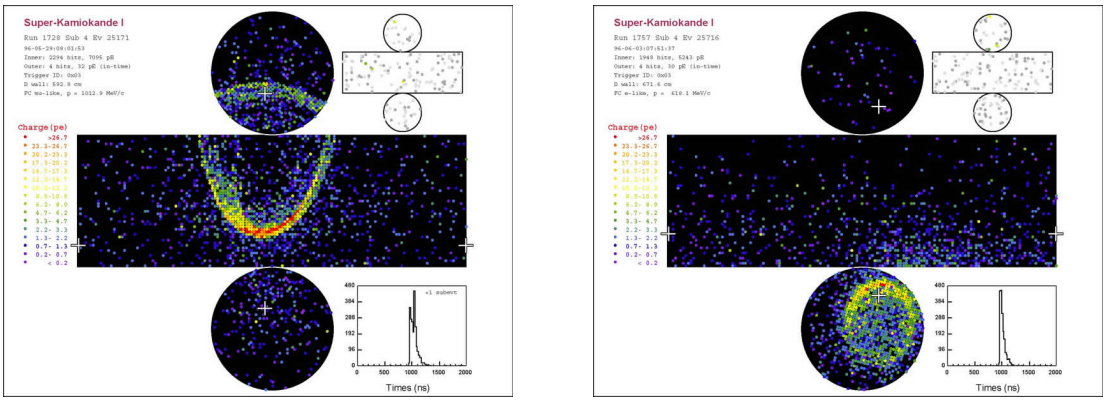

Figure 2.11: Event display of the SK. A left figure shows a muon-like ring and a right figure shows an electron-like ring.

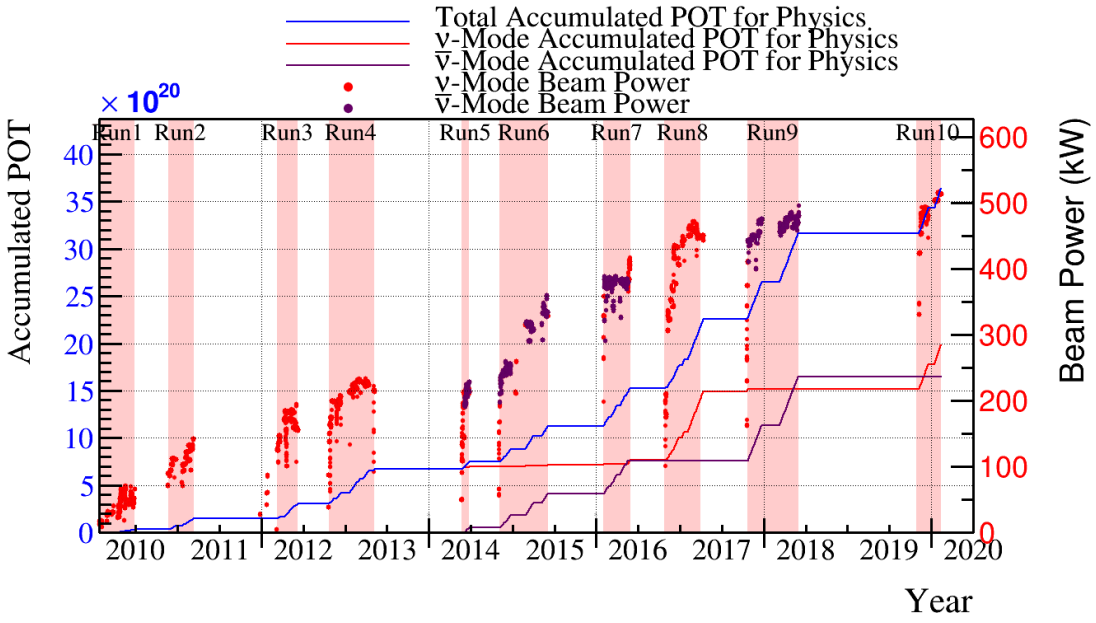

Figure 2.12: Accumulated POT and beam intensity between 2010 and 2020 for the T2K experiment.

Chapter 3

Neutrino Interaction

The uncertainty of neutrino-nucleus interaction is one of the main systematic uncertainty sources in the T2K oscillation analysis as discussed in Chapter 1. This chapter describes the details of the current understanding of neutrino-nucleus interaction models. First, we will describe the overview of the neutrino interaction models which are used in our analysis including the general description of its theoretical parts. Then, the details of the neutrino interaction with a nucleon and nuclear effects will be explained. Finally, we will also introduce the alternative interaction model candidates in our neutrino oscillation analysis. They are highly motivated to consider the potential bias by the "choice" of the interaction models in the analysis.

3.1 Introduction of Neutrino Interaction

For the measurement of the neutrino oscillation parameters, the neutrino-nucleus interaction model is used to describe the data quantitatively. However, it is difficult to understand and implement the uncertainties of these models due to the complexity of the nuclear effects. First, this section describes the general description of the neutrino interaction and then introduces NEUT which is a neutrino interaction simulation program used in our analysis.

3.1.1 General Description of the Neutrino Interaction

Neutrino interaction is based on the weak interaction in the Standard Model and the Lagrangian density of neutrino interaction on free nucleon target is given as,

$$\mathscr{L}_{int} = -\frac{g}{2\sqrt{2}} J_{\mu}^{\mathrm{CC}} W^{+\mu} + h.c. - \frac{g}{2cos\theta_W} J_{\mu}^{\mathrm{NC}} Z^{\mu} \tag{3.1}$$

where J_{μ}^{CC} and J_{μ}^{NC} are hadronic currents for CC and NC reactions, $W^{+\mu}$ and Z^{μ} are gauge fields of positively charged boson and neutral weak boson, respectively.

Using this Lagrangian density for free nucleon, that for neutrino-nucleus interaction is written as,

$$\mathscr{L}_{int} = -\frac{G_F}{\sqrt{2}} a J_{\mu}^{h} l^{\mu} + h.c. \tag{3.2}$$

where G_F is the Fermi coupling constant, and J^h_μ and l^μ are hadronic and leptonic current respectively. This Lagrangian density will be used in the later discussion of the neutrino-nucleus interaction. Following this effective interaction Lagrangian, we can calculate the differential cross section and it is given as,

$$\frac{d\sigma}{dq^2} = \frac{1}{32\pi}\frac{1}{M^2E_\nu^2}G_F^2c_{EW}^2L_{\mu\nu}H^{\mu\nu} \tag{3.3}$$

where $L^{\mu\nu}$ is the leptonic tensor and $H_{\mu\nu}$ is the hadronic tensor. The leptonic tensor can be given as,

$$L^{\mu\nu} = 8\left[k^\mu k'^\nu + k'^\mu k^\nu - g^{\mu\nu}k\dot{k}' \pm i\epsilon^{\mu\nu\alpha\beta}k'_\alpha k_\beta\right]. \tag{3.4}$$

While $L^{\mu\nu}$ can be written easily, the hadronic tensor can not be given simply because it includes nuclear physics. Therefore, each neutrino interaction model yields a different cross section due to the treatment of the hadronic tensor.

3.1.2 Neutrino Interaction Simulation using NEUT

In our oscillation analysis in the T2K experiment, the cross section of the neutrino interactions is calculated using NEUT which is the software to simulate neutrino-nucleus interaction [41]. NEUT focuses on a precise neutrino-nucleus scattering simulation as with the GENIE [52], NuWro [53], NUANCE [54] and GIBUU [55]. NEUT was originally developed for studying atmospheric neutrino and nucleon decay in SK, and so far has been developed by many physicists for the Kamiokande series of experiments including the T2K experiment. It is capable of simulating the interaction for neutrinos between 100 MeV and a few TeV of energy in a number of the reaction channels. This energy region is well-suited for the analysis in the T2K experiment.

3.2 Neutrino-Nucleon Interaction

In the current oscillation analysis, a set of neutrino interaction models is used as the baseline model which is plausible. This section will explain the theory description of the neutrino interaction with a single nucleon. In the energy region of the T2K, such interactions are dominant and the understanding of their models is essential. The nuclear effects including multi-body effects will be described in the next section.

3.2.1 Charged Current Quasi Elastic (CCQE) Interaction

Charged current quasi elastic (CCQE) interaction is a two-body reaction of neutrinos and nucleons as shown in Fig.3.1. The fundamental neutrino interaction for the CCQE scattering is given by :

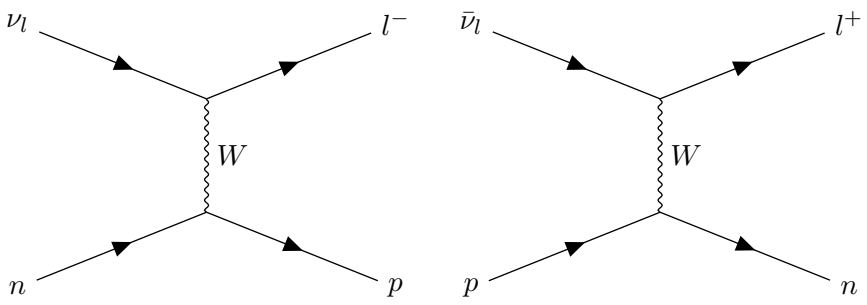

Figure 3.1: Diagrams of CCQE neutrino (left) and anti-neutrino (right) interactions.

$$\nu_l(k) + n(p) \to l^-(k') + p(p') \tag{3.5}$$
$$\bar{\nu}_l(k) + n(p) \to l^+(k') + p(p'). \tag{3.6}$$

On the other hand, that for the neutral current is written as,

$$\nu_l(k) + n(p) \to \nu_l(k') + n(p') \tag{3.7}$$
$$\bar{\nu}_l(k) + n(p) \to l^+(k') + p(p') \tag{3.8}$$

where $l = e, \mu, \tau$. These CCQE interactions are commonly described using Llewellyn-Smith formalization [56].

Using Eq. 3.2, the invariant matrix for these reactions is written as

$$\mathscr{M} = \frac{G_F}{\sqrt{2}} \cos\theta_C l_\mu J^\mu \tag{3.9}$$

where θ_C is the Cabibbo angle, l_μ is the leptonic current and J^μ is the hadronic current. This hadronic current can be separated into two components which consist of the vector and axial vector parts and given as,

$$\begin{aligned} J^\mu &= \bar{u}(k')\Gamma_\mu u(k) \\ &= \bar{u}(k')(V_\mu - A_\mu)u(k) \end{aligned} \tag{3.10}$$

where V_μ is the vector part and A_μ is the axial part respectively. For each part, the matrix

elements with each nucleon can be calculated as follows,

$$\begin{aligned}\left\langle N'(p')\middle|V_\mu\middle|N(p)\right\rangle &= \bar{u}(p')\left[\gamma_\mu f_1(Q^2) + i\sigma_{\mu\nu}\frac{q^\nu}{M+M'}f_2(Q^2)\right. \\ &+ \left.\frac{2q_\mu}{(M+M')}f_3(Q^2)\right]u(p)\end{aligned} \tag{3.11}$$

$$\begin{aligned}\left\langle N'(p')\middle|A_\mu\middle|N(p)\right\rangle &= \bar{u}(p')\left[\gamma_\mu\gamma_5 g_1(Q^2) + i\sigma_{\mu\nu}\frac{q^\nu}{M+M'}\gamma_5 g_2(Q^2)\right. \\ &+ \left.\frac{2q_\mu}{(M+M')}\gamma_5 g_3(Q^2)\right]u(p)\end{aligned} \tag{3.12}$$

where N', N are each nucleon(n, p), Q^2 is the four momentum transfer squared, and M, M' are the masses of the initial and the final nucleon respectively.

Given these equations and using the Mandelstam variables s, t, u the differential cross section for Q^2 is written as,

$$\frac{d\sigma}{dQ^2} = \frac{G_F^2 M^2\cos^2\theta_C}{8\pi E_\nu^2}\left[A(Q^2) \mp B(Q^2)\frac{(s-u)}{M^2} + C(Q^2)\frac{(s-u)^2}{M^4}\right]. \tag{3.13}$$

Here the factors $A(Q^2)$, $B(Q^2)$, and $C(Q^2)$ are written as,

$$\begin{aligned}A(Q^2) &= \frac{m^2-q^2}{4M^2}\left[\left(4-\frac{Q^2}{M^2}\right)g_1^2(q^2) - \left(4+\frac{Q^2}{M^2}\right)f_1^2(Q^2) - \frac{Q^2}{M^2}\left(1+\frac{Q^2}{4M^2}\right)f_2^2(Q^2)\right. \\ &- \frac{4Q^2}{M^2}f_1(Q^2)f_2(Q^2) - \frac{m_l^2}{M^2}\{(f_1(Q^2)+f_2(Q^2)\}^2 + \{g_1(Q^2)+2g_3(Q^2)\}^2 \\ &+ \left.\left(\frac{Q^2}{M^2}-4\right)g_3^2(Q^2)\right]\end{aligned} \tag{3.14}$$

$$B(Q^2) = -\frac{Q^2}{M^2}g_1^2(Q^2)\left[f_1(Q^2)+f_2(Q^2)\right] \tag{3.15}$$

$$C(Q^2) = \frac{1}{4}\left[g_1^2(Q^2) + (f_1(Q^2))^2 - \frac{Q^2}{4M^2}(f_2(Q^2))^2\right] \tag{3.16}$$

where $f_{1,2}$ are the vector form factors and f_3 is the scalar form factor. The factors $g_{1,2}$ are the axial-vector form factors and g_3 is the pseudoscalar form factor. Especially axial vector form factor $(g_1(Q^2))$ is parametrized as a dipole model in our analysis,

$$g_1(q^2) = g_A(0)\left[1-\frac{q^2}{M_A^2}\right]^{-2} \tag{3.17}$$

where $g_A(0)$ is determined by the β decay experiments [57]. M_A is called the axial mass which is determined by the several neutrino scattering experiments (NUISANCE [58], ANL [59], BNL [60] [61], BEBC [62], and FNAL [63]) and it takes an important role in the history of neutrino interaction which is represented by "MiniBooNE M_A puzzle" [64]. This problem was first indicated by the K2K experiment [65]. Measurement results by the MiniBooNE experiment indicated $M_A = 1.35 \pm 0.17$ MeV/c^2 which was much higher than the world average by the bubble chamber data for higher neutrino energy ($M_A = 1.03$ MeV/c^2). This discrepancy is now considered as the contribution of multi-nucleon correlation especially at low Q^2 region and it will be described in Sec. 3.3.2. In our current analysis, M_A is set to 1.03 ± 0.06 MeV/c^2 as the pre-fit value which is given by the global fit results [66].

3.2.2 Single Pion Production

Single pion production for the neutrino interactions can be divided into two main categories: resonant pion production and coherent pion production which are described in this subsection.

Resonant Pion Production

Resonant pion production occurs when the exchange boson has the four momenta necessary to excite the target nucleon to the resonance state which decays to produce a final-state pion. In general, the resonant pion production channels of the neutrino interaction are shown in Fig.3.2 and for the charged-current interactions are written as,

$$\begin{aligned}
\nu_l(k) + p(p) &\to l^-(k') + p(p') + \pi^+(t) \\
\nu_l(k) + n(p) &\to l^-(k') + n(p') + \pi^+(t) \\
\nu_l(k) + n(p) &\to l^-(k') + p(p') + \pi^0(t)
\end{aligned} \tag{3.18}$$

and for the neutral current interactions as:

$$\begin{aligned}
\nu_l(k) + p(p) &\to \nu_l(k') + n(p') + \pi^+(t) \\
\nu_l(k) + p(p) &\to \nu_l(k') + p(p') + \pi^0(t) \\
\nu_l(k) + n(p) &\to \nu_l(k') + n(p') + \pi^0(t) \\
\nu_l(k) + n(p) &\to \nu_l(k') + p(p') + \pi^-(t).
\end{aligned} \tag{3.19}$$

Rein Sehgal model [67] is used to describe the resonant pion production model and 18 baryon resonances are taken into account in invariant mass $W < 2$ GeV. In the Rein-Sehgal model, non-resonant isospin $I = 1/2$ background contribution is also added incoherently. On the other hand, the lepton mass effect is not considered in the Rein-Sehgal model. In NEUT, that effect is calculated based on Ref. [68]. Furthermore, there is the structure of the nucleon in the single pion production as with the CCQE interaction.

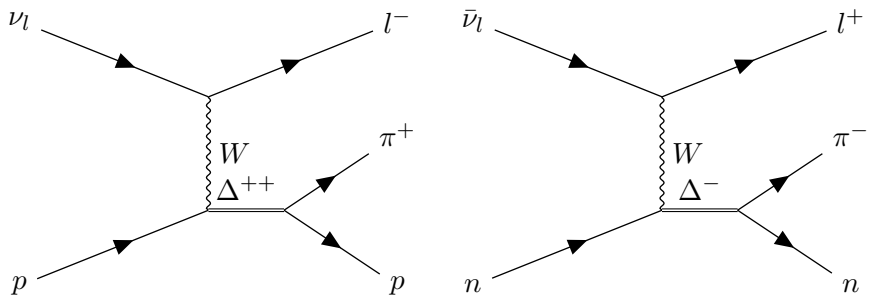

Figure 3.2: Diagrams of CC resonant pion production with neutrino (left) and anti-neutrino (right).

The $\Delta^{++}(1232)$ is the dominant mode in the T2K energy region of the pion production. The form factor of the $\Delta^{++}(1232)$ is the calculated based on Ref. [69]. It is separated into axial part and vector part as with the CCQE interaction and how it is determined will be described in Sec. 4.3. In NEUT, a second-order derivative ($W(\theta, \phi) = \frac{d\sigma}{d\Omega} = \frac{d^2\sigma}{dQ^2 dW}$) is introduced to generate the interaction events within the Rein-Sehgal model. This value is calculated using the density matrix elements calculated by the Fynman-Kislinger-Ravndal (FKR) model [70] as the transition from N to Δ.

Coherent Pion Production

Coherent pion production is a reaction where neutrinos interact on the whole nucleus without knocking out any nucleon. It contributes especially to the cross section at low Q^2 region of the single pion production and the cross section is small compared to the resonant pion production in the T2K energy region. In past NEUT, the Rein-Sehgal model [71, 72] based on Partially Conserved Axial Current (PCAC) [73] was originally used to simulate the coherent pion production. However, it is well known that the prediction of this model does not match the data at the lower energy region. Thus, the current model in NEUT is tuned to the Berger-Sehgal model [74]. The Berger-Sehgal model predicts the better agreements at the low Q^2 region with data of MINERνA experiment [75].

3.2.3 Deep Inelastic Scattering (DIS)

In deep inelastic scattering (DIS) interactions, the neutrino directly interacts with a quark inside a nucleon. The DIS interactions become dominant in the neutrino energy more than a few GeV which is much larger than the typical T2K beam energy. In NEUT, the measurement results are well implemented for $W > 2$ GeV using PYTHIA [76]. On the other hand, for $W < 2$ GeV, the DIS interactions are calculated using a parton distribution function (PDF) with Bodek-Yang (BY) correction [77]. This correction improved the form factors for the DIS at low W region. There is a little uncertainty which is implemented as a fraction of the difference between the GRV98 PDFs with and without the BY correction.

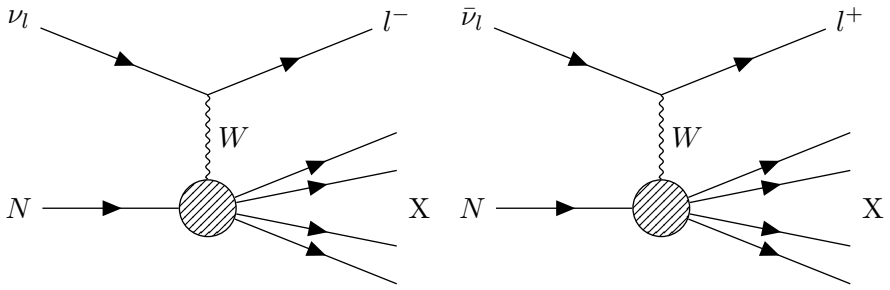

Figure 3.3: Example diagrams of DIS neutrino (left) and anti-neutrino (right) interactions.

3.3 Nuclear Effects

In the previous section, we introduce the basics of the neutrino interaction with a nucleus and form factors. However, several nuclear effects such as the Fermi motion, and nucleon-nucleon correlation should be considered to treat the neutrino-nucleus interactions more sophisticatedly. This section describes how nuclear effects are modeled in our analysis. First, we will describe the nuclear modeling of the fundamental CCQE interaction. Then, we will explain 2 particle 2 hole interaction related to the short-range correlation between nucleus. Furthermore, several effects that are related to the strong interaction and the electrostatic interaction inside the nucleus will be described.

3.3.1 Nuclear Modeling for CCQE Interaction

In this subsection, first, we will describe the Relativistic Fermi Gas (RFG) model which was used in the past analysis for the CCQE components. Then, we will introduce the Benhar Spectral Function (SF) model used in the current analysis.

Relativistic Fermi Gas Model

Relativistic Fermi Gas (RFG) model [78] is one of the common nuclear models and used for the analysis in several neutrino experiments including the past analysis in the T2K. In the RFG model, it is assumed that all nucleons behave as an ideal Fermi gas uniformly spreading in a nucleus. The momentum states are filled up from the ground state to the highest state. This highest momentum state is called Fermi momentum (p_{Fp}). The Fermi momentum of the RFG model is given as the constant with the radius of the Fermi sphere (ρ_p) as follows,

$$p_{Fp} = (3\pi^2\rho_p)^{\frac{1}{3}}. \tag{3.20}$$

This Fermi momentum is extracted from the electron scattering data, and $p_F = 217$ MeV/c for Carbon and $p_F = 225$ MeV/c for Oxygen in NEUT. The RFG model prohibits interactions that scatter nucleons with momenta below this Fermi momentum due to the Pauli exclusion principle. Thus, momentum distributions of a nucleon can be given with the binding energy

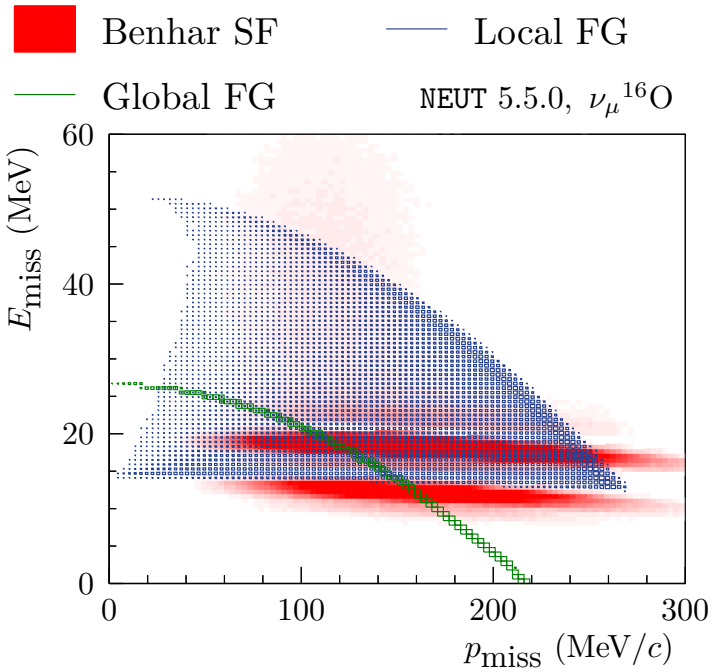

Figure 3.4: Comparison of the missing energy and missing momentum distributions for SF (red-shaded region), LFG (blue-shaded region) and Global Fermi gas (green-shaded region) models for oxygen in NEUT. Taken from [41].

(E_b) to describe Fermi motion effect,

$$P(\vec{p}, E) = \theta(p_F - |\vec{p}|)\delta(E + \sqrt{M_N^2 + |\vec{p}|^2} - E_b). \tag{3.21}$$

Here θ is the step function and M_N is the mass of a nucleon. The RFG model itself cannot consider the long-range correlation between nucleons and then Random Phase Approximation (RPA) [79] is used to describe it in NEUT. The RPA is originally to describe the excited states of nuclei and suppresses the cross section at low Q^2 region.

Spectral Function Model

Benhar Spectral Function (SF) [80] is a model to describe nuclear effects, especially for CCQE components. This model is based on the impulse approximation, and momenta of nucleons and nuclear removal energies which corresponds to the binding energy in the Fermi gas model are implemented two-dimensionally. This two-dimensional probability function is extrapolated from the electron scattering experiments based on the shell model. In that sense, the SF model is more sophisticated to describe the nuclear effects in the neutrino interactions. As a result, the SF model is that the electron scattering data agrees better with the SF model than the RFG model. Therefore, this SF model is used in our oscillation analysis.

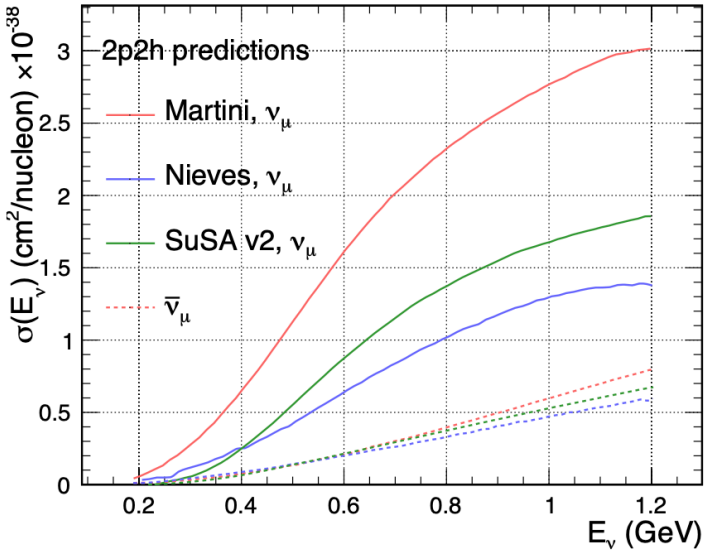

Figure 3.5: Comparison of cross section predictions for Nieves, Martini and SuSA v2 models. Taken from [84].

As shown in Fig. 3.4, each nuclear model predicts clearly different missing energy and momentum distributions. The local Fermi gas model will be introduced in Sec. 3.4.2.

3.3.2 2 Particle 2 Hole Interaction (2p2h Interaction)

As discussed in the previous section, we introduced the RPA to describe the long range correlation between nucleons. However, electron scattering experiments indicate the existence of 2 particle 2 hole interaction (2p2h interaction) which derives from the short-range correlation between nucleons. The 2p2h is an interaction where two correlated nucleons interact via meson exchange and nucleon-nucleon correlation. In NEUT, the Nieves model is adopted to describe the 2p2h interaction [81]. To consider the variation for the different 2p2h interaction models such as Martini et al. model [82] and SuSAv2 [83], several parameters are introduced to cover that uncertainty and predictions of these three models are shown in Fig. 3.5.

3.3.3 Final State Interaction (FSI)

The pions from neutrino interaction can be absorbed, exchange charge, transfer energy, change direction or produce more pions inside the nucleus as shown in Fig. 3.6. It is due to the various processes with nucleons through strong interaction and it is called final state interaction (FSI). The outgoing pion kinematics from the neutrino interactions can be changed by the FSI. Furthermore, the single pion production events can be misidentified as the CCQE events by the pion absorption of the FSI. Such changing kinematics and misidentifications have a large impact on our analysis. Furthermore, the outgoing particles also interact with the detector materials before being detected. Such reactions are referred to as Secondary Interaction (SI).

In NEUT, the semi-classical nuclear cascade model by Salcedo and Oset [85] is adopted for lower momentum pion ($p_\pi < 500$ MeV/c). For higher momentum pion, it is mainly tuned to modern π-A scattering data [86].

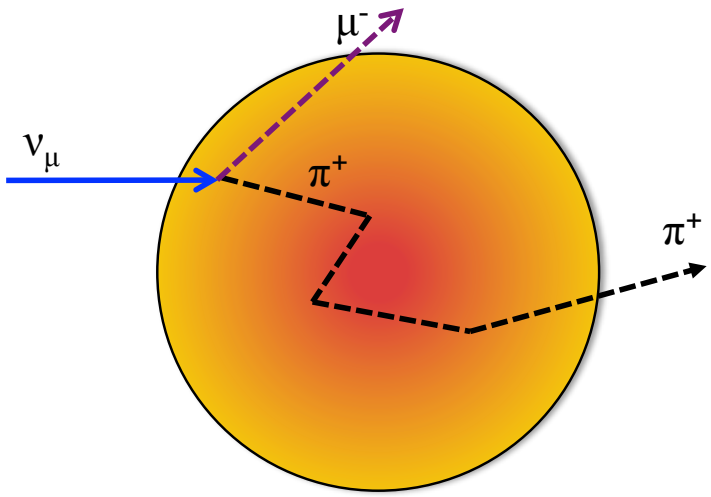

Figure 3.6: Image of final state interaction of a pion in the nucleon.

3.3.4 Coulomb Correction

In a charged-current neutrino-nucleus interaction, the electrostatic interaction between residual nucleons and outgoing charged leptons can shift the lepton's momentum. This shift is taken into account as the Coulomb correction and its size is determined with the electron scattering data [87].

3.4 Alternative Neutrino Interaction Models

As described in Sec. 3.2 and 3.3, the several neutrino interaction models are used as the baseline models in our analysis. On the other hand, there are some alternative model candidates which are not considered in our analysis. Thus, our choice of the baseline models can be a potential bias in the analysis. The effects on the analysis results will be discussed in Chapter 6 and the theoretical descriptions of these models are explained in this section. The alternative models and corresponding nominal models which should be considered in our analysis are summarized in Tab. 3.1. We will describe each alternative model in order.

3.4.1 Alternative Axial Form Factors

A Dipole model is used in our current oscillation analysis to describe the axial form factor as mentioned in Sec 3.3.1. However, this model cannot describe well bubble chamber data for high momentum transfer region and three parameters are implemented to cover it in the current

Table 3.1: Summary of the alternative neutrino interaction models used in our analysis.

	Nominal Model	Alternative Model
Axial Form Factor	Di-pole Model	Z-expansion 3-Component
Nuclear Model	SF Model	LFG Model CRPA Model
Single Pion Production	Rein-Sehgal Model	Martini Model Pion Kinematics Alternation Low Q^2 Suppression Derived From MINERνA

analysis. To confirm the robustness of this model itself, we should take into account for the alternative model of the axial form factors. The Z-expansion [88] and 3-Component models are considered as representatives.

Z-Expansion The Z-expansion model is based on the QCD sum rules and the axial form factor of this model is given as the Taylor expansion of Q^2 as follows,

$$F_A(Q^2) = \sum_{k=0}^{\infty} a_k z(Q^2)^k. \tag{3.22}$$

Here a_k is a coefficient which is bounded to guarantee the convergence of the series and z is defined as,

$$z = \frac{\sqrt{t_c + Q^2} - \sqrt{t_c - t_0}}{\sqrt{t_c + Q^2} + \sqrt{t_c - t_0}} \tag{3.23}$$

where $t_c = 9m_\pi^2$ and $t_0 = -0.280$ GeV^2. The value of t_0 is chosen to ensure that the maximum size of $|z|$ is small enough for specific Q^2 region which interest T2K.

3-Component The 2-Component model originally was introduced to describe the deviation of the data from the dipole model for the form factors of a nucleon [89]. The form factor of this model is given as,

$$F_A(Q^2) = g_A(1 + \gamma Q^2)^{-2} \times \left(1 - \alpha + \alpha \frac{m_\alpha^2}{m_\alpha^2 + Q^2}\right) \tag{3.24}$$

where $g_A(1 + \gamma Q^2)^{-2}$ with free parameter γ describes the form factors from the quark core of the nucleon. The rest of the equation with free parameter α represents the axial meson quark-antiquark cloud. However, this 2-Component model cannot describe properly high Q^2 region of the bubble chamber data. The 3-Component model has the additional shape freedom compared

to the 2-Component model and is written as,

$$F_A(Q^2) = g_A(1+\gamma Q^2)^{-2} \times \left(1 - \alpha + \alpha \frac{m_\alpha^2}{m_\alpha^2 + Q^2}\right) + g_A \theta' Q^2 e^{-\beta Q^2} \tag{3.25}$$

where $\theta' = sign(\theta)\sqrt{|\theta|\beta}$, and θ and β are the additional free parameters.

In NEUT, the parameters of these two alternative models are tuned to the bubble chamber data. Figure 3.7 shows the comparisons of the form factor as a function of Q^2 with the dipole model.

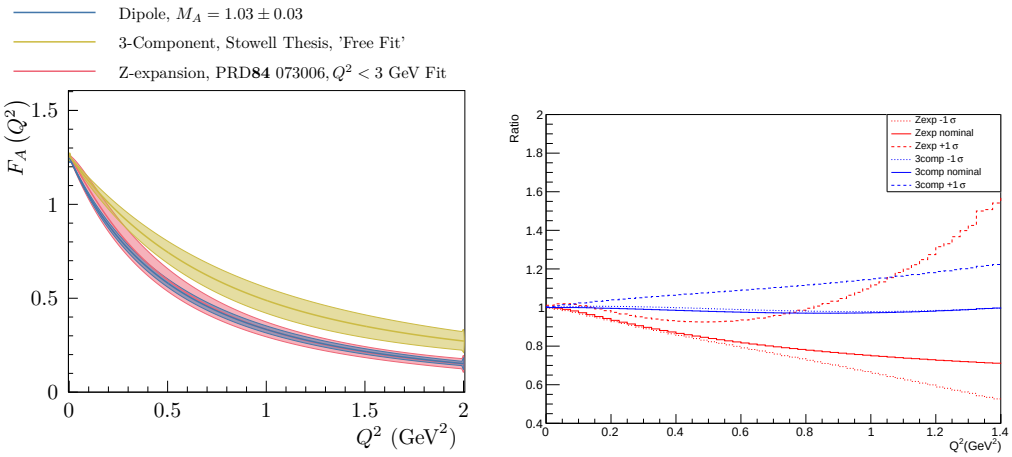

Figure 3.7: The form factors for the di-pole, Z-expansion and 3-Component models with uncertainties as a function of Q^2 (left) and the ratio to the dipole model for the alternative form factor models as a function of Q^2 (right).

3.4.2 Alternative Nuclear Model

Local Fermi Gas (LFG) Model

In the RFG model, it is assumed that the nucleon density is uniform in each nucleon. For a more sophisticated approach, local density should be considered and local Fermi gas (LFG) model is the natural extension to cover it. The nuclear density $\rho(r)$ is extrapolated from the electron scattering measurements and Fermi momentum (p_{Fn}) is formalized in the LFG model as,

$$p_{Fn} = (3\pi^2 \rho_n(r))^{\frac{1}{3}}. \tag{3.26}$$

The LFG model is also combined with Random Phase Approximation (RPA) to describe the long-range correlation as with the RFG model.

Continuous Random Phase Approximation (CRPA) Model

As discussed in the previous section, several Fermi gas models are used to describe the nuclear effects of the neutrino-nucleus interactions. However, there is a discrepancy between the prediction of these models and data especially at low Q^2 region. Continuous RPA (CRPA) model (Hartree Fock + CRPA model) is originally motivated by that discrepancy [90].

In this approach, the nuclear correlation contributions such as the particle-hole excitations are treated in the way of the Green's function based on the calculation with the Hartree Fock approach. One of the important characters of this model is that it has different effect on each target, each flavor of neutrino and anti-neutrino. It indicated the unique impact on the analysis, for example, the CCQE cross section as a function of low Q^2 differs significantly between the near and far detectors compared to the other models. In spite of the agreement at that low Q^2 region, there are difficulties to parametrize this model for our analysis unlike to the other Fermi gas models. Hence, this model is not used as the baseline model in our analysis directly.

3.4.3 Alternative Models for the Single Pion Production

Martini Model for Single Pion Production

The Martini model [82, 91] is to describe the multi-nucleon effect over a wide range of neutrino energy based on the calculation using RPA and the Δ resonance excitations. A main difference to the nominal pion production model in NEUT is that the Martini model can include the nuclear effect with the theoretical calculation.

Pion Kinematics Alternation Related to $\Delta(1232)$ Resonance

In NEUT, the cross section of $\Delta(1232)$ resonance is calculated with the density matrix elements based on the Rein Sehgal model as discussed in the previous section. However, there is no rich theoretical ground for the density matrix to calculate the differential cross section. Thus, so far, they are defined 30% variation of the cross section as 1σ error in our analysis by comparing data and model predictions [70]. The 1σ (-1σ) variation of this alternation increase (decrease) the cross section at low pion momentum region.

Low Q^2 Suppression Derived from MINERνA Experiment

The MINERνA experiment data showed that the number of events in single pion production at low Q^2 region is over-predicted in NEUT. To take into account this suppression effect in the MINERνA data, we created the simulated data used in the robustness study which will be discussed later.

Chapter 4

Neutrino Oscillation Analysis

This chapter describes the method of neutrino oscillation analysis. We analyze the data of the near detector and the far detector to measure the oscillation parameters.

4.1 Flow of Oscillation Analysis

Oscillation analysis is performed by comparing the number of events and the energy spectra of data and simulation prediction at SK. The number of events of MC predictions at certain energy E_ν at the far detector are given as,

$$N_{SK}(E_\nu, \theta) = \phi_{SK}(E_\nu)\sigma(E_\nu)\epsilon_{SK}(E_\nu)P(\nu_\alpha \to \nu_\beta, E_\nu, \theta) \tag{4.1}$$

where $N_{SK}(E_\nu, \theta)$ is the number of ν_β events, $\phi_{SK}(E_\nu)$ is the neutrino flux, $\sigma(E_\nu)$ is the neutrino-nucleus interaction cross-section, $\epsilon_{SK}(E_\nu)$ is the detection efficiency of SK and $P(\nu_\alpha \to \nu_\beta, E_\nu, \theta)$ is the oscillation probabilities from ν_α to ν_β.

However, there is a systematic uncertainty by the uncertainties of neutrino interaction and beam flux models via the prediction at certain neutrino energy. In the T2K experiment, there are mainly two ways to measure the oscillation parameters while reducing such systematic uncertainties. One is a frequentist way and the other one is a Bayesian analysis way. This thesis discusses mainly the frequentist way. Figure 4.1 shows the overview of the analysis flow in our frequentist way. First, we build the models for flux, neutrino interaction, and the near and far detectors. The tunings and uncertainties of these models are given by the external experimental data and theory. Next, near detector fit is performed by comparing the prediction from these models and the data of the near detector. Systematic uncertainties of neutrino interaction and flux are reduced by the near detector fit. Finally, values of oscillation parameters are derivable by comparing the data and MC prediction at the far detector.

Each section of this chapter explains the details of those analyses in order.

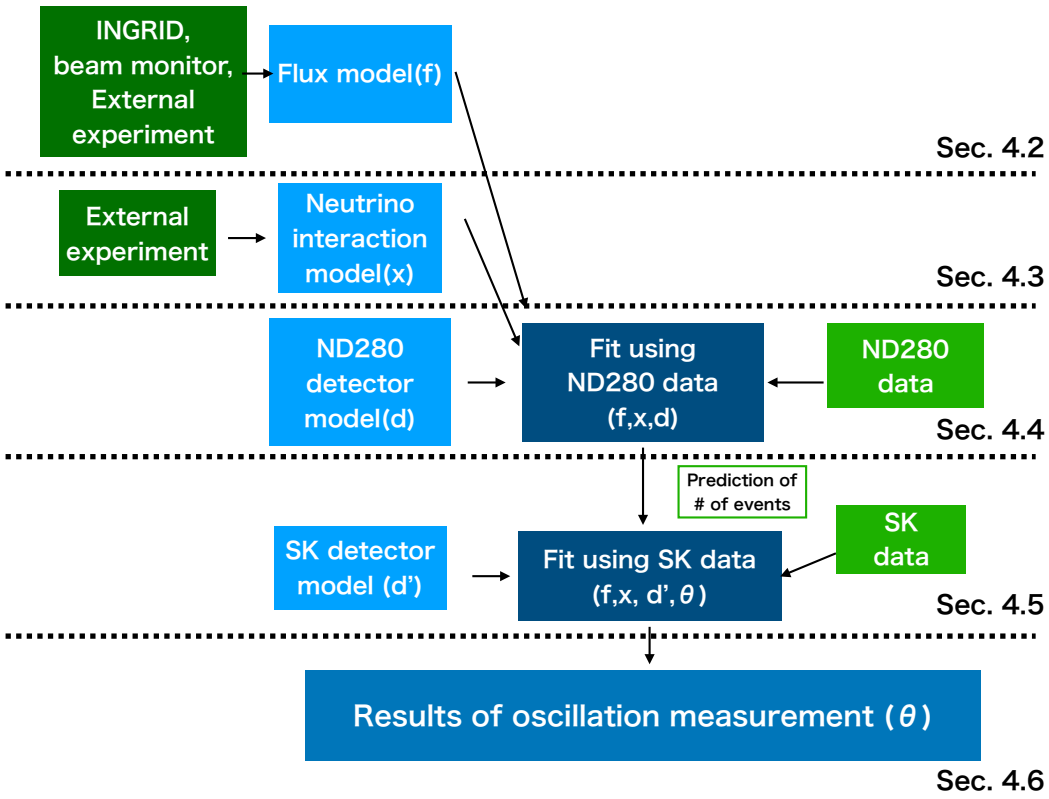

Figure 4.1: Overview of our oscillation analysis in the T2K experiment. Section 4.2 describes the neutrino flux model which is based on the neutrino beam monitor and the external experiment data. Section 4.3 explains the neutrino interaction model whose uncertainty is the main source of the systematic uncertainty of our analysis. Sections 4.4 and 4.5 describe the detail of the near and far detector fit. In Sec. 4.6, we will discuss the results of our oscillation measurement.

4.2 Neutrino Flux

4.2.1 Neutrino Flux Model and Prediction

In our analysis, FLUKA [92] is used to simulate the hadronic production in the target. These hadronic interactions are tuned by the data of the NA61/SHINE experiment [93]. Next, the tracks and decays of outgoing particles from the target are simulated with JNUBEAM [94] which is a GEANT3-based software package. Figure 4.2 shows the flux predictions with a series of these simulations for each neutrino flavor at the near and far detectors.

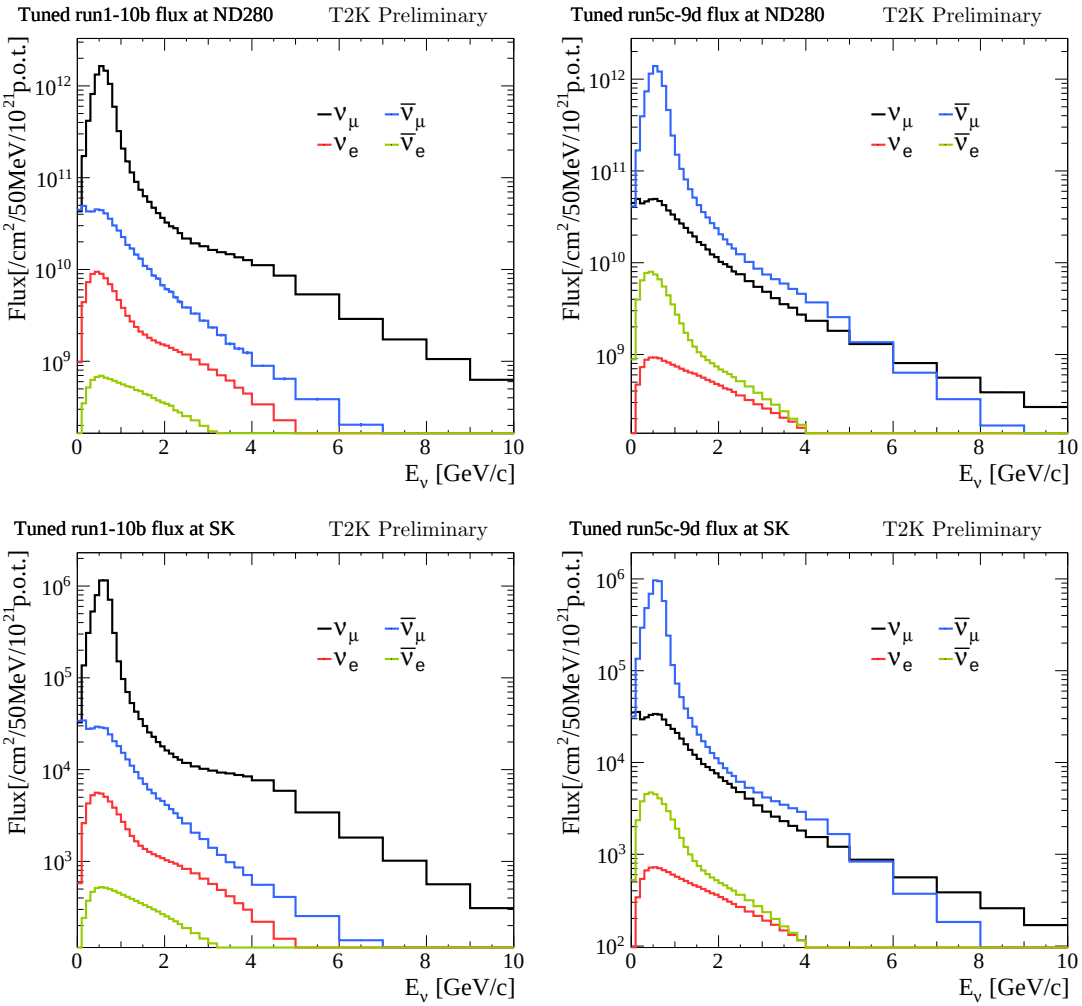

Figure 4.2: Prediction of neutrino flux in neutrino mode (left) and anti-neutrino mode (right) at ND280 (top) and SK (bottom).

4.2.2 Systematic Uncertainty of Neutrino Flux

There are several systematic uncertainty sources for neutrino flux, such as the hadron interactions, alignment and modeling of the beam line, horn current and field, and proton beam profiles. Figure 4.3 shows the fractional errors for each systematic source as a function of neutrino energy. The uncertainty which is driven by the hadron interaction dominates. As for the rest of the sources, the proton beam profile is most important for right-sign ν_μ since it causes peak energy shift due to its neutrino beam direction change. Beam alignment and horn filed asymmetries are important for wrong-sing ν_μ.

The errors for this analysis ($\sim 5\%$) are smaller than those of the past analysis ($\sim 9\%$) near the peak of the neutrino flux since the large uncertainties which are driven by proton production cross section are drastically reduced by using the data on a replica of the T2K production target in the NA61/SHINE [95].

Figure 4.4 shows the covariance matrix of the flux uncertainty which is used as the input of the near detector fit. There are strong correlations between near detector flux and far detector flux parts. Thus, uncertainties of far detector flux are strongly constrained by measuring near detector flux via the correlation. Binning for ν energy of this covariance matrix is as follows,

- 1 - 25 : ND280 ν mode
- 26 - 50 : ND280 anti-ν mode
- 51 - 75 : SK ν mode
- 76 - 100 : SK anti-ν mode

4.3 Parametrization of Neutrino Interaction Model

As described in Sec. 3.2, we used several neutrino interaction models as baseline models for our oscillation analysis. Almost all systematic parameters of the interaction models are implemented as normalization or shape parameters. The normalization parameters are applied as weights that affect all specific interaction events, while weights for shape parametrization are applied as the response functions of the kinematics information for the outgoing particles.

Cross section parameters are explained in detail below. Tables 4.1 and 4.2 summarize the nominal values, the uncertainties, and the parameter types of the cross section parameters

CCQE parameters

- M_A^{QE}: This parameter is the nucleon axial mass and its tunings and uncertainties are given by the global fit results as mentioned in Sec. 3.2.
- High Q^2 normalization: Theoretical uncertainty of high Q^2 region is large due to a lack of understanding of axial components in the neutrino-nucleus interaction. The uncertainties

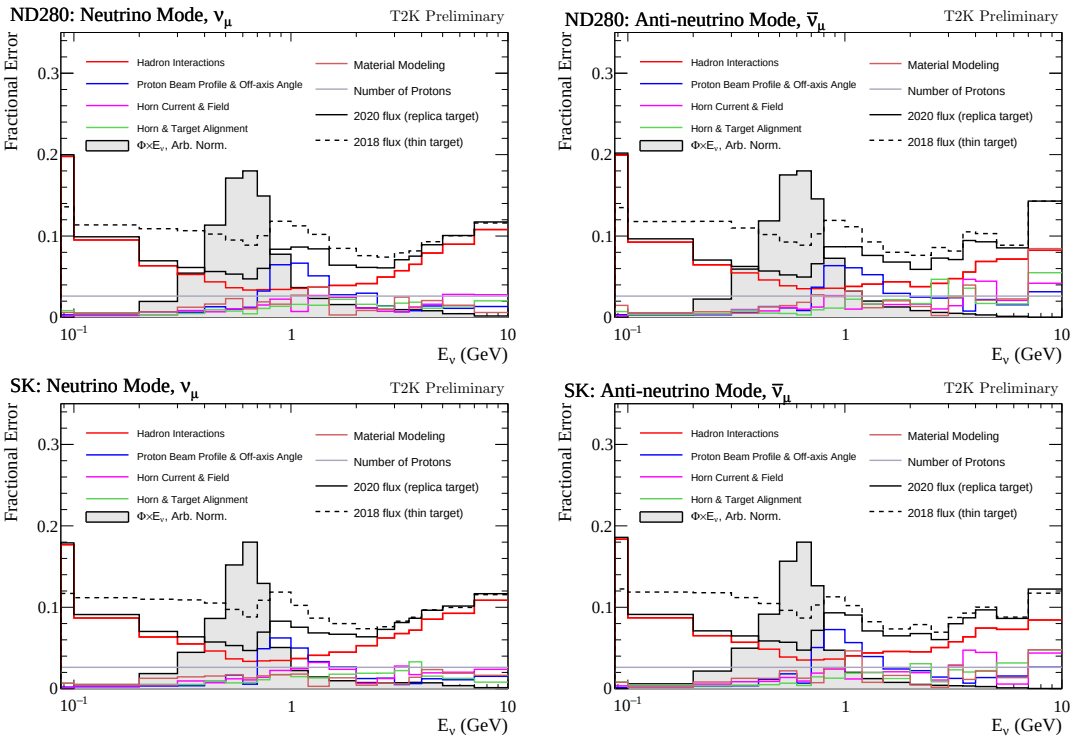

Figure 4.3: Uncertainty on the right sign neutrino flux in neutrino mode (left) and antineutrino mode (right) at ND280 (top) and SK (bottom), broken down by the sources (hadron interaction, proton beam profile, horn current, and alighnment) of uncertainty. The gray-shaded region shows the shape of the neutrino flux in the T2K experiment.

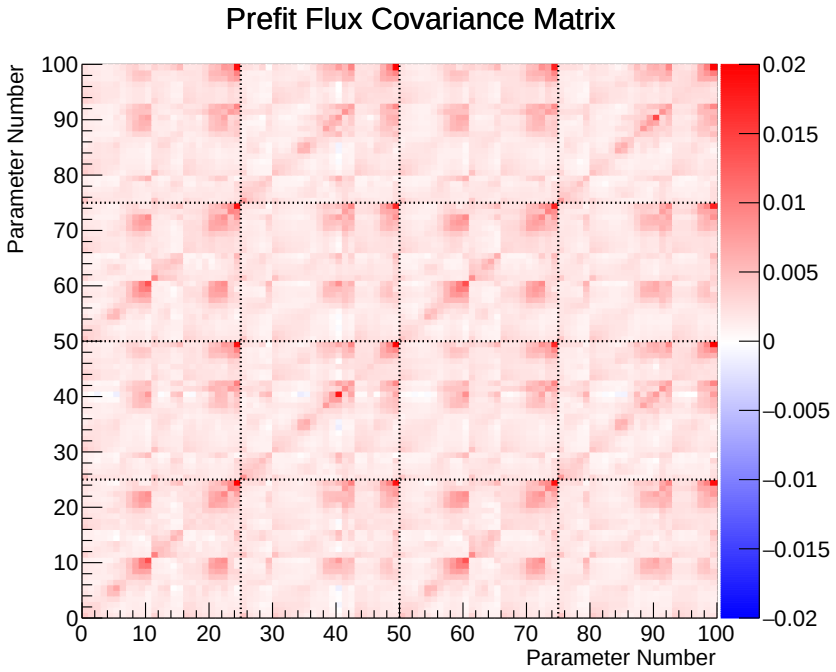

Figure 4.4: Flux covariance matrix for our oscillation analysis. The parameter number corresponds to the bin number of each neutrino energy.

of high Q^2 parameters are determined by the comparison of the dipole model with the Z-expansion model. Three parameters are introduced for three bins for Q^2(0.25-0.50 GeV^2, 0.50-1.0 GeV^2 and $>$ 1.0 GeV^2).

- Low Q^2 normalization: There is a lack of theoretical background for Q^2 parameters in SF model as described in Sec. 3.3. Thus, five low Q^2 parameters for five bins for Q^2 (0.00-0.05 GeV^2, 0.05-0.10 GeV^2, 0.10-0.15 GeV^2, 0.15-0.20 GeV^2 and 0.20-0.25 GeV^2) are treated as free parameters.

- Removal energy (E_b) : There are four removal energy parameters for oxygen or carbon target and neutrino or anti-neutrino. Compared to the past oscillation analysis, the uncertainties are drastically reduced by using the SF model and applying the electron scattering data. The details of this parameter are described in this paper [96].

2p2h parameters

- 2p2h normalization : This parameter describes the uncertainty of the normalization of the specific 2p2h contributions to the CC0π event topology. There are three parameters and two of them are overall normalization for neutrino or anti-neutrino 2p2h events. The other is to describe the ratio of 2p2h events on carbon to those on oxygen.

- 2p2h shape : The 2p2h shape parameters to cover the uncertainties of shifts in the transferred energy and transferred three momentum phase space between Δ or non-Δ like con-

tributions to 2p2h interaction. There are two shape parameters for each target (carbon or oxygen).

- 2p2h energy dependence : This parameter is to cover the theoretical discrepancy between Nieves, Martini, and SuSA v2 models as described in Sec. 3.3.2. There are four parameters to control the energy dependence of 2p2h interactions below and above $E_\nu = 600$ MeV for neutrino and anti-neutrino.

Single pion production parameters

- M_A^{RES} : This parameter is axial mass of the resonance production. This value is tuned with the several deuteron bubble chamber data (ANL [97, 98] and BNL [99, 100]).
- C_5^A : This parameter is to control the coefficient of the axial form factor of resonance production. This value corresponds to the axial form factor at zero transferred four momentum.
- $I_{1/2}$: This parameter is to control the normalization of $I_{1/2}$ isospin non-resonant pion production channels.
- $I_{1/2}$ for low momentum pions : This parameter is implemented to introduce the extra freedom of non-resonant pion production induced by anti-neutrino. This value is not constrained by near detector fit and the uncertainty is 100%.
- CC and NC Coherent : These parameters are to control the normalizations of CC and NC coherent cross sections. There are four parameters for each target (carbon or oxygen) and NC or CC scattering. Nominal values are determined by the calculation based on the Rein-Sehgal model. However, MINERνA data indicated a 30% difference and it is assigned to the uncertainty of this value.

DIS parameters

- CC Bodek-Yang DIS and Multi-Pi : This parameter is to treat the difference between with and without Bodek-Yang correction for DIS interaction in NEUT. This parameter is separated into two parameters for invariant mass W $<$ 2 GeV (multi-π) and W $>$ 2 GeV (DIS) interactions.
- CC AGKY Multi-Pi : This parameter is to consider the difference between our nominal model and AGKY model [101] for multi-π interactions.
- CC DIS Mult-Pi Norm ν, $\bar{\nu}$: This parameter is introduced to the normalization uncertainties by the difference between the NEUT nominal model and the world average measurements [102]. It is separated for ν and $\bar{\nu}$ interactions.
- CC Misc. : This parameter is to control the normalization of the other DIS events including several hadrons such as η and K which are not major contributions to the DIS event topology in the T2K experiment.

FSI parameters

Five shape parameters (π-FSI QE (Quasi Elastic scattering of pions), π-FSI QE for high E, π-FSI QE for low E, π-FSI Hadron Prod., π-FSI Absorption and Charge Exchange) are introduced to control the components of FSI. Their values and uncertainties are tuned with several physics theory and external experiments as mentioned in Sec. 3.3.3.

ν_e/ν_μ and $\bar{\nu}_e/\bar{\nu}_\mu$ differences

There are two normalization parameters to account for cross section difference between ν_e and ν_μ and that between $\bar{\nu}_e$ and $\bar{\nu}_\mu$. These differences are mainly caused by the mass difference of the outgoing lepton. On the other hand, radiative correction can be a large possible source of these differences. However, this uncertainty has not yet been included in the current analysis as the systematic parameter and it will be discussed in Chapter 6.

Other parameters

In addition to these CC parameters, there are several parameters to control neutral (NC) current processes. There are four following parameters which are applied in our analysis,

- NC 1γ : This parameter is to control the single photon emission process during a non-resonant NC scattering. There are no experimental data, and thus a conservative 100% Gaussian uncertainty is applied to this parameter.
- NC Other normalization : There are two normalization parameters to control the other NC contributions (DIS, multi-π production) for the near detector and the far detector respectively.

Furthermore, there are two normalization parameters in order to control the process of the coulomb effect for the neutrino-nucleus scattering [103, 104].

Table 4.1: Summary of the CCQE cross section parameters.

Parameter	Nominal	Uncertainty	Type
M_A^{QE}	1.03	0.06	Shape
Q^2 norm 0	1	1	Norm
Q^2 norm 1	1	1	Norm
Q^2 norm 2	1	1	Norm
Q^2 norm 3	1	1	Norm
Q^2 norm 4	1	1	Norm
Q^2 norm 5	1	0.11	Norm
Q^2 norm 6	1	0.18	Norm
Q^2 norm 7	1	0.40	Norm
$E_{b,\nu}^C$	2	6	Mom. Shift
$E_{b,\bar{\nu}}^C$	0	6	Mom. Shift
$E_{b,\nu}^O$	4	6	Mom. Shift
$E_{b,\bar{\nu}}^O$	0	6	Mom. Shift

4.4 Near Detector Fit

4.4.1 Overview of Near Detector Fit

The log likelihood for the near detector fit is able to be separated into two components. One accounts for the prior constraint which stems from the previous knowledge based on the external experiments and physics theory ($L_{penalty}$). The other one is the statistical part for the comparison between prediction and data statistics ($L_{stat.}$).

The systematic uncertainties for flux, cross sections, and detectors are modeled as the multivariate Gaussian distributions. Thus the former constraint component can be given as,

$$\begin{aligned} -2\ln L_{penalty} &= -2\ln\left[(2\pi)^{\frac{N_f}{2}}|V_f|^{\frac{1}{2}}\exp\left(-\frac{1}{2}\Delta\vec{f}V_f^{-1}\Delta\vec{f}\right) + (2\pi)^{\frac{N_x}{2}}|V_x|^{\frac{1}{2}}\exp\left(-\frac{1}{2}\Delta\vec{x}V_x^{-1}\Delta\vec{x}\right)\right. \\ &+ \left.(2\pi)^{\frac{N_d}{2}}|V_d|^{\frac{1}{2}}\exp\left(-\frac{1}{2}\Delta\vec{d}V_d^{-1}\Delta\vec{d}\right)\right] \\ &= \Delta\vec{f}(V_f^{-1})\Delta\vec{f} + \Delta\vec{x}(V_x^{-1})\Delta\vec{x} + \Delta\vec{d}(V_d^{-1})\Delta\vec{d} + const. \end{aligned} \tag{4.2}$$

where N_f, N_x and N_d are the number of parameters of flux, cross section, and detector respectively. The vectors $\Delta\vec{f}$, $\Delta\vec{x}$ and $\Delta\vec{d}$ are the deviation of these parameters from nominal values in the given iteration of the fit for each parameter. The operators V_f, V_x and V_d are the covariance matrix of them.

Under the assumption that statistical fluctuation for each bin of data follows Poisson distribution with a Barlow-Beeston correction [105], the latter statistical component is written as,

Table 4.2: Summary of cross section parameters other than CCQE.

Parameter	Nominal	Uncertainty	Type
2p2h norm. ν	1	1	Norm
2p2h norm. $\bar{\nu}$	1	1	Norm
2p2h norm. C to O	1	0.2	Norm
2p2h shape C	0	1	Shape
2p2h shape O	0	1	Shape
2p2h E. dep. low-E_ν	1	1	Shape
2p2h E. dep. high-E_ν	1	1	Shape
2p2h E. dep. low-$E_{\bar{\nu}}$	1	1	Shape
2p2h E. dep. high-$E_{\bar{\nu}}$	1	1	Shape
M_A^{RES}	1.07 GeV	0.15 GeV	Shape
C_5^A	0.96	0.15	Shape
$I_{1/2}$	0.96	0.4	Shape
$I_{1/2}$ low. p_π	0.96	1.3	Shape
CC norm. ν	1.00	0.02	Norm
CC norm. $\bar{\nu}$	1.00	0.01	Norm
ν_e/ν_μ	1.000	0.028	Norm
$\bar{\nu}_e/\bar{\nu}_\mu$	1.000	0.028	Norm
CC BY DIS	0	1	Shape
CC BY Multi-Pi	0	1	Shape
CC AGKY Multi-Pi	0	1	Shape
CC Misc.	1	1	Norm
CC DIS Multi-Pi Norm ν	1.000	0.035	Norm
CC DIS Multi-Pi Norm $\bar{\nu}$	1.000	0.035	Norm
CC Coherent C ν	1.0	0.3	Norm
CC Coherent O $\bar{\nu}$	1.0	0.3	Norm
NC Coherent	1.0	0.3	Norm
NC 1γ	1.0	1	Norm
NC Other Near	1.0	0.3	Norm
NC Other Far	1.0	0.3	Norm
π-FSI QE	1.069	0.313	Shape
π-FSI QE high	1.824	0.859	Shape
π-FSI Hadron Prod.	1.002	1.101	Shape
π-FSI Absorption	1.404	0.432	Shape
π-FSI Charge Exchange	0.697	0.305	Shape

$$\ln L_{stat.} = \sum_{i}^{\text{total number of bin}} \ln\left(\frac{N_i^{data}}{N_i^{MC}(\vec{f},\vec{x},\vec{d})}\right) + N_i^{data} - N_i^{MC}(\vec{f},\vec{x},\vec{d}) - \frac{(\beta_i - 1)^2}{2\sigma_{\beta_i}^2} \quad (4.3)$$

where N_i^{data} is the number of events for i-the bin of data, and N_i^{MC} is that of MC as a function

of flux ($\vec{f}$), cross-section ($\vec{x}$), detector parameters ($\vec{d}$). The factor β_i is the scaling parameter to account for the MC statistical fluctuation based on the Barlow-Beeston correction such that $N_i^{MC} = \beta N_i^{MC,gen}$ where $N_i^{MC,gen}$ is the number of generated events in the simulation. The first three terms represent the Poisson likelihood term and the last term corresponds to the Barlow-Beeston correction. In the limit of infinite MC statistics, this statistical part gives Poisson Likelihood ($\sigma_{\beta_i} \to 0,\ \beta_i \to 1$)

Considering these two contributions, the negative log likelihood is written as,

$$\begin{aligned} -2\ln L_{ND} &= -2\ln L_{stat} - 2\ln L_{penalty} \\ &= -2\sum_i \left[N_i^{data} - N_i^{MC}(\vec{f},\vec{x},\vec{d}) \ln\left(\frac{N_i^{data}}{N_i^{MC}(\vec{f},\vec{x},\vec{d})} \right) \right] - \frac{(\beta_i - 1)^2}{2\sigma_{\beta_i}^2} \\ &+ \Delta\vec{f}(V_f^{-1})\Delta\vec{f} + \Delta\vec{x}(V_x^{-1})\Delta\vec{x} + \Delta\vec{d}(V_d^{-1})\Delta\vec{d} \\ &\equiv \chi^2_{ND280} \end{aligned} \tag{4.4}$$

Here the constant term is dropped and we assume a Gaussian distribution for the β_i and minimize this likelihood for β_i. Thus, the analytic solution for β_i is given as,

$$\beta_i^2 + (N_i^{MC,gen}\sigma_{\beta_i}^2 - 1)\beta_i - N_i^{data}\sigma_{\beta_i}^2 = 0. \tag{4.5}$$

The near detector log likelihood is minimized using the MIGRAD algorithm which is based on the quasi-Newton method in the MINUIT package of ROOT [106]. When the statistics is sufficient, $-2\ln L_{ND}$ can be well approximated to χ^2 distribution based on Wilks' theorem [107]. Thus, χ^2_{ND280} before the minimization is used as the pre-fit χ^2 value and that after the minimization is used as the post-fit χ^2 value.

4.4.2 Event Selection

Near detector data used in the fit

Table 4.3 shows the collected data used in the near detector fit. We used 115.31 $\times$ 10^{19} POT for the ν mode and 83.36 $\times$ 10^{19} POT for the $\bar{\nu}$ mode.

Event Categorization

For the event categorization of the near detector fit, we used the measurement only with FGD and TPC and chose the events where ν_μ or $\bar{\nu}_\nu$ CC interactions took place in FGD and the muon from the interactions is scattered to the TPC. The following six selection criteria are applied to meet this requirement.

- Event bunching : The tracks are grouped in the same beam bunch as one neutrino interaction event to avoid accidental pile-up events.
- Crossing track requirement : It is required that at least one reconstructed track crossing TPC2 or TPC3. This requirement is needed for the momentum measurement and the

Table 4.3: Summary of collected data for the near detector fit.

Run number	Beam mode	POT at ND280 ($\times 10^{19}$)
2	ν mode	7.93
3	ν mode	15.81
4	ν mode	34.26
5	$\bar{\nu}$ mode	4.35
6	$\bar{\nu}$ mode	34.09
7	$\bar{\nu}$ mode	24.38
8	ν mode	57.31
9	$\bar{\nu}$ mode	20.54
Total	ν mode	115.31
Total	$\bar{\nu}$ mode	83.36

particle identification.

- Track quality and fiducial volume : It is required that the starting position of at least one reconstructed track is inside the FGD1 or FGD2 fiducial volume. In addition to that, only tracks with more than 18 clusters, vertical or horizontal are selected in order to reject short tracks which is less reliable for reconstruction in TPC.

- Nearby track veto : One track produced at the P0D that undergoes a large scattering to the FGD1 can be mis-reconstructed separately as the two tracks. To avoid such failures, a cut vetoes events with the second highest momentum track starts 150 mm upstream of the muon candidate track are rejected.

- Broken track : This cut intends to reject the mis-reconstructed events in which one muon candidate track originating in the FGD fiducial volume is broken into two components: one FGD only track (fully contained in FGD) followed by second track which starts in last layers of FGD and passes the TPC module. Thus, the second track is considered as muon candidate. To remove such events, it is required that start position of muon candidate track is not in the last two layers of the FGD if the same event has at least one reconstructed FGD-only track.

- Muon PID : We require one of the tracks is identified as muon. Muon particle identification is performed with the energy deposits and the momentum of the tracks in the TPC using the likelihood of Eq. 2.5. This PID cut is defined for ν_μ CC events as follows,

$$L_\mu > 0.1 \tag{4.6}$$

$$L_{MIP} = \frac{L_\mu + L_\pi}{1 - L_p} > 0.9 \qquad \text{if } p < 500 \text{ MeV}/c. \tag{4.7}$$

where L_{MIP}, L_μ, L_π, and L_p are the likelihoods for the PID of Minimum Ionized Particle

(MIP), muon, pion and proton. p is the momentum of the muon candidate. For $\bar{\nu}_\mu$ CC selection, it is defined as follows,

$$0.1 < L_\mu < 0.8 \tag{4.8}$$

$$L_{MIP} > 0.7 \qquad \text{if } p < 500 \text{ MeV}/c. \tag{4.9}$$

When an event passes these six criteria, it is categorized as the ν_μ CC candidate events.

Furthermore, pion selection is applied to divide the ν_μ CC events into three categories which depend on the pion multiplicity. Using the same likelihood, the condition of the pion PID cut is defined as follows,

$$L_{MIP} > 0.8 \qquad \text{if } p < 500 \text{ MeV}/c \tag{4.10}$$

$$L_\pi > 0.3. \tag{4.11}$$

Events are categorized into 18 samples which are split into nine samples for FGD1 and FGD2 which are determined by whether the interaction point is FGD1 or FGD2. Furthermore, each of the nine samples is separated into three samples for ν_μ in ν mode, $\bar{\nu}_\mu$ in ν mode and $\bar{\nu}_\mu$ in $\bar{\nu}$ mode. Each of the three samples is separated by the pion multiplicity which is determined by the pion selection criteria. When the number of reconstructed pions is zero, it is categorized as CC0π sample. A single charged pion with an opposite charge to the muon makes CC1π sample. Any other number of charged pions or the existence of neutral pions is grouped as CCOther sample.

The binning of muon kinematics distributions for each event category is optimized considering the statistics in our current collected data. Figure 4.5 shows the comparison of the data and pre-fit prediction for ν mode FGD1.

4.4.3 Detector Systematics

Detector systematics of the near detector is treated through bin-by-bin covariance matrix in our analysis framework. The detector covariance matrix includes not only general detector systematics effects but also pion secondary interaction (SI) effects. Contribution of Pion SI effects is so large compared to the other detector systematics errors and its ratio is 70-95% of total detector uncertainty. Implementation ways of these near detector systematics are divided into three ways: observable-like, efficiency-like and normalization systematics. Table 4.4 summarizes how each detector systematics are implemented in our analysis.

4.4.4 Near Detector Fit Results

Table 4.5 summarizes the results of the event rate for the data and MC prediction before and after the near detector fit. Compared to the event rates of the prefit, those of the postfit are in drastically good agreement with the data for each sample. Furthermore, Fig. 4.6 shows the MC

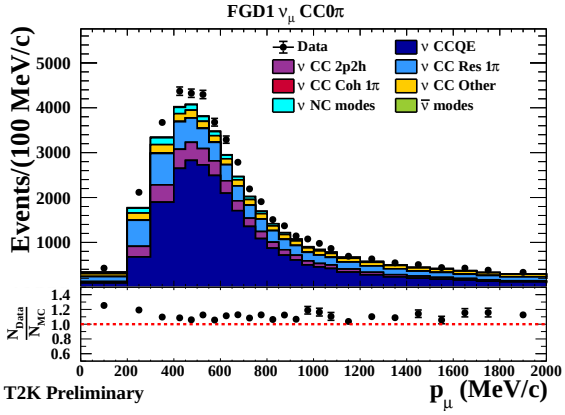

(a) ν mode CC0π momentum distribution

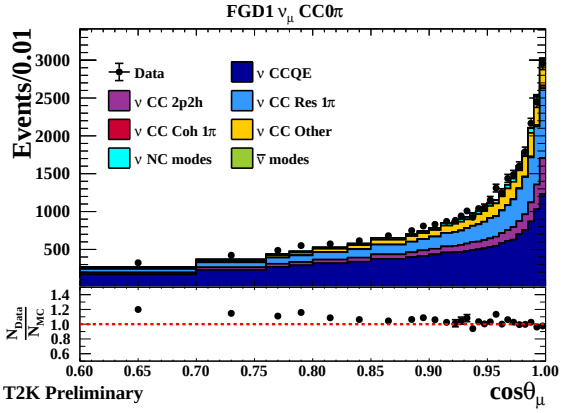

(b) ν mode CC0π $\cos\theta$ distribution

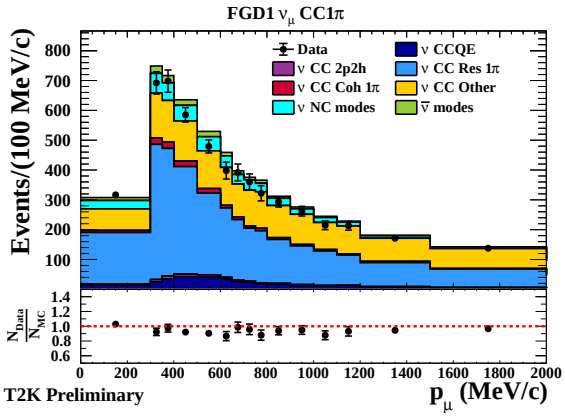

(c) ν mode CC1π momentum distribution

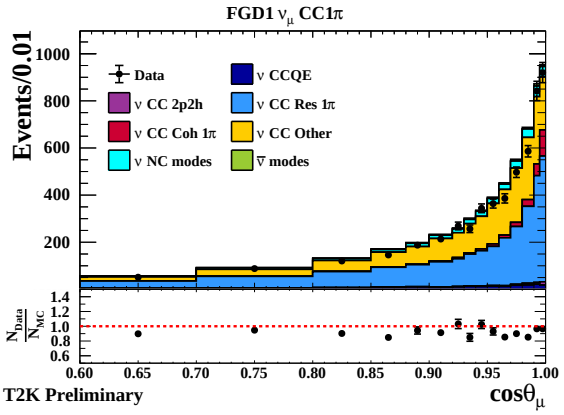

(d) ν mode CC1π $\cos\theta$ distribution

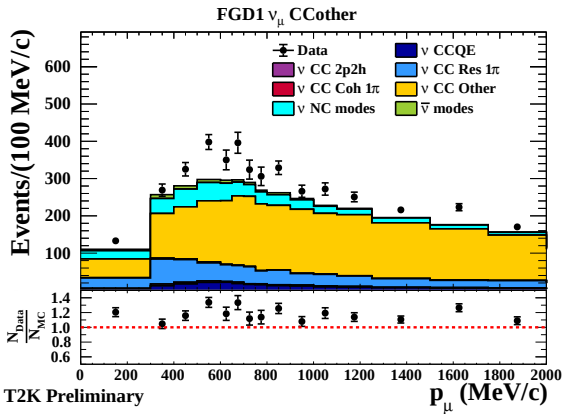

(e) ν mode CCOther momentum distribution

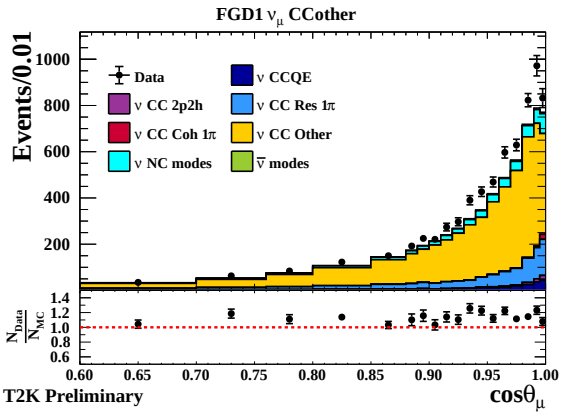

(f) ν mode CCOther $\cos\theta$ distribution

Figure 4.5: Pre-fit predictions and data points of muon momentum (left) and angular (right) distributions interaction mode by mode for CC0π, CC1π and CCOther samples of ν mode. The black points and error bars represent the data with the statistical uncertainty. The shaded regions show the contributions of the ν CCQE, ν 2p2h, ν CC resonant 1π, ν CC coherent 1π, ν CC other, ν NC modes, and $\bar{\nu}$ modes. The bottom insets show the ratio of data to simulation

Table 4.4: Systematic error sources in our near detector fit and error propagation model.

Systematic Error Sources	Propagation Model
TPC related	
B Field distortion	Observable variation
TPC momentum scale	Observable variation
TPC momentum resolution	Observable variation
TPC PID	Observable variation
TPC cluster efficiency	Efficiency-like
TPC tracking efficiency	Efficiency-like
TPC charge ID efficiency	Efficiency-like
FGD-TPC related	
TPC-FGD matching efficiency	Efficiency-like
FGD related	
FGD PID	Observable variation
FGD hybrid tracking efficiency	Efficiency-like
Michel electron efficiency	Efficiency-like
Background related	
OOFV background	Normalization
Sand muon background	Normalization
Pile-up	Normalization
MC modeling related	
Pion secondary interactions	Normalization
Proton secondary interactions	Normalization
FGD mass	Normalization

prediction with the values after the near detector fit. The MC prediction gets better agreement with the data bin by bin compared to Fig. 4.5.

Figure 4.7 and 4.8 show the neutrino flux and cross section parameters respectively before and after the near detector fit. As for the flux parameters for the ν mode, post-fit values for lower neutrino energy are higher by $\sim 10\%$ than the pre-fit values of them. On the other hand, for the higher neutrino energy, post-fit values are lower by $\sim 10\%$ than the pre-fit values. This is due to the correlation with CCQE cross section parameters such as M_{QE}^{A} and Q^2 parameters as shown in Fig. 4.9 which shows the correlation matrix for neutrino flux and cross section parameters. Clear anti-correlation between flux and cross section parameters can reduce total systematics uncertainties on the oscillation parameters measurement. That is because the number of ν events at the far detector is calculated as the product of the flux and the cross section. For the CC0π parameters, M_{A}^{QE} is pulled 2σ above its nominal value. The post-fit values of the low Q^2 parameters are consistent with other cross section data while high Q^2 parameters are pulled up from the nominal values to compensate the Q^2 difference in CCQE events. More detailed discussion including the updated oscillation analysis results will be described in the Sec. 7.1.

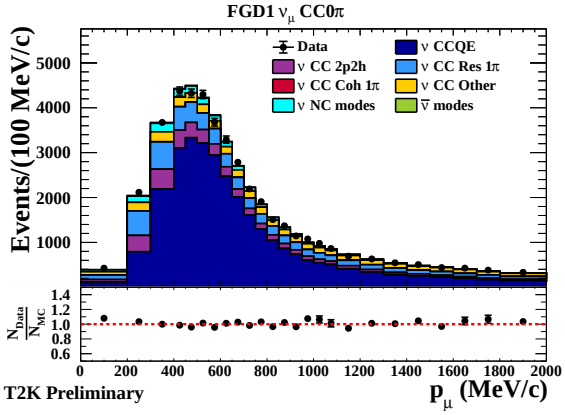

(a) ν mode CC0π momentum distribution

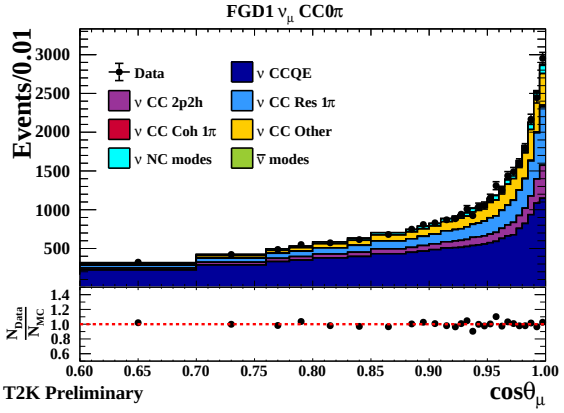

(b) ν mode CC0π $\cos\theta$ distribution

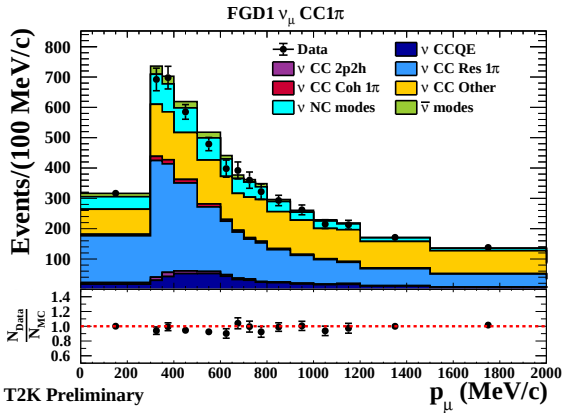

(c) ν mode CC1π momentum distribution

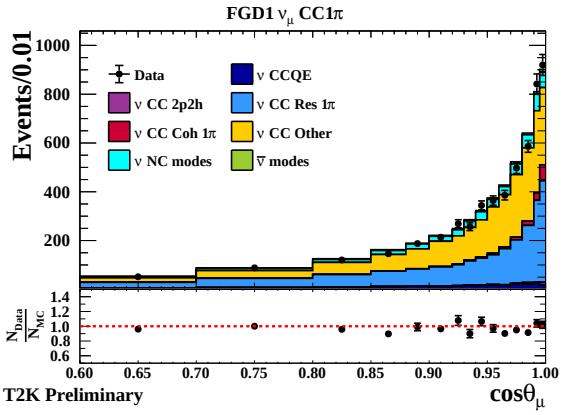

(d) ν mode CC1π $\cos\theta$ distribution

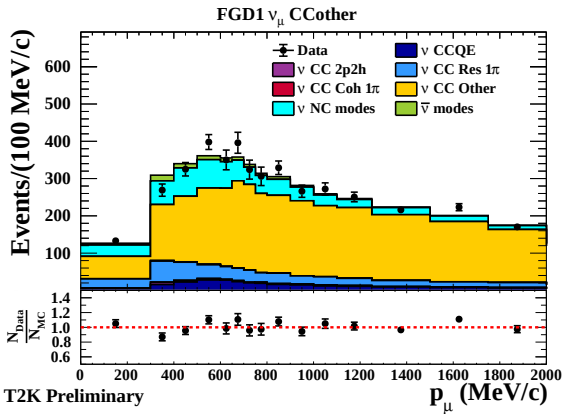

(e) ν mode CCOther momentum distribution

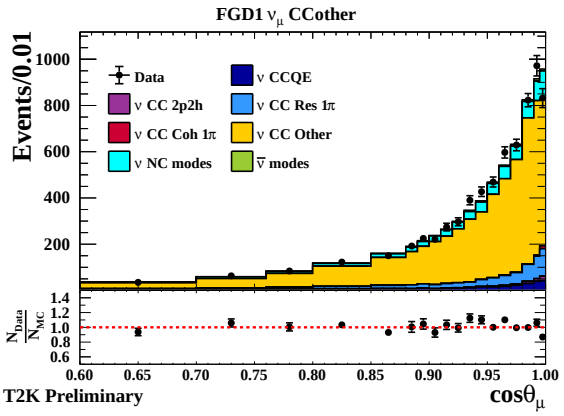

(f) ν mode CCOther $\cos\theta$ distribution

Figure 4.6: Post-fit predictions and data points of muon momentum (left) and angular (right) distributions for CC0π, CC1π and CCOther samples of ν mode. The black points and error bars represent the data with the statistical uncertainty. The shaded regions show the contributions of the ν CCQE, ν 2p2h, ν CC resonant 1π, ν CC coherent 1π, ν CC other, ν NC modes, and $\bar{\nu}$ modes. The bottom insets show the ratio of data to simulation.

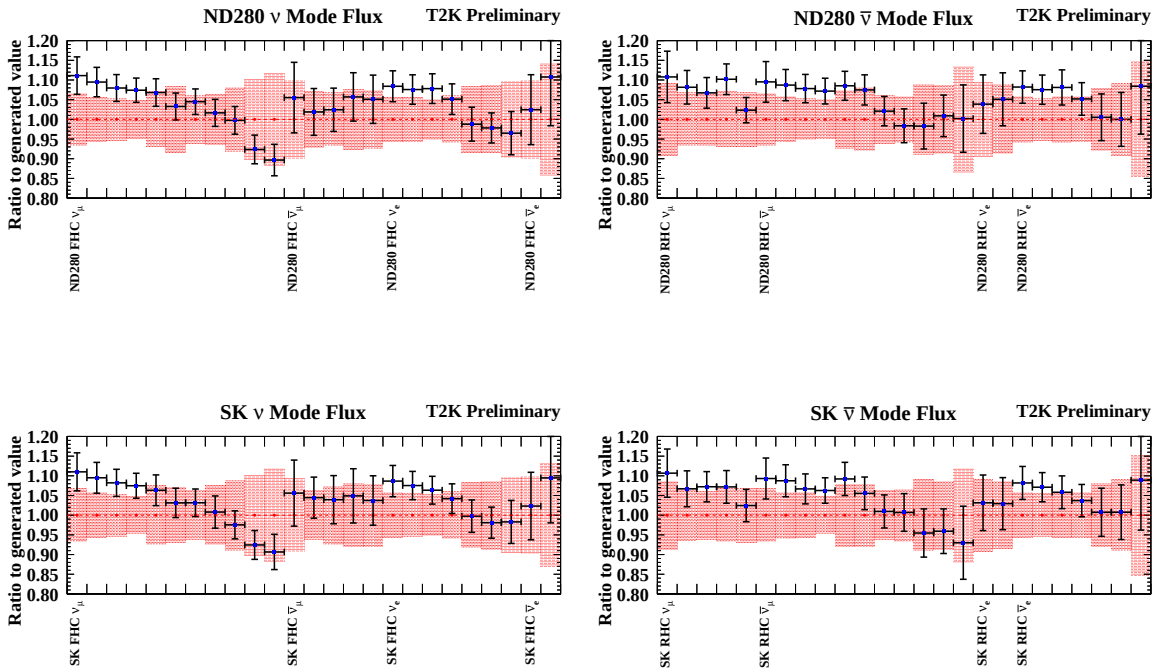

Figure 4.7: Pre- (red band) and post-fit (blue dots and black error bands), flux parameters for the ν mode (left) and the $\bar{\nu}$ mode (right), and for the ND280 (top) and SK (bottom) from the near detector fit to the data.

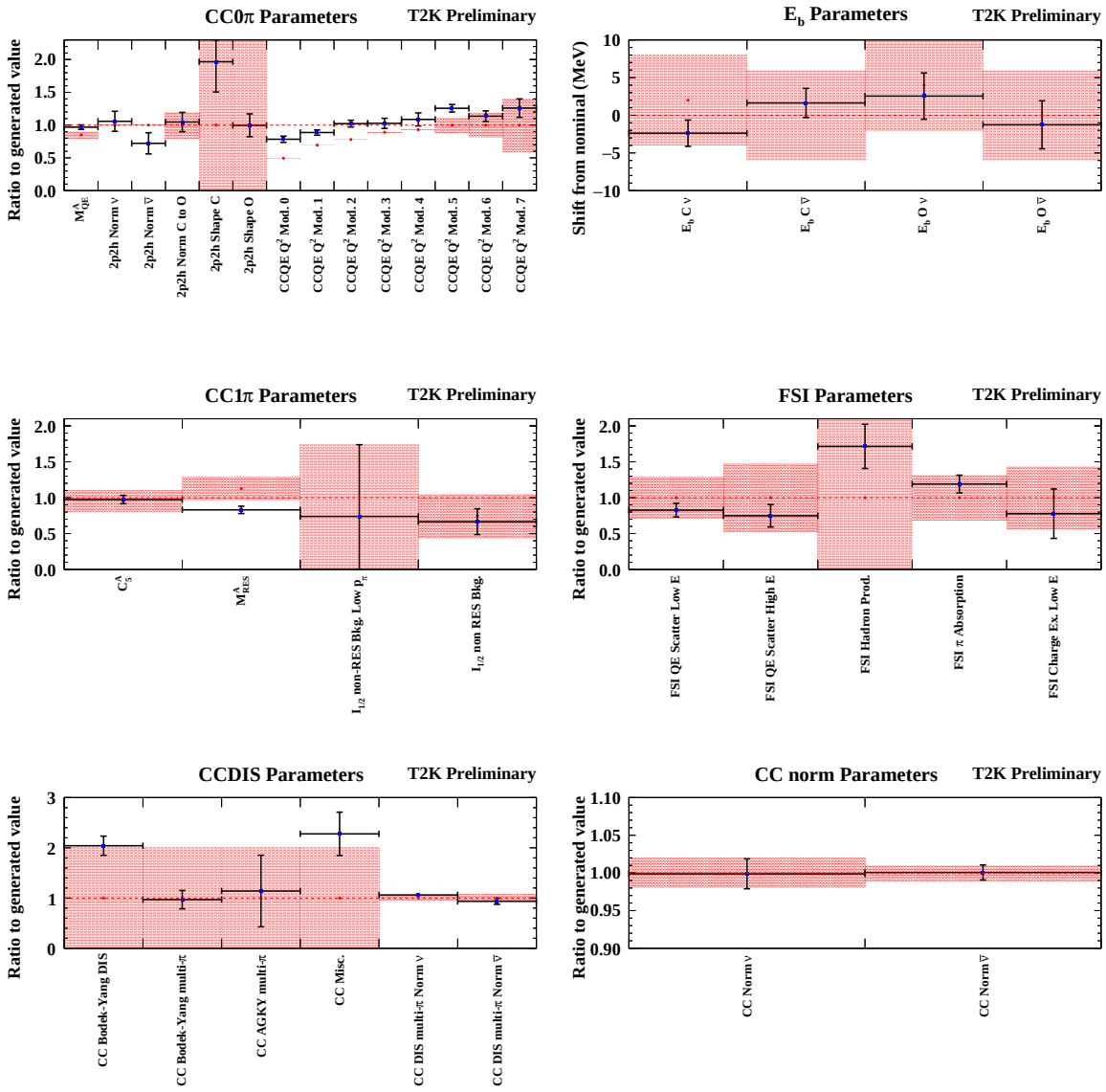

Figure 4.8: Pre- (red band) and post-fit (blue dots and black error bands), cross section parameters for CC0π (CCQE and 2p2h), E_b, CC1π, FSI, CCDIS, and CC normalization from the near detector fit to the data.

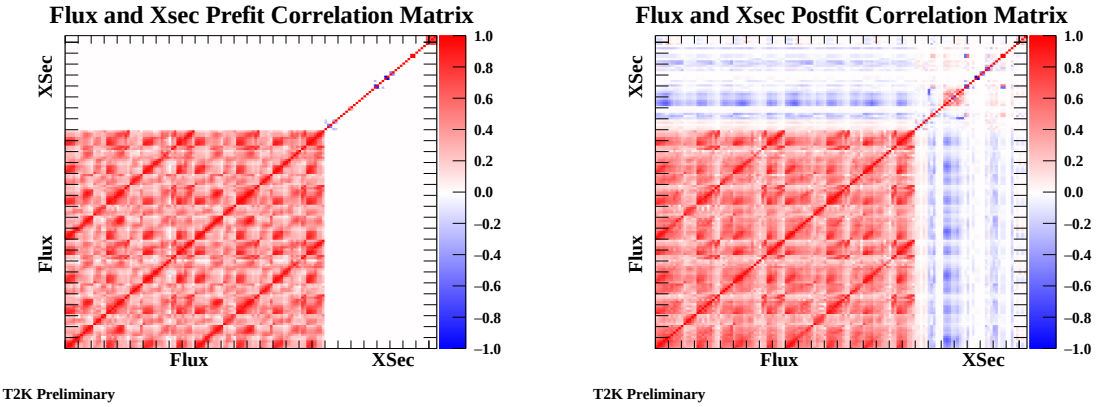

Figure 4.9: Correlation matrix of flux and cross section (XSec) parameters. There is a clear anti-correlation between flux parameters and cross section parameters in the post-fit correlation matrix (right) while there is no correlation in the pre-fit matrix (left).

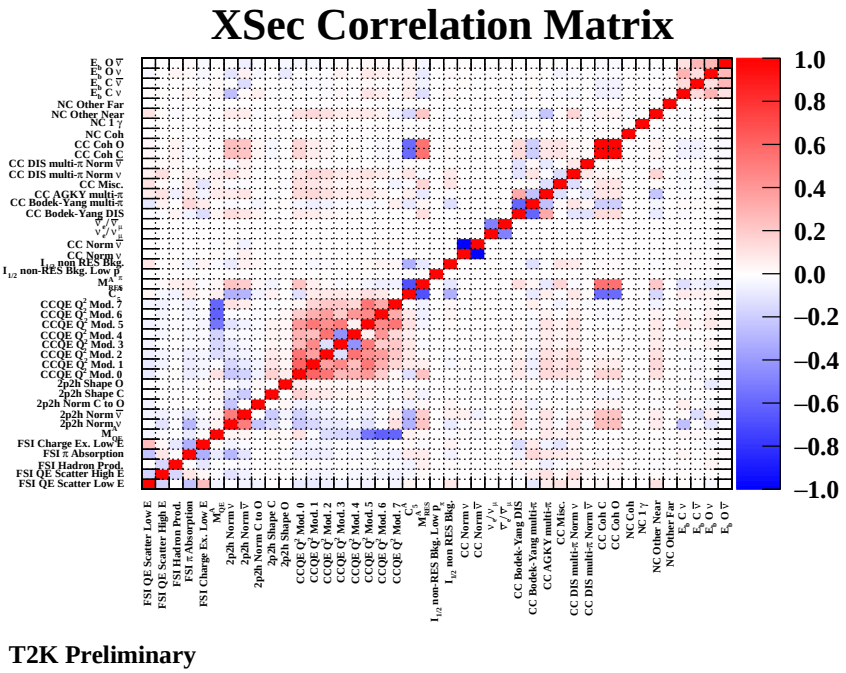

Figure 4.10: Correlation matrix of cross section (XSec) parameters.

Table 4.5: Summary of the number of events at each event selection for data and the MC prediction before (Prefit) and after (Postfit) the near detector fit to the data.

Beam	Event Topology	Target	Data	Prefit	Postfit
ν mode ν_μ CC	0π	FGD1	33443	27951.80	33387.70
		FGD2	33156	27558.87	33150.90
	1π	FGD1	7713	8358.62	7930.96
		FGD2	6281	6723.79	6423.44
	Other	FGD1	8026	7031.49	7946.17
		FGD2	7700	6454.74	7313.67
$\bar{\nu}$ mode $\bar{\nu}_\mu$ CC	0π	FGD1	8388	7270.33	8430.25
		FGD2	8334	7036.50	8184.52
	1π	FGD1	698	694.32	681.54
		FGD2	650	624.69	636.19
	Other	FGD1	1472	1286.79	1469.29
		FGD2	1335	1176.53	1377.96
$\bar{\nu}$ mode ν_μ CC	0π	FGD1	3594	3035.59	3580.46
		FGD2	3433	3012.40	3528.39
	1π	FGD1	1111	1159.01	1154.22
		FGD2	926	930.64	920.74
	Other	FGD1	1344	1073.13	1290.46
		FGD2	1245	1000.39	1196.24

4.5 Far Detector Analysis

4.5.1 Ring Reconstruction Algorithm (fiTQun)

In SK, charges and timing of PTM hits for the Cherenkov ring are used in order to measure the kinematics information of outgoing charged particles from neutrino interaction. A new ring reconstruction algorithm (fiTQun) [108] is used to reconstruct the Cherenkov ring more precisely. This algorithm was originally developed for the MiniBooNE experiment and now it is adopted for the reconstruction at SK. Variables such as vertex, direction, and momentum of each ring are simultaneously fitted using the maximum likelihood method based on the charge and time information of all PMTs. This simultaneous fit with much information enables the precise reconstruction.

4.5.2 Fiducial Volume at the Far Detector

Figure 4.11 illustrates the fiducial volume parameters. "Wall" refers to the shortest distance from the particle vertex to the detector inner wall, and "towall" refers to the distance to the detector inner wall along the reconstructed track. Previously, only the condition that "wall" parameter is large enough was used to select the fully-contained events in the fiducial volume. Ideally, events with smaller "wall" should be selected to obtain larger statistics. However, in

areas with smaller "wall", the background event rate is relatively high and the reconstruction purity is worse. Thus, it is necessary to optimize the fiducial volume cut in terms of increasing the statistics. Then, we introduce a "towall" parameter to optimize the fiducial volume cut. In the events with small "wall" and large "towall", Cherenkov rings are generally well imaged. On the other hand, events with both small "wall" and "towall" have few PMT hits and poorly imaged Cherenkov rings. Such events should be removed and we optimized these two parameters.

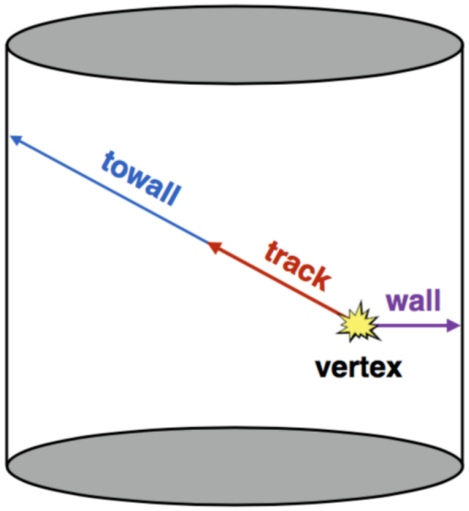

Figure 4.11: Overview of the fiducial volume parameters for the far detector analysis.

4.5.3 Event Selection

Far detector data used in the fit

Table 4.6 shows the collected data used in the far detector analysis. We used 1.9663×10^{21} POT for the ν mode and 1.6344×10^{21} POT for the $\bar{\nu}$ mode.

Event Categorization

There are three samples for ν mode: a CCQE-like ν_e (ν-mode 1Re), a CCQE-like ν_μ (ν-mode 1Rμ), and a CC single pion-like ν_e sample (ν mode 1Re1de). On the other hand, for $\bar{\nu}$-mode, there are two samples : a CCQE like $\bar{\nu}_\mu$ ($\bar{\nu}$-mode 1Rμ), and a CCQE-like $\bar{\nu}_e$ ($\bar{\nu}$-mode 1Re).

ν_e event selection

The ν_e selection criteria are given as follows,

1. Fully-contained event in the SK fiducial volume.
2. Number of rings found is one.

Table 4.6: Summary of collected data for the far detector analysis.

Run number	Beam mode	POT at SK ($\times 10^{19}$)
1	ν mode	3.26
2	ν mode	11.22
3	ν mode	15.99
4	ν mode	35.97
5	$\bar{\nu}$ mode	5.12
	ν mode	2.44
6	$\bar{\nu}$ mode	35.46
	ν mode	1.92
7	$\bar{\nu}$ mode	34.98
	ν mode	4.84
8	ν mode	71.69
9	$\bar{\nu}$ mode	87.88
	ν mode	2.04
10	ν mode	47.26
Total	ν mode	196.63
Total	$\bar{\nu}$ mode	163.44

3. The ring is identified as electron-like.

4. Visible energy is greater than 100 MeV.

5. Neutrino energy reconstructed E_{rec} is less than 1250 MeV.

6. The number of decay electron is zero.

7. Rejection of π^0.

The second and third criteria is to select the single electron-like ring events. By the fourth criterion, we can reject the low energy background events which are difficult to reconstruct the neutrino energy. The fifth cut is applied in order to reject the beam intrinsic ν_e background which is contained in the high energy region. The sixth cut rejects the NC interaction and invisible $\mu^{\pm}$ events. We reject the NCπ^0 background by the last criterion. This cut is determined with the reconstructed π^0 mass and the log-likelihood ratio of π^0 and e from the fiTQun. These selection cuts are summarized in Fig. 4.12.

ν_μ event selection

The ν_μ selection criteria are given as follows,

1. Fully-contained event in the SK fiducial volume.

2. Number of rings found is one.

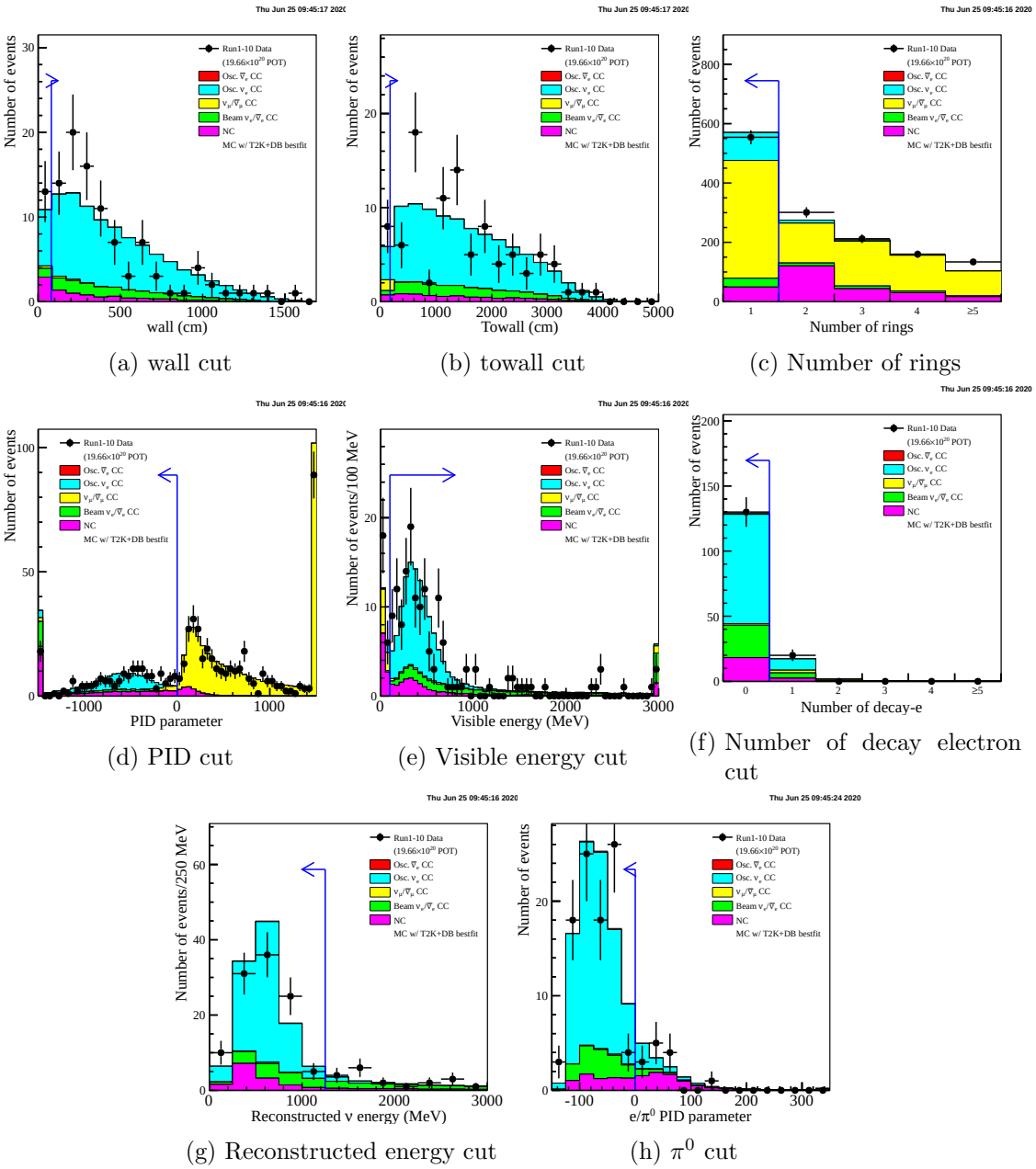

(a) wall cut (b) towall cut (c) Number of rings

(d) PID cut (e) Visible energy cut (f) Number of decay electron cut

(g) Reconstructed energy cut (h) π^0 cut

Figure 4.12: Selection criteria for ν_e events. "Wall" and "towall" parameters are described in Sec. 4.5.2.

3. The ring is identified as a muon-like single-ring.
4. Reconstructed muon momentum of μ-like ring is larger than 200 MeV/c.
5. The number of decay electrons is zero or one.
6. Rejection of π^+.

The second and third criteria is to select the single μ-like ring events. By the fourth criterion, we can select the low energy background events which are difficult to reconstruct the neutrino energy. The fifth cut is applied in order to reject non-CCQE interaction. We reject the NCπ^+ background by the last criterion. This cut is determined with the reconstructed muon momentum and the log-likelihood ratio of π^+ and μ from the fiTQun. These selection cuts are summarized in Fig. 4.13.

ν_e CC1π (ν mode 1Re1de) event selection

This selection has been applied in order to increase the statistics since 2016. This selection criteria are characterized by tagging the e-like ring and one decay electron, and given as follows,

1. Fully-contained event in the SK fiducial volume.
2. Number of rings found is one.
3. The ring is identified as electron-like.
4. Visible energy of the electron-like ring reconstructed is greater than 100 MeV.
5. The number of decay electron is one.
6. Reconstructed neutrino energy E_{rec} is less than 1250 MeV.
7. Rejection of π^0.

Compared to the ν_e selection criteria, we only change the fifth criterion in order to tag one decay electron.

4.5.4 Detector Systematics

SK detector systematics is evaluated based on "Vertex position", "Number of decay electrons", "PID", "Number of ring counting" and "Momentum" variables. Most of these systematic uncertainties are evaluated by comparing data and MC prediction with cosmic ray and atmospheric neutrino samples. As for the uncertainty on the π^0 rejection efficiency in $1R_e$ samples, it is estimated using "hybrid" π^0 sample which consists of an e-like event from the atmospheric neutrino or decay electron from cosmic ray muon data with a simulated γ kinematics from NCπ^0 events in the MC. The systematic uncertainty is evaluated by comparing π^0 rejection efficiency of the data-MC with the MC-MC samples.

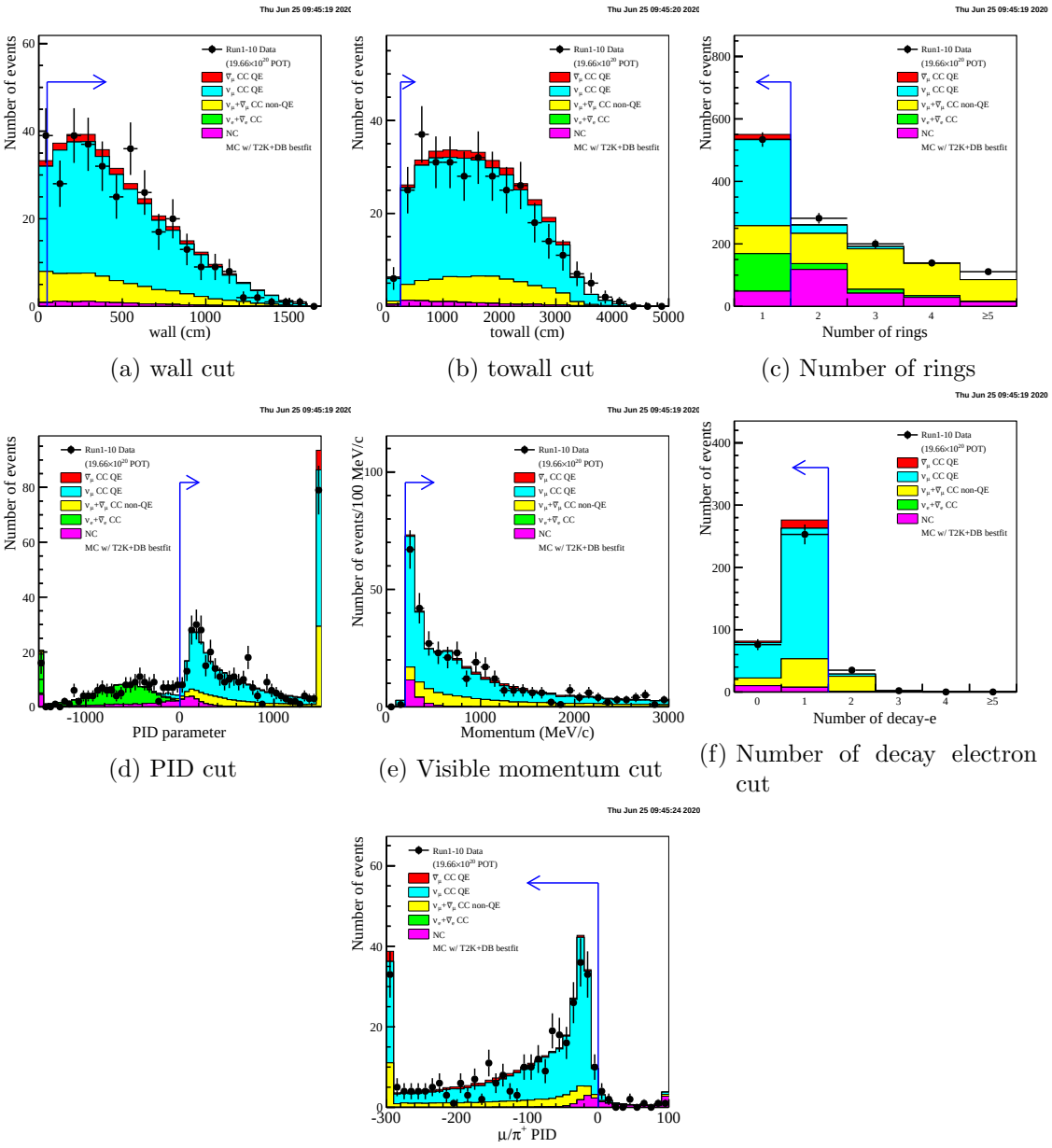

(a) wall cut (b) towall cut (c) Number of rings

(d) PID cut (e) Visible momentum cut (f) Number of decay electron cut

(g) π^+ cut

Figure 4.13: Selection criteria for ν_μ events. "Wall" and "towall" parameters are described in Sec. 4.5.2.

Furthermore, the photo-nuclear (PN) effect is also included in the SK detector systematics. In the PN effect, a photon from a π^0 is absorbed by the nucleus. The photon reconstruction efficiency can be changed since the emitted Cherenkov light yield may be changed by the PN effect.

4.5.5 Fit Procedure

This subsection describes the fit procedure using the systematic parameters and the event selections.

Likelihood of Far Detector Fit

Binned likelihood L_{SK} is introduced to extract the oscillation parameters from the SK data as follows,

$$L_{SK}(\{N_s^{\rm obs}, \vec{x}_s^{\rm obs}\}_{\forall s}, \vec{o}, \vec{f}) = \prod_{s \in \text{samples}} [L_{SK,s}(N_s^{\rm obs}, \vec{x}_s^{\rm obs}, \vec{o}, \vec{f})] \times L_{syst.}(\vec{f}) \tag{4.12}$$

where N_s^{obs} is the number of events observed for sample s, $\vec{x}_s^{obs}$ represents measurement variables (lepton momentum p_l and scattering angle θ for e-like events, and reconstructed energy E_{rec} and scattering angle θ for μ like events.), $\vec{o}$ represents the oscillation parameters. $L_{syst.}(\vec{f})$ is the likelihood for the systematic part which is given as the covariance matrix and mean values for the systematics parameters. It is given as,

$$L_{syst.}(\vec{f}) = \exp\left\{ -\sum_{i,j}^{N^f} \Delta\vec{f}_i V_{i,j}^{-1} \vec{f}_j \right\} \tag{4.13}$$

where N^f is the number of systematic parameters and indices i, j run through all systematics parameters. The likelihood of sample s ($L_{SK,s}$) is the statistical part to compare the MC predictions and the data. It is the sum of the log Poisson likelihood and can be written as,

$$\ln L_{SK,s}(N_s^{obs}, \vec{x}_s^{\rm obs}, \vec{o}, \vec{f}) = \sum_{i \in \text{bins}} [(N_{s,i}^{\rm exp.} - N_{s,i}^{\rm obs.}) + N_{s.i}^{\rm obs.} \times \ln (N_{s,i}^{\rm obs.}/N_{s,i}^{\rm exp.})] \tag{4.14}$$

where i runs through each $p_l - \theta$ or $E_{rec} - \theta$ bin. The values $N_{s,i}^{obs.}$ and $N_{s.i}^{exp.}$ are the number of observed and expected events for i th bin.

Marginal Likelihood

Equation 4.12 is minimized to calculate the best fit values of oscillation parameters $\vec{o}$ while there are some nuisance parameters $\vec{f}$ as the variables during the minimization. On the other hand, to calculate the confidence interval for each oscillation parameter, it is needed to construct the likelihood which only depends on $\vec{o}$. A Bayesian marginalization method is adopted and we

compute the marginal likelihood by integrating the full likelihood over the nuisance parameters $\vec{f}$ for fixed $\vec{o}$,

$$L_{SK,\mathrm{marg}}(N^{\mathrm{obs}}, \vec{x}^{\mathrm{obs}}, \vec{o}) = \int d\vec{f} L_{SK}(N^{\mathrm{obs}}, \vec{x}^{\mathrm{obs}}, \vec{o}, \vec{f}). \tag{4.15}$$

In the actual analysis, we integrate numerically these nuisance parameters by throwing them $N = 100,000$ times for one-dimensional $\Delta\chi^2$ distributions and $N = 20,000$ times for two-dimensional $\Delta\chi^2$ contour according to their prior distributions and the marginal likelihood is given as,

$$L_{SK,\mathrm{marg}}(N^{\mathrm{obs}}, \vec{x}^{\mathrm{obs}}, \vec{o}) = \frac{1}{N}\sum_{i=1}^{N} \frac{1}{L_{syst.}(\vec{f})} L_{SK}(N^{\mathrm{obs}}, \vec{x}^{\mathrm{obs}}, \vec{o}, \vec{f}). \tag{4.16}$$

Confidence Interval

Using the marginal likelihood, the confidence interval for each oscillation parameter $\vec{o}$ is defined as follows,

$$\Delta\chi^2(\vec{o}) = -2 \times \ln \frac{L_{SK,\mathrm{marg}}}{L^{\max}_{SK,\mathrm{marg}}}, \tag{4.17}$$

where $L^{\max}_{SK,\mathrm{marg}}$ is the maximum of the marginal likelihood over the range of values of $\vec{o}$. Feldman Cousins method [109] is used to calculate the confidence interval in order to consider the boundary effects in our analysis.

Credible Interval

Bayesian credible intervals can be calculated by using the marginal likelihood. Posterior distributions for each oscillation parameter set $p(\vec{o}|N^{\mathrm{obs}}, \vec{x}^{\mathrm{obs}})$ can be given as follows,

$$p(\vec{o}|N^{\mathrm{obs}}, \vec{x}^{\mathrm{obs}}) = \frac{L_{\mathrm{marg}}(N^{\mathrm{obs}}, \vec{x}^{\mathrm{obs}}, \vec{o}) \times p(\vec{o})}{\int d\vec{o}' L_{\mathrm{marg}}(N^{\mathrm{obs}}, \vec{x}^{\mathrm{obs}}, \vec{o}') \times p(\vec{o}')}. \tag{4.18}$$

Using this posterior distribution, the credible interval can be written as,

$$\int_{\mathrm{interval}} d\vec{o}\; p(\vec{o}|N^{\mathrm{obs}}, \vec{x}^{\mathrm{obs}}) = \alpha. \tag{4.19}$$

4.6 Results of Oscillation Analysis

This section describes the results of the measurement of the oscillation parameters from the full data set as shown in Fig. 4.14 with the constraints from the near detector fit.

4.6.1 Effects of Near Detector Fit on Far Detector Samples

Figure 4.15 shows the comparison of the spectra with the pre-fit values and the post-fit values for each far detector spectrum. The shaded region shows the 1σ uncertainty band and the

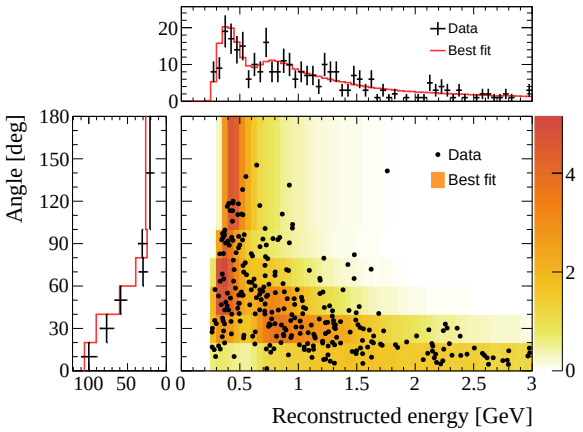

(a) ν mode 1Rμ

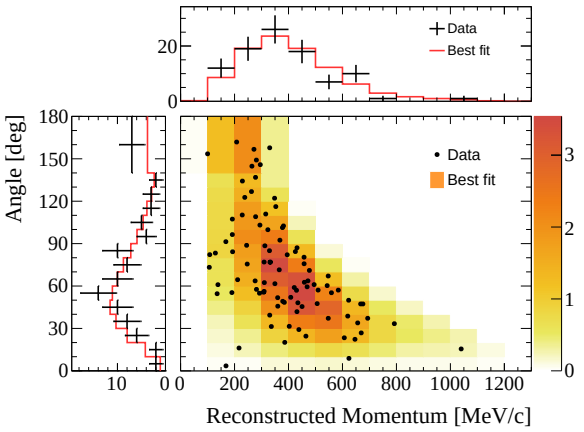

(b) ν mode 1Re

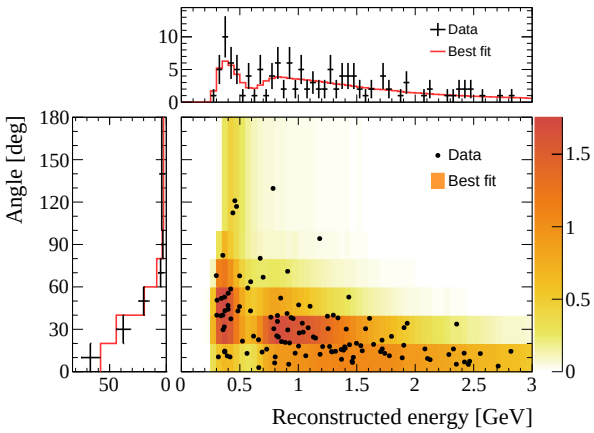

(c) $\bar{\nu}$ mode 1Rμ

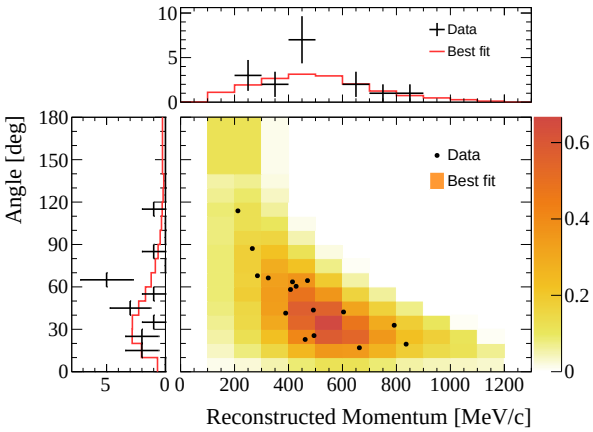

(d) $\bar{\nu}$ mode 1Re

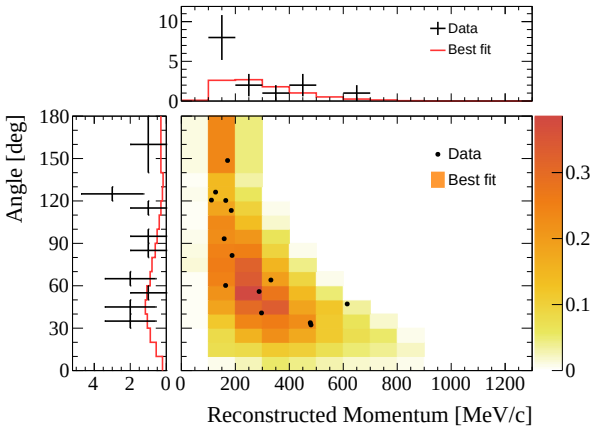

(e) ν mode 1Re1de

Figure 4.14: The events for the five far detector samples. The expected event rates using the best fit with the reactor constraint is shown in the colored background. The insets show the events projected onto each single dimension, and the red line is the expected number of events from the best-fit. The error bars represent the 1σ statistical uncertainty on the data.

constraint with the near detector fit effectively reduces the uncertainties on the event rates.

Systematic uncertainties for flux, cross section and detector (SK+SI+PN) with and without near detector constraint are summarized in Tabs. 4.7 and 4.8. Those of flux and cross section are reduced drastically by the near detector fit. Furthermore, total uncertainties of flux and cross section are small compared to that of two individually thanks to the anti-correlation between them as mentioned in Sec. 4.4.4.

Table 4.7: Summary of the systematic uncertainties for the number of events at the far detector before the near detector fit.

Error source (%)	1Rμ		1Re			
	ν mode	$\bar{\nu}$ mode	ν mode	$\bar{\nu}$ mode	ν mode CC1π^+	$\frac{\nu \text{ mode}}{\bar{\nu} \text{ mode}}$
Flux	5.1	4.7	4.8	4.7	4.9	2.7
Cross-section (all)	10.1	10.1	11.9	10.3	12.0	10.4
SK+SI+PN	2.9	2.5	3.3	4.4	13.4	1.4
Total	11.1	11.3	13.0	12.1	18.7	10.7

Table 4.8: Summary of the systematic uncertainties for the number of the events at the far detector after the near detector fit.

Error source (%)	1Rμ		1Re			
	ν mode	$\bar{\nu}$ mode	ν mode	$\bar{\nu}$ mode	ν mode CC1π^+	$\frac{\nu \text{ mode}}{\bar{\nu} \text{ mode}}$
Flux	2.9	2.8	2.8	2.9	2.8	1.4
Cross-section (ND constraint)	3.1	3.0	3.2	3.1	4.2	1.5
Flux + Cross-section (ND constraint)	2.1	2.3	2.0	2.3	4.1	1.7
Cross-section (ND unconstrained)	0.6	2.5	3.0	3.6	2.8	3.8
SK+SI+PN	2.1	1.9	3.1	3.9	13.4	1.2
Total	3.0	4.0	4.7	5.9	14.3	4.3

4.6.2 Fit Results of Oscillation Parameters

How the number of events in the selections varies the oscillation parameters is summarized in Fig. 4.16. This figure shows a two-dimensional scattered plot for the number of e-like events of ν mode and $\bar{\nu}$ mode at the far detector for each oscillation parameter. The electron-like events in ν mode and $\bar{\nu}$ mode are sensitive to $\sin\delta_{CP}$, the neutrino mass ordering, and the octant of θ_{23}, and their energy spectra has some sensitivity to $\cos\delta_{CP}$. Furthermore, the data favors the maximal CP violation ($\delta_{CP} = +\frac{\pi}{2}$), the normal mass ordering, and the upper octant ($\sin^2\theta_{23} > 0.5$).

Figure 4.17 shows the two-dimensional contours for $\sin^2\theta_{23}$ vs Δm^2_{23} and δ_{CP} vs $\sin^2\theta_{13}$. The contours are compatible for both mass orderings and prefer the upper octant. Figure 4.18 shows the $\Delta\chi^2$ distribution for δ_{CP}. The Feldman-Cousins method is used to calculate the

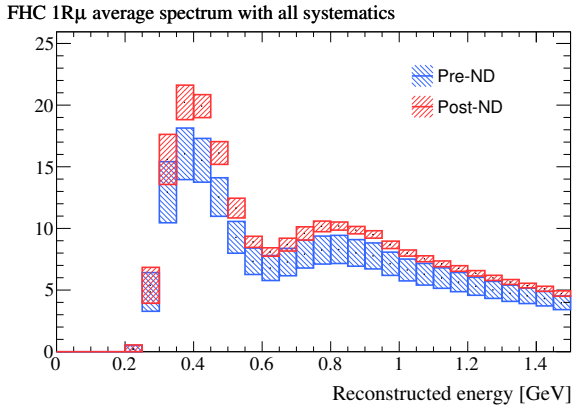

(a) ν mode 1Rμ

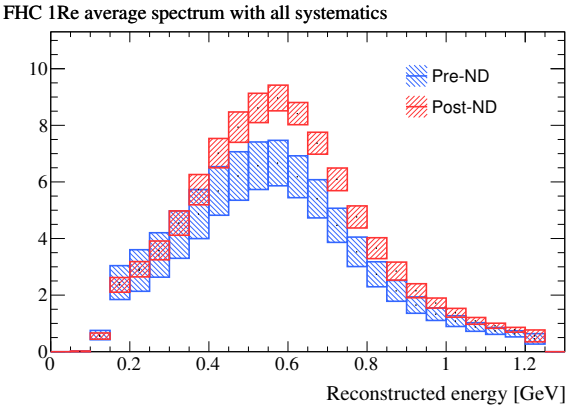

(b) ν mode 1Re

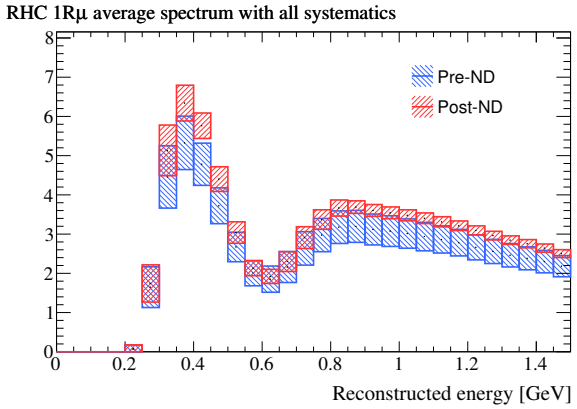

(c) $\bar{\nu}$ mode 1Rμ

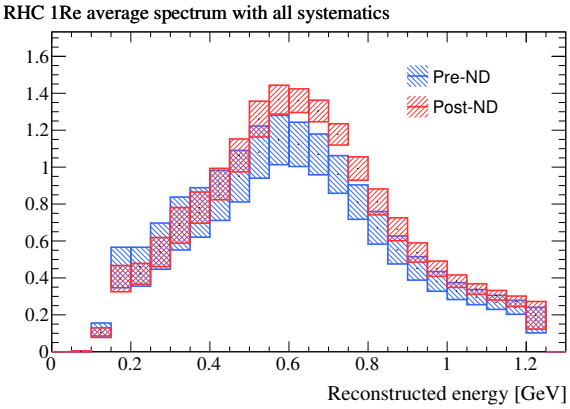

(d) $\bar{\nu}$ mode 1Re

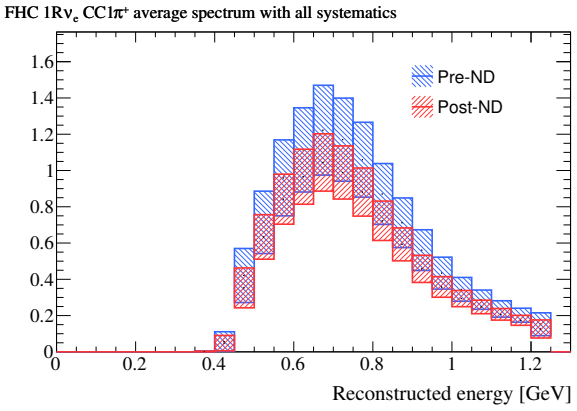

(e) ν mode 1Re1de

Figure 4.15: Comparison of the pre-fit and post-fit prediction with the total uncertainty for ν mode 1Rν, ν mode 1Re, $\bar{\nu}$ mode 1Rμ, $\bar{\nu}$ mode 1Re and ν mode 1Re1de samples as a function of reconstructed neutrino energy.

critical $\Delta\chi^2$ values to determine the 90%, 1σ and 2σ confidence level (CL). Consequently, 35% of the possible values for δ_{CP} are excluded at the 2σ CL and CP conserving values $\delta_{CP} = 0$ or π are excluded at 90% CL.

4.6.3 Discussion

We obtained the measurement results of the oscillation parameters with the world's highest precision. As a result, the best-fit values for each oscillation parameter are summarized in Tab. 4.9. Comparison of these results with those of external experiments will be discussed in Chapter 7 including the updated oscillation analysis results.

Table 4.9: Summary of the results with and without the reactor constraint using the confidence intervals estimated with the marginal likelihood.

Parameter	With reactor constraint		Without reactor constraint	
	Normal Ordering	Inverted Ordering	Normal Ordering	Inverted Ordering
δ_{CP}(rad.)	$-1.97^{+0.97}_{-0.62}$	$-1.44^{+0.56}_{-0.59}$	$-2.22^{+1.25}_{-0.81}$	$-1.29^{+0.72}_{-0.83}$
$\sin^2\theta_{13}/10^{-3}$	-	-	$28.0^{+2.8}_{-6.5}$	$31.0^{+3.0}_{-6.5}$
$\sin^2\theta_{23}$	$0.561^{+0.019}_{-0.038}$	$0.563^{+0.017}_{-0.012}$	$0.467^{+0.106}_{-0.018}$	$0.466^{+0.103}_{-0.019}$
$\Delta m^2_{23}/10^{-3}(\mathrm{eV}^2/\mathrm{c}^4)$	$2.494^{+0.040}_{-0.057}$	-	$2.495^{+0.040}_{-0.056}$	-
$\lvert\Delta m^2_{31}\rvert/10^{-3}(\mathrm{eV}^2/\mathrm{c}^4)$	-	$2.463^{+0.041}_{-0.055}$	-	$2.463^{+0.042}_{-0.054}$

Table 4.10: Confidence intervals of δ_{CP} and $\sin^2\theta_{23}$ for each confidence level with the reactor constraint, using the Feldman Cousins method. The 3σ confidence interval was not computed for $\sin^2\theta_{23}$.

Confidence level	δ_{CP} (rad.)		$\sin^2\theta_{23}$	
	Normal Ordering	Inverted Ordering	Normal Ordering	Inverted Ordering
1σ	[-2.67, -1.00]	-	[0.529, 0.582]	-
90%	[-3.01, -0.52]	[-1.74, -1.07]	[0.444, 0.593]	[0.536, 0.584]
2σ	[$-\pi$, -0.28]$\cup$[3.10, π]	[-2.16, -0.74]	[0.436, 0.598]	[0.512, 0.592]
3σ	[$-\pi$, 0.33]$\cup$[2.59, π]	[-2.83, 0.14]	N/A	N/A

While the measurement results were obtained with the world's highest precision, there is still room to improve in our analysis. One of them is related to the event selection in both the near detector and the far detector analyses. In order to constrain the nuclear model which is related to the outgoing hadron kinematics from neutrino interaction, event categorization with proton information is useful. Thus, a new event selection with proton multiplicity at the near detector is adopted in the update analysis. Furthermore, photon selection at the near detector can be also useful to tag the outgoing π^0 events. NC π^0 events are the main background sources of ν_e events at the far detector and precise prediction of that reduces the systematic uncertainties of the number of such events. As for the far detector analysis, resonant single 1 π production mode with multi-ring topology is the second dominant event after CCQE-like events. Therefore,

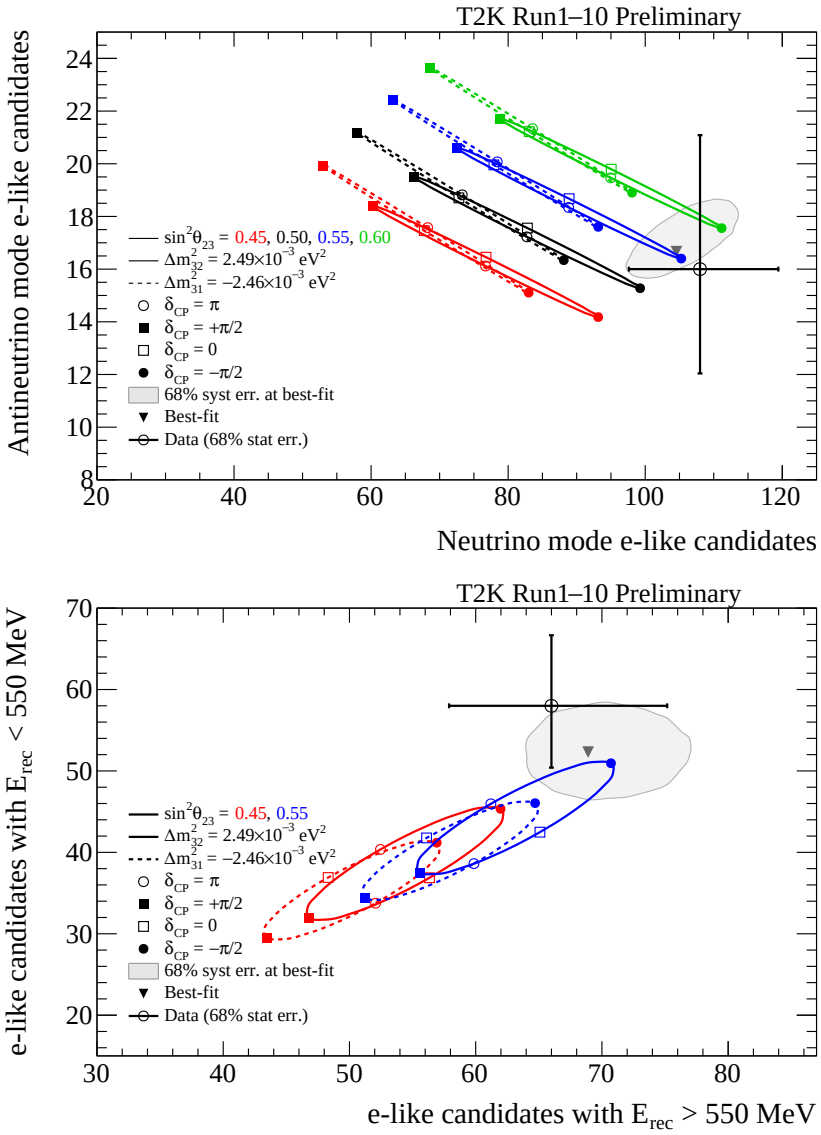

Figure 4.16: Bi-event plots of ν mode and $\bar{\nu}$ mode e-like events (top), and of above and below $E_{rec} = 550$ MeV (bottom) at the far detector for various oscillation parameters. The different colored ellipses represent the different values for $\sin^2\theta_{23}$ and mass hierarchy. The different points on each ellipse represent the different values for δ_{CP}. The overlaid triangle point shows the predicted number of events with oscillation and systematic uncertainty parameters at their best fit values for the data.

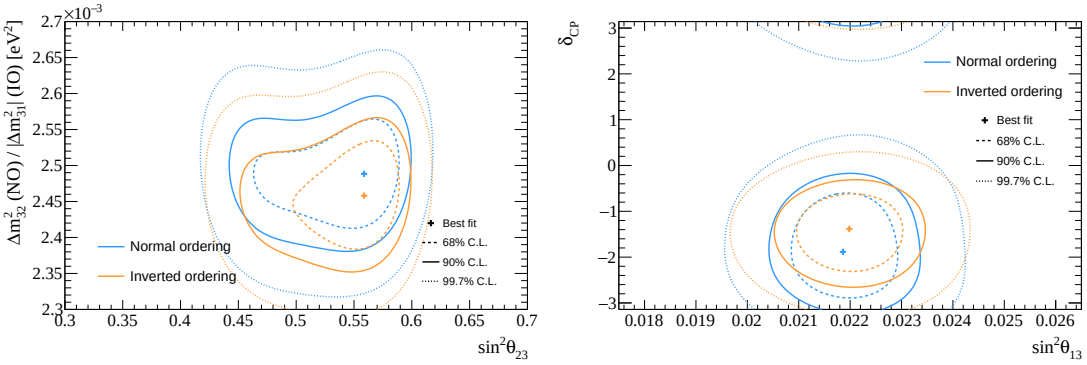

Figure 4.17: Two-dimensional confidence level contours of Δm^2_{23} vs $\sin^2\theta_{23}$ (left) and δ_{CP} vs $\sin^2\theta_{13}$ (right) for the normal and inverted mass orderings.

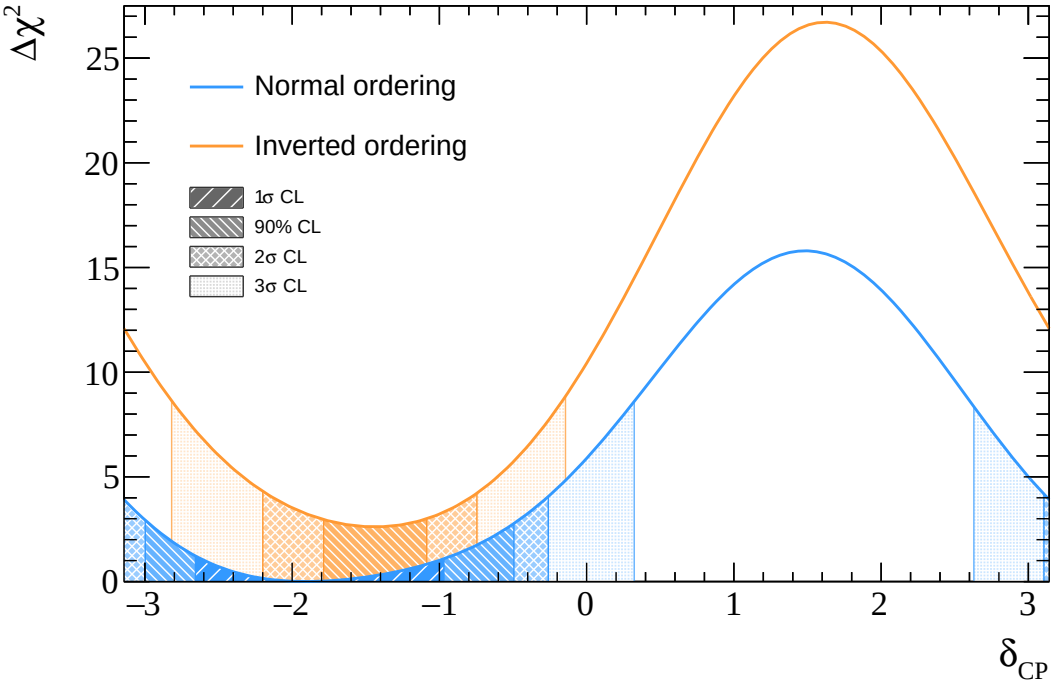

Figure 4.18: One-dimensional $\Delta\chi^2$ distribution as a function of δ_{CP}. Shaded regions show the confidence intervals at each confidence level.

a new multi-ring sample at the far detector is also added in order to measure the oscillation parameters more precisely by increasing the statistics.

Related to these improvements with these new event selections, neutrino interaction modeling should be updated. While new event selection with proton multiplicity is being added, there are several ad-hoc parameters such as low Q^2 parameters deeply related to the outgoing hadron kinematics. To replace them, a new parametrization of neutrino-nucleus interaction modeling is added in the updated analysis.

Chapter 5 describes these improvements for the updated analysis and Chapter 7 shows the updated results of the oscillation parameters measurement.

Part III

Improvements of Neutrino Oscillation Analysis

Chapter 5

Improvements of Oscillation Analysis

This chapter describes the improvements for the updated oscillation analysis. Following the discussion in Chapter 4, we updated several things in the oscillation analysis toward the more prisice measurements. Section 5.1 describes the updates of the neutrino flux inputs especially about the tuning with the T2K replica target in the NA61/SHINE experiment. This update is to reduce the uncertainty on the production cross section due to the difficulty in covering the large variety of possible interactions inside the target only with the thin target data. Sections 5.2 and 5.3 introduce the new event selection at the near and far detectors. Based on these selection updates, interaction modeling should be updated and the details will be described in Sec. 5.4.

5.1 Updates of Neutrino Flux

To reduce the large uncertainty on the production cross section, NA61/SHINE experiment performed the measurements with $\pi^{\pm}$, $K^{\pm}$ and p using a replica of the target in the T2K experiment [110]. In addition to this update, the hadronic interaction on horn cooling water is implemented in the nominal flux simulation.

Figure 5.1 shows the flux uncertainties for each neutrino mode and each detector and a comparison of the updated total uncertainties with the original analysis. The updated uncertainty for a wider energy range is reduced by using the new replica data. Especially for higher energy where $K^{\pm}$ exiting from the target dominates the flux, the uncertainty is reduced largely. On the other hand, the uncertainty the near neutrino energy peak becomes a little bit larger due to the hadron interaction on cooling water which is newly added in the nominal simulation.

5.2 Updates of Near Detector Fit

This section describes the updates of the near detector fit mainly about the new event categorization.

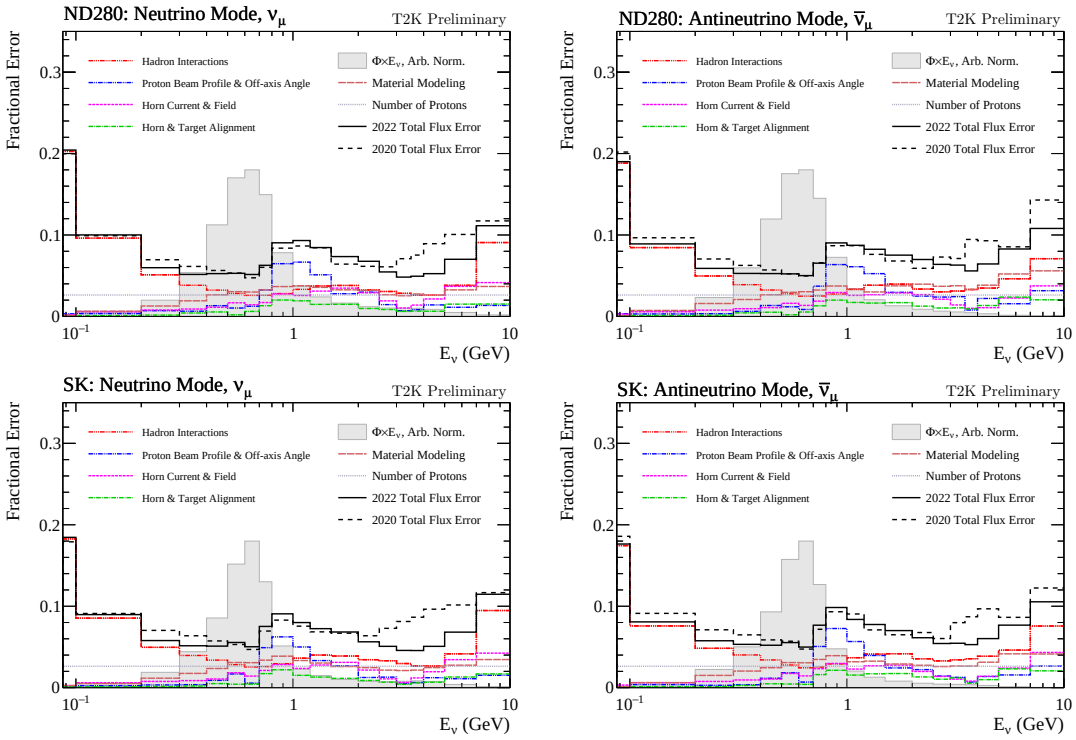

Figure 5.1: Updated uncertainty on the right sign neutrino flux in neutrino mode (left) and antineutrino mode (right) at ND280 (top) and SK (bottom). There is a comparison of the total uncertainty of the flux for the updated analysis (solid line) and original analysis (dotted line).

5.2.1 Event Selection

There are two improvements for the event categorization in the near detector fit in the updated oscillation analysis. One is the new event categorization based on the proton multiplicity in order to get better predictions of CCQE and 2p2h interactions. The other one is the photon tagging in order to improve the purity of the samples by separating the resonant π^0 production and DIS interaction modes which can produce photons. These modes can be main background sources for ν_e events at the far detector. Therefore, a more precise prediction of this event topology by the photon selection at the near detector is important. These new event selections are described in this subsection.

Photon Selection

Photon selection is performed by detecting photons in ECal. Most of these photons are mainly derived from the neutral π particles and this new selection targets to separate this channel. However, following decays including the π^0 decay should be considered,

- $\pi^0 \rightarrow \gamma + \gamma$
- $\eta \rightarrow \gamma + \gamma$
- $\eta \rightarrow \pi^0 + X \rightarrow \gamma + \gamma + X$
- $K \rightarrow \pi^0 + X \rightarrow \gamma + \gamma + X$
- $\Lambda \rightarrow \pi^0 + X \rightarrow \gamma + \gamma + X$

where X can be a variety of particles that depend on the specific decay.

In order to select photons, isolated objects in ECal are used (those not associated with the TPC or FGD tracks). It requires two criteria to tag the photon sample with the isolated objects. The first one is ECal PID which requires the object to be electromagnetic-like with a specific variable and its cut value is optimized to select a photon signal channel. This variable is designed to discriminate $e^{\pm}/\gamma$ from ionizing particles such as protons and is defined as the log-likelihood ratio of the proton and electron hypotheses with a combined likelihood. The combined likelihood is used for this PID and it uses the following inputs,

- Circularity : This input gives a measure of how round the cluster is. It makes it possible to separate shower-like clusters (short and fat) from track-like clusters (long and thin).
- QRMS : This is the standard deviation of the hit charges in the cluster. Electromagnetic showers tend to have larger QRMS than MIP-like muons.
- Truncated Max Ratio : This input is the ratio of the charge deposited in the ECal layers with the highest and lowest total charge.
- Front Back Ratio : This input is a measure of the dE/dx along a track. With this ratio, we can discriminate electrons from muons since muon showers tend to deposit most of their charge at the front end of a cluster.

The second criterion is that an isolated object in ECal must be identified as a photon by a certain variable which represents how many layers from upstream were hit (MostUpStreamLayerHit). This fact implies that the most of photons are likely to shower in the first layers of the ECal while the showers which start from the outer layers are more likely to be from pile-up in ECal. To reject such pile-up objects, it is required that MostUpStreamLayerHit < 6.

As a result, the purity for the CC0π and CC1π samples with this new photon selection gets $5-7$ % improvements compared to the past event selection as shown in Tab. 5.1.

Table 5.1: Efficiencies and purities for CC0π and CC1π samples with photon rejections and comparison with respect to the past analysis without the rejection.

Event Topology	Target	Efficiency (%)	Efficiency Change (%)	Purity (%)	Purity Change (%)
CC0π	FGD1	46.86	-1.14	76.3	+5.04
	FGD2	47.47	-0.53	72.8	+4.62
CC1π	FGD1	27.06	-1.94	60.2	+7.75
	FGD2	23.03	-0.97	58.5	+7.25

Proton Selection

First, proton PID criterion is required in order to select the proton selection. Using Eq. 2.5, the proton PID which is a reconstructed track in TPC is defined in a similar way as the pion selection as follows,

$$L_p > 0.5 \tag{5.1}$$

Furthermore, criteria to identify the particle which is an isolated track in FGD as proton by using the following $Pull$:

$$Pull^{FGD}_{proton} = \frac{E_{measured} - E_{proton}(L_{measured})}{\sigma_{E_{proton}}(L_{measured})} > -4 \tag{5.2}$$

where $E_{proton}(L_{measured})$ is the expected energy deposit for a track length $L_{measured}$ for proton. These cut values are based on previous cross-section studies which used proton selections [111]. Based on these criteria, the CC0π sample is split into :

- CC0π0p : 0 reconstructed photons and protons
- CC0πNp : 0 reconstructed photons and the sum of both reconstructed protons in TPC and isolated protons in FGD is greater than 0.

Summary of the new event selection

A flow of cuts with our new selections is shown in Fig. 5.2. There are five event categories for FGD1 and FGD2 and in total 10 event categories for ν mode. Figure 5.3 and Fig. 5.4 show

the comparison of the data and MC prediction for ν mode FGD1 with the new event selection. Finally, the purities for FGD1 (FGD2) samples are : CC0π 76.3% (72.8%), CC1π 60.2% (58.5%), CC-Photon 53.9% (54.2%) and CC-Other 52.2% (50.3%).

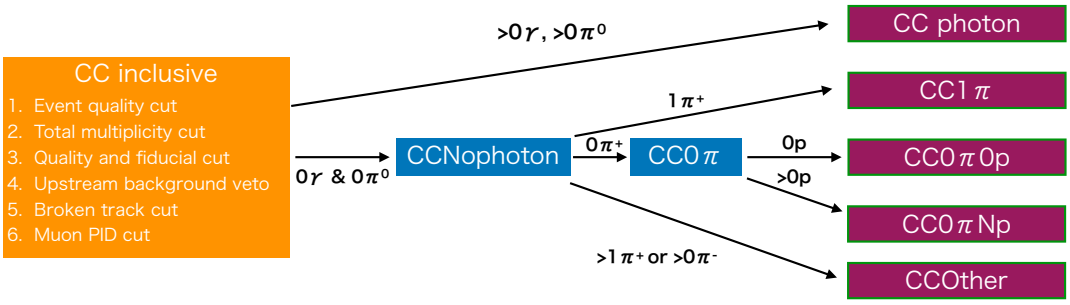

Figure 5.2: Diagram of the selection flow of the ν mode data for the near detector fit.

5.2.2 Detector Systematics

New several detector systematics should be considered especially for the photon selection in ECal. They are evaluated with the control samples in ECal which are dedicated for each systematic. The detail of these systematics is as follows,

- ECal Tracking Efficiency : This systematic is related to the reconstruction efficiency in the ECal. In order to evaluate this systematic, two efficiencies are defined for showers and tracks: ratio of the number of events for which are shower-like (track-like) TPC candidates and ECal shower (track) found to the number of events for which are shower-like (track-like) TPC candidate. The uncertainty is calculated by comparing data and MC prediction of these efficiencies for each momentum bin of each control sample.

- PID in ECal : To evaluate this systematics, dedicated control sub-samples for electrons, through-going muons, cosmic muons, and protons are used. An efficiency for each control sub-sample is defined with the cut value of the specific value of the first criterion for the photon selection. The uncertainty of this systematic is evaluated by comparing data and MC prediction of this efficiency as with the other systematics.

- TPC-ECal Matching Efficiency : In order to evaluate this systematic, we defined the track matching efficiencies, which is the ratio of the number of tracks passing selection only with an ECal to the number of tracks passing selection with an ECal segment matched with the selected TPC track. The uncertainty is evaluated by comparing data and MC prediction of this efficiency as with the other systematics.

- ECal Photon Pile-up : To select a control sample for this systematic, it is required that there is no activity in FGD fiducial volume in the event. Then, efficiency is defined as the ratio of the number of events with ECal photons to the total number of events in this

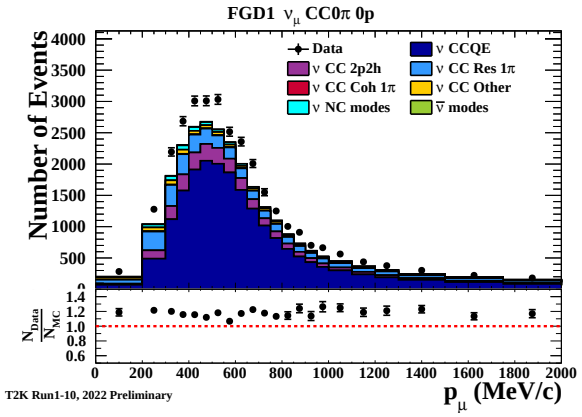

(a) ν mode CC0π0proton momentum distribution

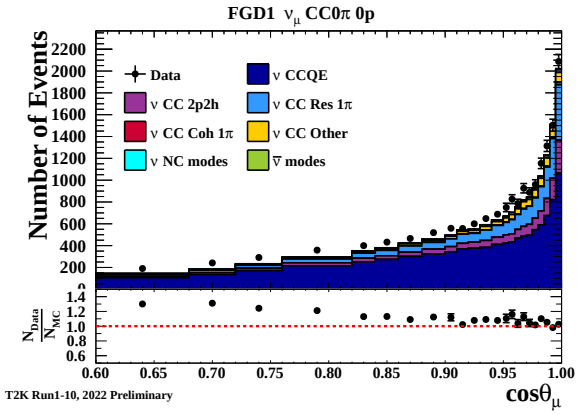

(b) ν mode CC0π0proton $\cos\theta$ distribution

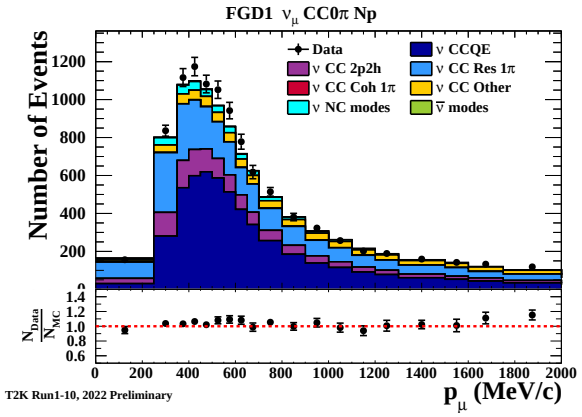

(c) ν mode CC0πNprotons momentum distribution

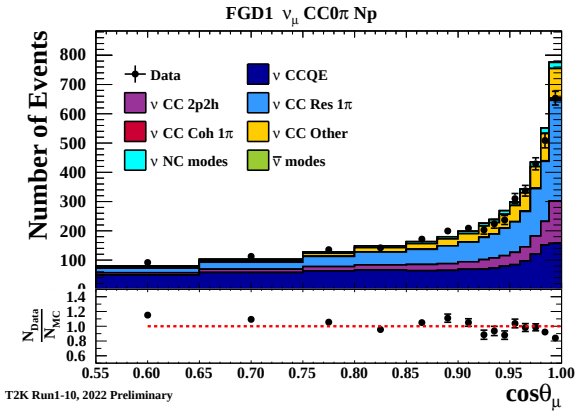

(d) ν mode CC0πNprotons $\cos\theta$ distribution

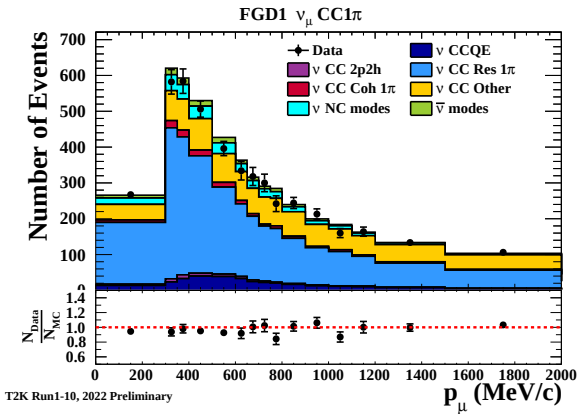

(e) ν mode CC1π momentum distribution

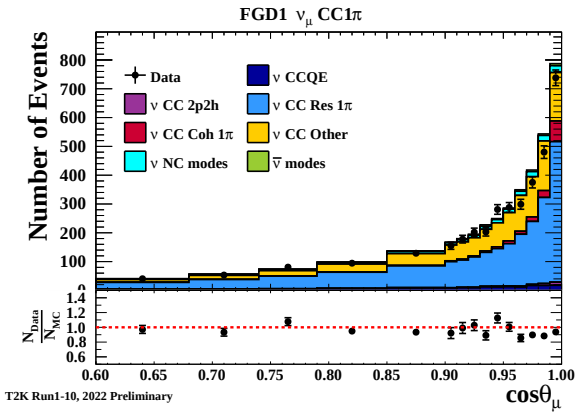

(f) ν mode CC1π $\cos\theta$ distribution

Figure 5.3: Pre-fit predictions and data points of muon momentum (left) and angular (right) distributions interaction mode by mode for CC0π0proton, CC0πNprotons and CC1π samples of ν mode. The black points and error bars represent the data with the statistical uncertainty. The shaded regions show the contributions of the ν CCQE, ν 2p2h, ν CC resonant 1π, ν CC coherent 1π, ν CC other, ν NC modes, and $\bar{\nu}$ modes. The bottom insets show the ratio of data to simulation.

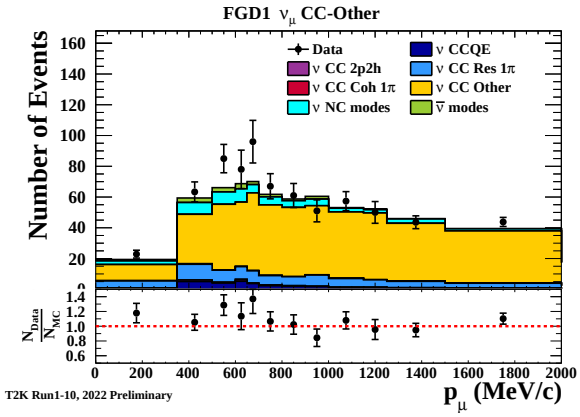

(a) ν mode CCOther momentum distribution

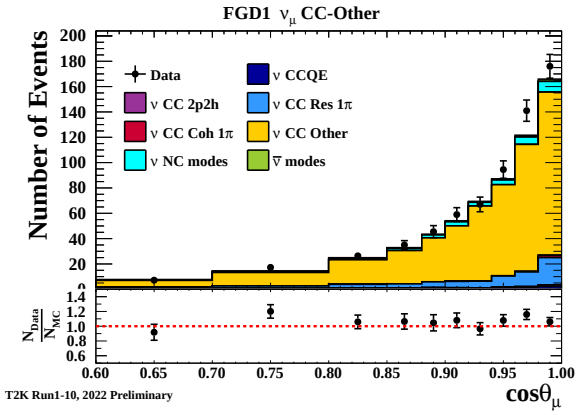

(b) ν mode CCOther $\cos\theta$ distribution

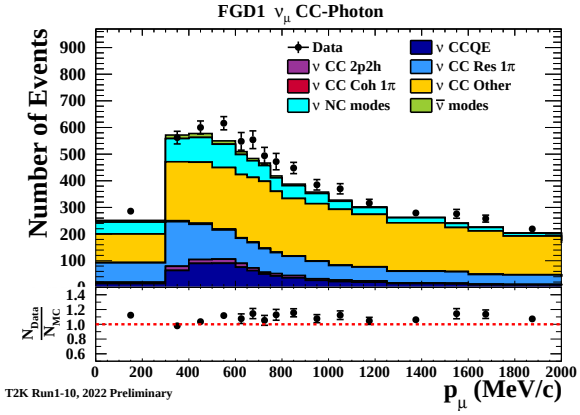

(c) ν mode CCphoton momentum distribution

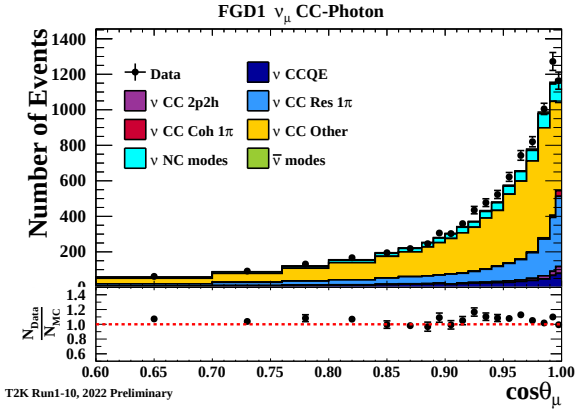

(d) ν mode CCphoton $\cos\theta$ distribution

Figure 5.4: Pre-fit predictions and data points of muon momentum (left) and angular (right) distributions interaction mode by mode for CCphoton and CCOther samples of ν mode. The black points and error bars represent the data with the statistical uncertainty. The shaded regions show the contributions of the ν CCQE, ν 2p2h, ν CC resonant 1π, ν CC coherent 1π, ν CC other, ν NC modes, and $\bar{\nu}$ modes. The bottom insets show the ratio of data to simulation.

control sample. The uncertainty is evaluated by comparing data and MC prediction of this efficiency as with the other systematics.

5.3 Updates of Far Detector Fit

This section describes the updates of the far detector fit mainly about the new multi-ring selection.

5.3.1 Event Selection

Given the spread of the neutrino beam flux at the T2K experiment, resonant 1π production events with multi-ring topologies are thought to be the second most dominant type of interaction. New ν_μCC1π multi-ring selection is introduced to tag this event topology and can increase the total number of the ν_μ events and reduce the statistical uncertainty. Thus, it improves the precision on the oscillation parameters.

ν_μCC1π multi-ring selection

Criteria of ν_μCC1π multi-ring selection is as follows,

1. Fully-contained event in SK fiducial volume.
2. Number of rings found is more than one.
3. The ring is identified as muon-like.
4. Visible energy is larger than 30 MeV.
5. The number of the decay electrons is one or two.
6. Optimized cuts by a log-likelihood ratio of fiTQun is dedicated to select signal events which have these two characters : One to three Cherenkov rings are detected and all the rings μ-like or $\pi^{\pm}$-like, not e-like.

5.3.2 Detector Systematics

Since new CC1π multi-ring selection is added, new detector systematics evaluation should be introduced while the evaluation for the single-ring events is not changed compared to the original analysis. To get an estimate of the systematic error for $1\mu + 1\pi^+$ event topology, hybrid $1\mu + 1\pi$ control sample is used in a similar way to the hybrid π_0 sample mentioned in Sec. 4.5.4. This hybrid sample combines multi-ring $1\mu + 1\pi^+$ events from the T2K MC with muon-like events from the SK data or MC. The difference between the hybrid data and MC samples can be interpreted as a systematic source.

5.4 Improvements of Parametrization of Neutrino Interaction Model

Related to the updates on the near and far detector analysis, the neutrino interaction modeling is also updated and this section describes it.

5.4.1 Overview of the Updates of the Interaction Model

Compared to the analysis discussed in Chapter 4, the systematics uncertainties of neutrino interaction models are updated as follows.

- Low Q^2 normalization parameters are replaced by the more sophisticated parametrization.
- Updates of the 2p2h parametrization to consider the nucleon pair fraction for each type.
- New parameters are added and several prior constraints are updated to control the resonance 1π production processes.
- A new parameter is introduced to describe the contribution from nucleon FSI.
- New DIS and Multi-Pi parameters which are motivated by the updated theory are introduced.

5.4.2 Parametrization of Updated Interaction Model

CCQE parameters

In the original analysis, there are five parameters for the normalization of low Q^2 bins. To remove these ad-hoc parameters and parametrize more sophisticatedly, shell modification parameters of the two-dimensional SF distribution and Pauli Blocking parameters are introduced. Furthermore, optical potential parameters are introduced to control the effects of the FSI on the lepton kinematics.

- Shell modification parameters : In our spectral function model, two-dimensional template histograms are used and it can be divided into two contributions : mean field (MF) and short-range correlated nucleus (SRC). As for the MF part, there are normalization and shape parameters for the P and S shells for carbon nucleus, and for the $P_{1/2}$, $P_{3/2}$, and S shells for oxygen nucleus. For the SRC part, there are two normalization parameters for carbon and oxygen respectively.
- Pauli blocking : This parameter is motivated to treat the uncertainty driven by the Fermi momentum for each nucleon. There are four parameters for carbon and oxygen and for neutrino and anti-neutrino.
- Optical potential : Spectral function model is based on the pulse wave impulse approximation and doesn't include the FSI effect on the cross section. In order to cover this deficit in the original analysis, a new optical potential parameter is implemented by using two-dimensional template histograms in energy and three momentum transfer.

2p2h parameters

- Nucleon pair fraction : 2p2h interactions for neutrinos can occur in either nn or pn pairs. To control the ratio of them, a new "PNNN shape" parameter has been implemented. The number of outgoing protons is different between them and this new parameter is important to adapt the new sample selection in the ND280 based on the proton multiplicity.

CC1π parameters

- Delta decay : This parameter is to treat the variation between two different methods to calculate the differential cross-section of CC1π resonance production based on the Rein-Sehgal model. One method is isotropically ejecting the pion and the nucleon back to back in the resonance rest frame, without the preferred direction for either particle. The other method is to calculate matrix elements for the nucleon to Δ resonance transition and contract them with the relevant spherical harmonics.

- E_B^{RES}: This parameter is dedicated to controlling the binding energy for resonant interactions. There are four parameters for each nucleon and for ν_μ and $\bar{\nu}_\mu$.

FSI parameters

In addition to the pion FSI dials which are introduced in the original analysis, one new parameter is added to account for the nucleon FSI. This new parameter is to change the number of events involving the nucleon FSI while the total inclusive cross section is not changed.

DIS parameters

Two new parameters are introduced to treat the Bodek-Yang uncertainties based on the updated theoretical DIS model for low momentum transfer region [112]. One is to describe the vector part (CC BY Multi-Pi Vector) and the other one is to describe the axial part (CC BY Multi-Pi Axial). These parameters replace "CC BY Multi-Pi" in the original analysis.

In the original analysis, only the normalization parameter of the total cross section of a Multi-π model is introduced. For the updated analysis, one additional shape parameter is added to account for the variation of the shapes between our nominal model and the AGKY model.

5.4.3 Summary of Updated Interaction Model

Cross section parameters including the new additional parameters are summarized in Tabs. 5.2 and 5.3. Although these improvements allow us to evaluate more precisely the systematic uncertainties, there is still room to introduce the additional study to cover the potential bias. It will be discussed in Chapter 6.

Table 5.2: Summary of the cross section CCQE and 2p2h parameters for the updated oscillation analysis.

Parameter	Nominal	Uncertainty	Type
M_A^{QE}	1.03	0.06	Shape
Q^2 norm 5	1	0.11	Norm
Q^2 norm 6	1	0.18	Norm
Q^2 norm 7	1	0.40	Norm
P shell MF norm C	0	0.2	Norm
S shell MF norm C	0	0.2	Norm
P 1/2 shell MF norm O	0	0.2	Norm
P 3/2 shell MF norm O	0	0.45	Norm
S shell MF norm O	0	0.75	Norm
P shell p_{miss}MF Shape C	0	1	Shape
S shell p_{miss}MF Shape C	0	1	Shape
P 1/2 shell p_{miss}MF Shape O	0	1	Shape
P 3/2 shell p_{miss}MF Shape O	0	1	Shape
S shell p_{miss}MF Shape O	0	1	Shape
SRC norm C	1	2	Norm
SRC norm O	1	2	Norm
Pauli blocking C ν	0	1	Shape
Pauli blocking O ν	0	1	Shape
Pauli blocking C $\bar{\nu}$	0	1	Shape
Pauli blocking O $\bar{\nu}$	0	1	Shape
Optical potential C	0	1	Shape
Optical potential O	0	1	Shape
$E_{b,\nu}^C$	2	6	Mom. Shift
$E_{b,\bar{\nu}}^C$	0	6	Mom. Shift
$E_{b,\nu}^O$	4	6	Mom. Shift
$E_{b,\bar{\nu}}^O$	0	6	Mom. Shift
2p2h norm. ν	1	1	Norm
2p2h norm. $\bar{\nu}$	1	1	Norm
2p2h norm. C to O	1	0.2	Norm
2p2h shape C	0	1	Shape
2p2h shape O	0	1	Shape
PNNN Shape	0	0.33	Shape
2p2h E. dep. low-E_ν	1	1	Shape
2p2h E. dep. high-E_ν	1	1	Shape
2p2h E. dep. low-$E_{\bar{\nu}}$	1	1	Shape
2p2h E. dep. high-$E_{\bar{\nu}}$	1	1	Shape

Table 5.3: Summary of cross section parameters other than CCQE and 2p2h for the update oscillation analysis.

Parameter	Nominal	Uncertainty	Type
M_A^{RES}	1.07 GeV	0.15 GeV	Shape
C_5^A	0.96	0.15	Shape
$I_{1/2}$	0.96	0.4	Shape
$I_{1/2}$ low. p_π	0.96	1.3	Shape
RES Eb C ν_μ	25 MeV	25 MeV	Shape
RES Eb O ν_μ	25 MeV	25 MeV	Shape
RES Eb C $\bar{\nu}_\mu$	25 MeV	25 MeV	Shape
RES Eb O $\bar{\nu}_\mu$	25 MeV	25 MeV	Shape
RS Delta Decay	1	1	Shape
SPP π_0 Norm ν_μ	1	0.3	Norm
SPP π_0 Norm $\bar{\nu}_\mu$	1	0.3	Norm
CC norm. ν	1.00	0.02	Norm
CC norm. $\bar{\nu}$	1.00	0.01	Norm
ν_e/ν_μ	1.000	0.028	Norm
$\bar{\nu}_e/\bar{\nu}_\mu$	1.000	0.028	Norm
CC BY DIS	0	1	Shape
CC Multi-Pi Total cross section	0	1	Shape
CC BY Multi-Pi Vector	0	1	Shape
CC BY Multi-Pi Axial	0	1	Shape
CC Multi-Pi Multi Shape	0	1	Shape
CC Misc.	1	1	Norm
CC DIS Multi-Pi Norm ν	1.000	0.035	Norm
CC DIS Multi-Pi Norm $\bar{\nu}$	1.000	0.035	Norm
CC Coherent C ν	1.0	0.3	Norm
CC Coherent O $\bar{\nu}$	1.0	0.3	Norm
NC Coherent	1.0	0.3	Norm
NC 1γ	1.0	1	Norm
NC Other Near	1.0	0.3	Norm
NC Other Far	1.0	0.3	Norm
π-FSI QE	1.069	0.313	Shape
π-FSI QE high	1.824	0.859	Shape
π-FSI Hadron Prod.	1.002	1.101	Shape
π-FSI Absorption	1.404	0.432	Shape
π-FSI Charge Exchange	0.697	0.305	Shape
Nucleon FSI	0	0.3	Shape

Chapter 6

Study of Neutrino Interaction Effects for Oscillation Analysis

The analysis framework was updated to constrain the uncertainty of neutrino interaction and flux as we discussed in Chapter 5. However, "the choice" of the neutrino interaction model is likely to introduce a bias in the measurement of neutrino oscillation parameters. There are several alternative model candidates described in Chapter 3 and the near detector fit cannot cover the bias. Therefore, additional studies should be done to consider it. To estimate the size of the bias, we performed the robustness study in which simulated data sets generated by the alternative models were used.

6.1 Procedure

6.1.1 Overview of Procedure of Robustness Studies

We will explain the detailed procedure of estimating the potential bias through our robustness studies. Figure 6.1 shows the overview of the procedure. First the simulated data sets with each alternative model were made at the near detector and the far detector. Using those data sets, the near detector fit was performed and then, the post-fit covariance matrix and parameters were given as the input for the next far detector analysis. Next, we performed the far detector fit with the simulated data sets. In parallel with this, we also performed the same analysis in two ways where the nominal model including systematic and statistical uncertainties, or only statistical uncertainty was used. We will describe later why these two ways are used. Finally, the results with the alternative model were compared with the nominal model and the bias for the oscillation parameters was estimated. As for the detail of the calculation way to estimate the bias in the comparison, we will describe in Sec. 6.3.

6.1.2 Alternative Models

There are several candidates of our alternative neutrino interaction model as described in Sec. 3.4. To choose the models for our robustness studies, the improvements of the updated analysis

were considered as the following three points.

1. A set of studies to vary nuclear effects in the CCQE interaction is desirable for the new proton sample in the near detector analysis.
2. More kinds of alternative models which are related to the pion production are needed because the new CC1π sample is added to the far detector analysis in this year's analysis.
3. New study which focused on differences between muon and electron neutrino cross section was needed.

Following these criteria, 16 simulated data sets were used as follows.

- Alternative nuclear models (LFG and CRPA models)
- Near detector data-driven model focusing on CC0π nonQE interaction
- Alternative axial form factors (Z-expansion ($\pm1\sigma$, Nominal), 3Component ($\pm1\sigma$, Nominal))
- Removal energy
- Pion kinematics theory-driven model (1π hadron kinematics related to Δ_{1324} resonance ($\pm1\sigma$), Martini 1π)
- Pion kinematics data-driven model (Near detector data-driven model focusing on pion kinematics, Low Q^2 suppression extrapolated from the MINERνA experiment)
- Radiative correction

First four models are related to the criterion 1 and the next two of those corresponds to the criterion 2. Following criterion 3, last one was selected. We have already discussed all those models except for the near detector data-driven model, radiative correction and removal energy in Sec. 3.4.

The radiative correction is related to the coulomb effect for the neutrino-nucleus scattering. The coulomb effect affects event selection criteria at SK via a real photon emission. We studied this potential effect on our analysis as the radiative correction, where we made the simulated data set as with the other alternative models. Furthermore, we also studied the robustness study where the removal energy parameters are set to extreme value (15 MeV). This study is to understand the parametrization of the removal energy in our analysis framework since it was difficult technically to parametrize the removal energy in the past oscillation analysis framework. Regarding the data driven model, they will be described in the next section.

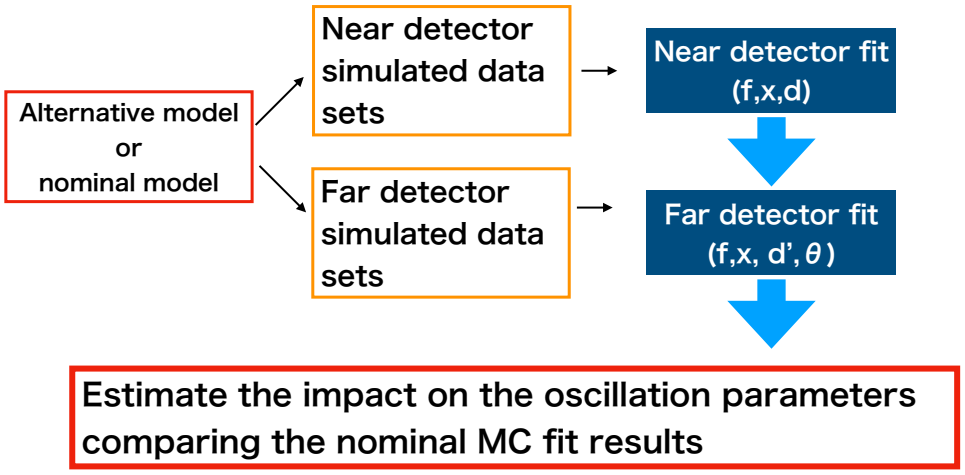

Figure 6.1: Overview of analysis flow with our robustness studies in the T2K oscillation analysis. Simulated data sets of each alternative model and nominal model are produced for the near and far detector respectively. They are analyzed in the same procedure.

6.1.3 Near Detector Data-driven Model

Focus on CC0π nonQE interaction

There is a lot of degrees of freedom in our CCQE interaction model in the current near detector fit to correct the discrepancy between data and nominal model prediction in the near detector CC0π sample. On the other hand, we do not understand well the nonQE contribution to the CC0π event topology and do not know how much degrees of freedom can be assigned to the shape of CCQE interactions. Therefore, we need to introduce the data driven study which was motivated by lack of theoretical ground in our neutrino interaction model, especially for the nonQE interaction (2p2h, final state interactions and etc).

This study was done with the FGD CC0π0γ sample which combines FGD CC0π0proton0γ and CC0πNprotons0γ samples. In this sample, the distribution was binned as a function of Q^2_{QE} which is defined as follows,

$$Q^2_{QE} = -m_l^2 + 2E_{\nu,QE}(E_l - p_l \cos(\theta_l)) \tag{6.1}$$

where m_l, E_l, p_l, and θ_l are the outgoing muon mass, energy, momentum and angle, and $E_{\nu,QE}$ is the neutrino energy reconstructed from the muon momentum and angle assuming CCQE interaction. Using the Q^2_{QE} distribution, we got the scaling factors to make the simulated data set in the following procedure.

- We take the post-fit results of the data fit in which all CCQE parameters were fixed at the nominal values in order to assign the compensation of the discrepancy between data and prediction in the near detector to the nonQE contribution.
- Reconstructed Q^2_{QE} distribution is built for the CC0π0γ sample for data and modified post-fit simulation which was made in the first step.
- The nonQE contribution in the prediction was scaled as a function of reconstructed Q^2_{QE} in the CC0π0γ sample to compensate the difference between data and our modified prediction.
- We apply the scale factors which are obtained in the previous step, to the true nonQE contribution as a function of true Q^2_{QE}.

Results of this procedure are shown in Fig. 6.2. We calculated the scaling factors which are applied to the nonQE contribution in the CC0π0γ topology in order to compensate the differences between post-fit prediction and data. Those scaling factors were calculated to generate the simulated data set and the green shaded areas in the left plots show the modified nonQE contribution after the application.

Focus on Pion Kinematics

Figure 6.3 shows the true pion momentum distribution and efficiency for the CC1π events at the far detector. This selection efficiency is not flat as a function of true pion momentum

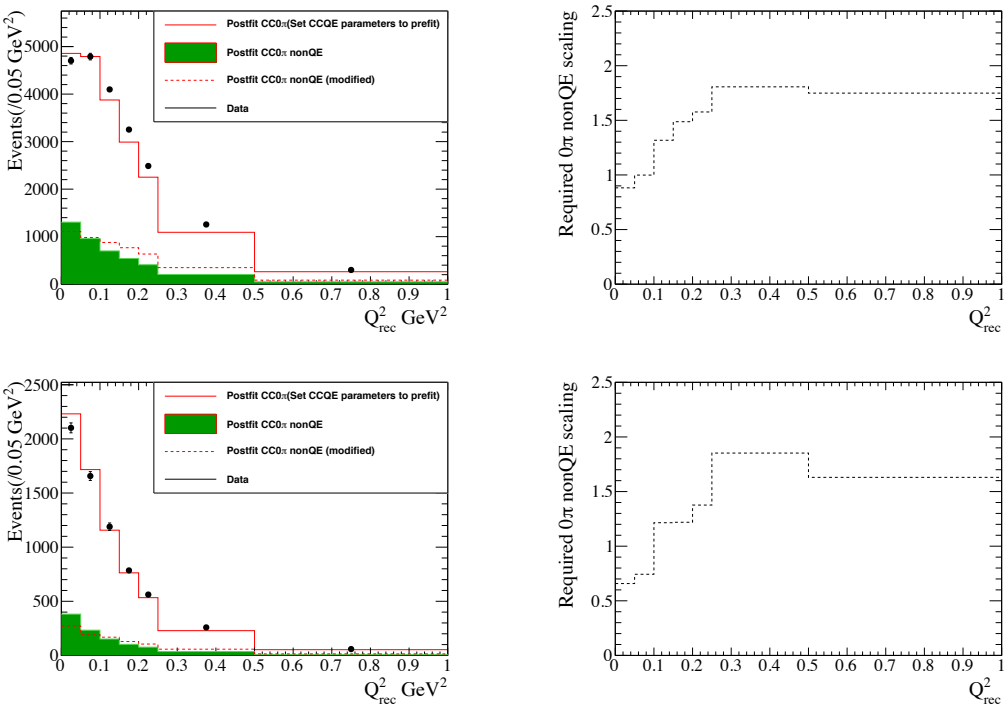

Figure 6.2: **Left:** The post-fit near detector prediction with all the CCQE parameters set to their nominal values for the FGD1 CC0π0γ of ν mode (upper) and $\bar{\nu}$ mode (lower) samples is shown with the data, where the nonQE contribution is shown in shaded green. The nonQE distribution is scaled so the overall prediction matches the data in the reconstructed space shown. The modified nonQE is shown in the dotted red line. **Right:** The scaling factors extracted are shown, calculated as the ratio of the dotted red line to the shaded green.

because this sample is designed to predominantly select events with pions below the Cherenkov threshold. Given this non-flatness, the observed event rates are affected by the shape of the pion momentum prediction from our near detector fit. This effect can be a potential systematic source in our oscillation analysis. However, there is a sizable discrepancy between data and the post-fit prediction in the near detector as shown in Fig. 6.4 and it is not surprising because pion kinematics information is not included in our likelihood of the near detector fit. Therefore, we need to introduce this robustness study of data-driven model at the near detector to cover such uncertainties of our pion kinematic models.

To generate this data-driven model, a set of scale factors is extracted in a coarse two dimensional reconstructed pion momentum and angle binning as shown in Fig. 6.5. We apply these factors as a function of true pion kinematics variables.

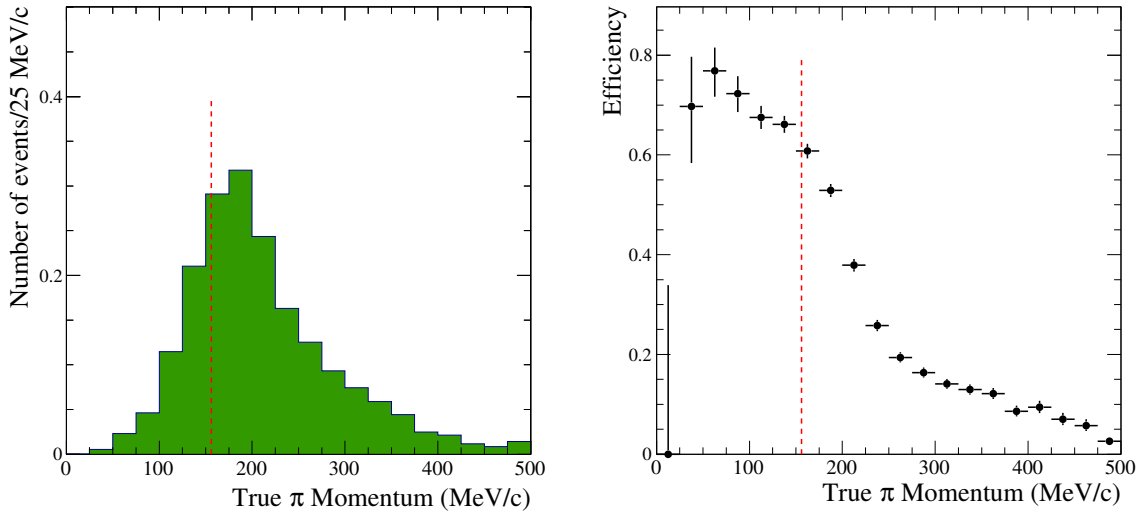

Figure 6.3: The true pion momentum distribution for selected simulated signal events in the CC1π^+ candidate sample with 1 electron-ring and 1 Michel electron at SK (left) and the selection efficiency for these events (right). The red dashed line indicates the Cherenkov threshold for charged pions.

6.2 Results of Robustness Study

Robustness study for all simulated data sets was done and we will describe mainly the detail of the two data sets (Data-drive model focused on CC0π nonQE and CRPA model) which caused the largest bias. As for the other alternative models, there is no such large bias as shown in the the results of the nonQE and the CRPA models. They are summarized in Appendix to avoid redundant repetition.

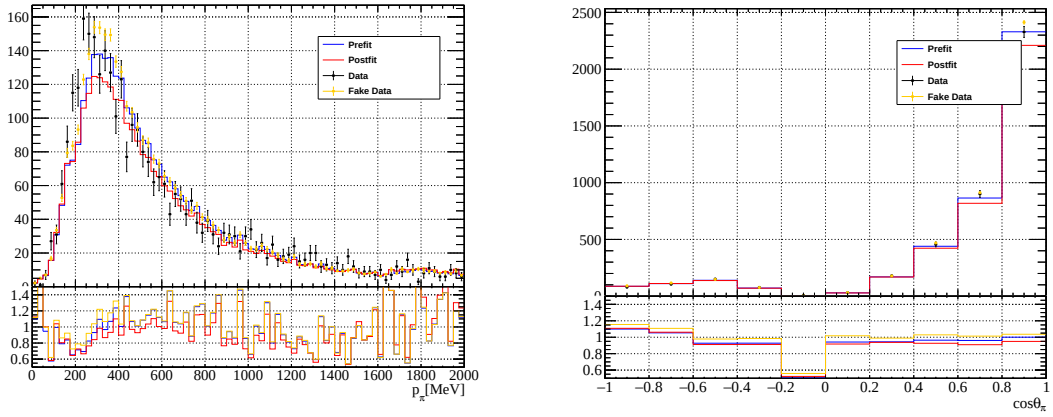

Figure 6.4: Reconstructed pion momentum (left) and angular (right) distributions at the near detector, after applying the weights in Fig. 6.5. Black dots represent the data, orange dots the simulated data, blue lines correspond to the pre-fit and red lines to the postfit. The ratio as a function of each kinematic variable is given beneath the plots.

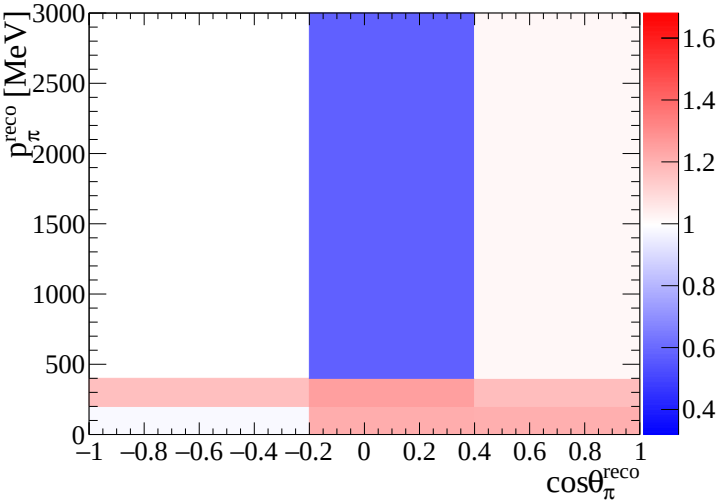

Figure 6.5: Weights applied at generator level to obtain this simulated data set, as function of reconstructed muon momentum and angle. Each bin content is taken as a multiplicative factor applied which increases or decreases the weight of an event whose true kinematics fall inside the bin.

6.2.1 Data-driven model focusing on CC0π nonQE

Near Detector Fit Results

Figures 6.6 and 6.7 show the fitting results of the cross section and flux parameters using this alternative model. The CCQE normalizations as a function of Q^2 and several other parameters which are related to the 2p2h and final state interactions move slightly as expected. As for the flux parameters, there are small shifts to compensate the difference between the nominal model and this alternative model.

Using the covariance matrices which are based on that near detector fit, we made the reconstructed neutrino energy prediction at the far detector as shown in Fig. 6.8. If the near detector fit describes the alternative model perfectly, these predictions from that matrix should cover the simulated data of this alternative model which is generated at the far detector. On the other hand, if there is any discrepancy between them, it indicates a bias which stems from the incompleteness of our near detector fit. As a whole, we can see that the event rates of this alternative model are decreased at 0.5 GeV compared to the nominal model as expected.

Far Detector Fit Results

Figures 6.9 shows the one-dimensional likelihood surfaces for Δm^2_{32}, $\sin^2\theta_{23}$ and $\delta_{\rm cp}$ with the reactor constraint on $\sin^2\theta_{13}$. There is a large shift in the contour for Δm^2_{32} and we will describe how it is treated in our oscillation analysis. Regarding $\delta_{\rm cp}$ and $\sin^2\theta_{23}$, there are only small shifts compared to that of Δm^2_{32}. Whether they are small enough will also be discussed in the next section.

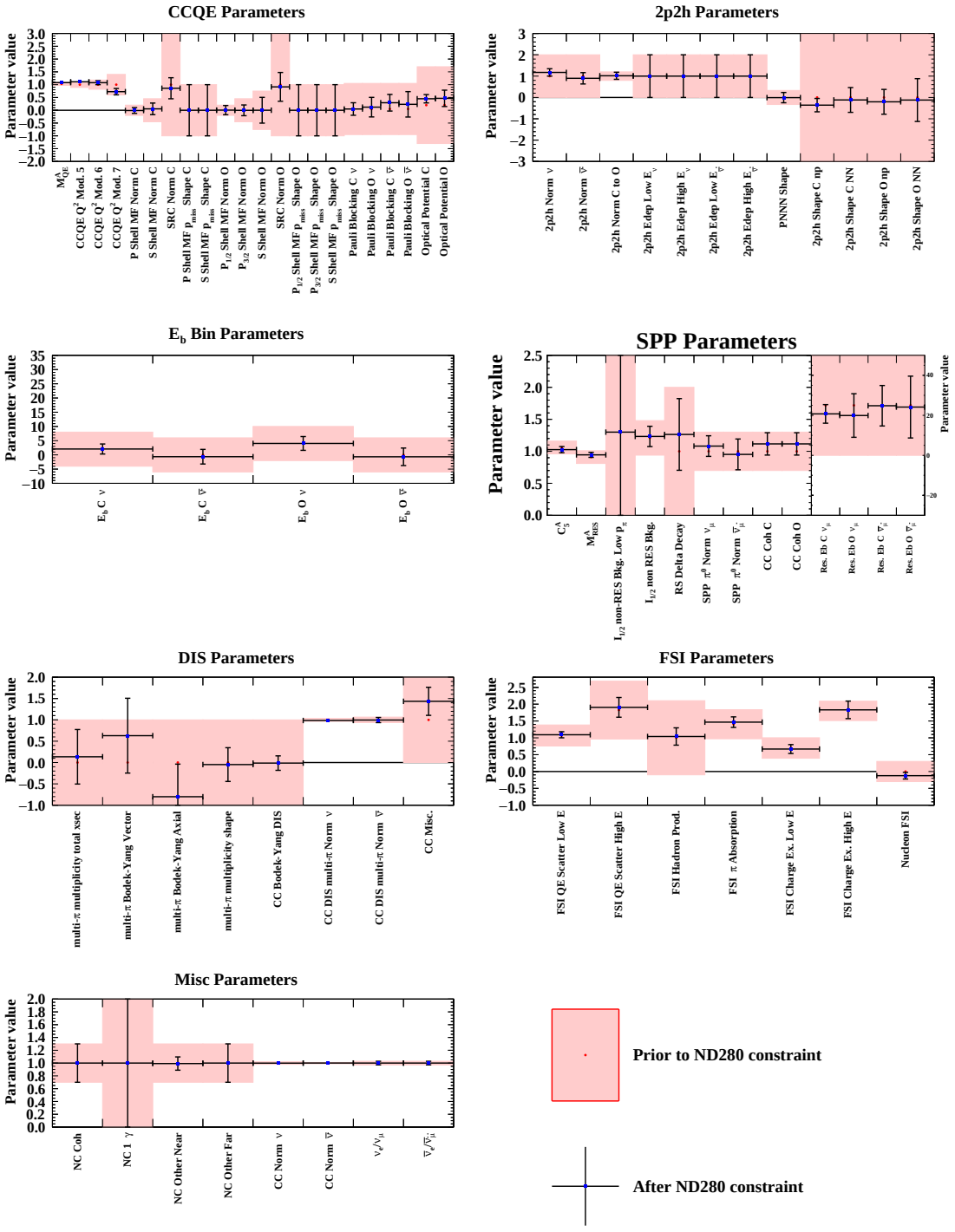

Figure 6.6: Pre-(red band) and post-fit (blue dots and black error bands), cross-section parameters for CCQE, 2p2h, E_b, Single Pion Production (SPP), FSI, DIS, and misc from the near detector fit to the simulated data set of data driven model focused on CC0π nonQE model.

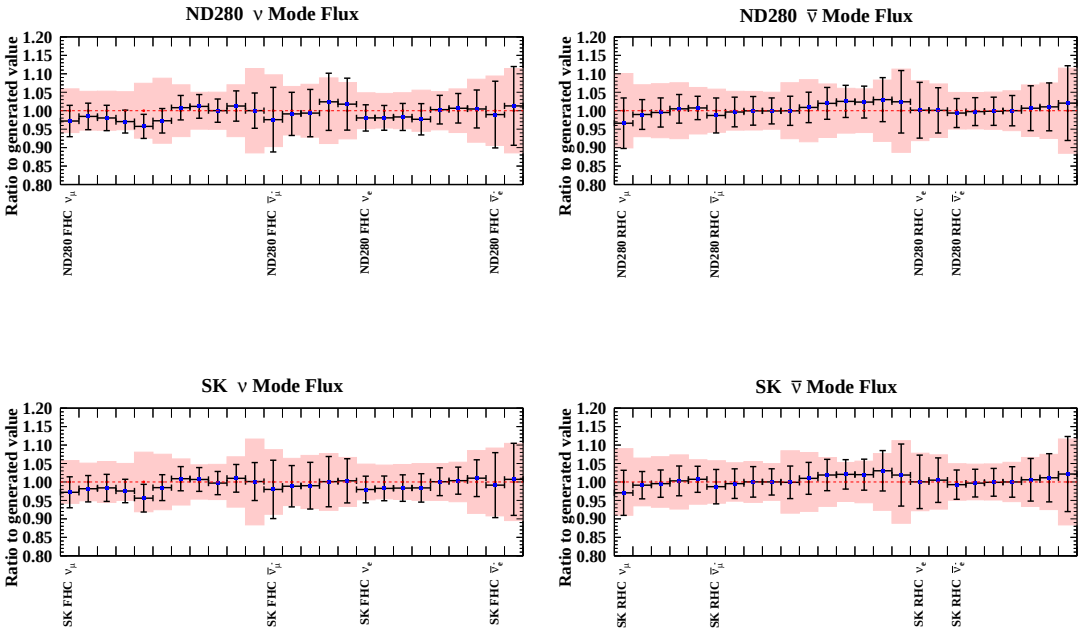

Figure 6.7: Pre- (red band) and post-fit (blue dots and black error bands), flux parameters for the ν mode (left) and the $\bar{\nu}$ mode (right), and for the ND280 (top) and SK (bottom) from the near detector fit to the simulated data set of data driven model focused on CC0π nonQE model.

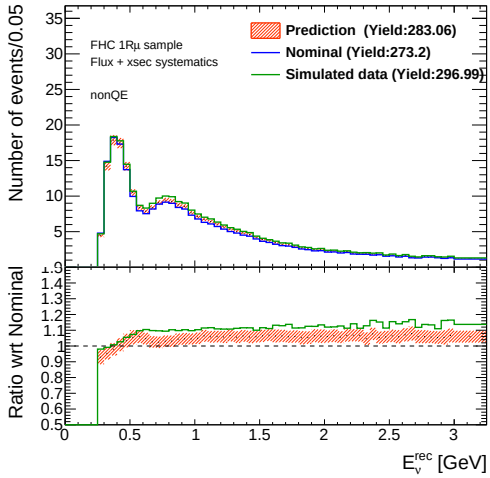

(a) ν mode 1Rμ

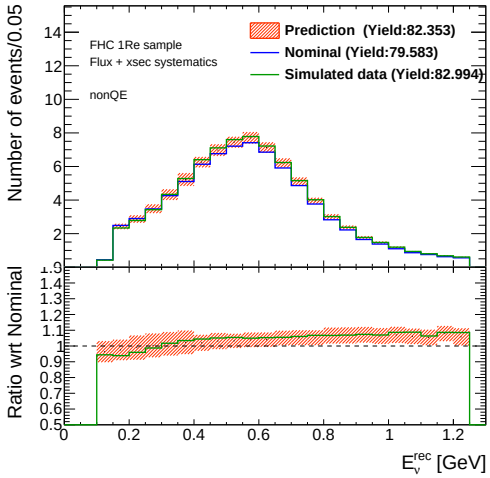

(b) ν mode 1Re

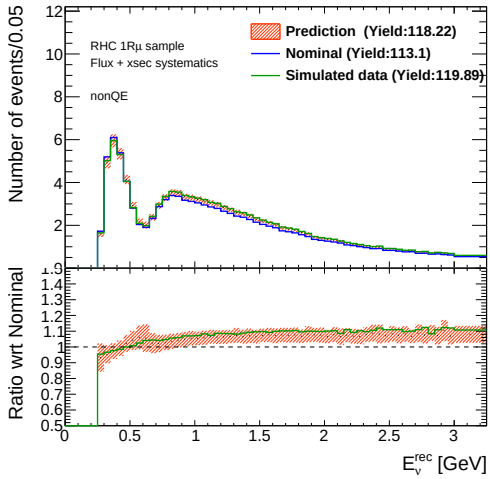

(c) $\bar{\nu}$ mode 1Rμ

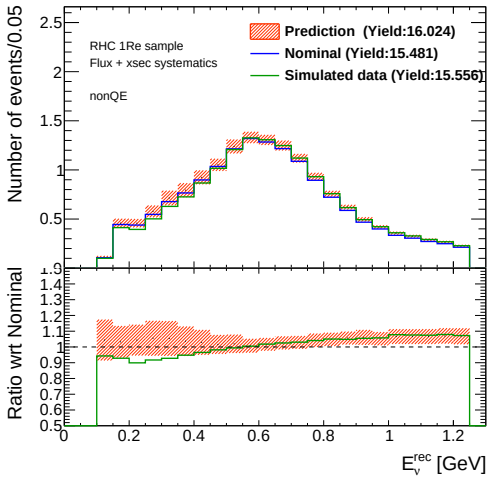

(d) $\bar{\nu}$ mode 1Re

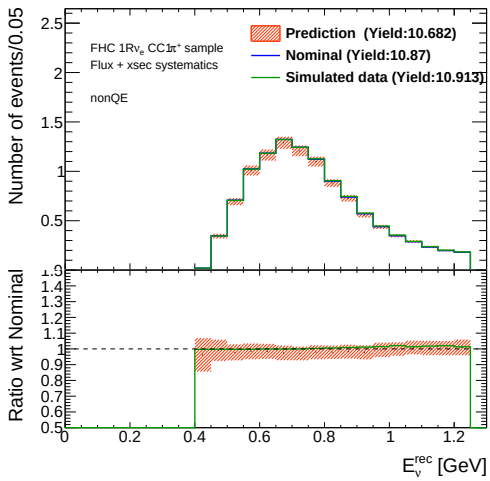

(e) ν mode 1Re1de

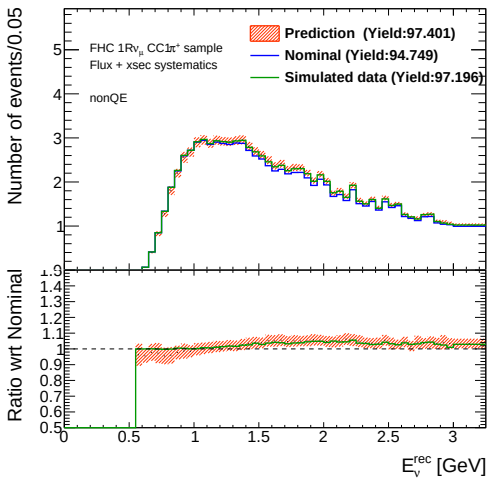

(f) ν mode CC1π multi-ring

Figure 6.8: Comparison plots of the number of events between the nominal far detector sample (blue solid line), the simulated data of the alternative model (green solid line) and the prediction from the near detector fit (red band) as a function of the reconstructed neutrino energy. The bottom insets show the ratio of data to simulation.

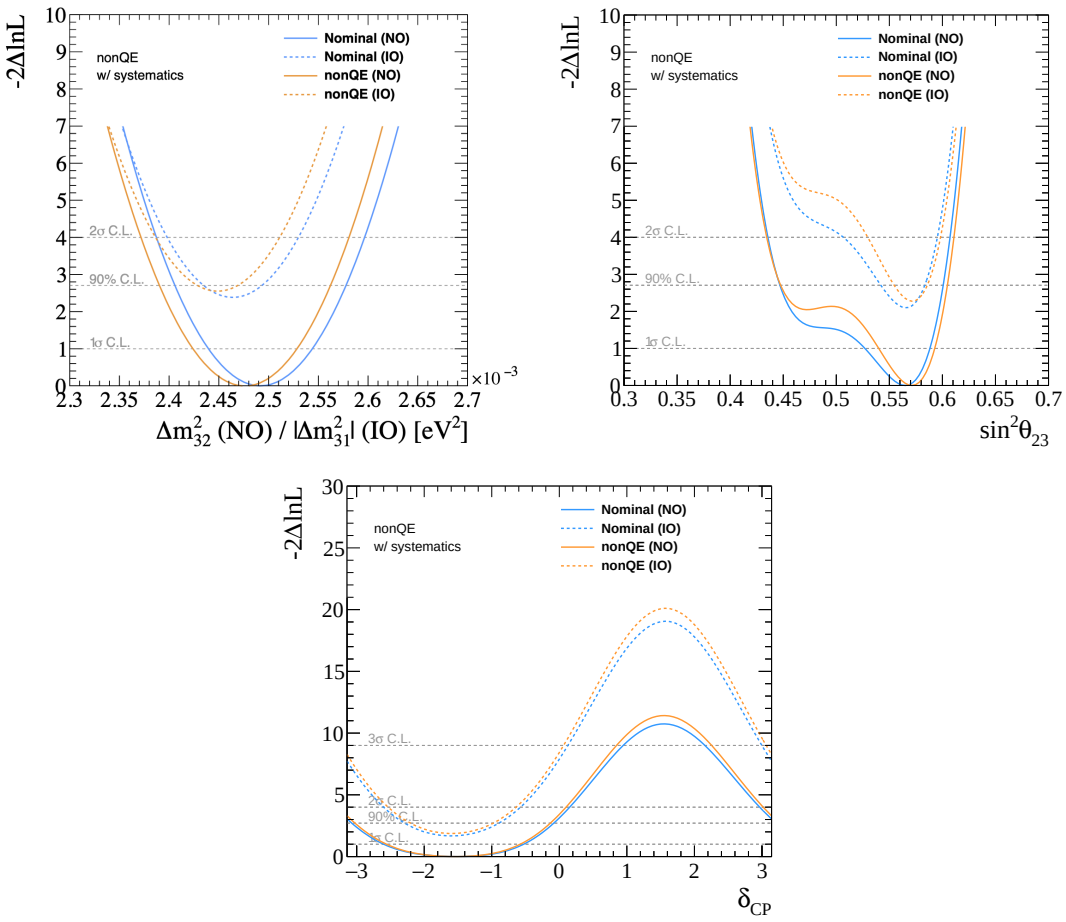

Figure 6.9: Comparison of likelihood surface for Δm^2_{32}, $\sin^2\theta_{23}$ and δ_{CP}. Orange lines show those from nonQE robustness studies and blue lines show those of nominal MC for the normal and inverted mass orderings.

6.2.2 CRPA model

Near Detector Fit Results

Figures 6.10 and 6.11 show the near detector fit results of cross section and flux using this alternative model. To compensate the low Q^2 suppression of this alternative model, the CCQE cross-section parameters which are especially related to the Pauli Blocking and Optical Potential were moved.

Figure 6.12 shows the comparison between prediction of the near detector fit results, simulated data of this alternative model at the far detector and the nominal far detector sample. Especially, the shape of the ν mode and the $\bar{\nu}$ mode 1Rμ sample is changed around 0.5 GeV. As a whole, the prediction from the near detector fit and the simulated data at the far detector are not very good agreement within the systematic uncertainty band. This disagreement is mainly caused by the differences of the target between the near detector and the far detector. The CRPA model has different effects on each target. This extrapolation issue can be a source of the bias for the oscillation parameters.

Far Detector Fit Results

Figure 6.13 shows the one dimensional likelihood surfaces for Δm^2_{32}, $\sin^2\theta_{23}$ and δ_{cp} with the reactor constraint on $\sin^2\theta_{13}$. There is a large shift in the contour only for Δm^2_{32} same as the nonQE model.

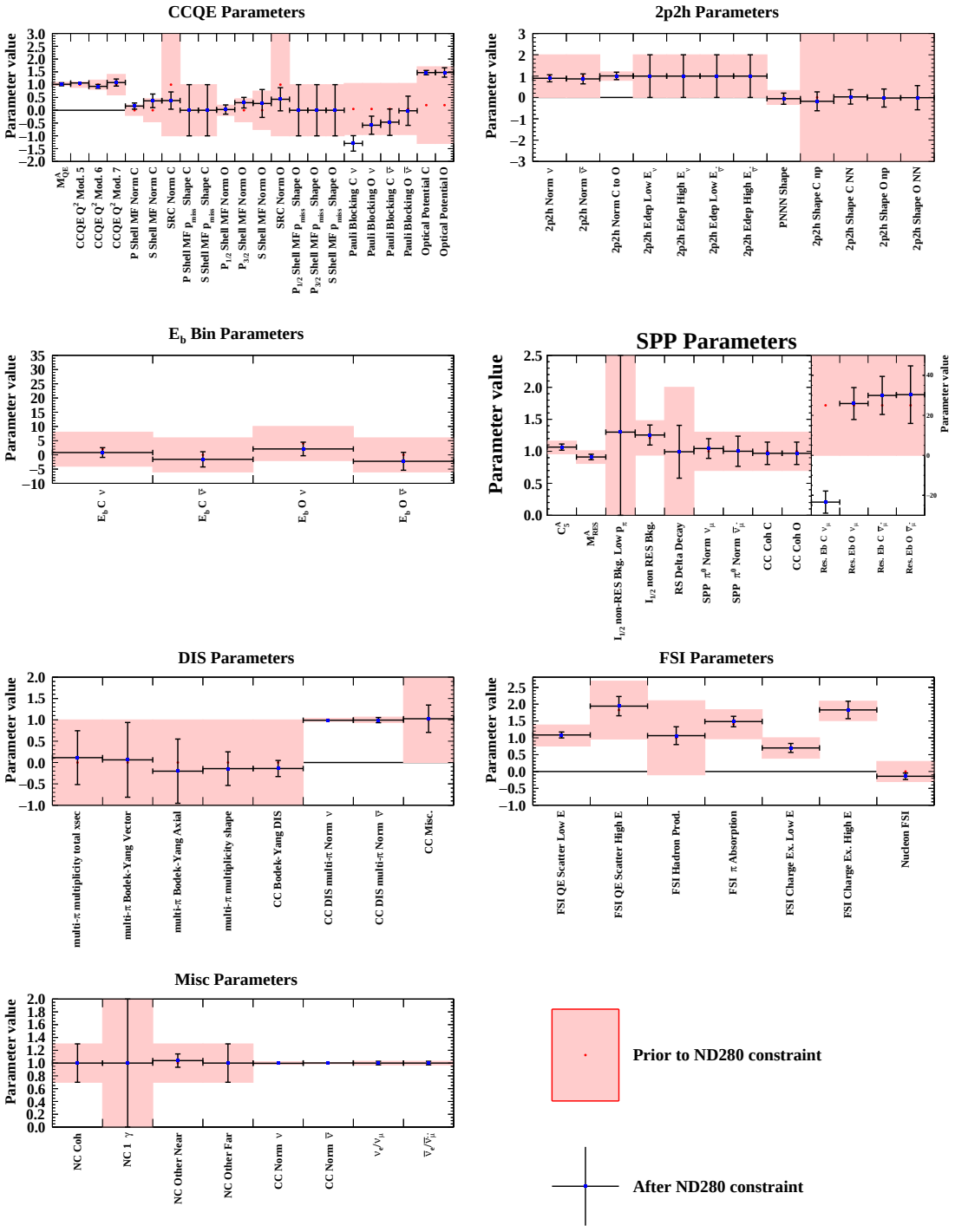

Figure 6.10: Pre-(red band) and post-fit (blue dots and black error bands), cross-section parameters CCQE, 2p2h, E_b, Single Pion Production (SPP), FSI, DIS, and misc from the near detector fit to the simulated data set of CRPA model.

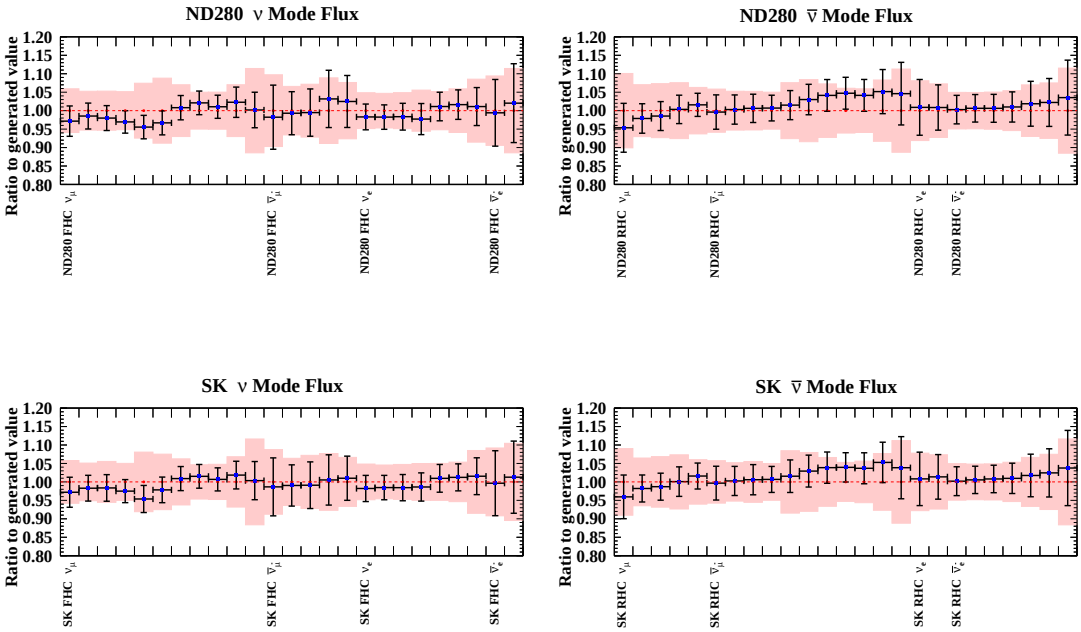

Figure 6.11: Pre- (red band) and post-fit (blue dots and black error bands), flux parameters for the ν mode (left) and the $\bar{\nu}$ mode (right), and for the ND280 (top) and SK (bottom) from the near detector fit to the simulated data set of CRPA model.

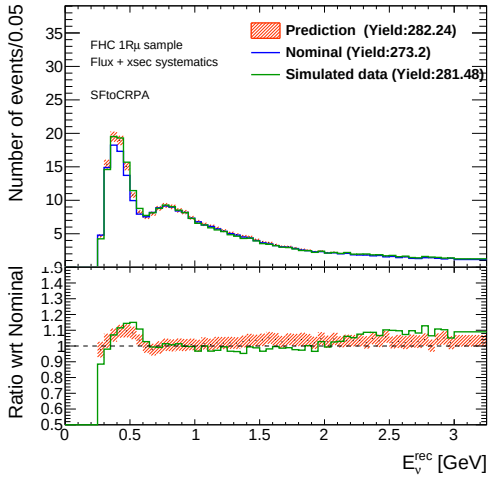

(a) ν mode 1Rμ

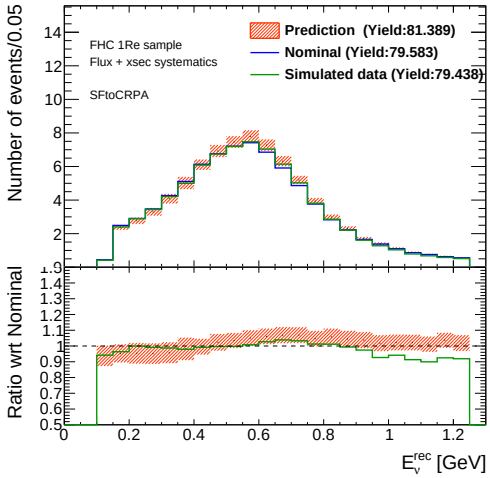

(b) ν mode 1Re

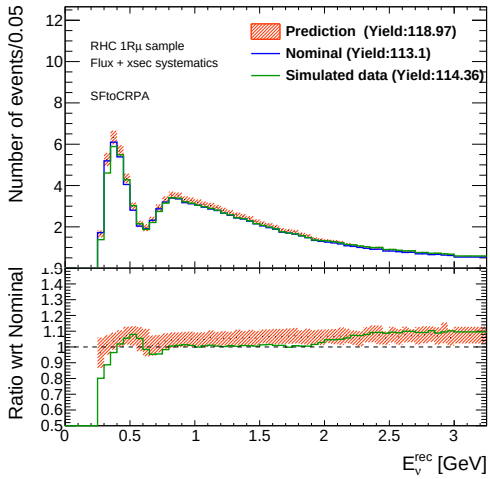

(c) $\bar{\nu}$ mode 1Rμ

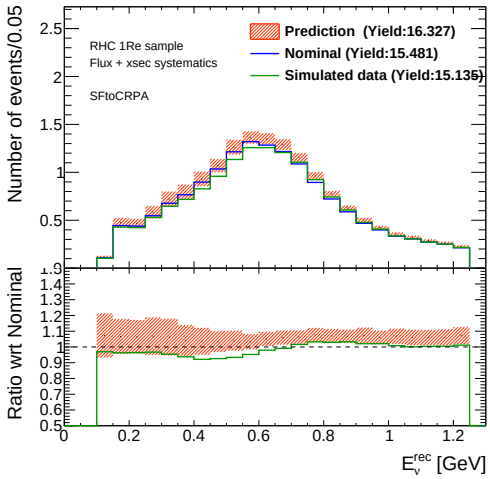

(d) $\bar{\nu}$ mode 1Re

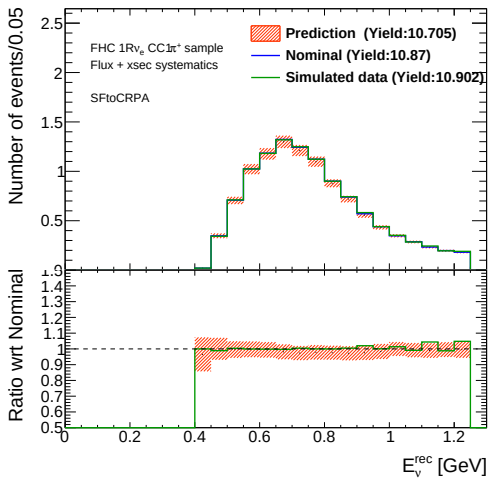

(e) ν mode 1Re1de

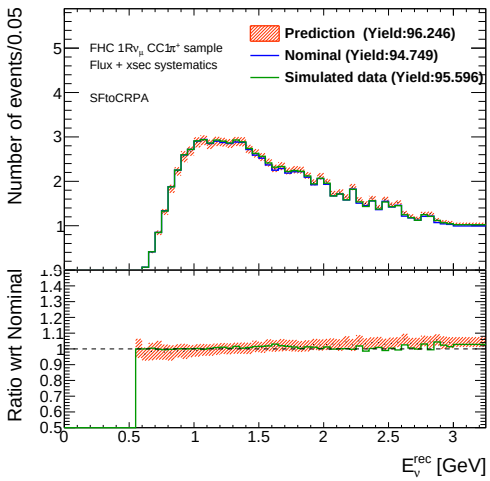

(f) ν mode CC1π multi-ring

Figure 6.12: Comparison plots of the number of events between nominal far detector sample (blue solid line), the simulated data of the alternative model (green solid line) and the prediction from the near detector fit (red band) as a function of the reconstructed neutrino energy. The bottom insets show the ratio of data to simulation.

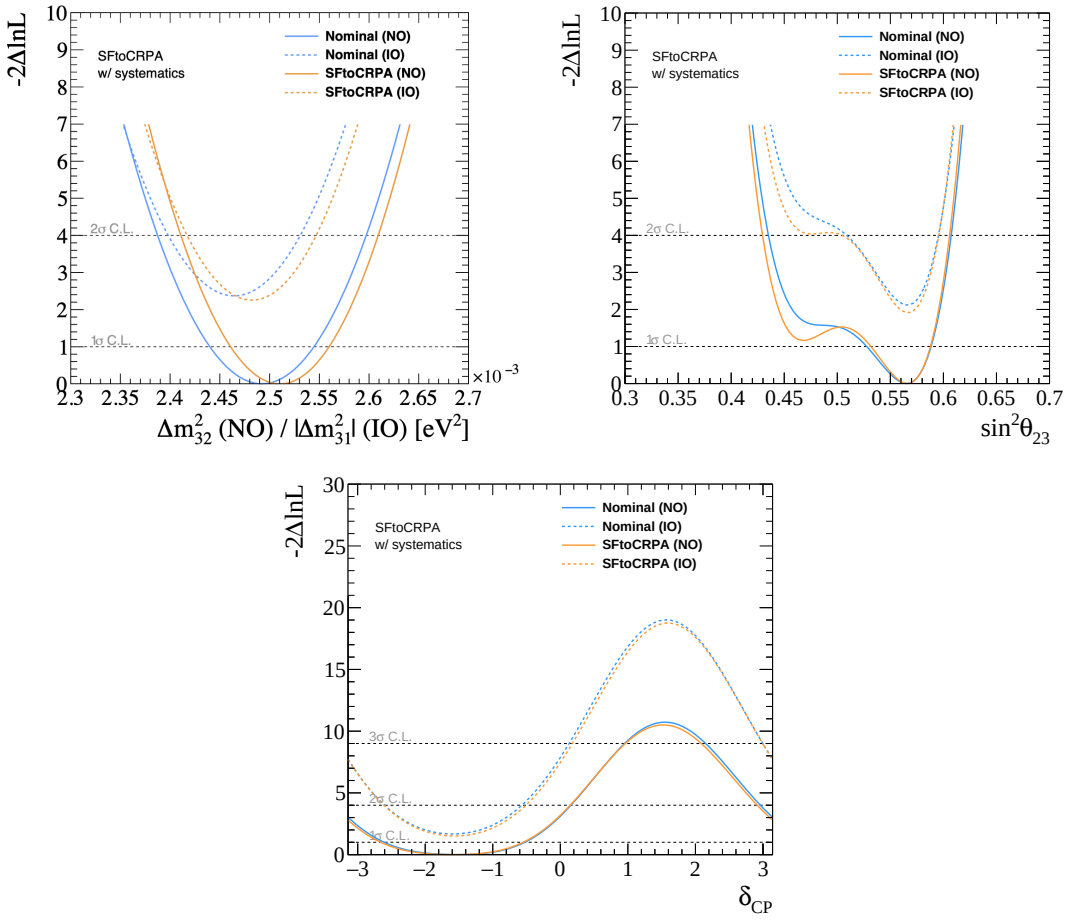

Figure 6.13: Comparison of likelihood surface for Δm^2_{32}, $\sin^2\theta_{23}$ and δ_{CP}. Orange lines show those from robustness studies of CRPA model and blue lines show those of nominal MC for the normal and inverted mass orderings.

6.3 Impact on Oscillation Parameters

In this section, we will describe how to evaluate the impact of our robustness studies on the oscillation parameters.

6.3.1 Bias Definition on Oscillation Parameters

We obtained the $\Delta\chi^2$ distribution for each oscillation parameter of the fit results for the alternative models, and also nominal model including only systematic uncertainties or systematic and statistical (total) uncertainties. The important quantities are one and two sigma ranges of the oscillation parameters.

Regarding Δm^2_{32} and $\sin^2\theta_{23}$, the bias was defined as the shift in the center of the 2σ intervals between the fit of each alternative model and the nominal model with the total uncertainties,

$$\Delta^{2\sigma} = \bar{x}^{2\sigma}_{\text{Nominal}} - \bar{x}^{2\sigma}_{\text{Alternative}} \tag{6.2}$$

where $\bar{x}^{2\sigma}_{\text{Nominal}}$ and $\bar{x}^{2\sigma}_{\text{Alternative}}$ are the shifts for fit with the nominal model and the alternative model respectively. Using them, we can define the primary bias metric relative to the 1σ systematic interval which we get from the nominal model with only systematic uncertainties as follows,

$$B^{\text{syst.}}_x = \frac{\Delta^{2\sigma}_x}{1\sigma^{\text{Nominal}}_{\text{syst.}}}. \tag{6.3}$$

In addition to this, we defined the secondary metric to evaluate a change in the uncertainty estimation as the relative size of the 2σ interval of the simulated data set ($2\sigma^{\text{Alternative}}_{\text{tot.}}$) to that of the nominal MC fit with the total uncertainty ($2\sigma^{\text{Nominal}}_{\text{tot.}}$) as follows,

$$R^{2\sigma}_x = \frac{2\sigma^{\text{Alternative}}_{\text{tot.}}}{2\sigma^{\text{Nominal}}_{\text{tot.}}}. \tag{6.4}$$

When we evaluate this metric for $\sin^2\theta_{23}$, we have to take care of the physical boundary at maximal mixing because the interval width can shrink due to the nature of this boundary. The $R^{2\sigma}_x$ was redefined to consider this equivalent shrinkage on the interval on either side of maximal mixing when the center of the 2σ interval moves towards the physical boundary, as

$$R'^{2\sigma}_x = \frac{2\sigma^{\text{Alternative}}_{\text{tot.}} - 2\Delta^{2\sigma}_x}{2\sigma^{\text{Nominal}}_{\text{tot.}}}. \tag{6.5}$$

As for δ_{cp}, it is difficult to treat it in the same way as the other oscillation parameters because the gaussian approximation is not applicable due to its cyclic nature. Therefore, we evaluated the bias by investigating how $\Delta\chi^2$ curve is changed by the alternative model, as

$$\Delta\chi^2_{diff}(\delta_{\rm CP}) = \Delta\chi^2_{nom}(\delta_{\rm CP}) - \Delta\chi^2_{\rm Alternative}(\delta_{\rm CP}) \tag{6.6}$$

where $\Delta\chi^2_{nom}(\delta_{\rm cp})$ and $\Delta\chi^2_{\rm Alternative}(\delta_{\rm cp})$ are the $\Delta\chi^2$ curves for the nominal model and the alternative model. Using this curve, we can make a shifted $\Delta\chi^2$ curve against the data as follows,

$$\Delta\chi^2_{shift}(\delta_{\rm CP}) = \Delta\chi^2_{data}(\delta_{\rm CP}) + \Delta\chi^2_{diff}(\delta_{\rm CP}) \tag{6.7}$$

where $\Delta\chi^2_{data}(\delta_{\rm cp})$ is the $\Delta\chi^2(\delta_{\rm cp})$ curve from the fit to the data.

To determine if those calculation results from fit to each alternative model have significant impact on our oscillation analysis, we established criteria as follows.

1. A bias of Δm^2_{32} and $\sin^2\theta_{23}$ is larger than 50% of the size of the systematic uncertainty of the nominal MC fit ($|B_x^{\rm syst.}| > 0.5$).

2. The interval width changes are larger than 10% relative to total error for Δm^2_{32} and $\sin^2\theta_{23}$ ($|R_x^{2\sigma} - 1| > 0.1$).

3. A change of $\Delta\chi^2$ for $\delta_{\rm cp}$ changes our result of the exclusion regions.

6.3.2 Results

Results of the bias for Δm^2_{32} and $\sin^2\theta_{23}$ from our robustness studies are summarized in Tab. 6.1. The biases for Δm^2_{32} of the CRPA and nonQE data driven model are quite large and over the threshold which we discussed in Sec. 6.3. Thus, we need to apply the smearing to our data fit result for Δm^2_{32}. For more conservative approach, we applied them including not only CRPA and nonQE but also all the other robustness studies.

Based on this table, total bias for Δm^2_{32} is calculated by quadratically summing of all biases as follows,

$$S = 1\sigma^{\rm Nominal}_{\rm syst.} \sqrt{\sum_{\rm Alternative} (B^{\rm syst.Alternative}_{\Delta m^2_{32}})^2}. \tag{6.8}$$

As a result of this calculation, we got $S = 2.7 \times 10^{-5}$ eV^2/c^4. This value is applied as a smearing factor to the data fit results and it will be described in Chapter 7. As for $\delta_{\rm cp}$and $\sin^2\theta_{23}$, there is no significant bias which changes our conclusion about exclusion regions as shown in Tab. 6.2.

Table 6.1: The summary of the alternative model bias and uncertainty metrics for Δm^2_{32} and $\sin^2\theta_{23}$. Note that is any study requires action, all observed biases for that parameter are included in the smearing value. Values in this table are truncated relative to the full precision used in the referenced tables, and those that are negligible are removed for ease of interpretation.

Fake Data Study	$B^{\text{syst.}}_{\Delta m^2_{32}}$	$R^{2\sigma}_{\Delta m^2_{32}}$	$B^{\text{syst.}}_{\sin^2\theta_{32}}$	$R^{2\sigma}_{\sin^2\theta_{32}}$
Z-exp -1σ	-6%	0.99	—	0.99
Z-exp Nominal	—	0.98	—	0.99
Z-exp +1σ	-26%	0.95	-1%	0.98
3Comp -1σ	-3%	0.95	1%	0.97
3Comp Nominal	-6%	0.95	1%	0.98
3Comp +1σ	-10%	0.94	7%	0.97
LFG	-46%	0.99	—	0.97
CRPA	85%	0.95	-25%	1.02
Removal Energy	-17%	—	-2%	0.99
1π Low Q^2	19%	0.98	14%	1.02
1π Kin. -3σ	7%	—	-6%	0.99
1π Kin. $+3\sigma$	-8%	—	1%	1.01
Martini 1π	-19%	0.99	-5%	—
Rad. Corr.	16%	—	-8%	0.98
Data-driven nonQE	-76%	0.99	10%	1.03
Data-driven 1π	-8%	—	-2%	—

Table 6.2: The summary of the alternative model $\delta_{\rm cp}$ interval shift studies. Values in this table are truncated relative to the full precision used in the referenced tables, and those that are negligible are removed for ease of interpretation.

	$b_{\delta_{\rm cp}}^{1\sigma,\downarrow}$	$b_{\delta_{\rm cp}}^{1\sigma,\uparrow}$	$b_{\delta_{\rm cp}}^{90\%,\downarrow}$	$b_{\delta_{\rm cp}}^{90\%,\uparrow}$	$b_{\delta_{\rm cp}}^{2\sigma,\downarrow}$	$b_{\delta_{\rm cp}}^{2\sigma,\uparrow}$	$b_{\delta_{\rm cp}}^{3\sigma,\downarrow}$	$b_{\delta_{\rm cp}}^{3\sigma,\uparrow}$
Data	-2.70	-0.98	-3.07	-0.43	-3.26	-0.17	-3.84	0.49
Robustness Study	$\Delta b_{\delta_{\rm cp}}^{1\sigma,\downarrow}$	$\Delta b_{\delta_{\rm cp}}^{1\sigma,\uparrow}$	$\Delta b_{\delta_{\rm cp}}^{90\%,\downarrow}$	$\Delta b_{\delta_{\rm cp}}^{90\%,\uparrow}$	$\Delta b_{\delta_{\rm cp}}^{2\sigma,\downarrow}$	$\Delta b_{\delta_{\rm cp}}^{2\sigma,\uparrow}$	$\Delta b_{\delta_{\rm cp}}^{3\sigma,\downarrow}$	$\Delta b_{\delta_{\rm cp}}^{3\sigma,\uparrow}$
Z-exp -1σ	0.007	-0.008	0.007	-0.010	0.008	-0.010	0.011	-0.011
Z-exp Nominal	0.005	-0.006	0.004	-0.010	0.004	-0.009	0.003	-0.009
Z-exp +1σ	-0.011	-0.004	-0.008	0.004	-0.006	0.005	-0.003	0.003
3Comp -1σ	0.003	-0.013	0.004	-0.013	0.004	-0.012	0.003	-0.009
3Comp Nominal	0.013	-0.013	0.012	-0.019	0.012	-0.020	0.011	-0.021
3Comp +1σ	0.021	-0.004	0.018	-0.016	0.017	-0.017	0.017	-0.018
LFG	0.010	0.025	0.010	0.014	0.011	0.009	0.016	-0.003
CRPA	-0.023	-0.036	-0.021	-0.024	-0.021	-0.021	-0.022	-0.013
Removal Energy	-0.005	0.003	-0.005	0.006	-0.005	0.006	-0.006	0.007
1π Low Q^2	0.037	-0.040	0.038	-0.058	0.039	-0.060	0.051	-0.069
1π Kinematics -3σ	-0.019	-0.010	-0.018	0.002	-0.017	0.005	-0.021	0.012
1π Kinematics $+3\sigma$	0.004	-0.004	0.005	-0.006	0.005	-0.007	0.007	-0.010
Martini 1π	-0.009	0.005	-0.007	0.009	-0.006	0.009	-0.005	0.007
Radiative Corrections	0.003	-0.005	0.004	-0.007	0.005	-0.008	0.009	-0.012
Data-driven nonQE	0.029	-0.015	0.030	-0.032	0.031	-0.036	0.042	-0.048
Data-driven 1π	0.008	0.006	0.007	0.0001	0.007	-0.0013	0.007	-0.004

6.4 Discussion

Robustness study was done for the updated analysis and the significant bias for Δm^2_{32} was found. Next Chapter 7 describes the results of the oscillation analysis including this bias as the systematic uncertainty.

On the other hand, there is room to improve this study toward the future analysis. For example, we don't have any good way to apply the smearing to the non-gaussian parameters such as $\delta_{\rm cp}$ and $\sin^2\theta_{23}$. There has been no significant bias for these parameters so far. However, we should investigate that way to apply the smearing for these parameters. Furthermore, we should reconsider the criteria to determine whether the bias is sufficiently large because the balance of statistical and systematic uncertainty will be changed by the increase of total statistic.

Overall these calculation ways and criteria should be discussed again in the near future when the oscillation analysis will be more sensitive to a new physics. However, it is still difficult to do that in a rigorous way and the systematics sources due to the neutrino interaction modeling should be reduced. It is due to a lack of understanding of the interaction models in the energy region of the T2K experiment and that understanding should be made deeper. To accomplish it, more precise measurement with the upgraded near detector is planned to accomplish it and

it will be described in Chapter 8.

Chapter 7

Updated Results of Neutrino Oscillation Analysis

This chapter describes the results of the updated oscillation analysis. We confirmed the robustness of our interaction model in the updated analysis with the several simulated data sets of the alternative models as described in Chapter 6. With the nominal interaction models used in our analysis, first we performed the near detector fits using the updated event selections. Then, we got the updated oscillation analysis measurement results with the far detector analysis using the new multi-ring sample. This chapter describes these results in order.

7.1 Near Detector Fit Results

As described in the Sec. 5.2, new event selections are added in the updated analysis. The number of events for each event category in this new event selection is summarized in Tab. 7.1. The number of events of the post-fit shows much better agreement with the data than the prefit as with the original analysis. The post-fit prediction and the data on a bin-by-bin basis are good good agreement as shown in Figs. 7.1 and 7.2.

Fit results for cross section and flux parameters are shown in Figs. 7.3 and 7.4. For the flux parameters, the post-fit values of ν mode move upper by $\sim 8\%$ for lower energy region while they move down for higher energy region as with the original analysis.

As for the CCQE parameters, M_A^{QE} is pulled up by 1.3σ from its nominal values which indicates that the deviations from the nominal values are smaller than the original near detector fit results (2σ). The high Q^2 parameters are also pulled up from the nominal values. The effects of these parameters, combined with the flux parameters increase the number of CCQE events. It denotes that they bring up the events in the CC0π0p and CC0πNp samples while the 2p2h parameters and the other CCQE parameters such as the Pauli blocking parameters absorb that variation of these two samples.

Post-fit values of all Pauli Blocking parameters are pulled higher than their nominal values. It indicates that Fermi momentum value is set to higher and suppresses the cross section at low Q^2 region. In addition, Optical Potential parameters also are pulled higher and it means the

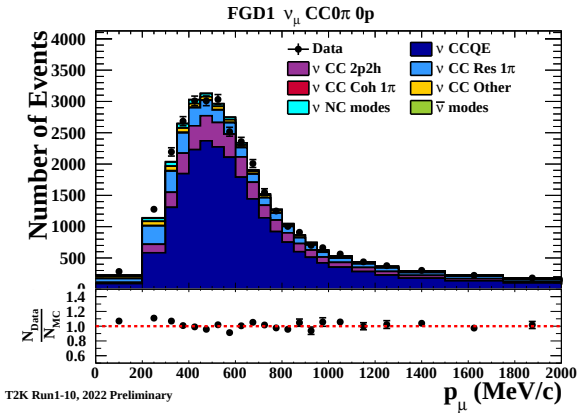

(a) ν mode CC0π0proton momentum distribution

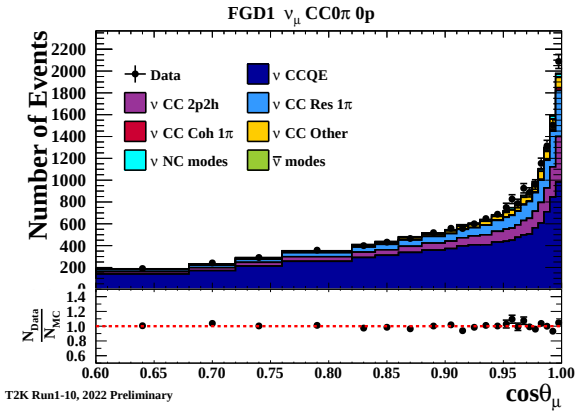

(b) ν mode CC0π0proton $\cos\theta$ distribution

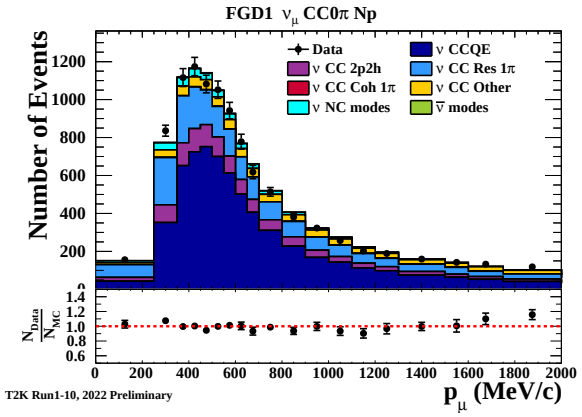

(c) ν mode CC0πNprotons momentum distribution

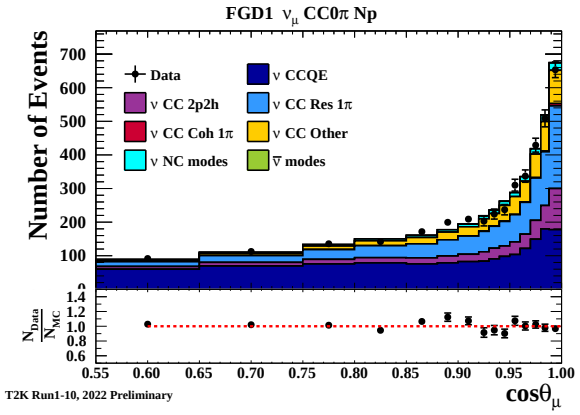

(d) ν mode CC0πNprotons $\cos\theta$ distribution

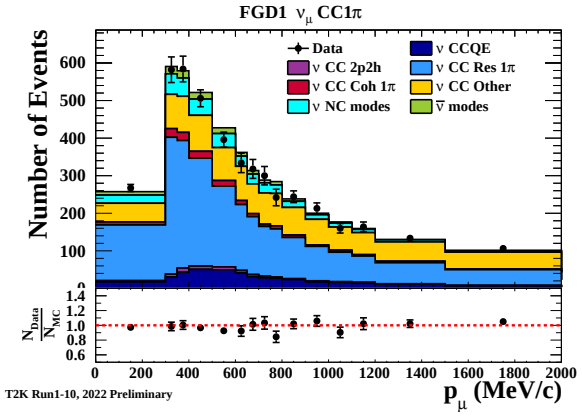

(e) ν mode CC1π momentum distribution

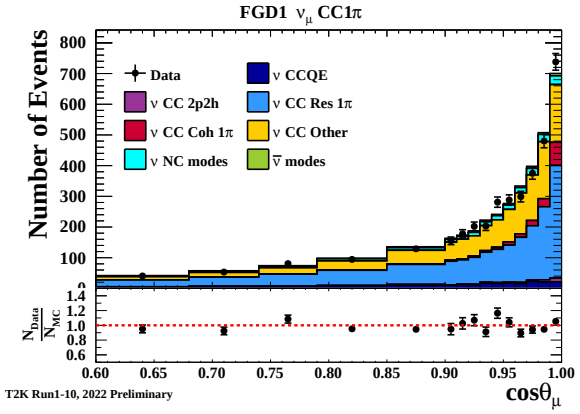

(f) ν mode CC1π $\cos\theta$ distribution

Figure 7.1: Post-fit predictions and data points of muon kinematic distribution for CC0π0proton, CC0πNprotons and CC1π sample selections of ν mode. The black points and error bars represent the data with the statistical uncertainty. The shaded regions show the contributions of the ν CCQE, ν 2p2h, ν CC resonant 1π, ν CC coherent 1π, ν CC other, ν NC modes, and $\bar{\nu}$ modes. The bottom insets show the ratio of data to simulation.

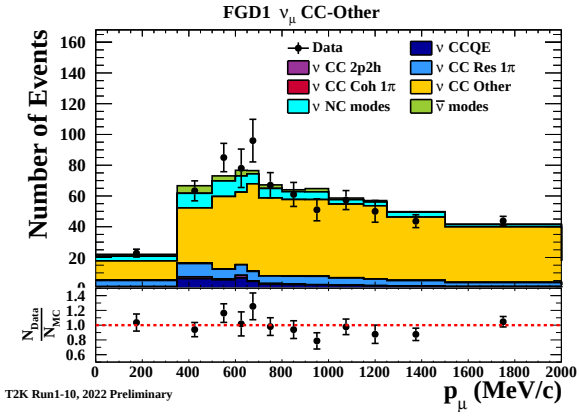

(a) ν mode CCOther momentum distribution

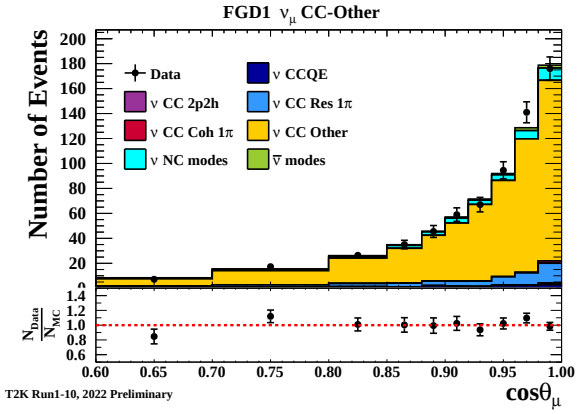

(b) ν mode CCOther $\cos\theta$ distribution

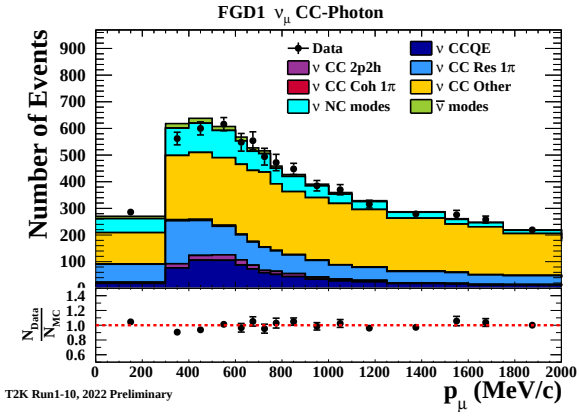

(c) ν mode CCphoton momentum distribution

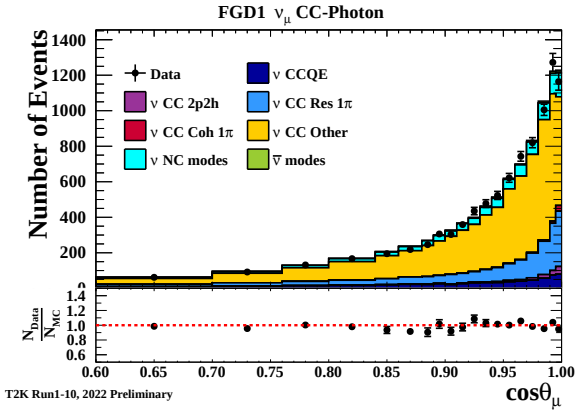

(d) ν mode CCphoton $\cos\theta$ distribution

Figure 7.2: Post fit predictions and data points of muon kinematic distribution for CCphoton and CCOther sample selections of ν mode. The black points and error bars represent the data with the statistical uncertainty. The shaded regions show the contributions of the ν CCQE, ν 2p2h, ν CC resonant 1π, ν CC coherent 1π, ν CC other, ν NC modes, and $\bar{\nu}$ modes. The bottom insets show the ratio of data to simulation.

Table 7.1: Summary of the number of events at each event selection for data and the MC prediction before (Pre-fit) and after (Post-fit) the near detector fit to the data in the updated analysis.

Beam	Event Topology	Target	Data	Pre-fit	Post-fit
ν mode ν_μ CC	0π0proton	FGD1	21329	18742.2	21123.5
		FGD2	22935	20144.9	22776.7
	0πNprotons	FGD1	9257	9280.5	9262.7
		FGD2	7373	7653.5	7497.7
	1π	FGD1	6224	6542.9	6310.2
		FGD2	5099	5345.9	5085.7
	Other	FGD1	1737	1640.9	1727.2
		FGD2	1620	1571.3	1592.7
	Photon	FGD1	11156	10751.9	11305.7
		FGD2	10406	9765.6	10235.8
$\bar{\nu}$ mode $\bar{\nu}_\mu$ CC	0π	FGD1	8676	8493.9	8671.1
		FGD2	8608	8493.9	8671.1
	1π	FGD1	719	712.4	718.5
		FGD2	660	668.0	681.7
	Other	FGD1	1533	1408.3	1479.7
		FGD2	1396	1263.3	1331.0
$\bar{\nu}$ mode ν_μ CC	0π	FGD1	3714	3568.4	3791.4
		FGD2	3537	3511.5	3715.6
	1π	FGD1	1147	1235.9	1227.4
		FGD2	955	987.6	968.6
	Other	FGD1	1425	1189.3	1293.0
		FGD2	1334	1124.8	1200.0

increased FSI for leptons. Those new parameter behaviors denote the low Q^2 suppression effect on CCQE interaction which is consistent with the behavior of the ad-hoc low Q^2 parameters in the original analysis. All 2p2h shape parameters are pulled toward non-PDD like, which is the opposite of the effects seen in the original analysis. This can be attributed to the new sample separation with the proton multiplicity and the proton kinematic information might favors the non-PDD like. The PNNN shape parameter gently favors the nn pairs while the post-fit value is within the nominal uncertainty.

For the single pion production parameters, C_5^A is pulled 2σ away from the nominal value while M_A^{RES} remains close to the nominal value, unlike the original analysis. C_5^A and M_A^{RES} are anti-correlated and they compensate for each other's variation. The new RS delta decay parameter remains at the nominal value and it favors delta-like decay. The new resonant binding energy parameters have been pulled toward 0. It denotes that the overall resonant decay cross section is reduced, and the outgoing lepton and hadron kinematics are changed. Almost all pions FSI parameters are not pulled except for the FSI absorption parameter which is pulled by 1σ. On the other hand, new nucleon FSI parameter is pulled by 2σ and it denotes the increase in the

amount of the nucleon FSI.

The cross section and flux correlation matrix after the near detector fit is shown in Fig. 7.5. There are strong anti-correlations between flux and cross section and it reduces the total systematic uncertainties as with the original analysis.

The size of the systematic uncertainties for each component before and after the near detector fit is summarized in Tabs. 7.2 and 7.3. Compared to the original analysis, there is a little large error for cross section parameters such as ν mode 1Rμ sample while the other sources are almost unchanged. This is partly because conservative error estimation for new parametrization for RES binding energy. Furthermore, Pauli Blocking and Optical Potential parameters for each target are implemented while the original low Q^2 parameters affect each target in the similar way. The slight increase in error due to the new parametrization implies the near detector fit constraints on the far detector prediction can be weaker in the updated analysis.

Figure 7.6 shows the reconstructed energy distribution for each sample at the far detector with the 1σ uncertainty band with and without the constraint by the near detector fit. The constraint with the updated near detector fit effectively reduces the uncertainties from $\sim 15\%$ to $\sim 5\%$ as with the original analysis except for ν mode CC1π sample. The uncertainty is reduced from $\sim 20\%$ to $\sim 14\%$ for the ν mode CC1π sample.

Table 7.2: Summary of the systematic uncertainties before the near detector fit in the updated oscillation analysis.

Error source (%)	1Rμ		MR	1Re			
	ν mode	$\bar{\nu}$ mode	ν mode CC1π^+	ν mode	$\bar{\nu}$ mode	ν mode CC1π^+	$\frac{\nu \text{ mode}}{\bar{\nu} \text{ mode}}$
Flux	5.0	4.6	5.2	4.9	4.6	5.1	4.5
Cross-section (all)	15.8	13.6	10.6	16.3	13.1	14.7	10.5
SK+SI+PN	2.6	2.2	4.0	3.1	3.9	13.6	1.3
Total	16.7	14.6	12.5	17.3	14.4	20.9	11.6

Table 7.3: Summary of the systematic uncertainties after the near detector fit in the updated oscillation analysis.

Error source (%)	1Rμ		MR	1Re			
	ν mode	$\bar{\nu}$ mode	ν mode CC1π^+	ν mode	$\bar{\nu}$ mode	ν mode CC1π^+	$\frac{\nu \text{ mode}}{\bar{\nu} \text{ mode}}$
Flux	2.8	2.9	2.8	2.8	3.0	2.8	2.2
Cross-section (ND const.)	3.7	3.5	3.0	3.8	3.5	4.1	2.4
Flux + Cross-section (ND const.)	2.7	2.6	2.2	2.8	2.7	3.4	2.3
Cross-section (ND unconst.)	0.7	2.4	1.4	2.9	3.3	2.8	3.7
SK+SI+PN	2.0	1.7	4.1	3.1	3.8	13.6	1.2
Total	3.4	3.9	4.9	5.2	5.8	14.3	4.5

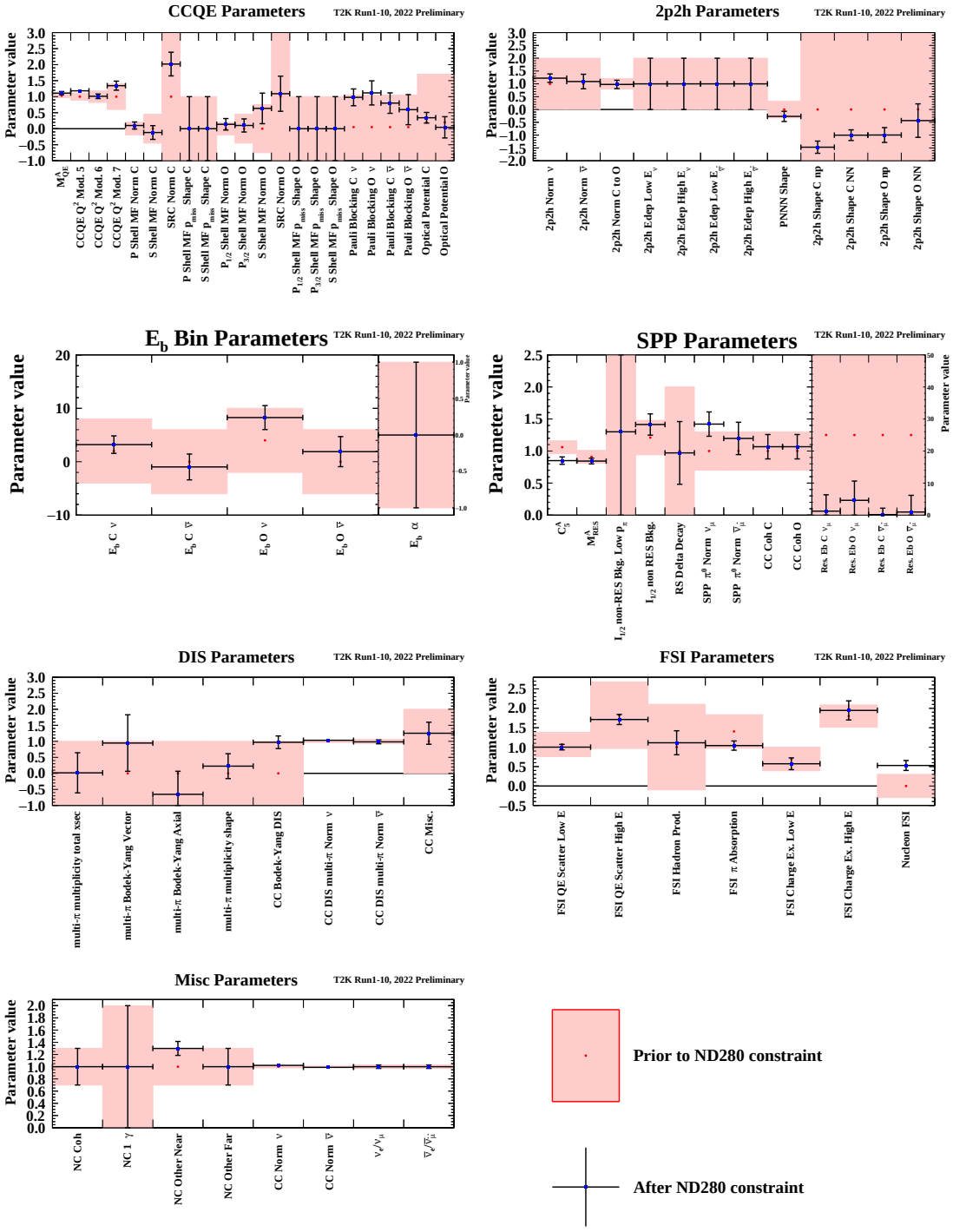

Figure 7.3: Pre-(red band) and post-fit (blue dots and black error bands), cross-section parameters CCQE, 2p2h, E_b, Single Pion Production (SPP), FSI, DIS, and misc from the near detector fit to the data.

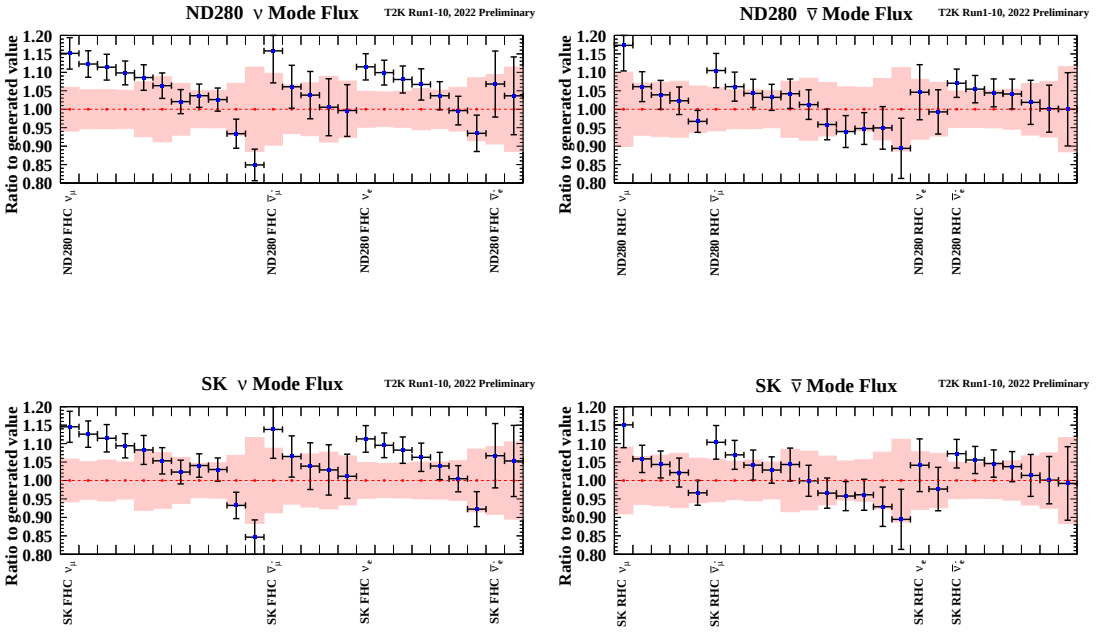

Figure 7.4: Pre- (red band) and post-fit (blue dots and black error bands), flux parameters for the ν mode (left) and the $\bar{\nu}$ mode (right), and for the ND280 (top) and SK (bottom) from the near detector fit to the data.

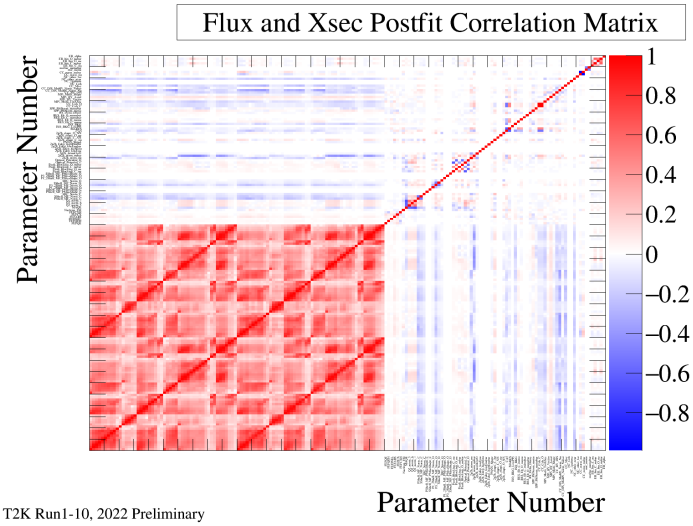

Figure 7.5: Pre-(red band) and post-fit (blue dots and black error bands), flux parameters from the near detector fit to the data.

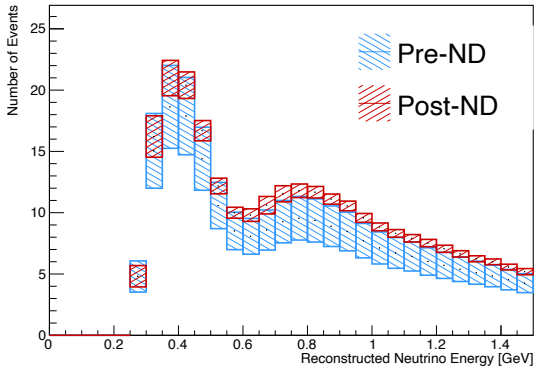

(a) ν mode 1Rμ

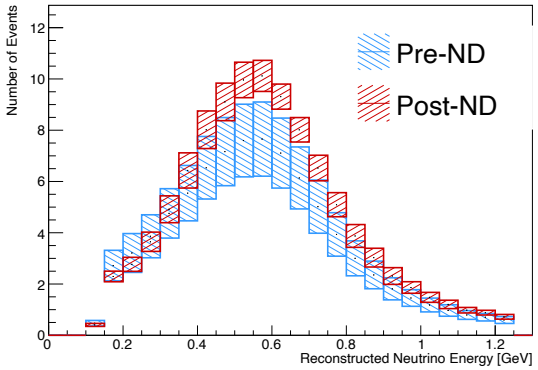

(b) ν mode 1Re

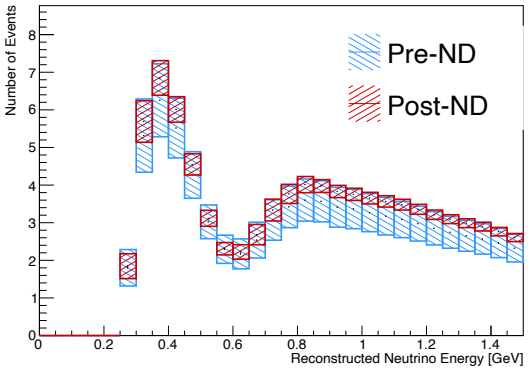

(c) $\bar{\nu}$ mode 1Rμ

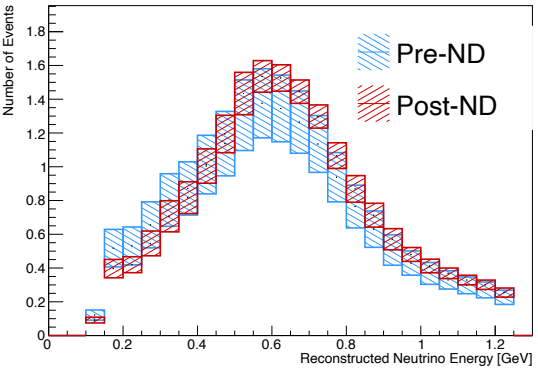

(d) $\bar{\nu}$ mode 1Re

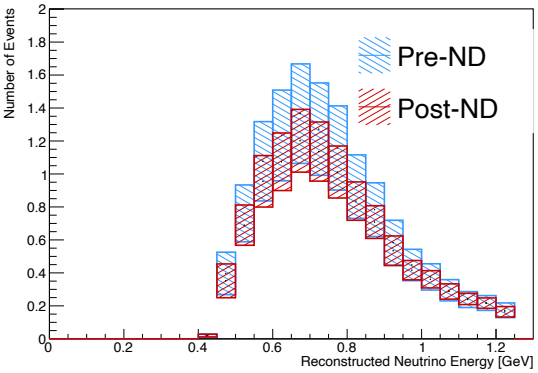

(e) ν mode 1Re1de

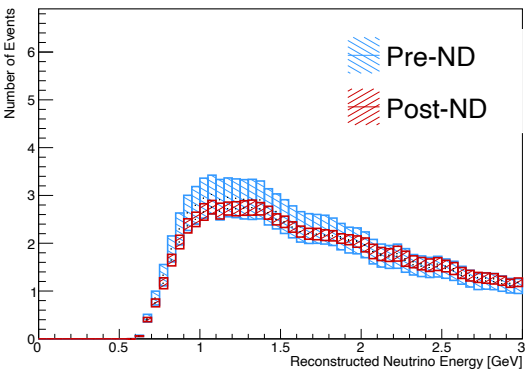

(f) ν mode CC1π multi-ring

Figure 7.6: Comparison of the pre-fit and post-fit prediction with the total uncertainty for ν mode 1Rν, ν mode 1Re, $\bar{\nu}$ mode 1Rμ, $\bar{\nu}$ mode 1Re, ν mode 1Re1de and ν mode CC1π multi-ring samples as a function of reconstructed neutrino energy

7.2 Results of Updated Oscillation Analysis

In order to obtain the oscillation analysis results, the smearing for Δm^2_{32} was done with the value (2.7×10^{-5} eV) based on the robustness study described in Chap. 6. Table 7.4 summarizes the global best fit results of the oscillation parameters in the updated analysis. The data and the expected number of events by the global best fit for each selection at the far detector are shown in the black points and the colored background in Fig. 7.7. Figure 7.8 shows the two-dimensional contours for $\sin^2\theta_{23}$ vs Δm^2_{32} and δ_{CP} vs $\sin^2\theta_{13}$. The contours are compatible for both mass orderings and prefer the upper octant as with the original analysis. Figure 7.9 shows the $\Delta\chi^2$ distribution for δ_{CP}, and the results of the confidence intervals for δ_{CP} and $\sin^2\theta_{23}$ with the Feldman Cousins method are shown in Table 7.5. As for $\sin^2\theta_{23}$, maximal-mixing for the normal mass ordering is excluded at 1σ confidence interval. Furthermore, both octants are within 1σ confidence region unlike the original analysis. The constraint on δ_{CP} changes very little from the original analysis although the 90% confidence interval shifts slightly. The CP conserving value ($\delta_{CP} = \pi$) is closer to the region compared to the original analysis.

Table 7.4: Summary of the updated results of the fit to data with and without the reactor constraint using the confidence intervals estimated with the marginal likelihood.

Parameter	With reactor constraint		Without reactor constraint	
	Normal Ordering	Inverted Ordering	Normal Ordering	Inverted Ordering
δ_{CP}(rad.)	$-2.18^{+1.22}_{-0.47}$	$-1.37^{+0.52}_{-0.68}$	$-2.25^{+1.23}_{-0.74}$	$-1.25^{+0.66}_{-0.90}$
$\sin^2\theta_{13}/10^{-3}$	-	-	$26.6^{+2.5}_{-6.2}$	$29.3^{+2.7}_{-6.5}$
$\sin^2\theta_{23}$	$0.559^{+0.018}_{-0.078}$	$0.560^{+0.019}_{-0.041}$	$0.466^{+0.107}_{-0.016}$	$0.465^{+0.100}_{-0.016}$
$\Delta m^2_{32}/10^{-3}(\mathrm{eV}^2/\mathrm{c}^4)$	$2.506^{+0.047}_{-0.052}$	-	$2.495^{+0.040}_{-0.056}$	-
$\lvert\Delta m^2_{31}\rvert/10^{-3}(\mathrm{eV}^2/\mathrm{c}^4)$	-	$2.473^{+0.071}_{-0.020}$	-	$2.463^{+0.042}_{-0.054}$

Table 7.5: Confidence intervals of δ_{CP} and $\sin^2\theta_{23}$ for each confidence level with the reactor constraint, using the Feldman Cousins correction. The 3σ confidence interval was not computed for $\sin^2\theta_{23}$.

Confidence level	δ_{CP} (rad.)		$\sin^2\theta_{23}$	
	Normal Ordering	Inverted Ordering	Normal Ordering	Inverted Ordering
1σ	[-2.76, -1.03]	-	[0.460, 0.491]∪[0.526, 0.578]	-
90%	[-3.08, -0.52]	[-1.92, -0.89]	[0.444, 0.589]	[0.525, 0.582]
2σ	[-π, -0.29]∪[3.04, π]	[-2.22, -0.69]	[0.437, 0.594]	[0.459, 0.588]
3σ	[$-\pi$, 0.31]∪[2.59, π]	[-2.80, 0.14]	N/A	N/A

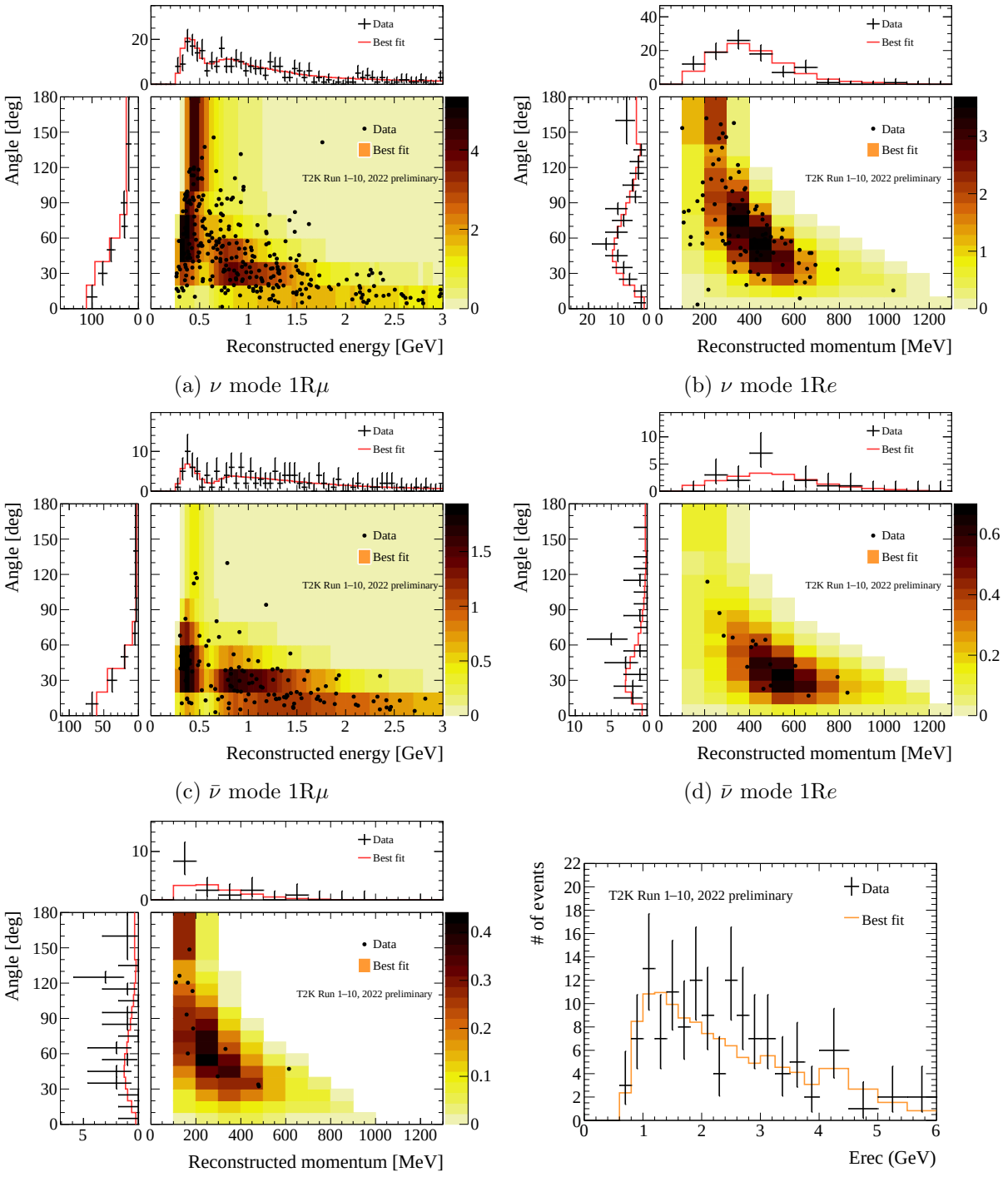

(a) ν mode 1Rμ (b) ν mode 1Re

(c) $\bar{\nu}$ mode 1Rμ (d) $\bar{\nu}$ mode 1Re

(e) ν mode 1Re1de (f) ν mode CC1π multi-ring

Figure 7.7: The events for the updated six far detector samples. The expected event rates using the best fit with the reactor constraint is shown in the colored background for the five samples as with the original analysis. The insets show the events projected onto each single dimension, and the red line is the expected number of events from the best-fit. The error bars represent the 1σ statistical uncertainty on the data. As for the bin width for the ν mode CC1π multi-ring sample, it was made coarser for the number of events to be meaningful in this comparison, but only for this plot. In the actual fit, the same binning as the other μ-like samples was used.

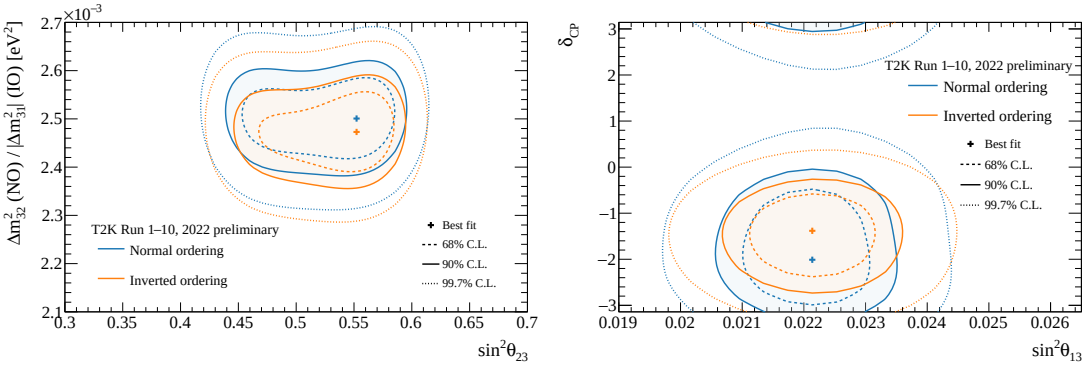

Figure 7.8: Two-dimensional confidence level contours of Δm^2_{32} vs $\sin^2\theta_{23}$ (left) and δ_{CP} vs $\sin^2\theta_{13}$ (right) for the normal and inverted mass orderings.

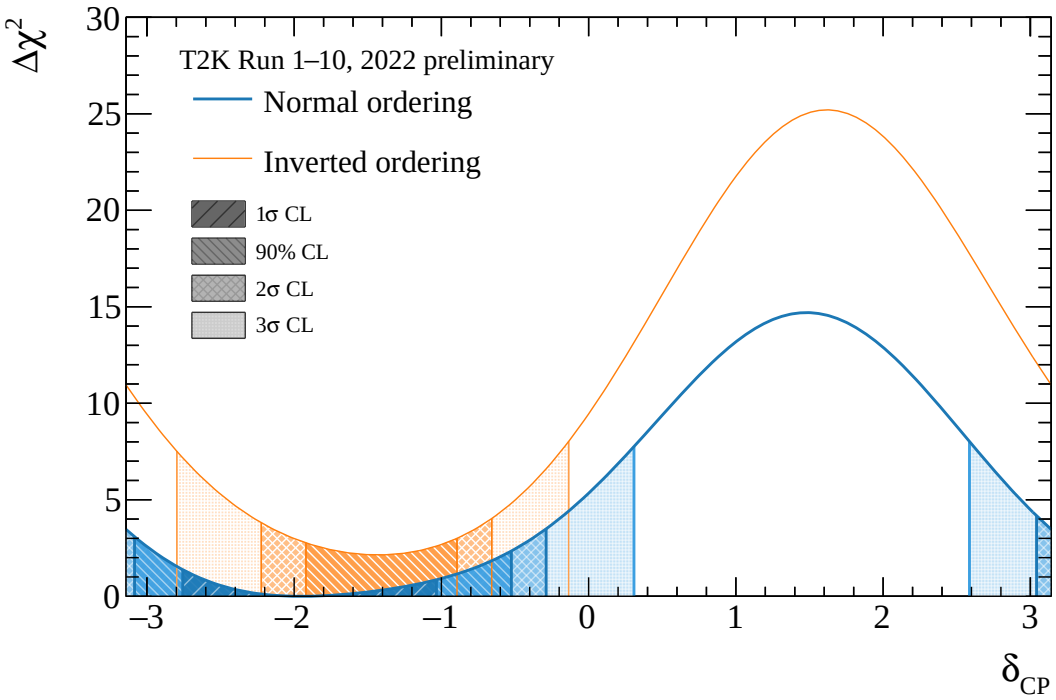

Figure 7.9: One-dimensional $\Delta\chi^2$ distribution as a function of δ_{CP} for the data fit. Shaded regions show the confidence intervals at each confidence level.

7.3 Discussion

Measurement of Atmospheric Neutrino Parameters ($\Delta m^2_{32}, \sin\theta_{23}$)

We obtained $\Delta m^2_{32} = 2.494^{+0.040}_{-0.057} \times 10^{-5}$ eV (NO), $\sin^2\theta_{23} = 0.561^{+0.040}_{-0.056}$ (NO) as the best fit values with the reactor constraint for the atmospheric neutrino parameters in the updated analysis. To compare the measurement results with those of the original oscillation analysis before the several updates, we checked the confidence regions for the various setups as follows,

- A : Original results in the T2K experiment described in Chapter 4.
- B (A + 2022 ν interaction model with the new near detector samples) : Only the neutrino interaction model parametrization and the near detector selections are updated compared to setup A.
- C (B + PDG 2021) : The reactor constraint is updated from PDG2019 [102] to PDG2021 [113] compared to setup B.
- D (C + Multi Ring ν_μ CC1π sample at the far detector) : The new multi-ring ν_μ CC1 sample was added to the far detector sample compared to setup C.

Figure 7.10 shows the comparison of two-dimensional contours for Δm^2_{32} and $\sin\theta_{23}$ between those analysis setups. Updates of the near detector fit selection and the interaction parametrization cause the largest change on the contour as shown in the difference between setups A and B. On the other hand, adding new Multi-ring selection at the far detector causes small visible effect on these parameters.

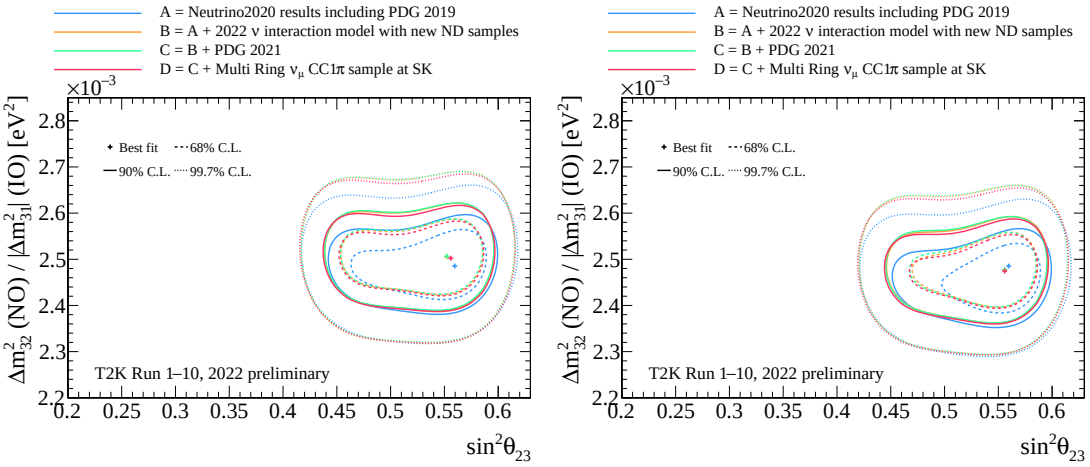

Figure 7.10: Comparisons of two-dimensional confidence level contours of Δm^2_{32} vs $\sin^2\theta_{23}$ for normal (left) and inverted (right) mass ordering between setup A, B, C and D.

Figure 7.11 shows the comparison of the 90% confidence two-dimensional contours for Δm^2_{32} and θ_{23} with other experiments. The results of all those experiments are consistent with maximum mixing of θ_{23}. The θ_{23} octant indicated by the best fit value is different for each experiment

while all these experiments do not have sufficient precision to determine the octant. Overall, they are comparable and T2K has the strongest limitation on that.

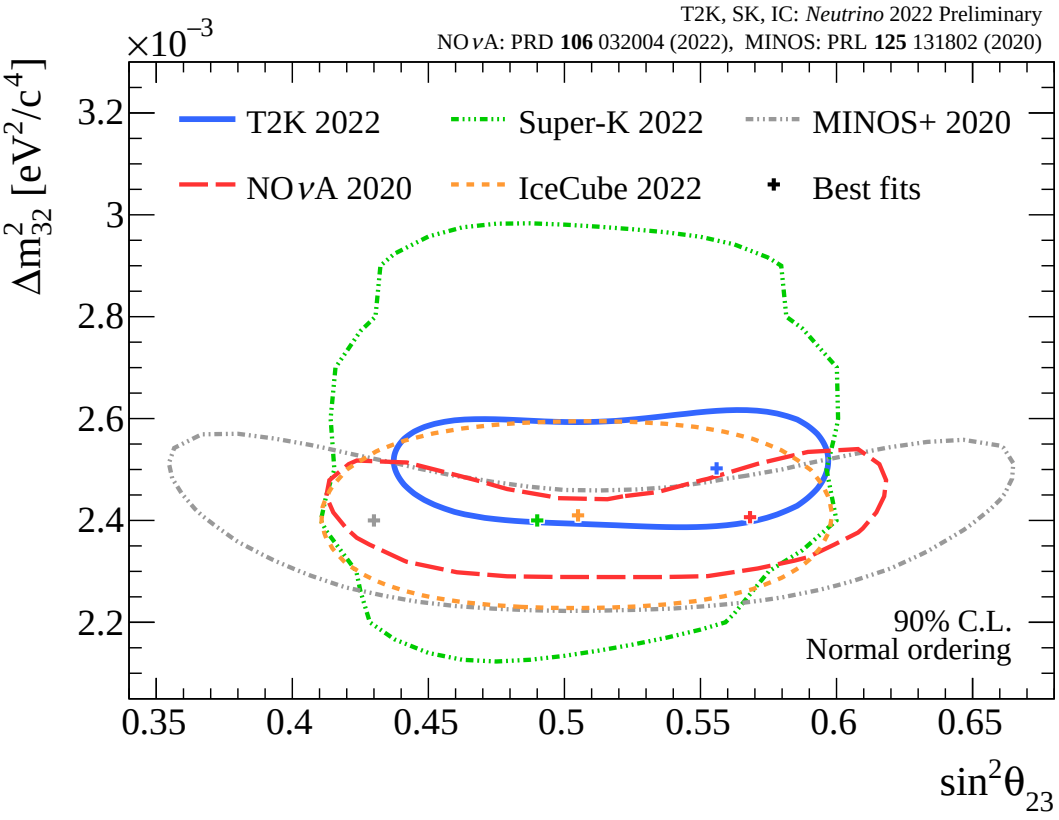

Figure 7.11: Comparison of two-dimensional confidence level contours of Δm^2_{32} vs $\sin^2\theta_{23}$ between T2K, NOνA [26], SuperK [114], IceCube [115] and MINOS+ [116].

Mass ordering and $\sin^2\theta_{23}$ octant

In order to evaluate hypotheses of the mass ordering and $\sin^2\theta_{23}$ octant, we calculate the posterior probabilities using marginal likelihood as shown in Eq. 4.18. Tables 7.6 and 7.7 summarize the posterior probabilities for the various combinations of the mass ordering and $\sin^2\theta_{23}$ octant. Here the Bayes factor with the reactor constraint for the upper over the lower $\sin^2\theta_{23}$ octant is 2.45 which is lower than the original analysis of 3.76. On the other hand, the factor for the preference to the normal ordering of the mass ordering is of 3.71 which is weaker than the original analysis of 4.88. The T2K data still favors the normal mass ordering and the higher octant, however it is not sufficient to determine them.

Measurement of δ_{CP}

We got $\delta_{CP} = -2.18^{+1.22}_{-0.47}$ assuming normal neutrino mass ordering and using the reactor constraint. On the other hand, the NOνA experiment obtained $\delta_{CP} = 0.82^{+0.27}_{-0.87}$ (NO) [26] but it

Table 7.6: Posterior probabilities of each hypothesis about mass orderings and $\sin^2\theta_{23}$ octant with the reactor constraint in the updated (original) analysis.

	$\sin^2\theta_{23} < 0.5$	$\sin^2\theta_{23} > 0.5$	Total
Normal ordering	0.236 (0.195)	0.540 (0.613)	0.776 (0.808)
Inverted ordering	0.049 (0.035)	0.174 (0.157)	0.224 (0.192)
Total	0.285 (0.230)	0.715 (0.770)	1.000

Table 7.7: Posterior probabilities of each hypothesis about mass orderings and $\sin^2\theta_{23}$ octant without the reactor constraint in the updated (original) analysis.

	$\sin^2\theta_{23} < 0.5$	$\sin^2\theta_{23} > 0.5$	Total
Normal ordering	0.301 (0.260)	0.349 (0.387)	0.651 (0.647)
Inverted ordering	0.170 (0.152)	0.179 (0.201)	0.349 (0.353)
Total	0.471 (0.412)	0.529 (0.588)	1.000

lies in a region that T2K disfavors.

The results of the updated analysis for one-dimensional $\Delta\chi^2$ and two-dimensional contour of δ_{CP} vs $\sin\theta_{13}$ are compared with the original analysis in Figs. 7.12 and 7.13. Updates of the interaction parametrization and selection for the near detector fit have the largest impact on those as with the atmospheric parameters.

Future improvements

We obtained world-leading results for the neutrino oscillation parameter measurements as described in this Chapter. Furthermore, the T2K experiment is aiming to get the evidence of the CP violation in the neutrino oscillation and reduction of the statistical and systematic uncertainties are required to achieve it. To reduce the statistical uncertainties, we are planning the accelerator upgrade which will increase the beam power from 500 kW to 1.3 MW, and the horn current upgrade from 250 kA to 320 kA. Furthermore, ND280 upgrade is ongoing to reduce the systematic uncertainties of the neutrino interaction models by detecting the low momentum hadron and charged particles scattered in a large angle from the neutrino interaction. The detail of these upgrades will be discussed in the next chapter.

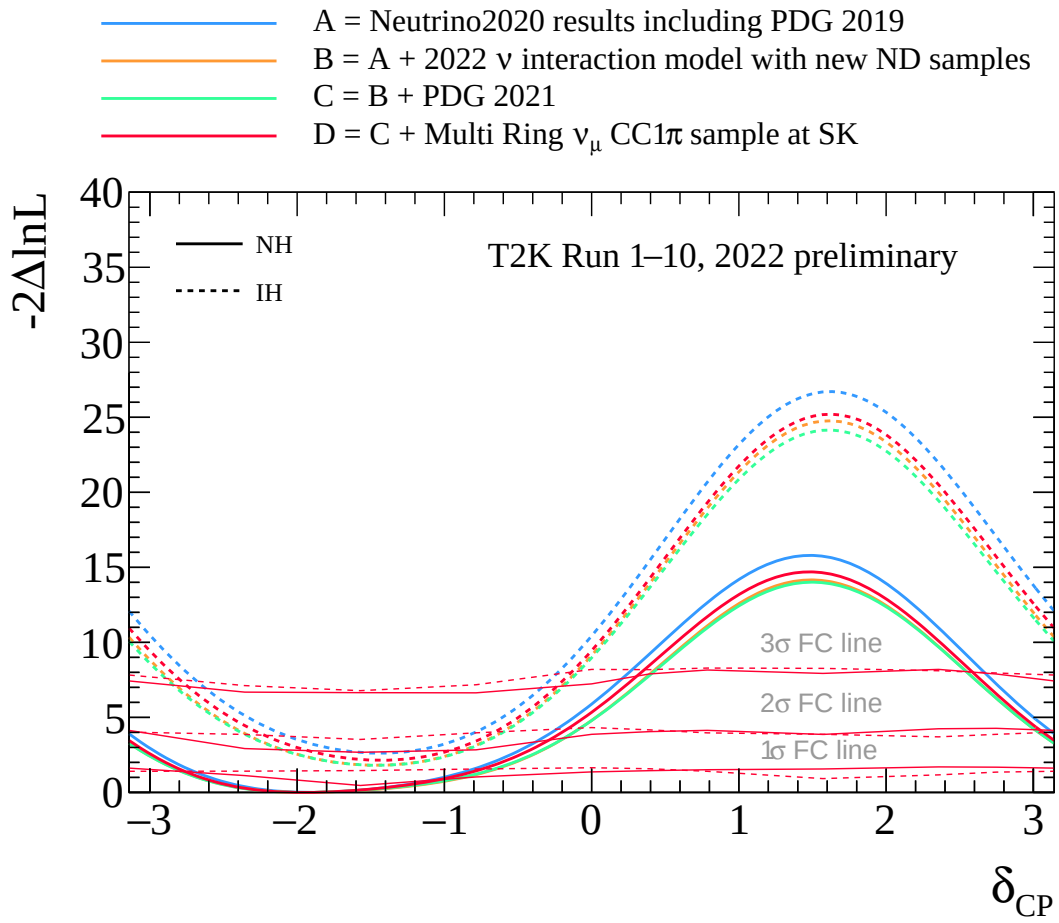

Figure 7.12: Comparisons of one-dimensional $\Delta\chi^2$ distribution as a function of δ_{CP} between setup A, B, C and D.

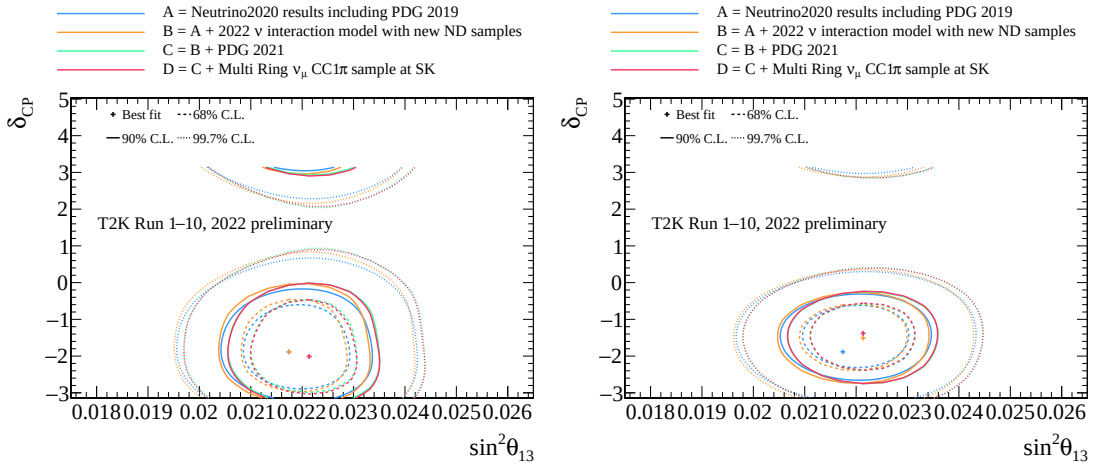

Figure 7.13: Comparisons of two-dimensional confidence level contours of δ_{CP} vs $\sin^2\theta_{13}$ for normal (left) and inverted (right) mass orderings between setup A, B, C and D.

Chapter 8

Prospects

This chapter describes the prospects mainly for the measurement of the oscillation parameters in the T2K experiment to get the evidence of the CP violation.

8.1 Goal of the T2K experiment

This section introduces the future prospect of the T2K experiment referring to this paper [117]. The goal of the T2K experiment is to measure the CP violation in the neutrino oscillations at 3σ confidence level. In order to achieve it, the statistical and systematic uncertainties should be reduced. The former one is dominant in the current measurement. A J-PARC main ring (MR) upgrade is ongoing to increase the statistics by increasing beam power from 500 kW to 1.3 MW. This upgrade is achieved through step-by-step process where MR power supply updates was done and MR RF improvement is planned. The power supply upgrade has been already done and the RF upgrade will be done by 2024. Furthermore, the electromagnetic horn current will be increased from the present 250 kA to 320 kA. This improvement will result in 10% greater neutrino flux while the wrong sign components are reduced. Figure 8.1 shows the projected plots for both beam power and POT in the near future. The statistics will be 1.0×10^{22} POT by 2027 which is the end of the next term of the T2K experiment with this beam upgrade. In addition to this statistical improvement, ND280 upgrade is also ongoing in order to reduce the systematic errors.

8.2 ND280 Upgrade

This section introduces the overview of the ND280 upgrade following this paper [118]. In our oscillation analysis, the ND280 data is used to reduce the systematic uncertainties, especially for neutrino interaction modeling. However, ND280 has potential disadvantages due to its structure. First one is low efficiency for the charged particles scattered at large angles. Current FGDs consist of bar-shaped plastic scintillators which are stacked perpendicularly to the direction of the neutrino beam as described in the Sec. 2.2.2. Therefore, charged particles scattered in directions perpendicular to the beam axis, i.e., at large angles, are difficult to track. Furthermore,

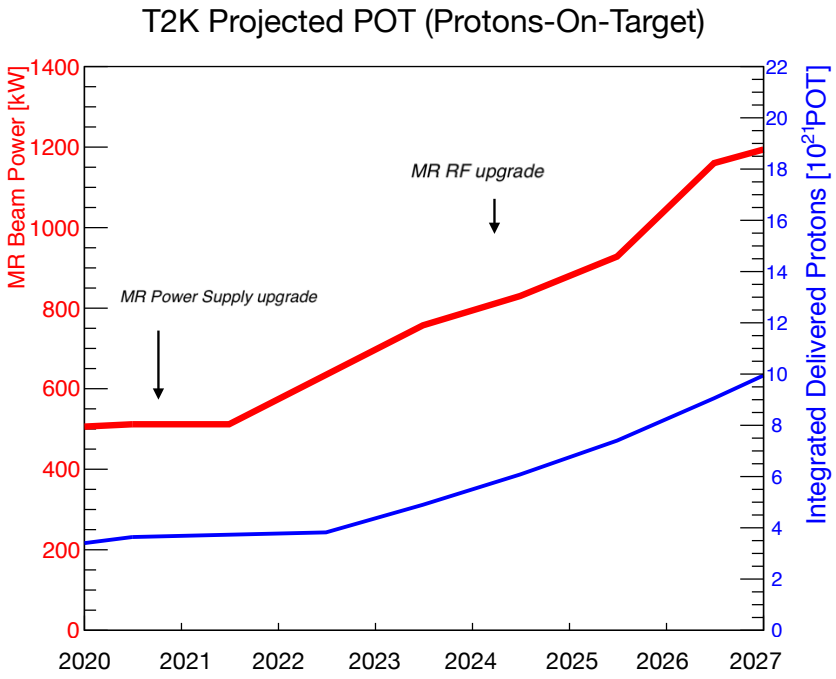

Figure 8.1: Annual plots of MR beam power (red line) and integrated delivered proton on target (blue line) in the T2K experiment. This figure has been updated from this paper [117].

the Super-Kamiokande, which serves as the far detector, has 4π acceptance for the charged particles from the neutrino interaction. The difference between measurable phase space cannot eliminate a part of the systematic errors between the near and far detectors. A second weakness is the difficulty of the detection for the low momentum hadron. Current FGDs require that the track length is longer than ~ 6 cm for the reconstruction and this length corresponds to a proton track with a momentum of 600 MeV/c. On the other hand, many protons from the neutrino interaction are below that momentum. It is difficult to understand the nuclear effects which is deeply related to such low momentum hadrons from the neutrino interaction. For example, in the 2p2h interaction, there are two low-momentum hadrons in the final states and it is nearly impossible to detect these hadrons in the current ND280.

To resolve these potential issues, the ND280 upgrade is ongoing now. Figure 8.2 shows the overview of the ND280 upgrade which consists of three types of new detector components. The gray object shows the Super FGD which is the new active scintillator target detector and two light brown objects are the High Angle TPCs (HA-TPC) to track the charged particles scattered at large angles. Time of flight (TOF) counters which have a time resolution better than 500 ps surround those detectors to measure the direction of the tracks and reject the out of fiducial volume events. This complex detector allows us to overcome the weakness of the current ND280 and how it can be achieved will be explained in the next subsection.

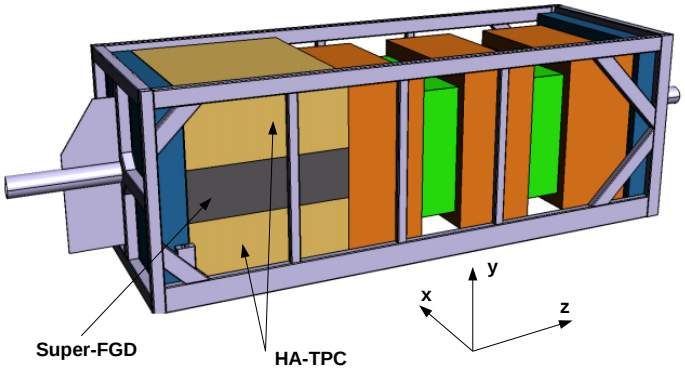

Figure 8.2: Overview of the ND280 upgrade. It consists of the new active scintillator target (Super-FGD), time projection chamber for high angle (HA-TPC) and time of flight counters (TOF) which surrounds the other two detectors. Taken from [118].

8.2.1 Super FGD

Super FGD is a new active scintillator target detector which consists of two million 1 cm^3 scintillator cubes and Fig. 8.3 shows the overview of this new detector. In the scintillator cube, there are holes in three orthogonal directions. Through these holes, three WLS fibers are inserted. The scintillation light from these scintillator cubes is yielded by the energy deposits of the charged particles and then wavelength shifting fibers read it out along three orthogonal directions. The light from the fiber edges is detected by sixty thousand MPPCs. The outer dimension of the scintillators of the Super FGD is 192 cm $\times$ 182 cm $\times$ 56 cm and the target mass is 2 t.

There are mainly two advantages related to the potential issues for the current ND280. First one is that the new detector structure can reduce the momentum threshold for hadrons. As for the protons, the threshold is reduced from $\sim$ 600 MeV/c to $\sim$ 300 MeV/c. This is because short track protons ($\sim$ 3 cm) can be reconstructed in the Super FGD with only three hits of cubes, while the FGD requires six or more hits since it demands three hits in both the vertical and horizontal scintillator bars. Second, the charged particles scattered at large angles can be detected as with the far detector which has a 4π acceptance. In addition, the Super FGD allows us to obtain more information of the neutrino nucleus interaction such as ν_e cross section and neutron kinematics from the neutrino interactions. The ν_e cross section can be measured precisely by the good separation between electrons from ν_e interaction and γ from the background sources for the measurements of the Super FGD.

Neutrons from the neutrino interactions also can be measured by using the Super FGD. Due to its sufficient volume and granularity, neutrons from the interactions can scatter off protons, and these protons can be measured. We can measure the energy of the neutrons by measuring the time difference between the hits near the vertex of the neutrino interactions and those for the recoiled protons. That allows for a deeper understanding of interactions which have neutrons, such as anti-neutrino interactions and 2p2h interactions. While the implementation of the neutron kinematics information into the near detector fit can be very useful, the implementation is difficult as described later in Sec. 8.3. As a whole, these advantages give us more information about neutrino nucleus interaction compared to the current FGD.

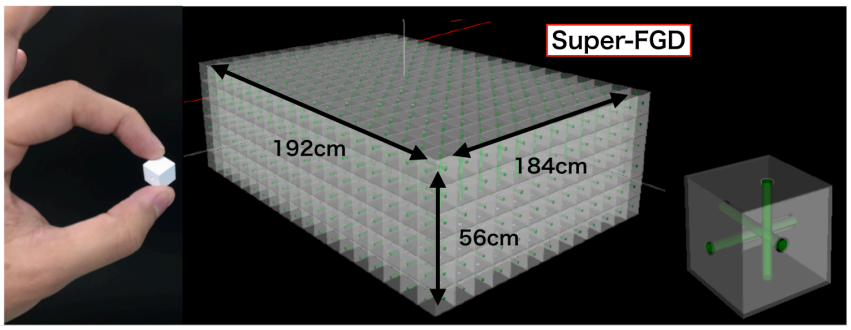

Figure 8.3: Overview of Super FGD. This new detector consists of two million scintillator cubes read out along three orthogonal directions by wavelength shifting fibers. Taken from [118].

8.2.2 High Angle TPC and TOF Counters

Super FGD has the new interesting structure which is capable of detecting charged particles scattered at large angles. In order to take advantage of this new active scintillator target, new TPCs which cover the high angle are required for the measurements of sign, momentum, and identification of such charged particles. The design of these new TPCs is based on the current TPCs with two major improvements which are updated technique for the Micromegas detector, and new field cage structure to minimize the dead space. The combination of these new TPCs and the Super FGD will allow us to detect the charged particles scattered at large angles with high detection efficiency as shown in Fig. 8.4.

In addition, the TOF counters are also newly installed for the ND280 upgrade. This new detector consists of the scintillator bars read out on both ends by arrays of MPPCs and surrounds the entire Super FGD and HA-TPCs. A timing measurement with the TOF counters and Super FGD allows the determination of the direction for the charged particles in order to separate neutrino interactions in the target from the backgrounds. The time resolution of the TOF counters themselves is 100-200 ps to achieve the requirement.

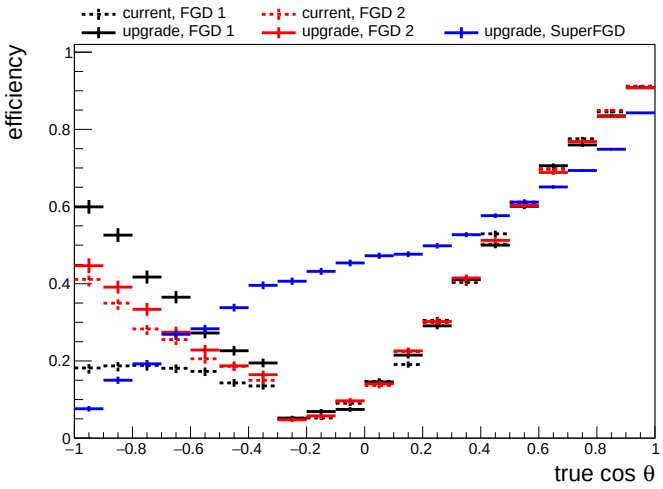

Figure 8.4: Comparison of the selection efficiency of ν_μ CC events for ND280 upgrade configuration (solid lines) and current-like configuration (dotted lines) as a function of the muon polar angle, with muons detected in TPC. Taken from [118].

8.3 Improvement of Near Detector Fit

The ND280 upgrade is capable of giving us new kinematic information from the neutrino interaction. This character allows us to understand new aspects of neutrino interaction. Furthermore, new constraints on the systematic parameters are expected if the new information is added directly in the fitting framework of our oscillation analysis. Therefore, adding such new kinematic information to the fit would be very meaningful.

Especially, proton kinematics information gives us more useful information about the nuclear effects. Momentum and angle values of the proton could be used directly as with the muon kinematics in the current analysis. However, other variables would be better to see more detailed nuclear effects. Transverse kinematic imbalance is one of the most useful variables to reflect the nucleon effects of the neutrino interactions on the analysis [119]. This kinematic variable is defined in the plane perpendicular to the beam direction as shown in Fig. 8.6 and separated into three variables (δp_T, $\delta\alpha_T$, $\delta\phi_T$). These variables are calculated with outgoing lepton momentum ($\vec{p_{l'}}$) and proton momentum ($\vec{p}_{N'}$) from the neutrino interaction.

First, we tried adding δp_T in the near detector fit i.e. three dimensional fit ($p_\mu \times \theta_\mu \times \delta p_T$) instead of our current two dimensional fit ($p_\mu \times \theta_\mu$) for muon kinematic variables. On the other hand, other transverse kinematic variables had also a unique impact on our analysis. These unique effects are summarized in this paper [120]. As a first attempt, we just implemented this new variable (δp_T) without the removal energy and detector systematics parameters for simplicity. Then, we tried adding the likelihood scan for the flux and cross section parameters near each nominal value. As a result, the constraint on the nucleon FSI parameter became stronger as shown in Fig. 8.6. Since this parameter is deeply related to the outgoing proton kinematics, this change was consistent with the expectation. So far, the impact of the addition of

the transverse kinematics on the most of parameters was very small due to the difficulties of the detection of the low momentum proton. After the measurement with the upgraded ND280 starts, this analysis improvement will allow us to use the lower momentum proton information directly in our near detector fit and the impact of this implementation on the systematic parameters will become even greater.

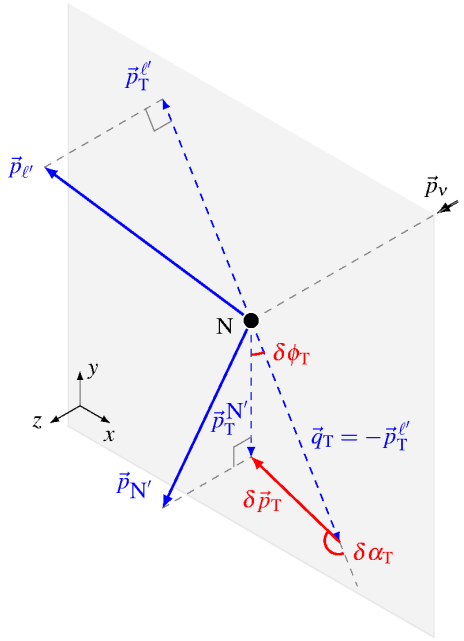

Figure 8.5: Schematic picture of the transverse kinematic imbalance ($\delta\phi_T$, δp_T and $\delta\alpha_T$). They are defined in the plane perpendicular to the neutrino beam direction. Taken from [119].

In addition to these improvements of our near detector fit, improvements of the event selection in the near detector are planned. For the event selection, we are trying to implement the photon selection and proton selection for $\bar{\nu}$ mode in order to get stronger constraints on the several cross section parameters for anti-neutrino. Overall, these improvements will be more important when the ND280 upgrade completes, since the measurement with the upgraded near detectors provides us new kinematics information with low momentum threshold and large angle acceptance.

8.4 Hyper-Kamiokande Experiment

Improvements of the near detector and the analysis in the T2K experiment may allow us to obtain the evidence of the CP violation, i.e. measure the CP violation at 3σ confidence level in the neutrino oscillations. However, they are insufficient to discover the CP violation (measurement at 5σ confidence level) in the wide region of δ_{CP}. Hyper-Kamiokande detector is being constructed in order to get more statistics toward this discovery by the 8.4 times larger fiducial volume

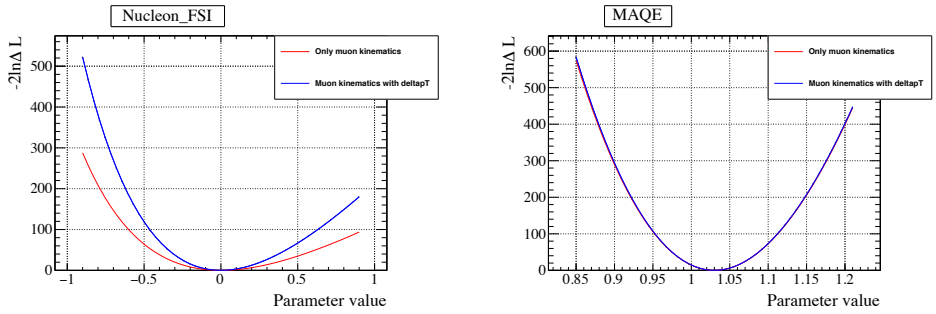

Figure 8.6: Comparison of the likelihood scan for nucleon FSI (left) and MAQE (right) with and without the transverse kinematics.

than Super-Kamiokande. The CP violation is expected to be discovered for 57% of the possible values of δ_{CP} with ten years exposure of 1.3 MW neutrino beam [39]. To achieve this goal in the Hyper-Kamiokande experiment, the reduction of the systematic uncertainty is more important since the size of the statistical uncertainty will become relatively smaller. Thus, understanding of the neutrino interaction model by the ND280 upgrade will be essential for the measurement in the Hyper-Kamiokande experiment.

Part IV

Summary

Chapter 9

Conclusion

Neutrino oscillation is an interesting phenomenon that the lepton flavor changed during its flight. There are several open questions about neutrino oscillations, such as CP violation, $\sin^2\theta_{23}$ octant and neutrino mass ordering. Especially, the CP violation in the lepton sector may be a key to unraveling the mystery of the matter-antimatter asymmetry in universe via leptogenesis. The T2K experiment measures the neutrino oscillation parameters using a neutrino beam which is generated by the J-PARC accelerator to resolve these open questions.

This thesis reported the neutrino oscillation measurements in the T2K experiment using 3.6×10^{21} protons on target at the far detector. The measurements are performed by comparing the prediction and data of the number of events and neutrino energy spectra at the far detector. For the precise measurement, a reduction of the systematic uncertainties which are derived from neutrino interactions and neutrino flux is important to achieve the precise measurements. These systematic uncertainties are reduced by comparing the muon kinematic distributions from ν_μ CC interactions between the prediction and the data at the near detector. With the constraint on the systematic uncertainties by this near detector fit, the far detector fit was performed and then we got $\delta_{CP} = -1.97^{+0.97}_{-0.62}$, $\sin^2\theta_{23} = 0.561^{+0.019}_{-0.038}$ and $\Delta m^2_{32} = 2.494^{+0.040}_{-0.057}$ eV^2/c^4 with the reactor constraint for θ_{13} and assuming the normal neutrino mass ordering. Toward more precise measurement, we update the analysis especially about the event selection. For the near detector fit, a new photon selection was adopted to predict more precisely the NC π^0 events which is the main background source of ν_e events at the far detector. In addition, we also added new selection criteria which are based on the proton multiplicity in order to get more precise prediction of the CCQE and 2p2h events. A new multi-ring selection at the far detector analysis was added in order to increase statistics. To cover these selection updates, neutrino interaction models were also improved.

In addition, our understanding of the neutrino interactions may not enough and there may be a potential bias due to the "choice" of the neutrino interaction models in the analysis. In order to evaluate it, we performed the robustness study with simulated data sets which are generated by the alternative models. In the robustness study, we performed the near and far detector fit against the simulated data sets of the nominal model and each alternative model. Then, we compared their analysis results and evaluate the bias on the oscillation parameters. Based on

the selection updates, in particular, we evaluated various interaction models related to the events that include protons or pions in the final state. As a result, there is no significant bias for δ_{CP} and $\sin^2\theta_{23}$. On the other hand, we find a significant bias of 2.7×10^{-5} eV^2/c^4 for Δm^2_{32} which should be considered as a systematic error. This bias is mainly caused by the data-drive model focused on CC0π nonQE and CRPA model. The result that a large bias was observed indicates a lack of our understanding of the neutrino interaction model. Therefore, we are upgrading the near detector to measure the neutrino interactions in detail and the measurements of the upgraded near detector will give us a new understanding of the neutrino interaction models. Furthermore, an upgrade of the analysis with a new kinematics variable in the near detector fit is planned to take advantages of the improvement.

Finally, using the reactor constraint and assuming the normal neutrino mass ordering, we obtained $\delta_{CP} = -2.18^{+1.22}_{-0.47}$, $\sin^2\theta_{23} = 0.559^{+0.018}_{-0.078}$ and $\Delta m^2_{32} = 2.506^{+0.047}_{-0.052}$ eV^2/c^4 with the updated analysis. These are the world's highest precision measurements, indicating the CP violation at a 90% confidence level. In the near future, the discovery of CP violation could be achieved and bring us one step closer to solving the mystery of the matter-antimatter asymmetry in universe.

Appendix A

Fit Results of the Other Data Sets

This Appendix reports the fit results of the other simulated data studies. We did not see any large biases which should be considered as the systematic errors.

A.1 Local Fermi Gas Model

This model is the alternative nuclear model for the CCQE interaction as discussed in Sec. 3.4.2. Figures A.1 and A.2 show fitting results of the cross section and flux parameters using this alternative model. The CCQE normalizations as a function of Q^2 and several other parameters which are related to the 2p2h interaction move slightly as expected. Using the covariance matrices which are based on that near detector fit, we made the reconstructed neutrino energy prediction at the far detector as shown in Fig. A.3. The near detector fit predictions cover the simulated data lines well.

Figure A.4 shows the fit results for three oscillation parameters. There is no large bias which should be considered as the systematic errors following the criteria discussed in Sec. 6.3.

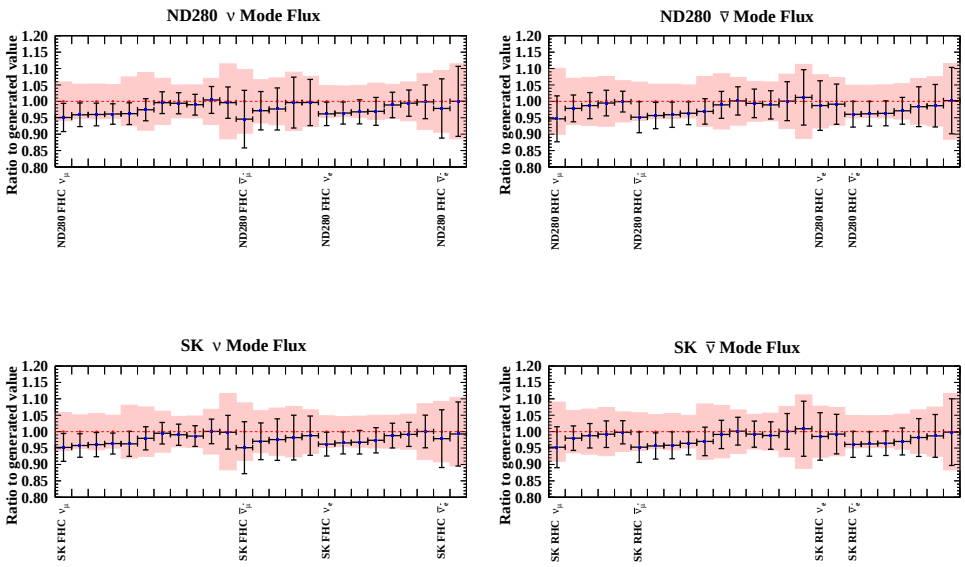

Figure A.1: Pre- (red band) and post-fit (blue dots and black error bands), flux parameters for the ν mode (left) and the $\bar{\nu}$ mode (right), and for the ND280 (top) and SK (bottom) from the near detector fit to the simulated data set of LFG model.

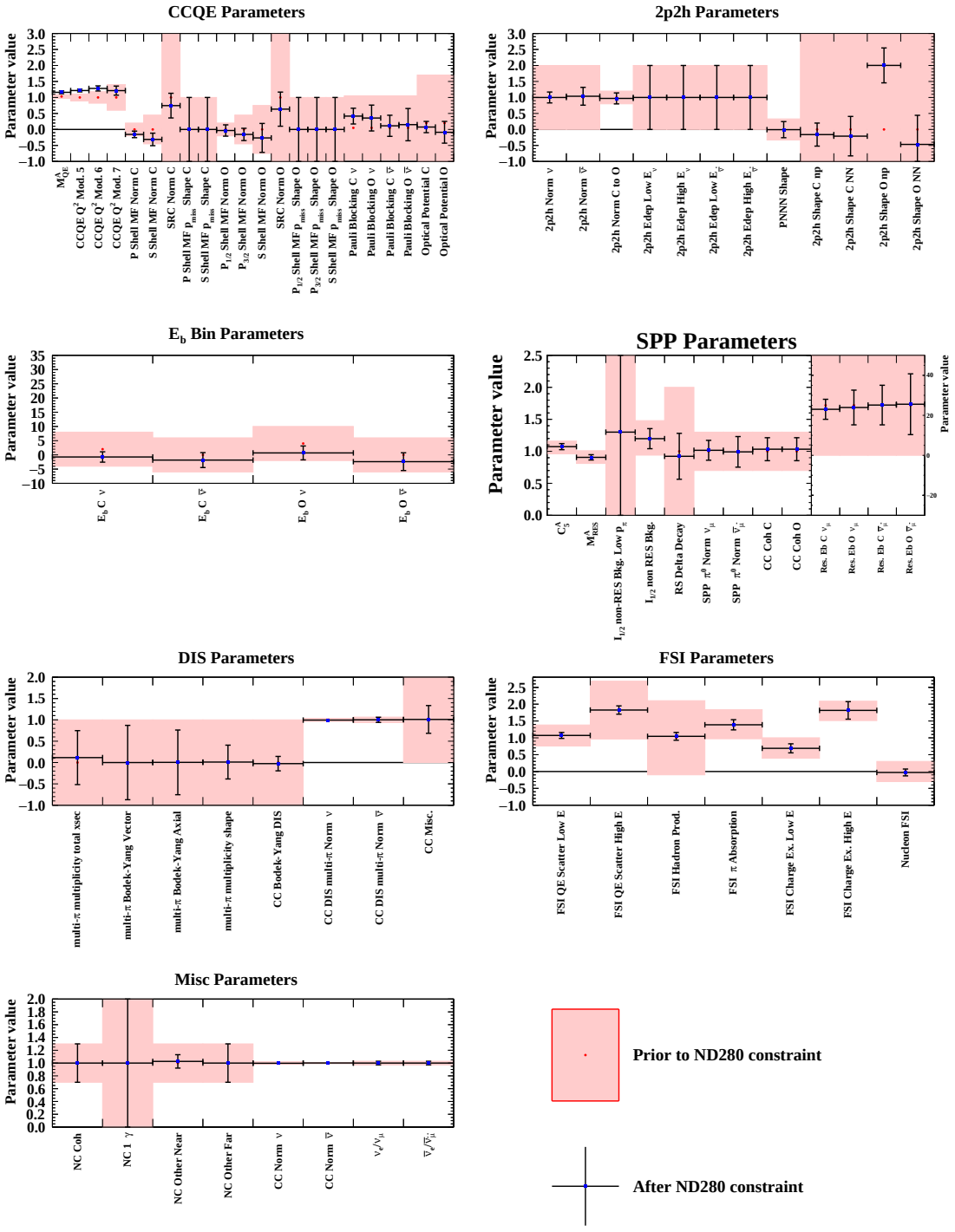

Figure A.2: Pre-(red band) and post-fit (blue dots and black error bands), cross-section parameters for CCQE, 2p2h, E_b, Single Pion Production (SPP), FSI, DIS, and misc from the near detector fit to the simulated data set of LFG model.

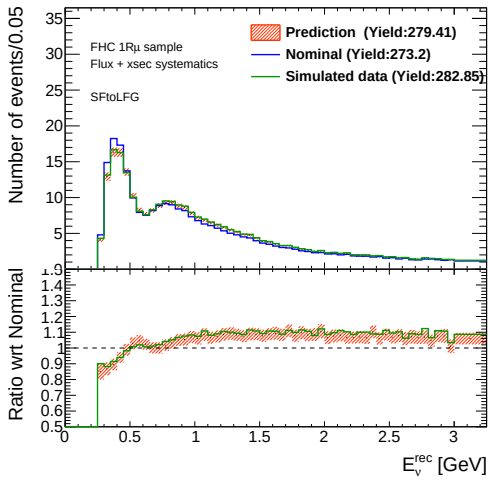

(a) ν mode 1Rμ

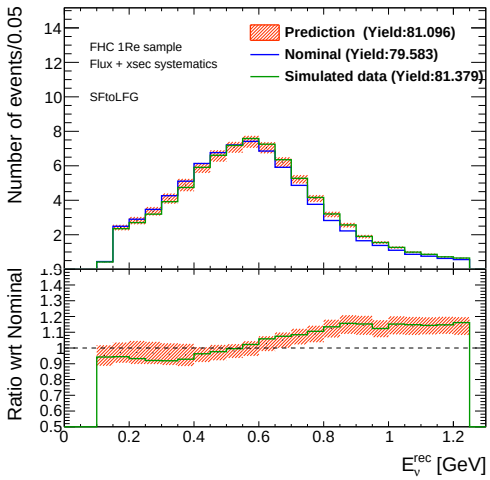

(b) ν mode 1Re

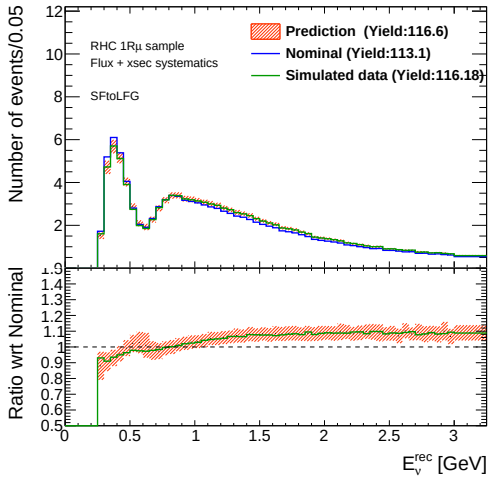

(c) $\bar{\nu}$ mode 1Rμ

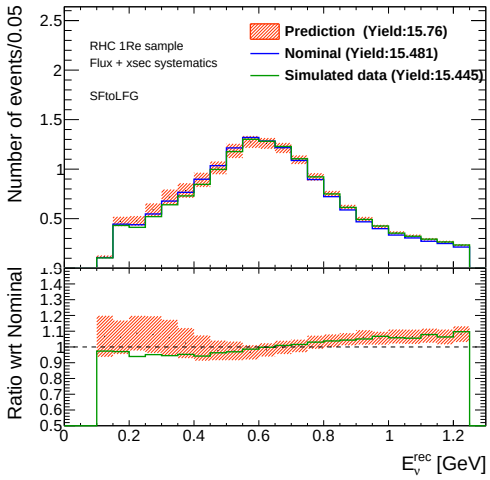

(d) $\bar{\nu}$ mode 1Re

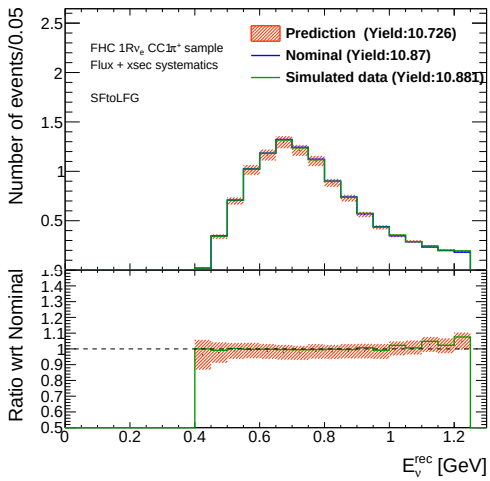

(e) ν mode 1Re1de

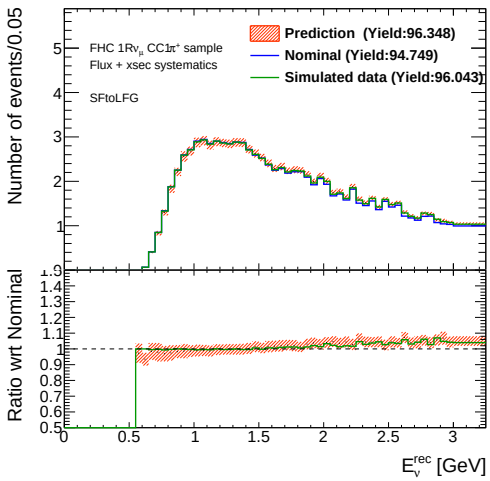

(f) ν mode CC1π multi-ring

Figure A.3: Comparison plots of the number of events between the nominal far detector sample (blue solid line), the simulated data of the alternative model (green solid line) and the prediction from the near detector fit (red band) as a function of the reconstructed neutrino energy. The bottom insets show the ratio of data to simulation.

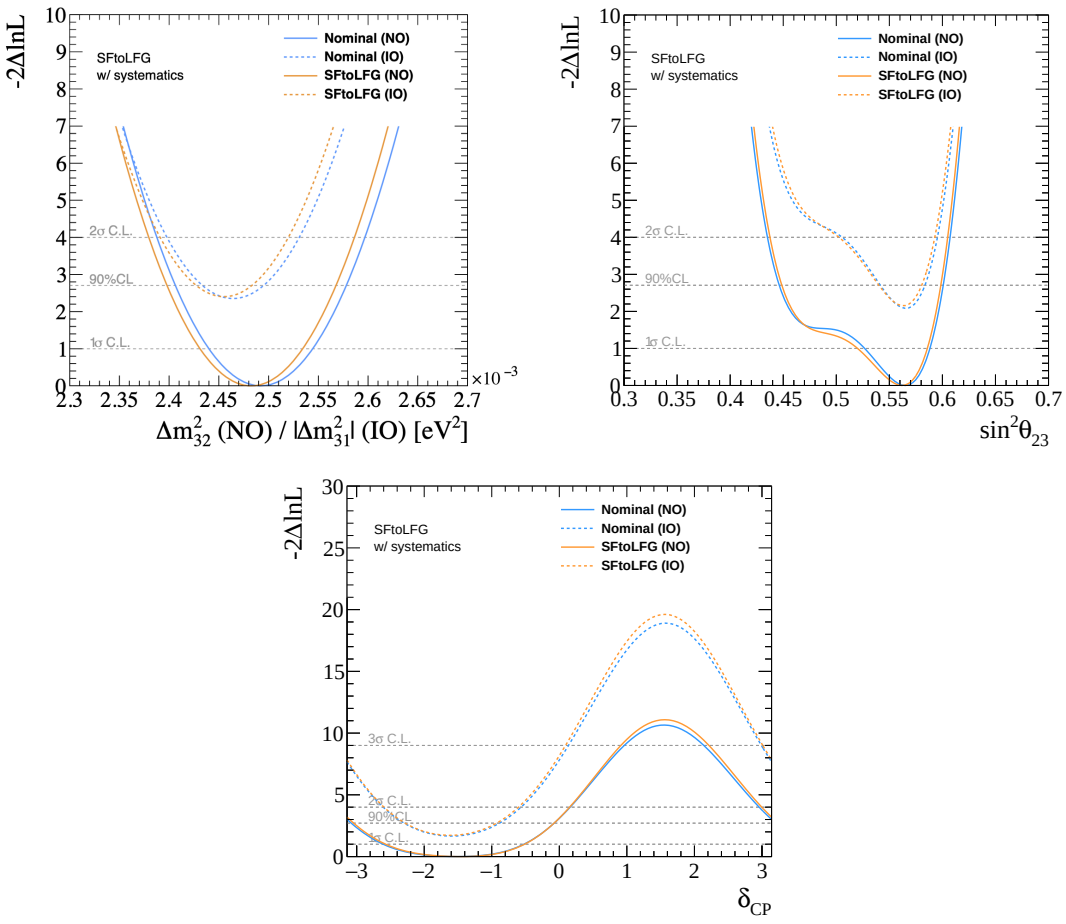

Figure A.4: Comparison of likelihood surface for Δm^2_{32}, $\sin^2\theta_{23}$ and δ_{CP}. Orange lines show those from LFG robustness studies and blue lines show those of nominal MC for the normal and inverted mass orderings.

A.2 Removal Energy

This study is motivated by the difficulties of this parametrization in our analysis framework. The removal energy parameters are set to extreme value (15 MeV) to produce this simulated data. Figures A.5 and A.6 show fitting results of the cross section and flux parameters using this alternative model. The removal energy parameters move at $\sim$ 15 MeV as expected. Using the covariance matrices which are based on that near detector fit, we made the reconstructed neutrino energy prediction at the far detector as shown in Fig. A.7. The near detector fit predictions cover the simulated data lines well.

Figure A.8 shows the fit results for three oscillation parameters. There is no large bias which should be considered as the systematic errors following the criteria discussed in Sec. 6.3.

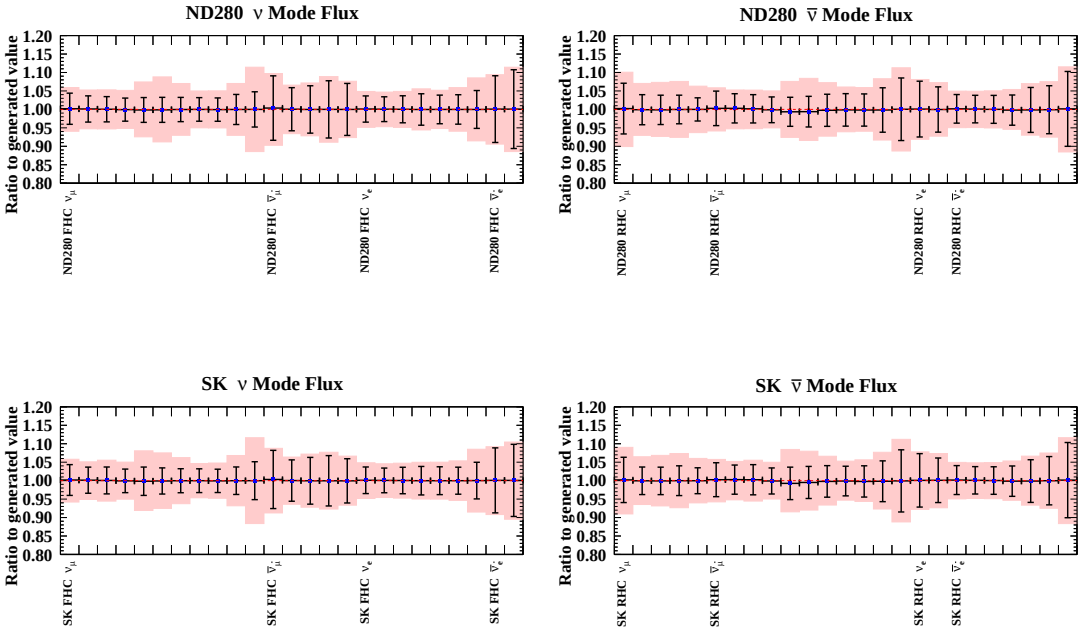

Figure A.5: Pre- (red band) and post-fit (blue dots and black error bands), flux parameters for the ν mode (left) and the $\bar{\nu}$ mode (right), and for the ND280 (top) and SK (bottom) from the near detector fit to the simulated data set of extreme values for the removal energy.

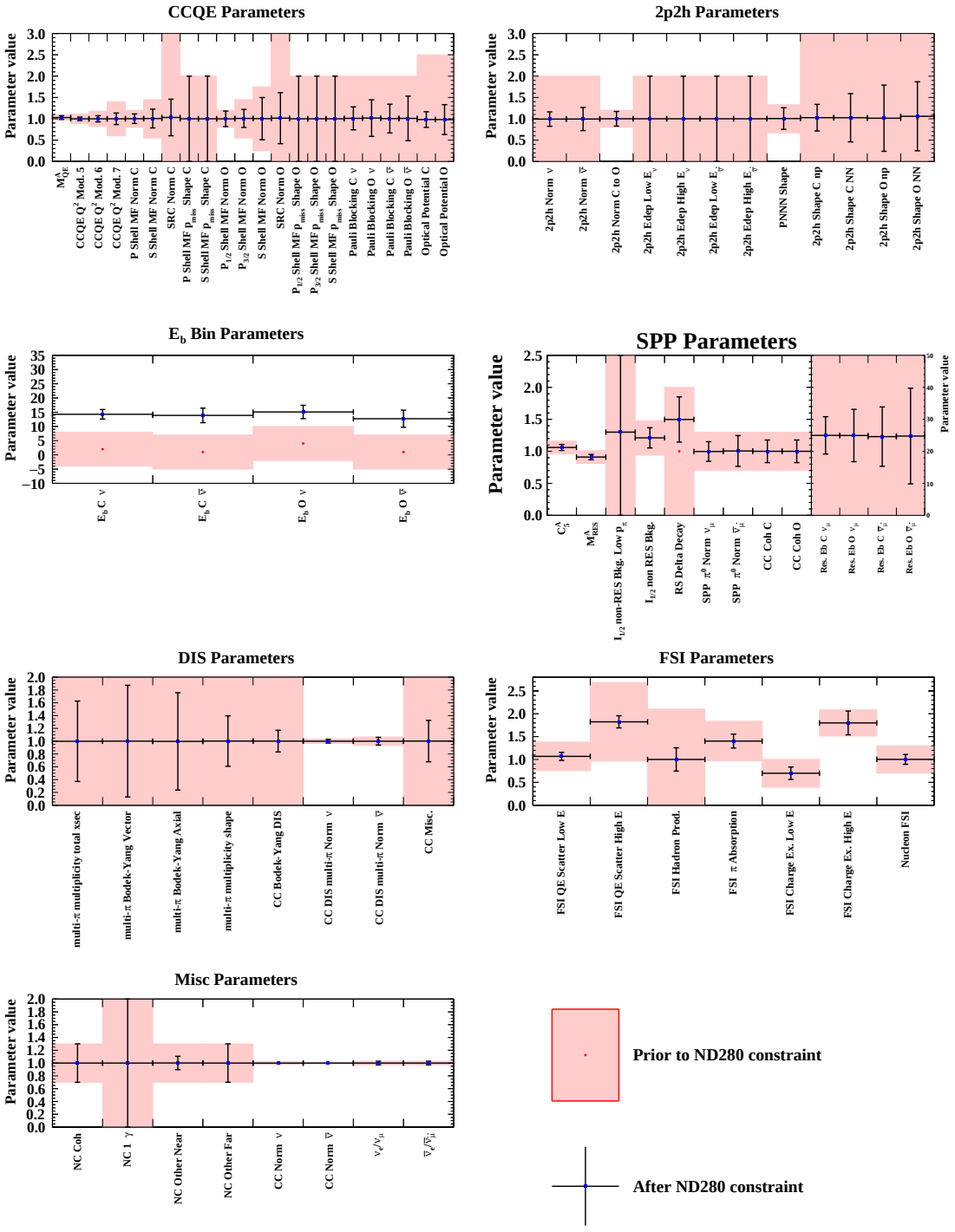

Figure A.6: Pre-(red band) and post-fit (blue dots and black error bands), cross-section parameters for CCQE, 2p2h, E_b, Single Pion Production (SPP), FSI, DIS, and misc from the near detector fit to the simulated data set of extreme values for the removal energy.

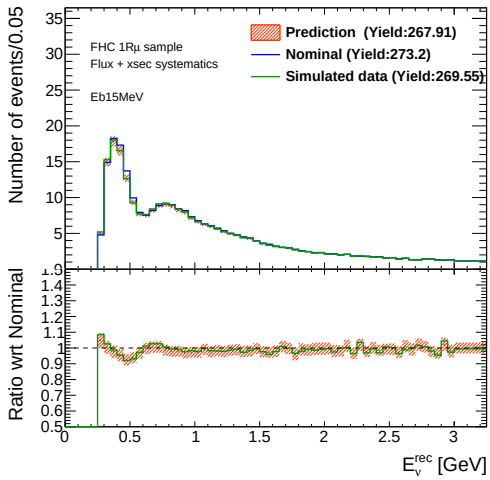

(a) ν mode 1Rμ

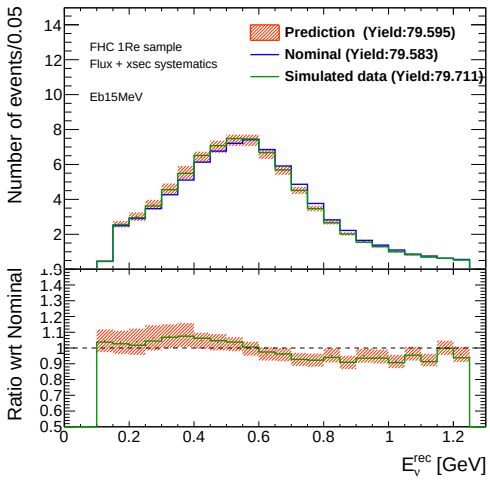

(b) ν mode 1Re

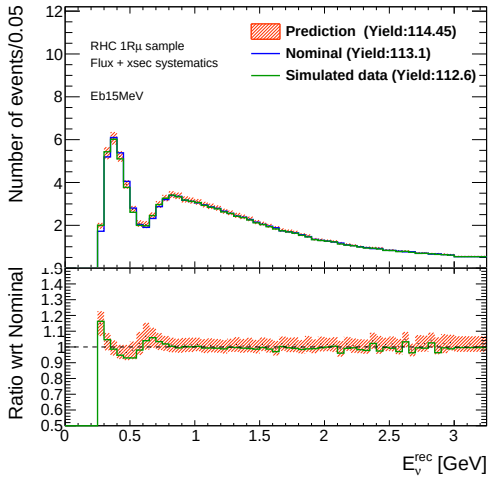

(c) $\bar{\nu}$ mode 1Rμ

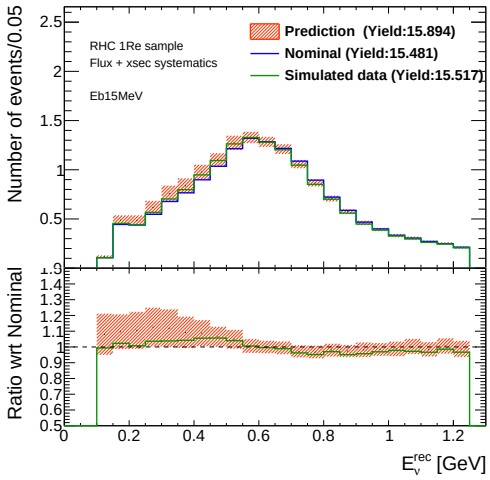

(d) $\bar{\nu}$ mode 1Re

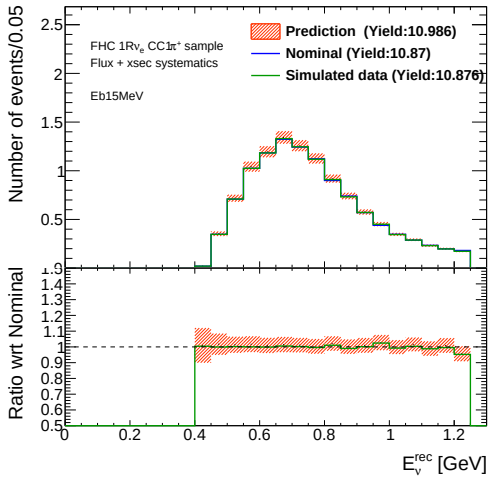

(e) ν mode 1Re1de

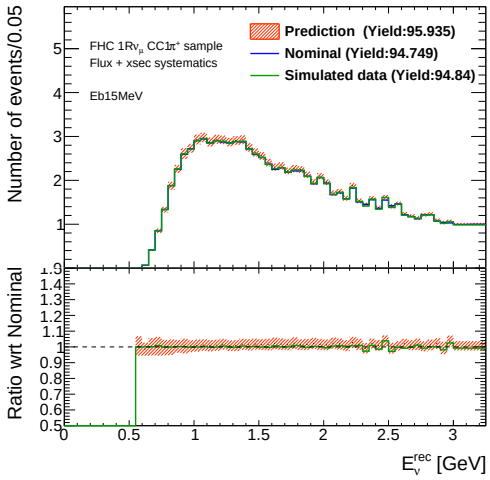

(f) ν mode CC1π multi-ring

Figure A.7: Comparison plots of the number of events between the nominal far detector sample (blue solid line), the simulated data of the alternative model (green solid line) and the prediction from the near detector fit (red band) as a function of the reconstructed neutrino energy. The bottom insets show the ratio of data to simulation.

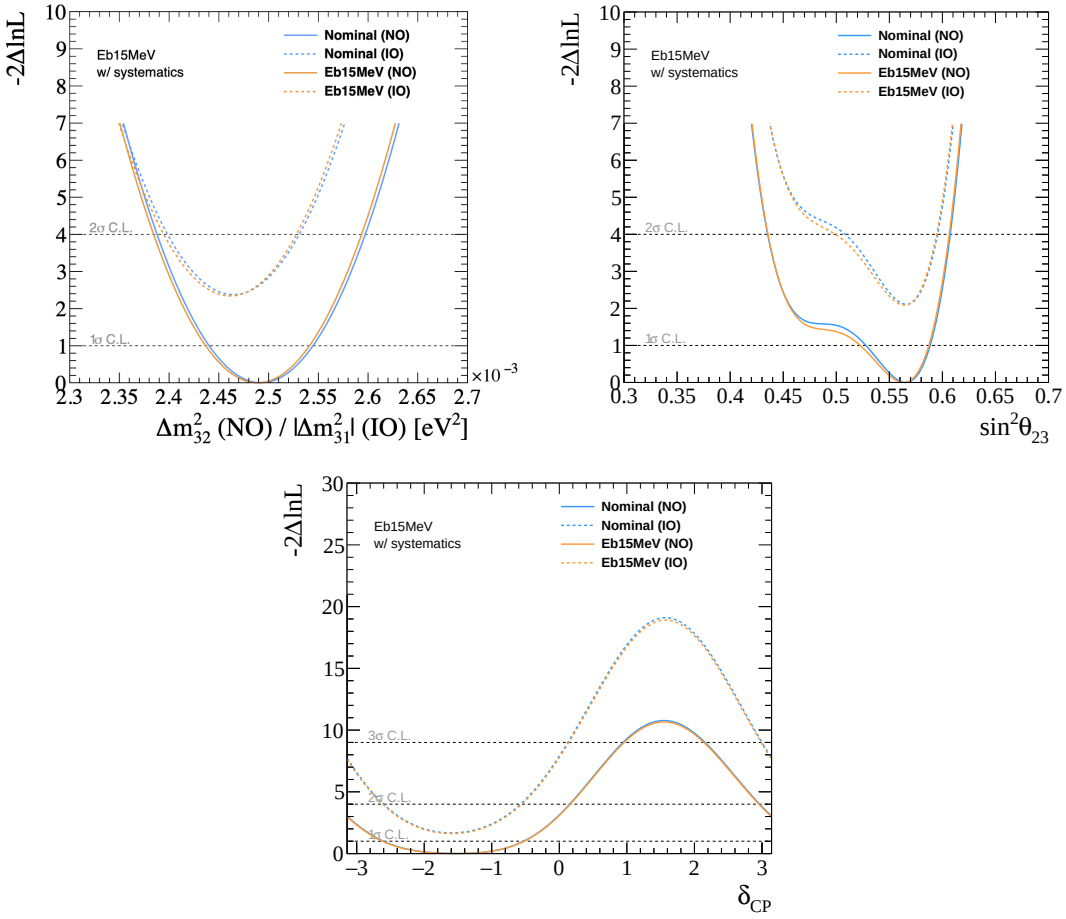

Figure A.8: Comparison of likelihood surface for Δm^2_{32}, $\sin^2\theta_{23}$ and δ_{CP}. Orange lines show those from removal energy robustness studies and blue lines show those of nominal MC for the normal and inverted mass orderings.

A.3 Z-Expansion

This section summarize the results of the fit to the simulated datasets with the Z-expansion model discussed in Sec. 3.4.1. We produce the three simulated data sets (nominal, $\pm 1\sigma$) based on the variation resulting from the fit to the external experiment data. Figures A.9, A.10, A.13, A.14, A.17 and A.18 show fitting results of the cross section and flux parameters using this alternative model. We could see the shifts of the high Q^2 parameters as expected. Using the covariance matrices which are based on that near detector fit, we made the reconstructed neutrino energy prediction at the far detector as shown in Figs. A.11, A.15 and A.19. The near detector fit predictions cover the simulated data lines well.

Figures A.12, A.16 and A.20 show the fit results for three oscillation parameters. There is no large bias which should be considered as the systematic errors following the criteria discussed in Sec. 6.3.

A.3.1 Z-Expansion Nominal

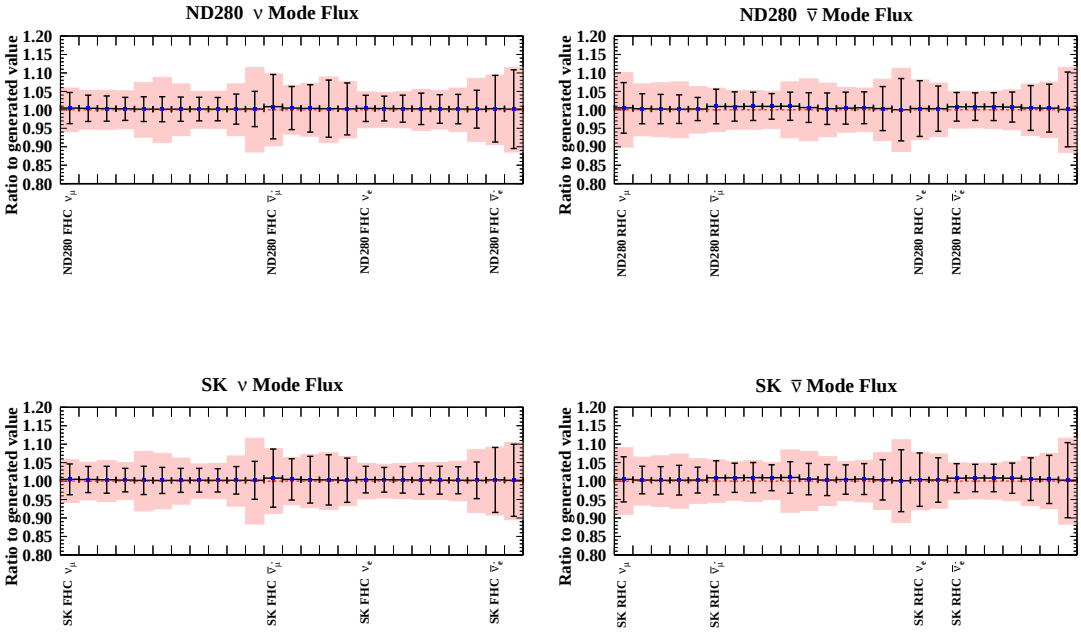

Figure A.9: Pre- (red band) and post-fit (blue dots and black error bands), flux parameters for the ν mode (left) and the $\bar{\nu}$ mode (right), and for the ND280 (top) and SK (bottom) from the near detector fit to the simulated data set of the nominal Z-expansion model.

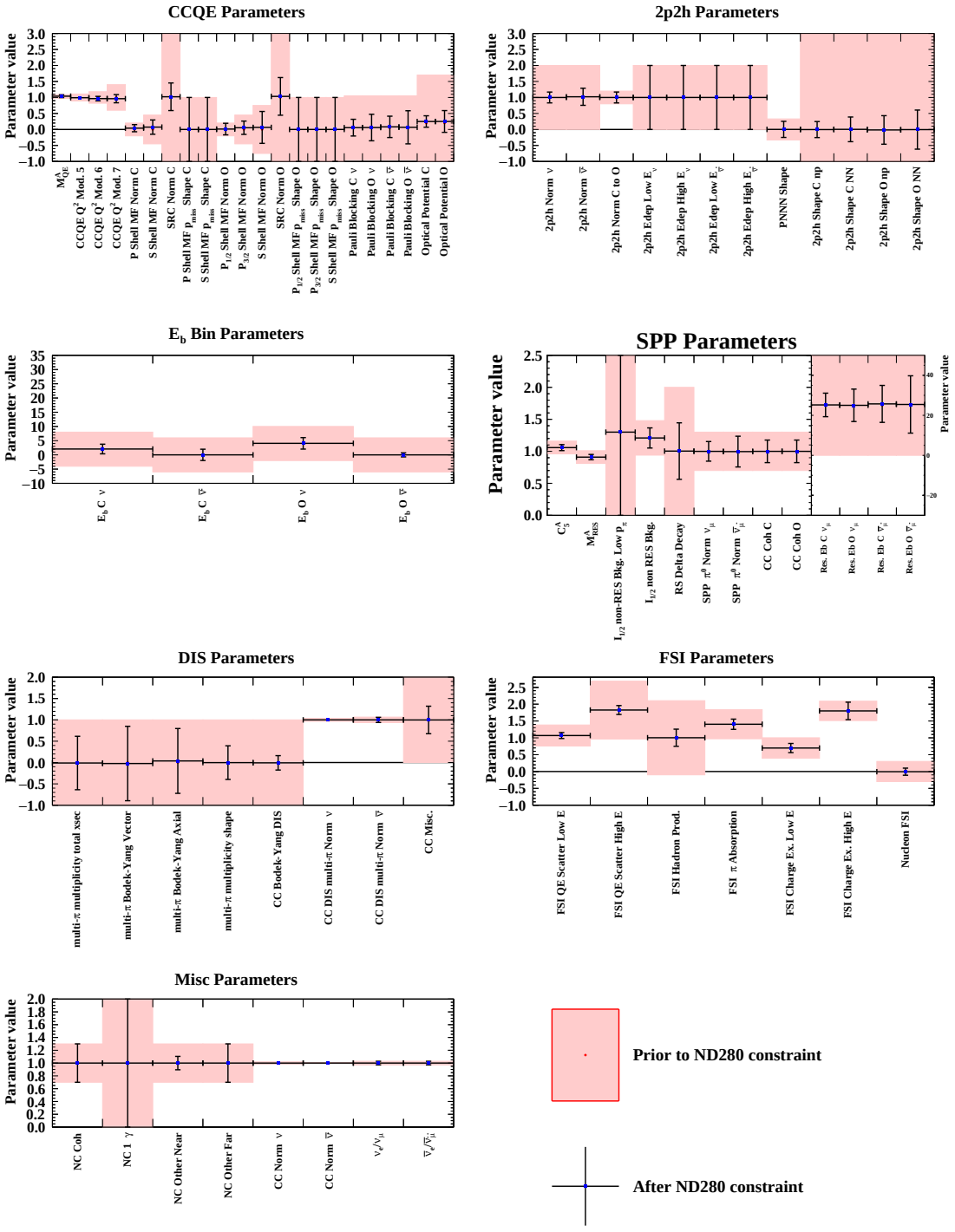

Figure A.10: Pre-(red band) and post-fit (blue dots and black error bands), cross-section parameters for CCQE, 2p2h, E_b, Single Pion Production (SPP), FSI, DIS, and misc from the near detector fit to the simulated data set of the nominal Z-expansion model.

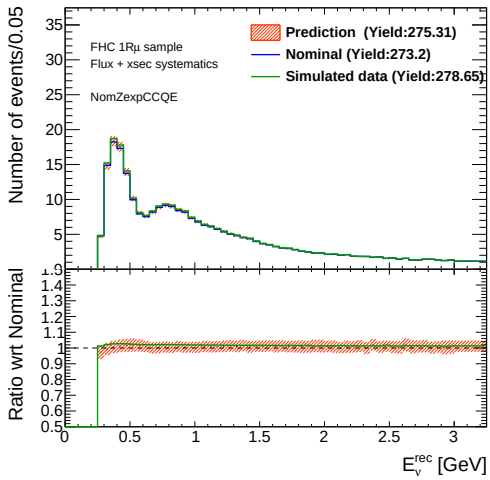

(a) ν mode 1Rμ

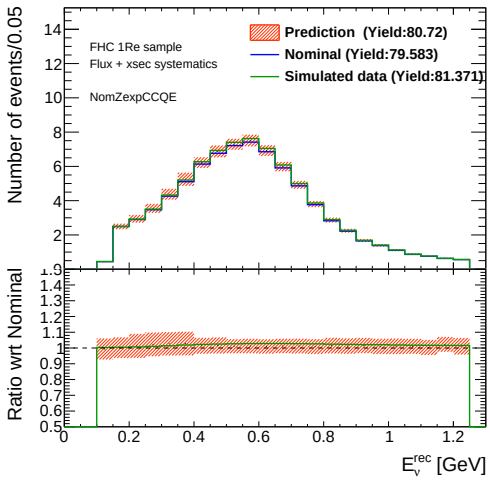

(b) ν mode 1Re

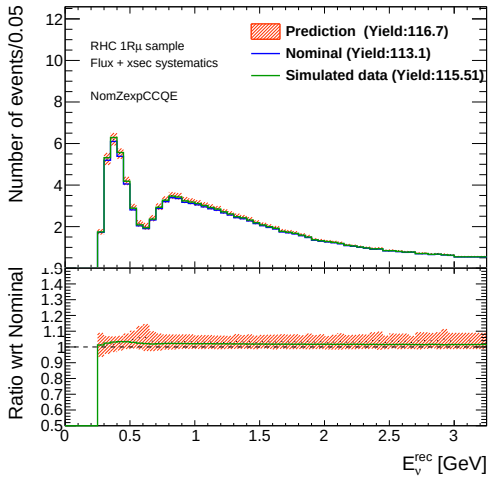

(c) $\bar{\nu}$ mode 1Rμ

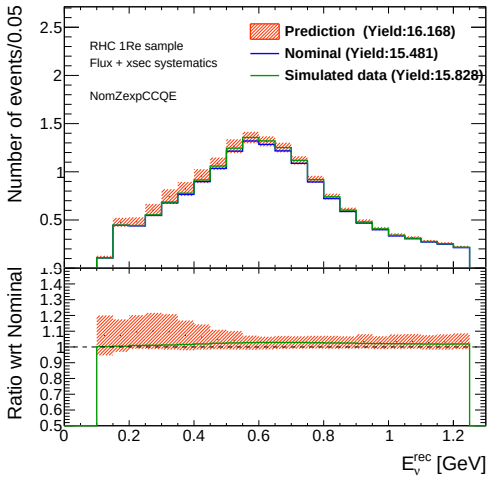

(d) $\bar{\nu}$ mode 1Re

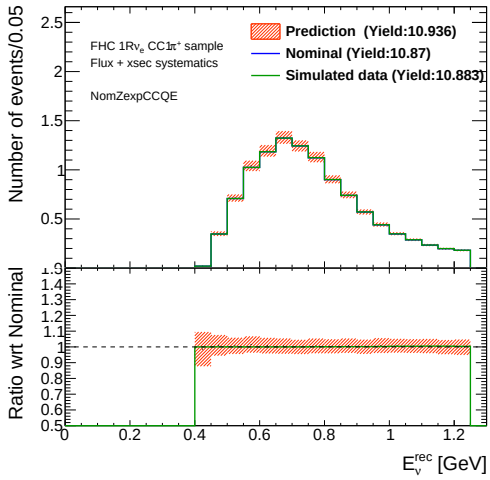

(e) ν mode 1Re1de

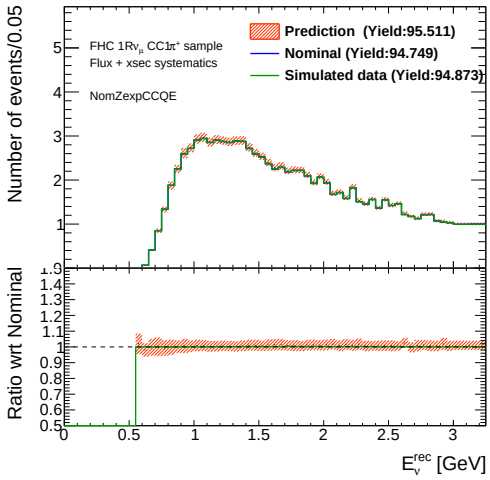

(f) ν mode CC1π multi-ring

Figure A.11: Comparison plots of the number of events between the nominal far detector sample (blue solid line), the simulated data of the alternative model (green solid line) and the prediction from the near detector fit (red band) as a function of the reconstructed neutrino energy. The bottom insets show the ratio of data to simulation.

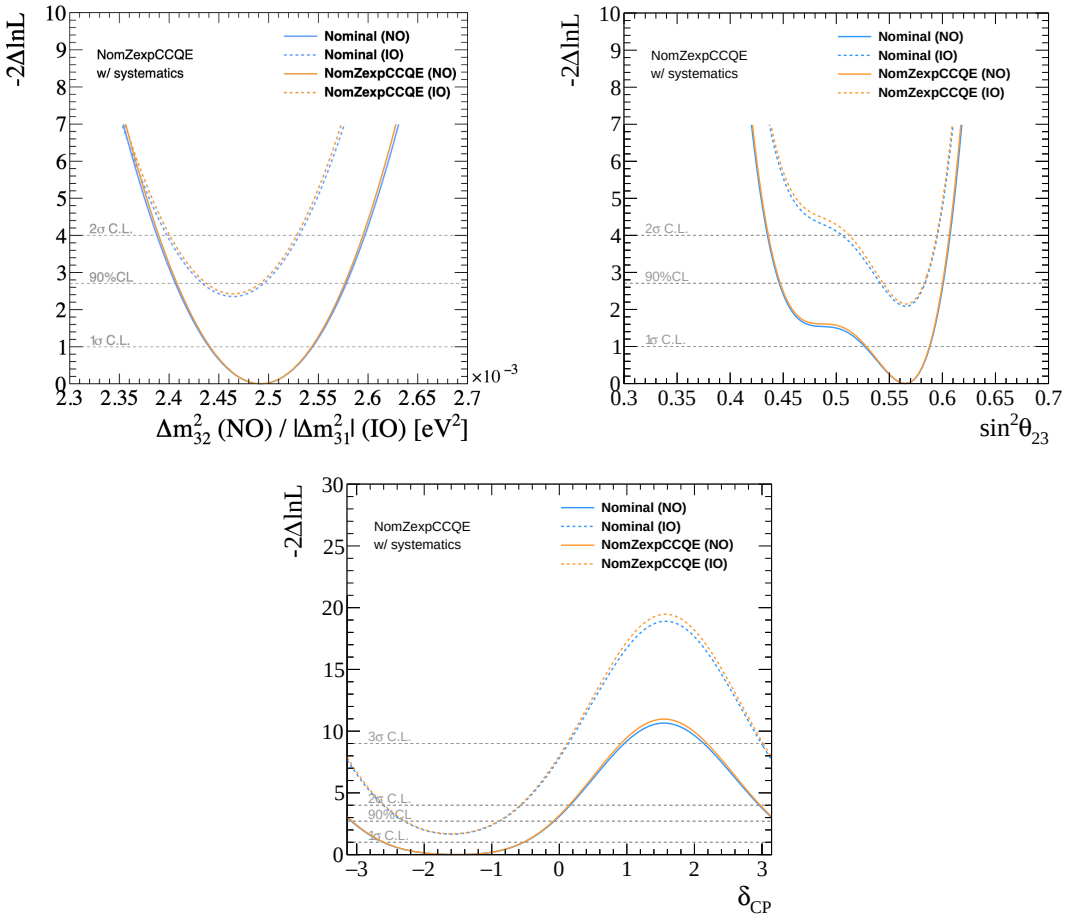

Figure A.12: Comparison of likelihood surface for Δm^2_{32}, $\sin^2\theta_{23}$ and δ_{CP}. Orange lines show those from nominal Z-expansion robustness studies and blue lines show those of nominal MC for the normal and inverted mass orderings.

A.3.2 Z-Expansion $+1\sigma$

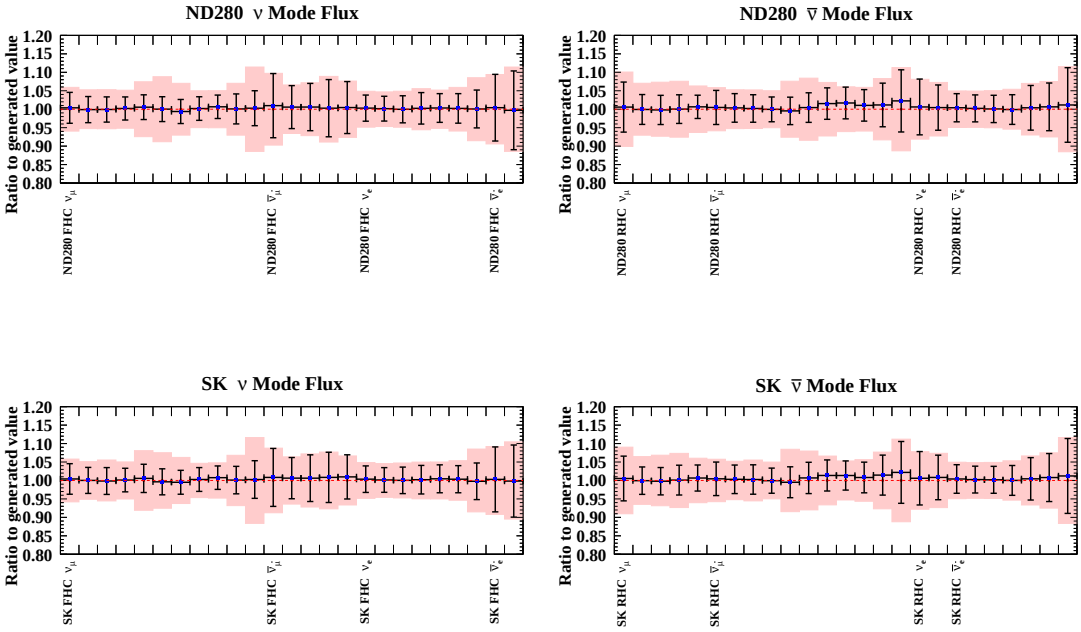

Figure A.13: Pre- (red band) and post-fit (blue dots and black error bands), flux parameters for the ν mode (left) and the $\bar{\nu}$ mode (right), and for the ND280 (top) and SK (bottom) from the near detector fit to the simulated data set of the $+1\sigma$ Z-expansion model.

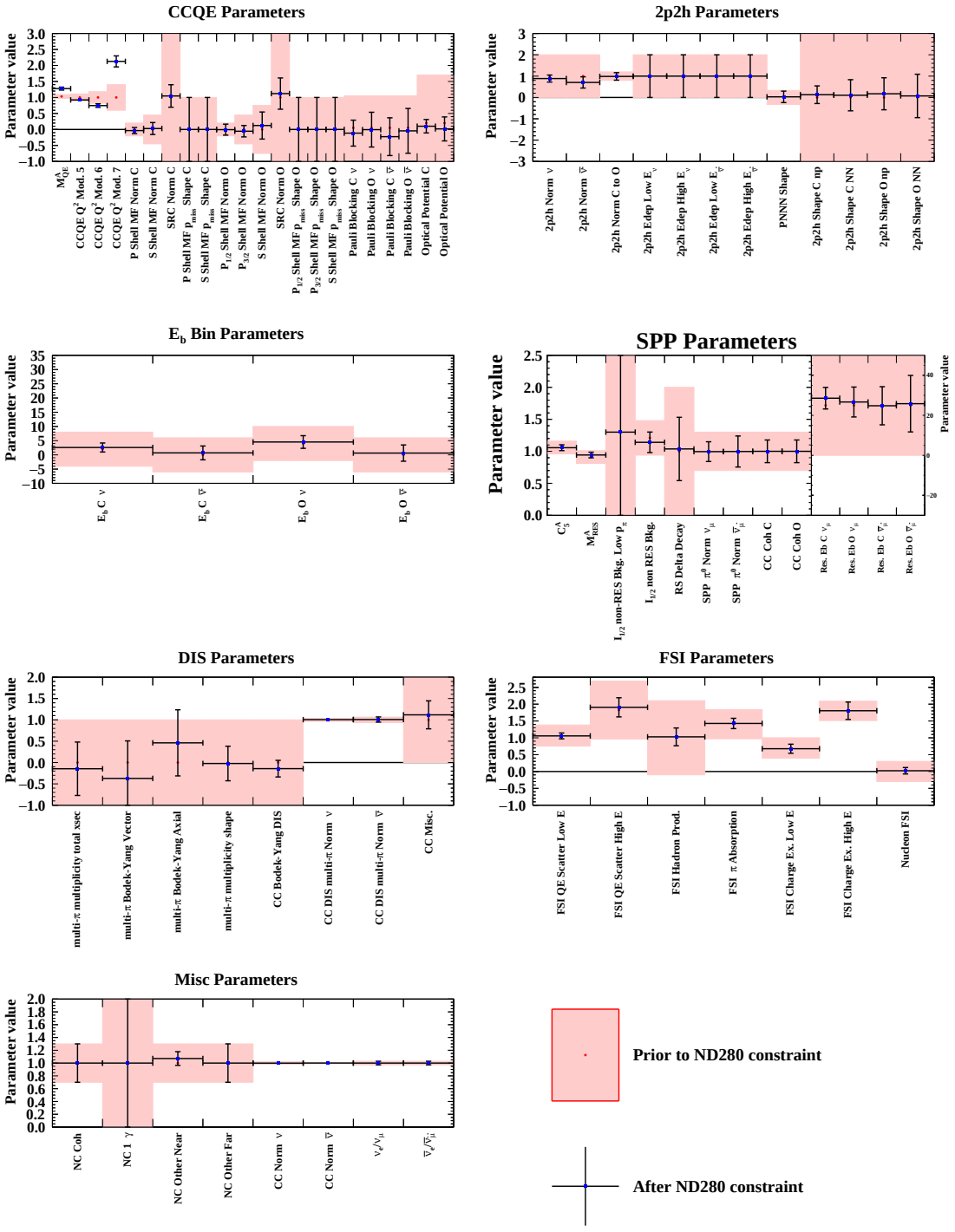

Figure A.14: Pre-(red band) and post-fit (blue dots and black error bands), cross-section parameters for CCQE, 2p2h, E_b, Single Pion Production (SPP), FSI, DIS, and misc from the near detector fit to the simulated data set of the $+1\sigma$ Z-expansion model.

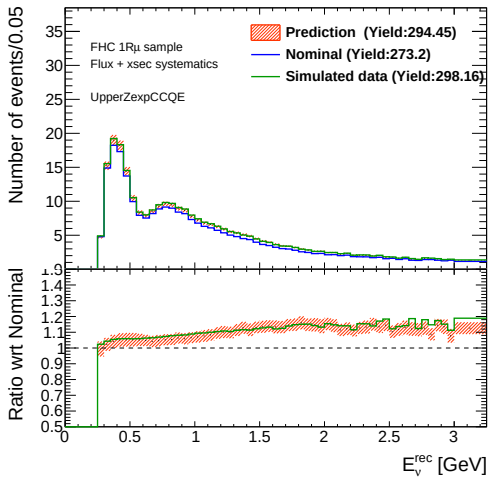

(a) ν mode 1Rμ

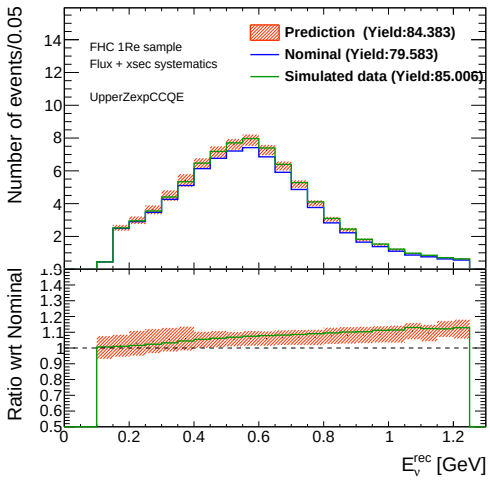

(b) ν mode 1Re

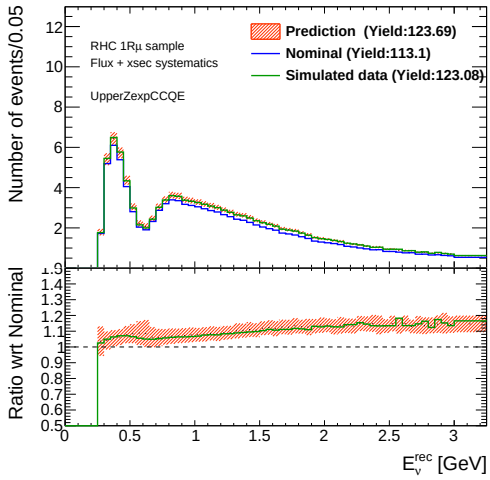

(c) $\bar{\nu}$ mode 1Rμ

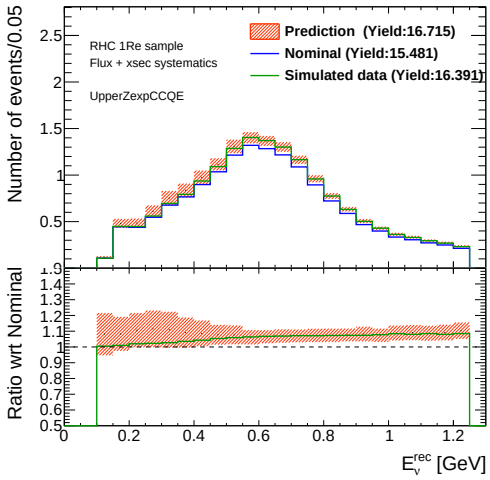

(d) $\bar{\nu}$ mode 1Re

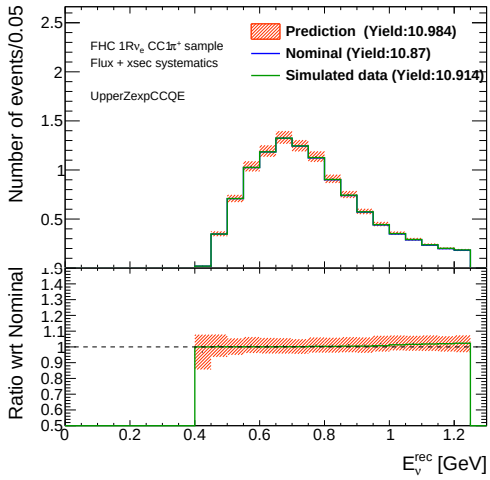

(e) ν mode 1Re1de

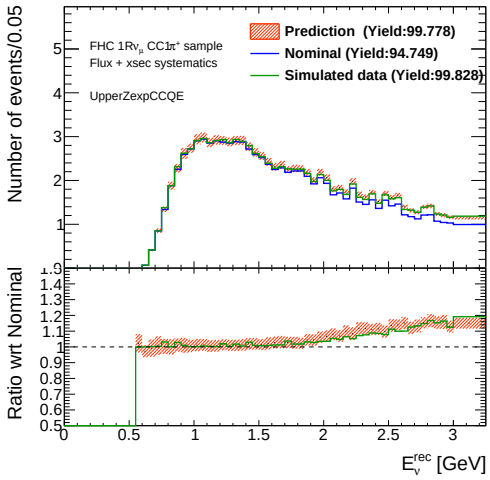

(f) ν mode CC1π multi-ring

Figure A.15: Comparison plots of the number of events between the nominal far detector sample (blue solid line), the simulated data of the alternative model (green solid line) and the prediction from the near detector fit (red band) as a function of the reconstructed neutrino energy. The bottom insets show the ratio of data to simulation.

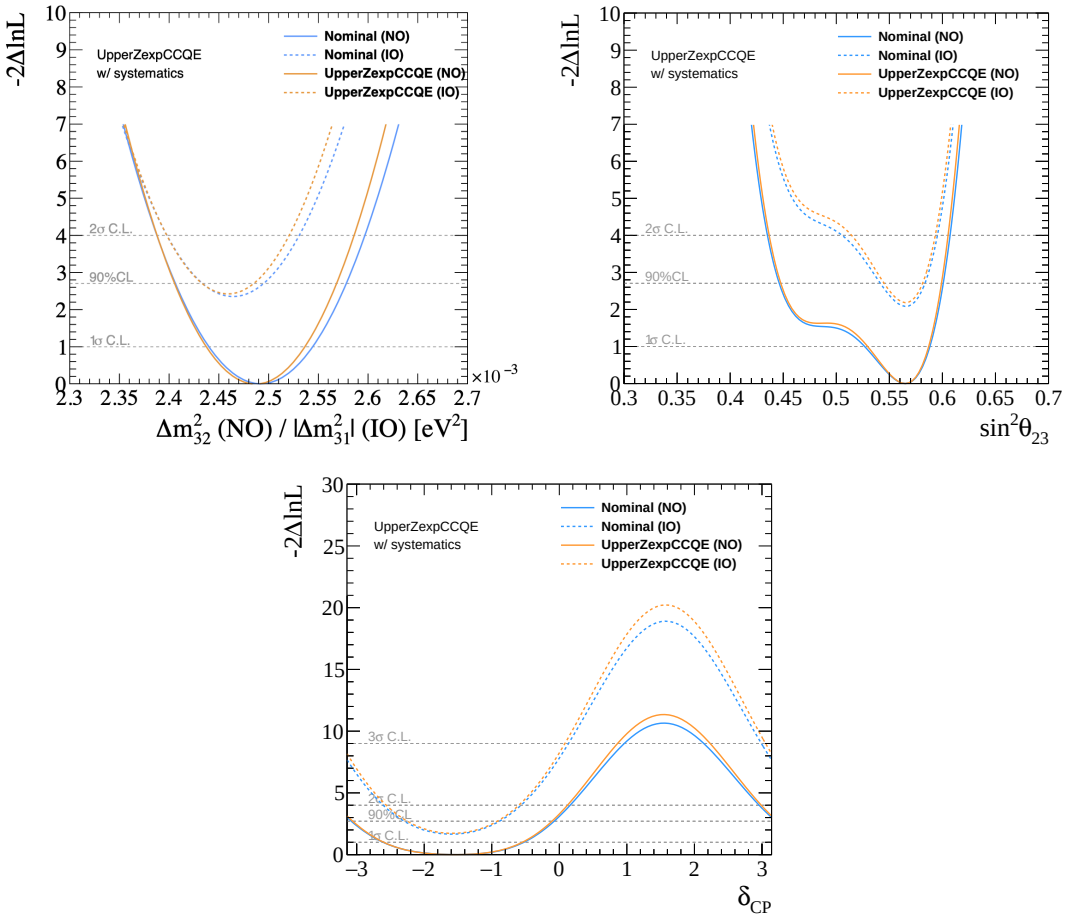

Figure A.16: Comparison of likelihood surface for Δm^2_{32}, $\sin^2\theta_{23}$ and δ_{CP}. Orange lines show those from $+1\sigma$ Z-expansion robustness studies and blue lines show those of nominal MC for the normal and inverted mass orderings.

A.3.3 Z-Expansion -1σ

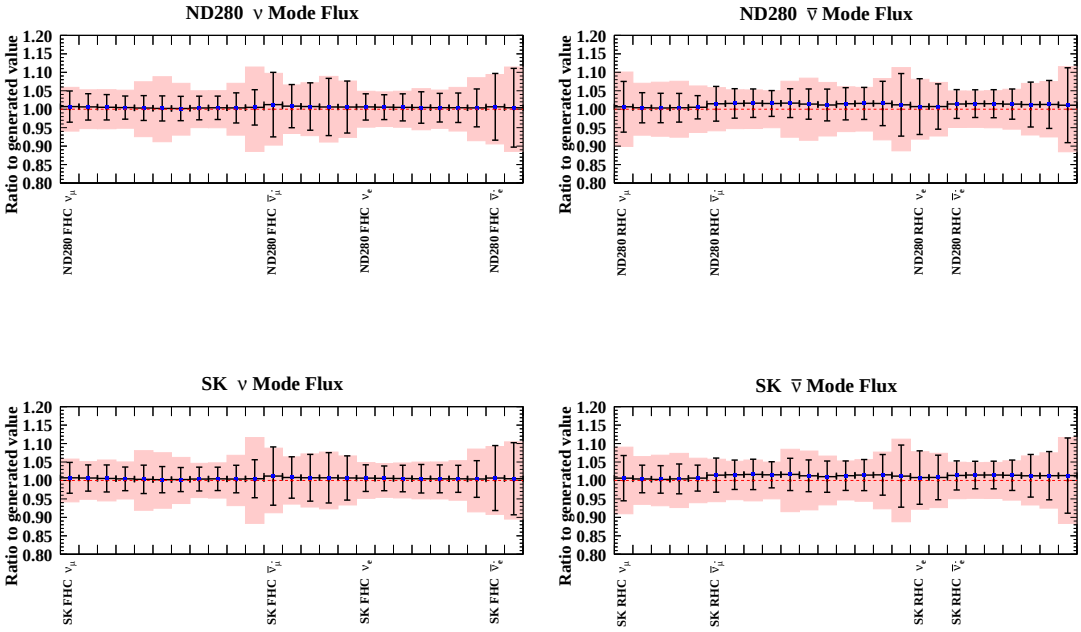

Figure A.17: Pre- (red band) and post-fit (blue dots and black error bands), flux parameters for the ν mode (left) and the $\bar{\nu}$ mode (right), and for the ND280 (top) and SK (bottom) from the near detector fit to the simulated data set of the -1σ Z-expansion model.

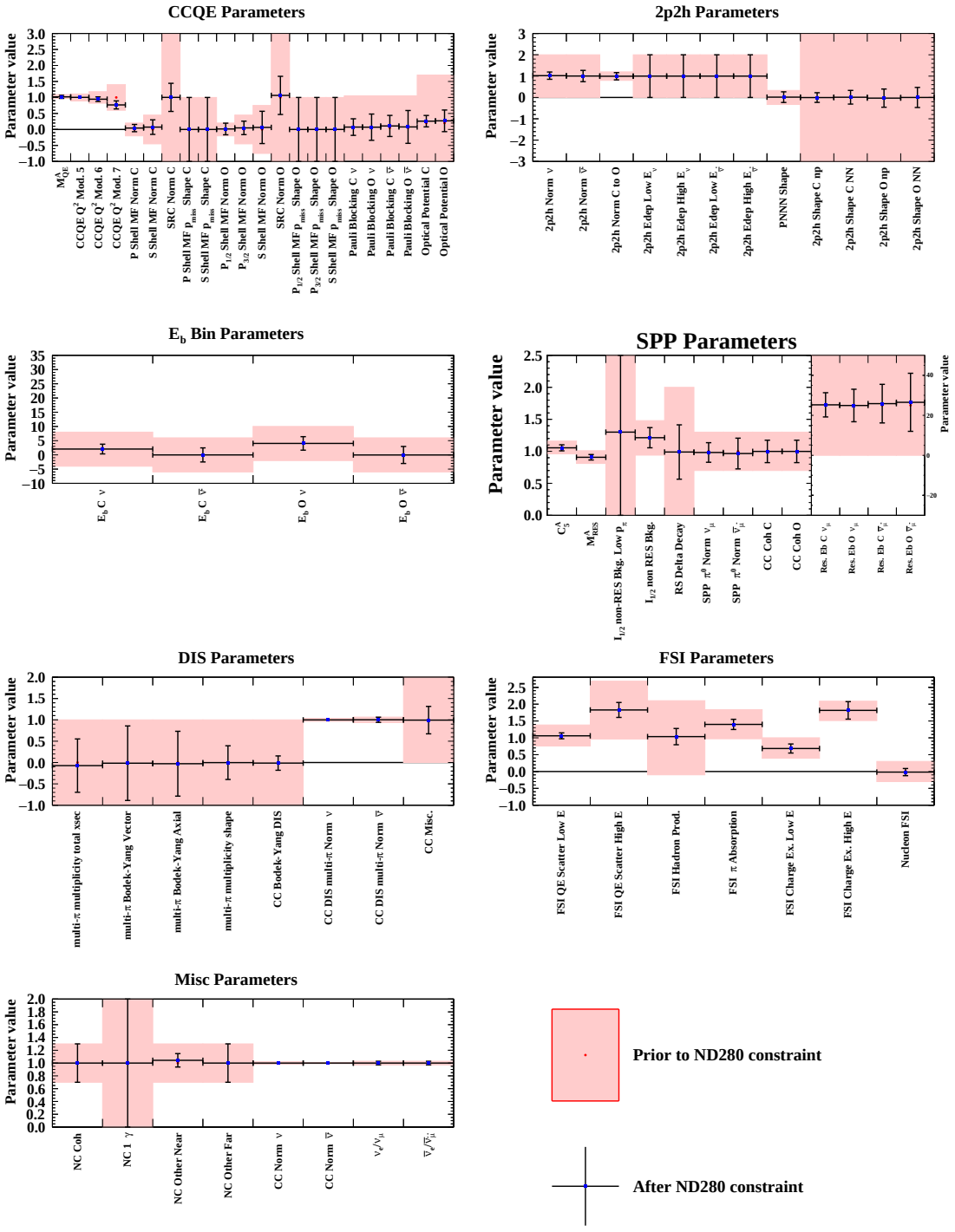

Figure A.18: Pre-(red band) and post-fit (blue dots and black error bands), cross-section parameters for CCQE, 2p2h, E_b, Single Pion Production (SPP), FSI, DIS, and misc from the near detector fit to the simulated data set of the -1σ Z-expansion model.

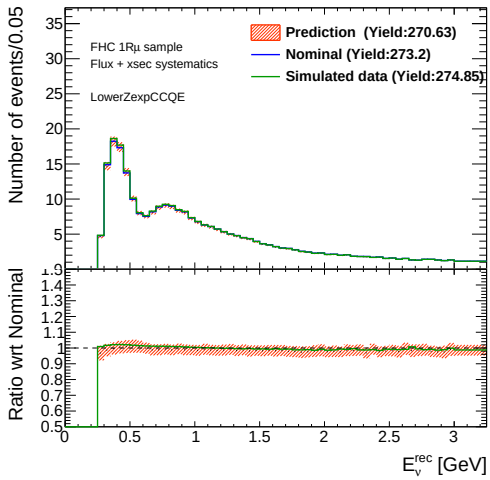

(a) ν mode 1Rμ

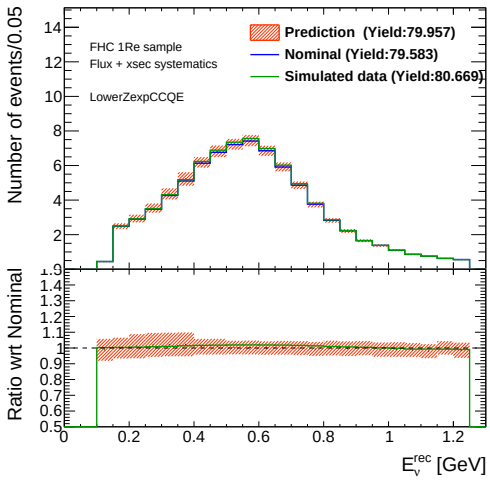

(b) ν mode 1Re

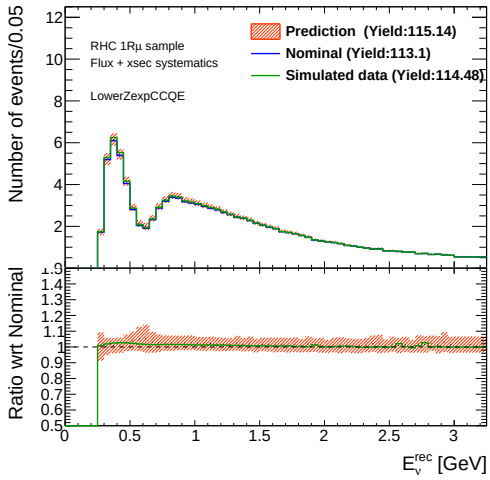

(c) $\bar{\nu}$ mode 1Rμ

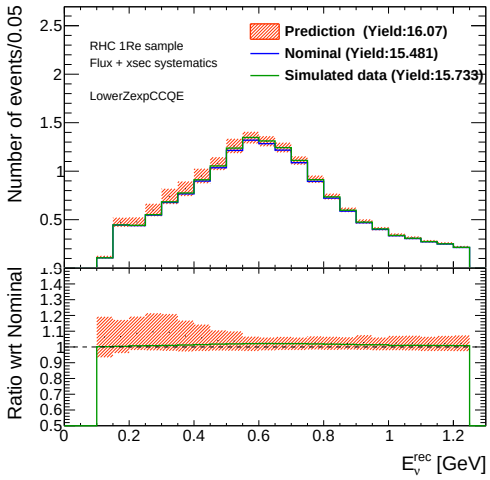

(d) $\bar{\nu}$ mode 1Re

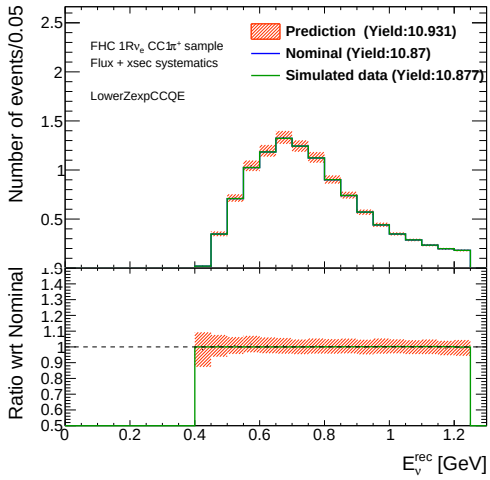

(e) ν mode 1Re1de

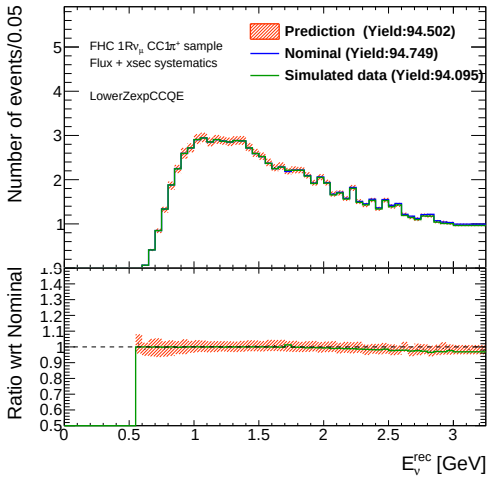

(f) ν mode CC1π multi-ring

Figure A.19: Comparison plots of the number of events between the nominal far detector sample (blue solid line), the simulated data of the alternative model (green solid line) and the prediction from the near detector fit (red band) as a function of the reconstructed neutrino energy. The bottom insets show the ratio of data to simulation.

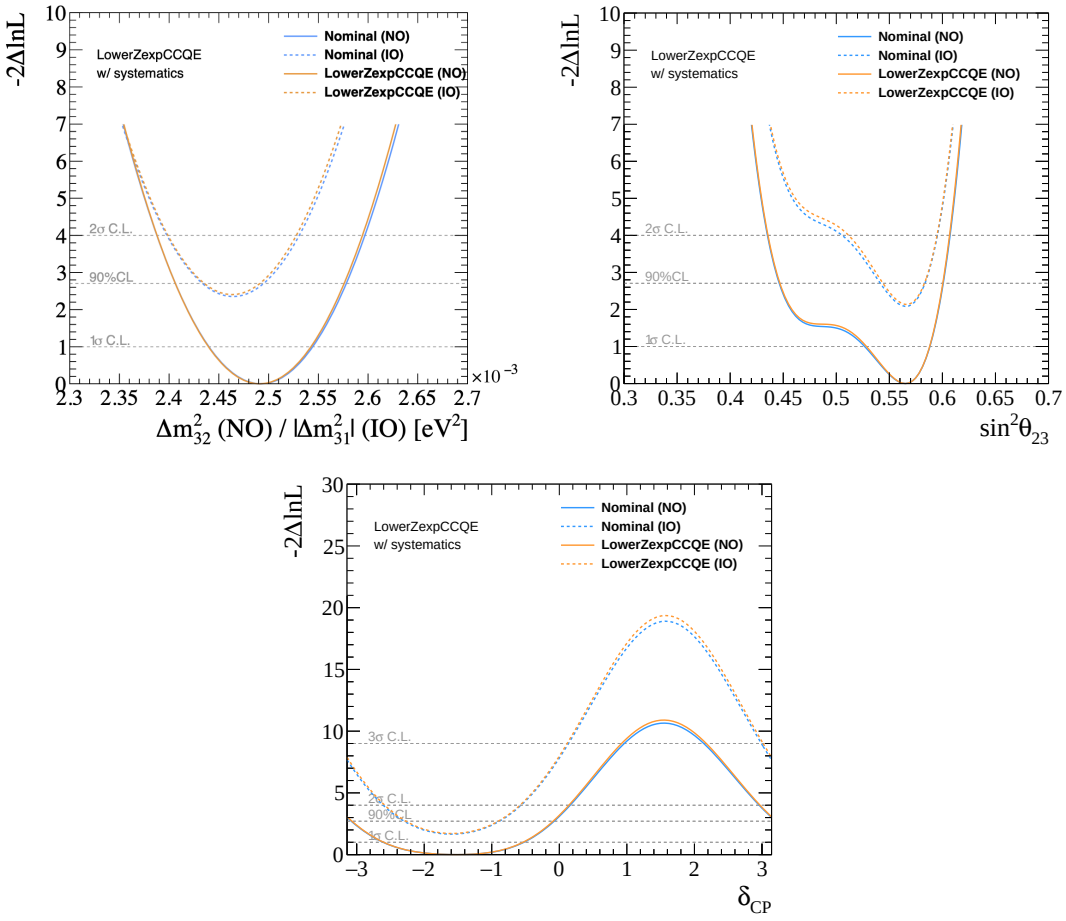

Figure A.20: Comparison of likelihood surface for Δm^2_{32}, $\sin^2\theta_{23}$ and δ_{CP}. Orange lines show those from -1σ Z-expansion robustness studies and blue lines show those of nominal MC for the normal and inverted mass orderings.

A.4 3Component

This section summarize the results of the fit to the simulated datasets with the 3Component model discussed in Sec. 3.4.1. We produce the three simulated data sets (nominal, $\pm 1\sigma$) based on the variation resulting from the fit to the external experiment data as with the Z-expansion model. Figures A.21, A.22, A.25, A.26, A.29 and A.30 show fitting results of the cross section and flux parameters using this alternative model. We could see the shifts of the high Q^2 parameters as expected. Using the covariance matrices which are based on that near detector fit, we made the reconstructed neutrino energy prediction at the far detector as shown in Figs. A.23, A.27 and A.31. The near detector fit predictions cover the simulated data lines well.

Figures A.24, A.28 and A.32 show the fit results for three oscillation parameters. There is no large bias which should be considered as the systematic errors following the criteria discussed in Sec. 6.3.

A.4.1 3Component Nominal

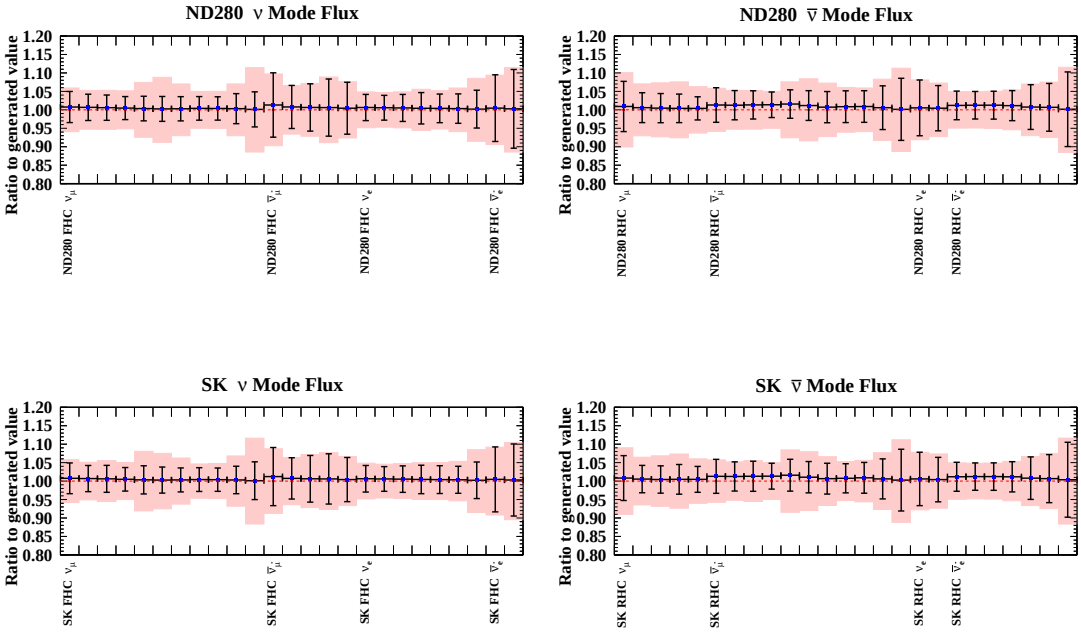

Figure A.21: Pre- (red band) and post-fit (blue dots and black error bands), flux parameters for the ν mode (left) and the $\bar{\nu}$ mode (right), and for the ND280 (top) and SK (bottom) from the near detector fit to the simulated data set of the nominal 3Component model.

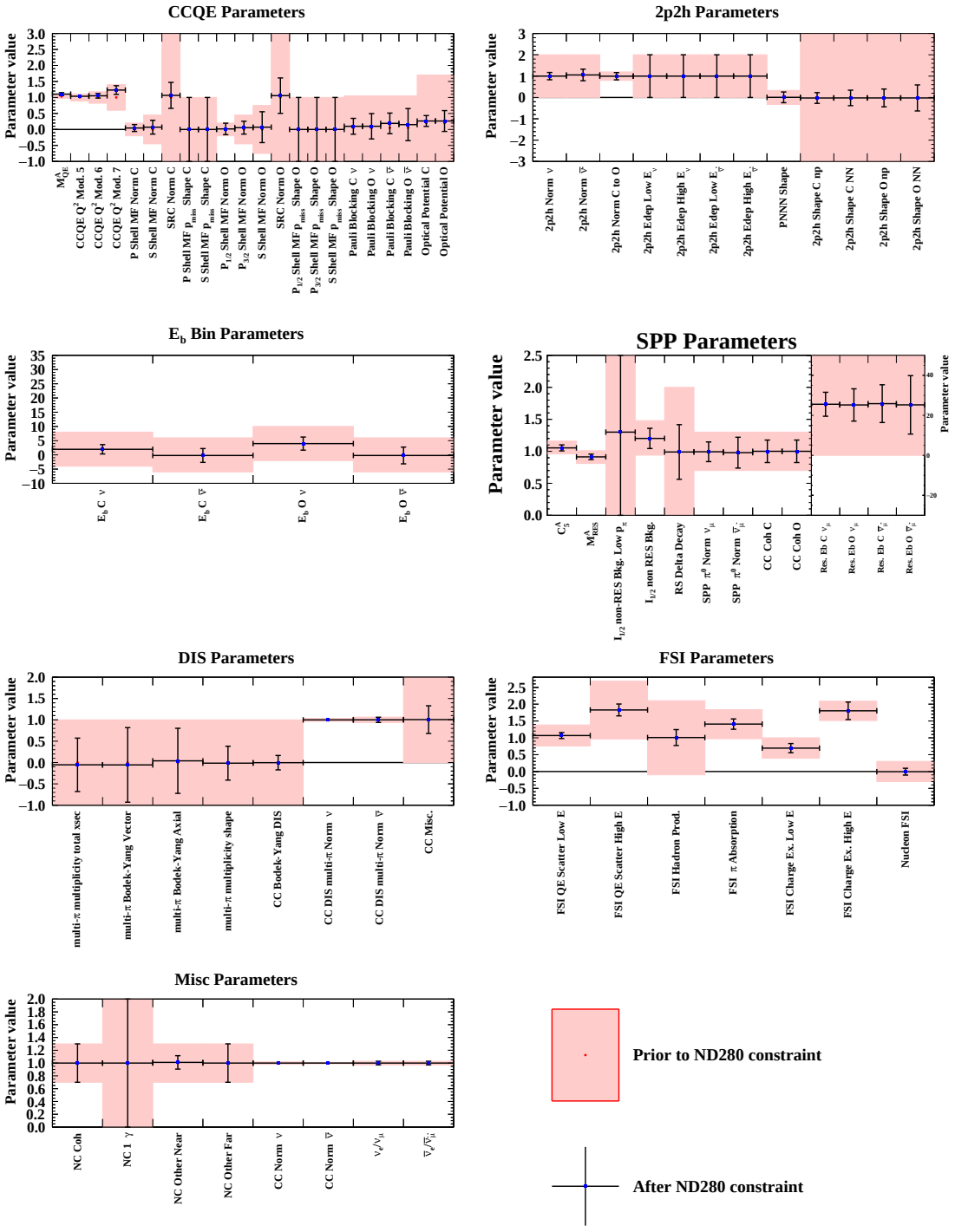

Figure A.22: Pre-(red band) and post-fit (blue dots and black error bands), cross-section parameters for CCQE, 2p2h, E_b, Single Pion Production (SPP), FSI, DIS, and misc from the near detector fit to the simulated data set of the nominal 3Component model.

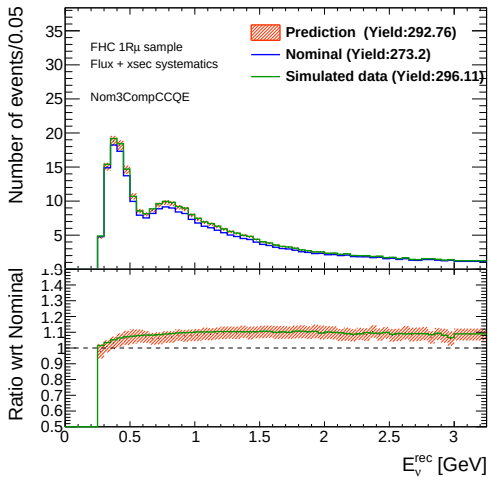

(a) ν mode 1Rμ

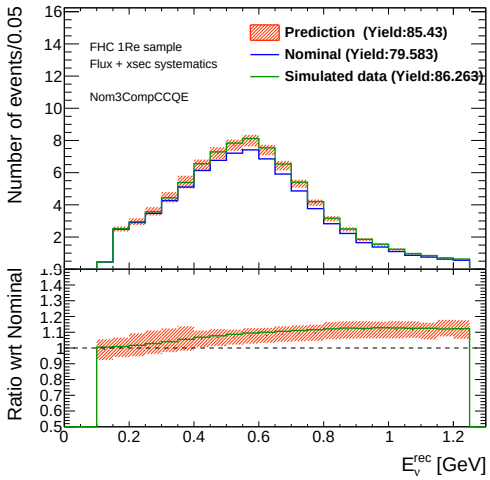

(b) ν mode 1Re

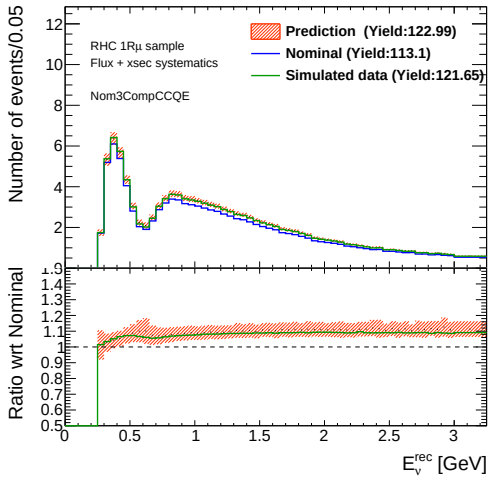

(c) $\bar{\nu}$ mode 1Rμ

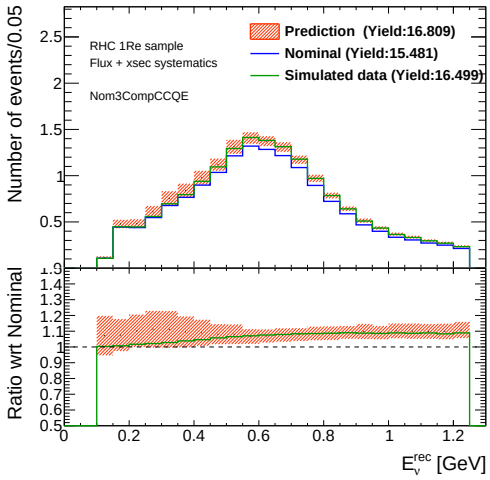

(d) $\bar{\nu}$ mode 1Re

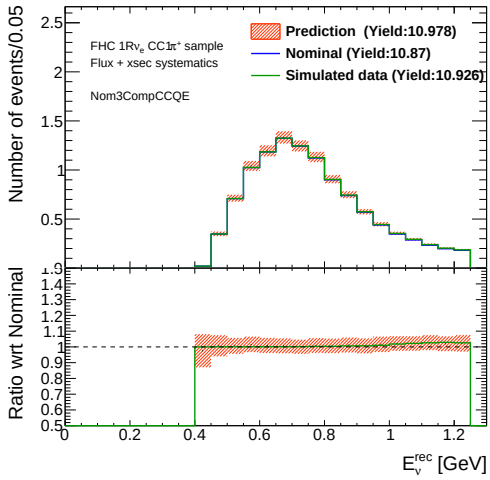

(e) ν mode 1Re1de

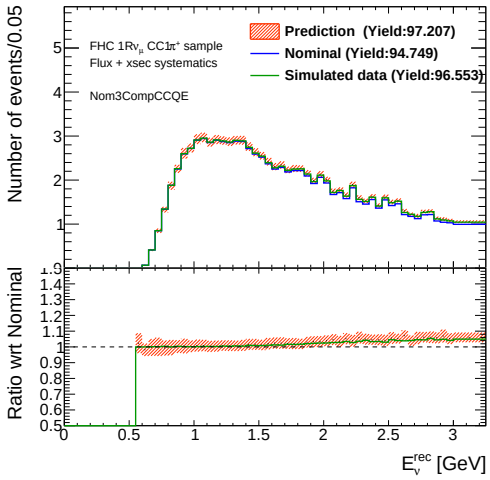

(f) ν mode CC1π multi-ring

Figure A.23: Comparison plots of the number of events between the nominal far detector sample (blue solid line), the simulated data of the alternative model (green solid line) and the prediction from the near detector fit (red band) as a function of the reconstructed neutrino energy. The bottom insets show the ratio of data to simulation.

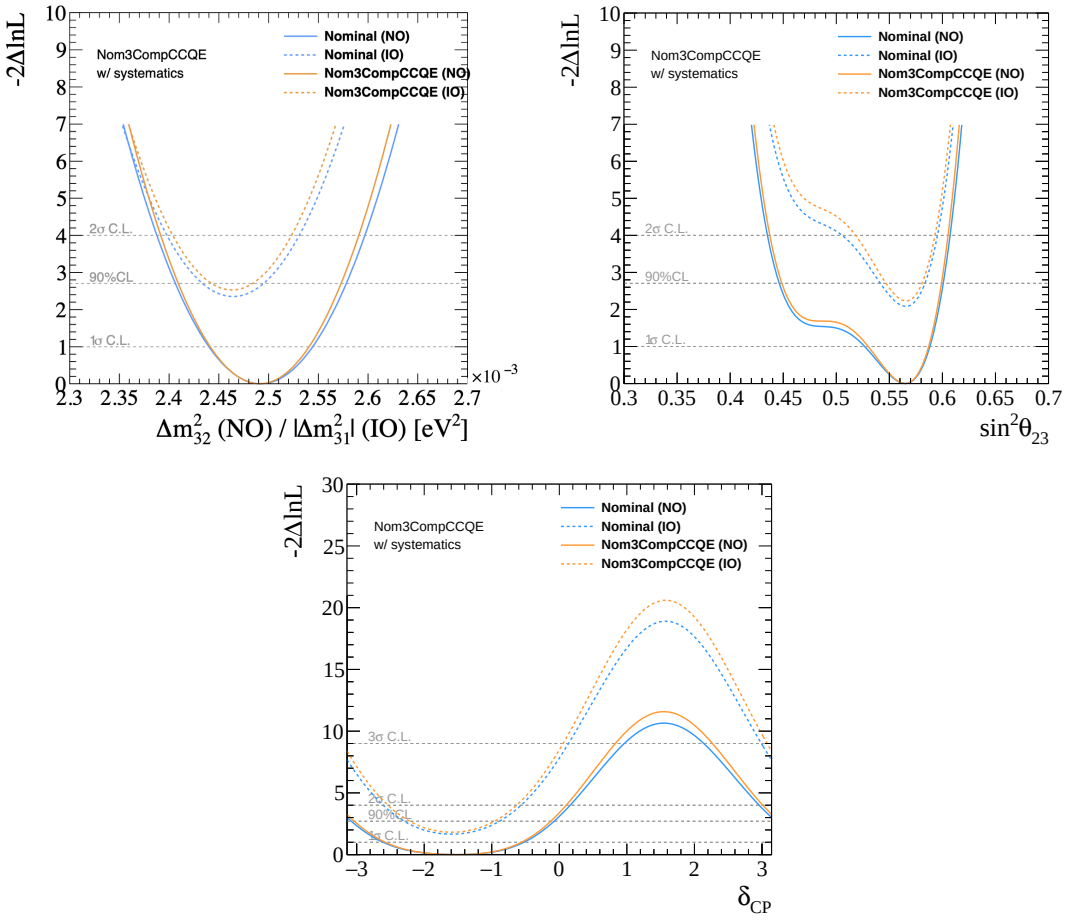

Figure A.24: Comparison of likelihood surface for Δm^2_{32}, $\sin^2\theta_{23}$ and δ_{CP}. Orange lines show those from the nominal 3Component robustness studies and blue lines show those of nominal MC for the normal and inverted mass orderings.

A.4.2 3Component $+1\sigma$

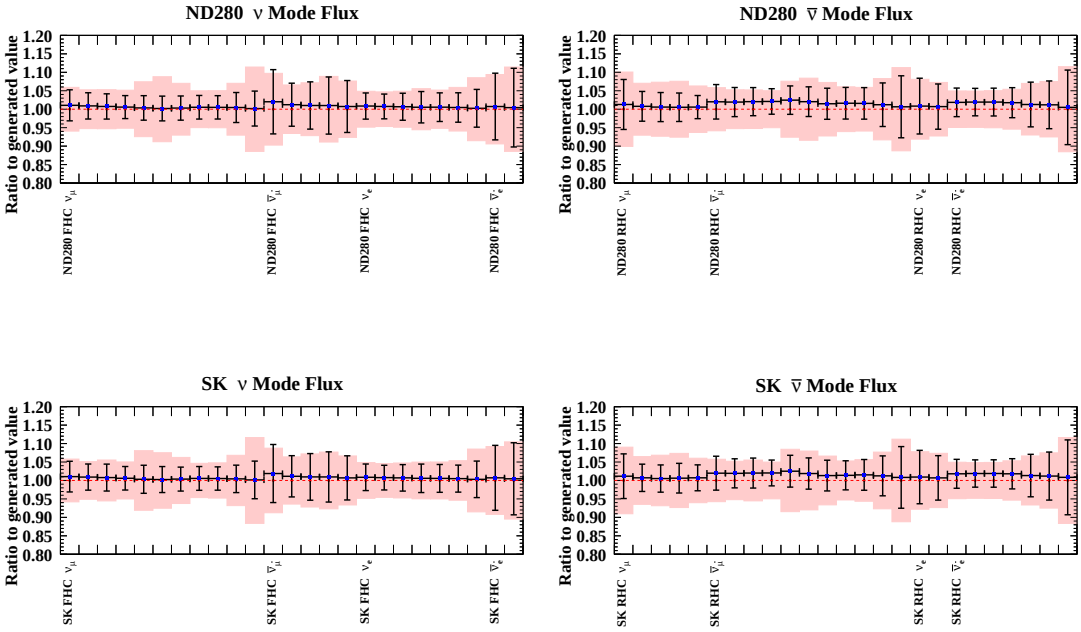

Figure A.25: Pre- (red band) and post-fit (blue dots and black error bands), flux parameters for the ν mode (left) and the $\bar{\nu}$ mode (right), and for the ND280 (top) and SK (bottom) from the near detector fit to the simulated data set of the $+1\sigma$ 3Component model.

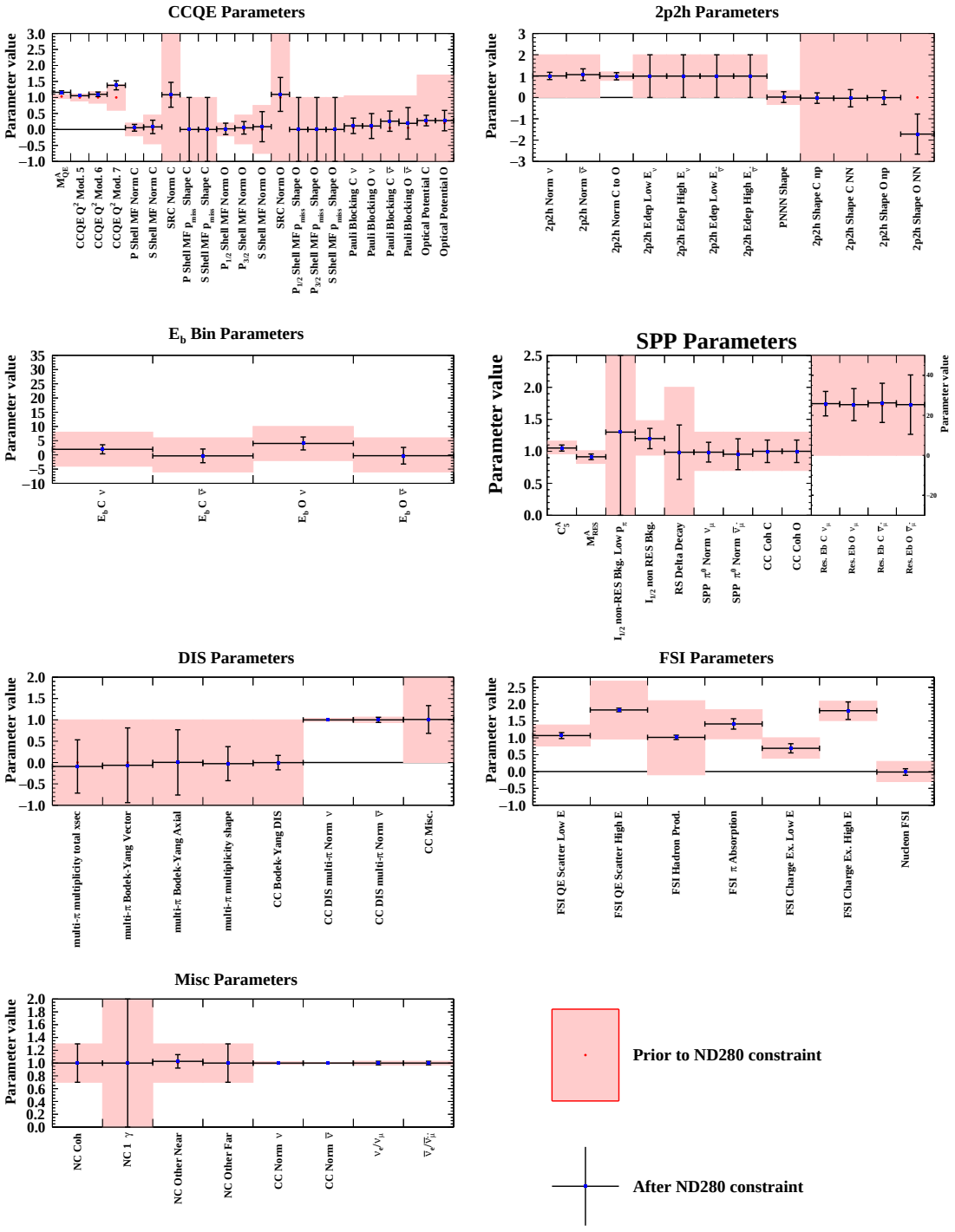

Figure A.26: Pre-(red band) and post-fit (blue dots and black error bands), cross-section parameters for CCQE, 2p2h, E_b, Single Pion Production (SPP), FSI, DIS, and misc from the near detector fit to the simulated data set of the $+1\sigma$ 3Component model.

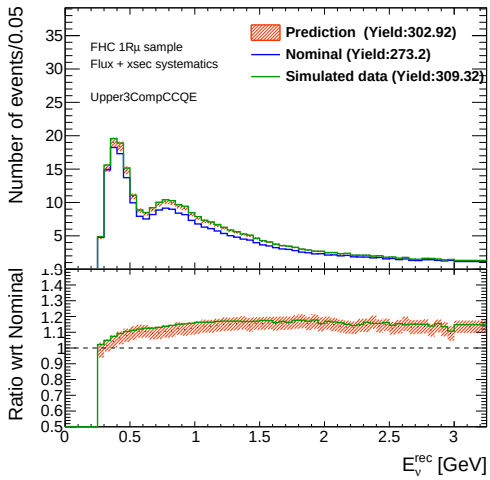

(a) ν mode 1Rμ

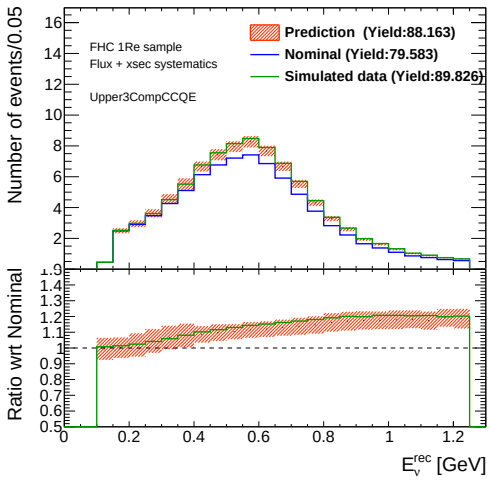

(b) ν mode 1Re

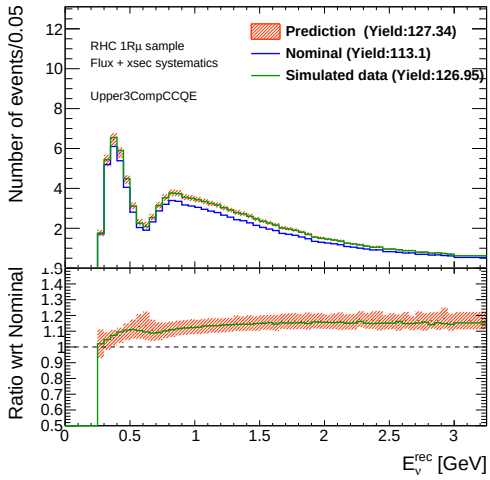

(c) $\bar{\nu}$ mode 1Rμ

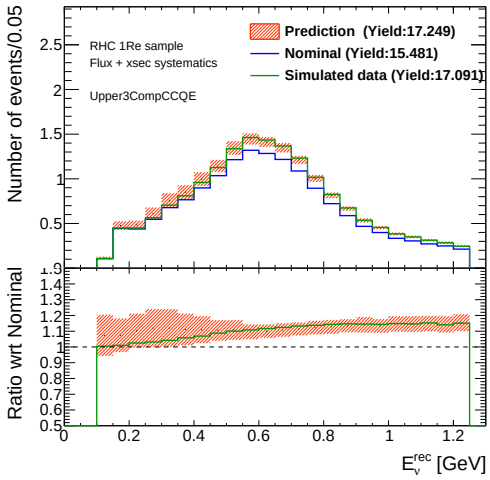

(d) $\bar{\nu}$ mode 1Re

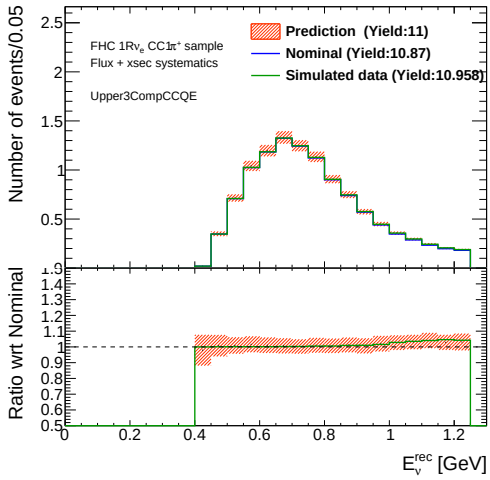

(e) ν mode 1Re1de

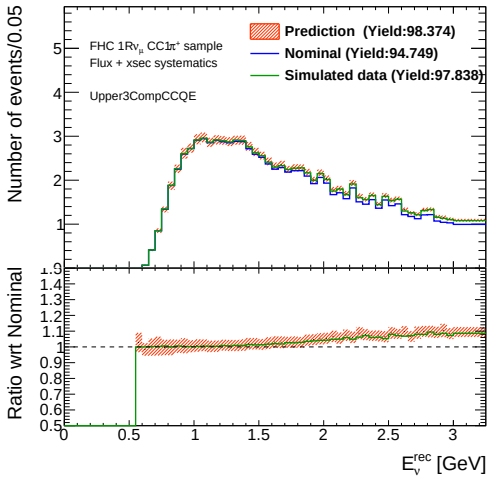

(f) ν mode CC1π multi-ring

Figure A.27: Comparison plots of the number of events between the nominal far detector sample (blue solid line), the simulated data of the alternative model (green solid line) and the prediction from the near detector fit (red band) as a function of the reconstructed neutrino energy. The bottom insets show the ratio of data to simulation.

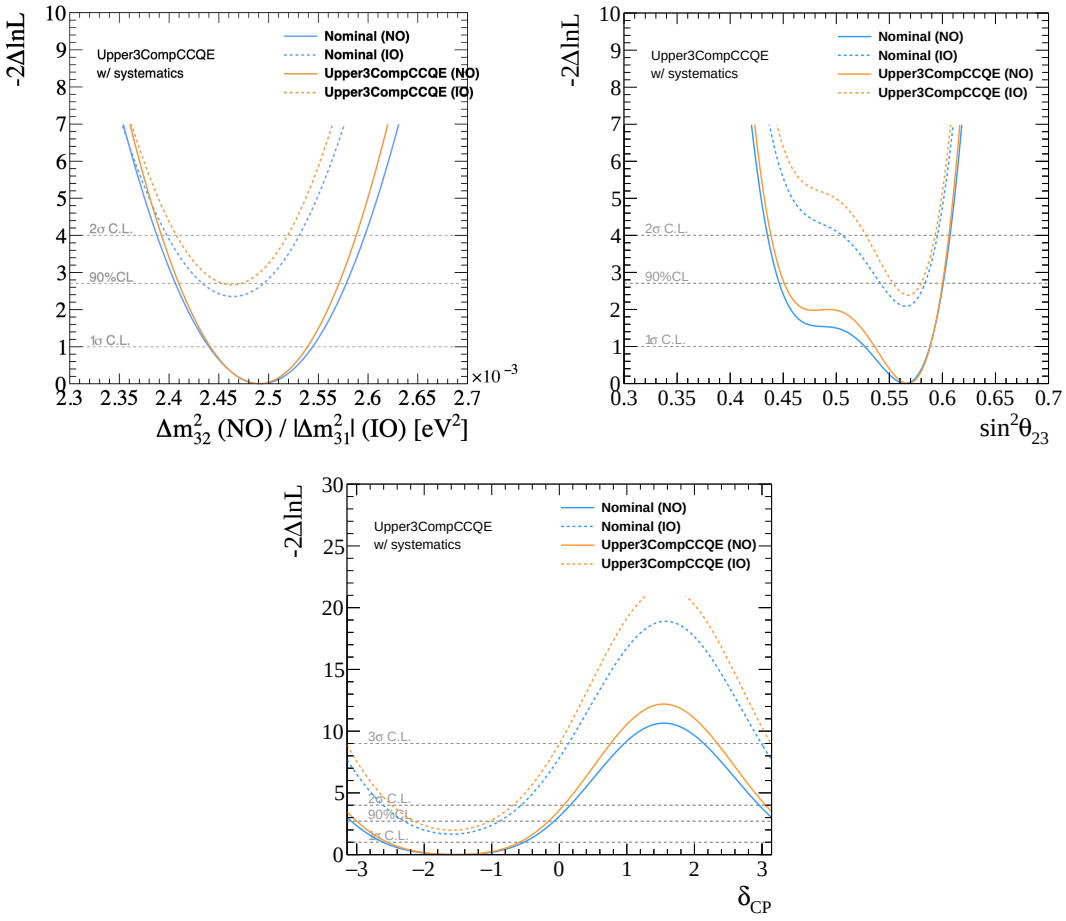

Figure A.28: Comparison of likelihood surface for Δm^2_{32}, $\sin^2\theta_{23}$ and δ_{CP}. Orange lines show those from $+1\sigma$ 3Component robustness studies and blue lines show those of nominal MC for the normal and inverted mass orderings.

A.4.3 3Component -1σ

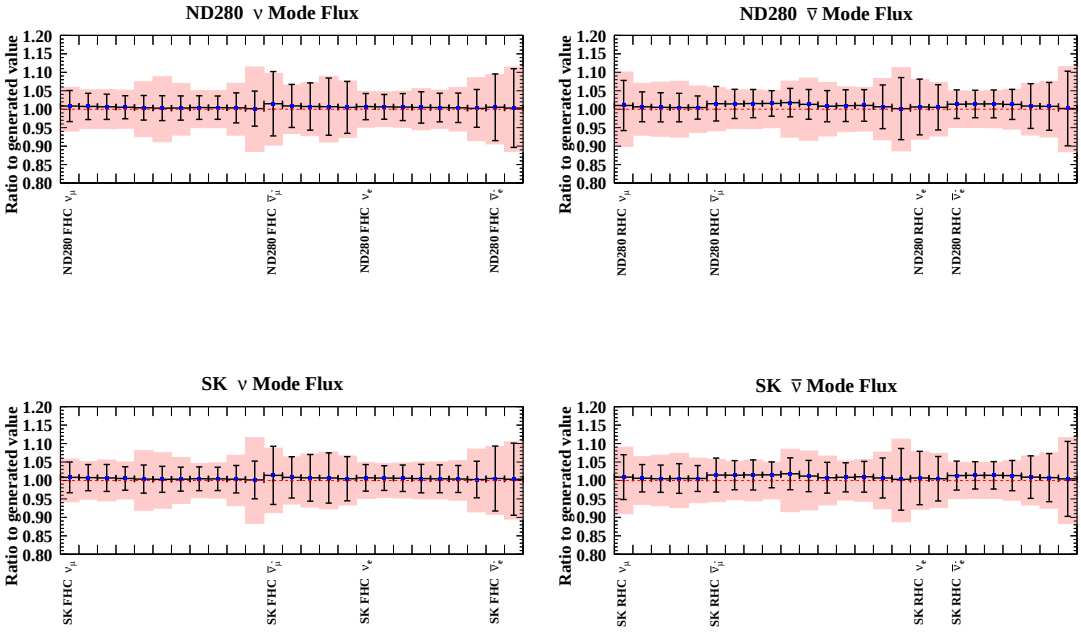

Figure A.29: Pre- (red band) and post-fit (blue dots and black error bands), flux parameters for the ν mode (left) and the $\bar{\nu}$ mode (right), and for the ND280 (top) and SK (bottom) from the near detector fit to the simulated data set of the -1σ 3Component model.

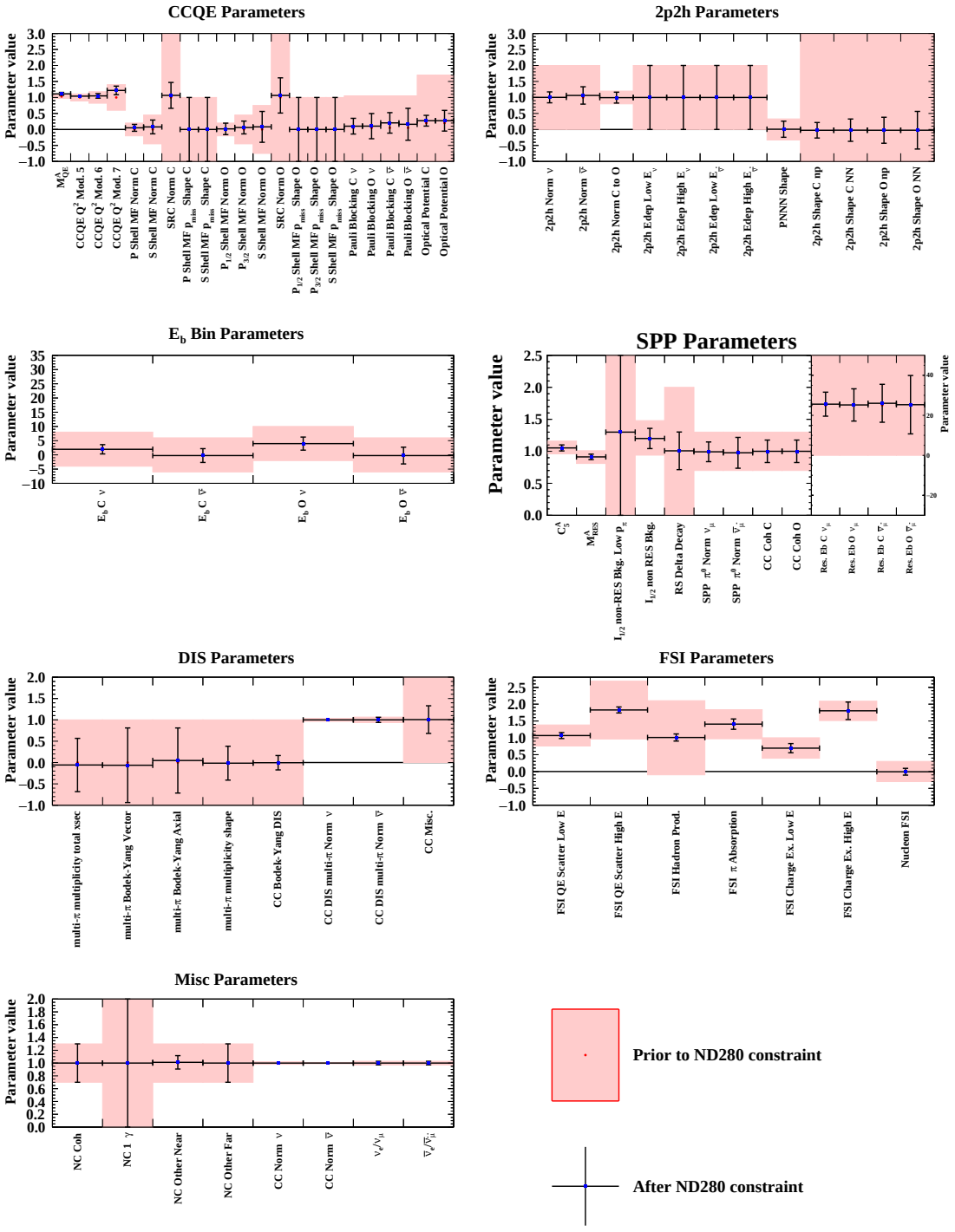

Figure A.30: Pre-(red band) and post-fit (blue dots and black error bands), cross-section parameters for CCQE, 2p2h, E_b, Single Pion Production (SPP), FSI, DIS, and misc from the near detector fit to the simulated data set of the -1σ 3Component model.

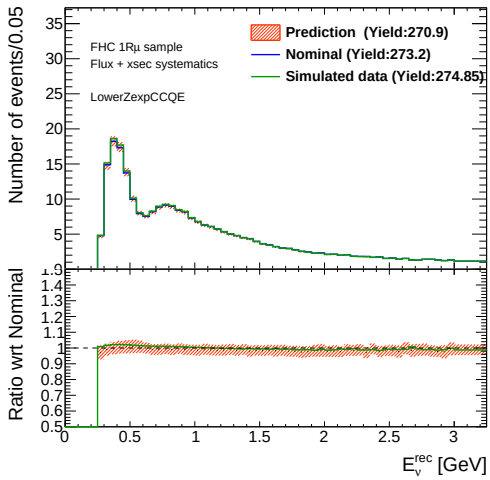

(a) ν mode 1Rμ

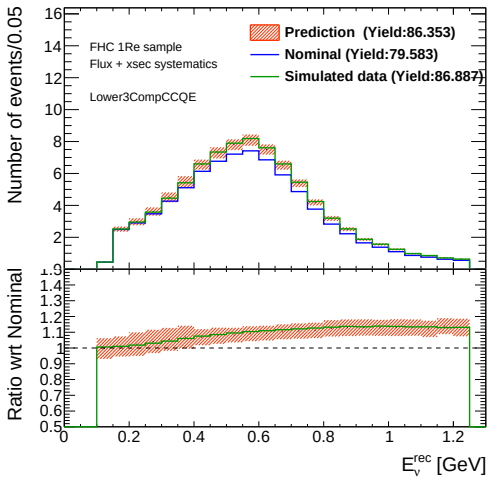

(b) ν mode 1Re

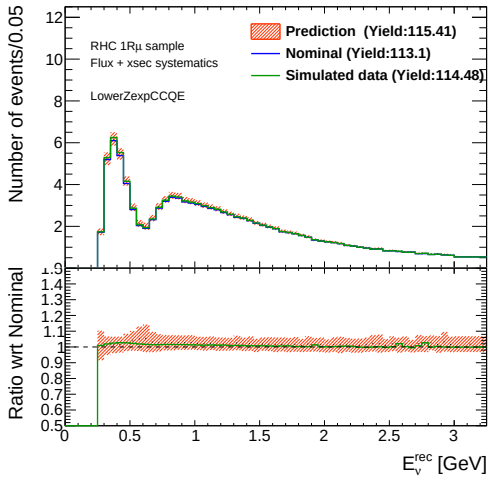

(c) $\bar{\nu}$ mode 1Rμ

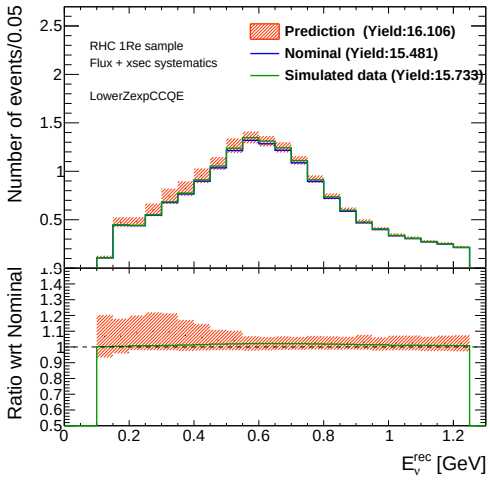

(d) $\bar{\nu}$ mode 1Re

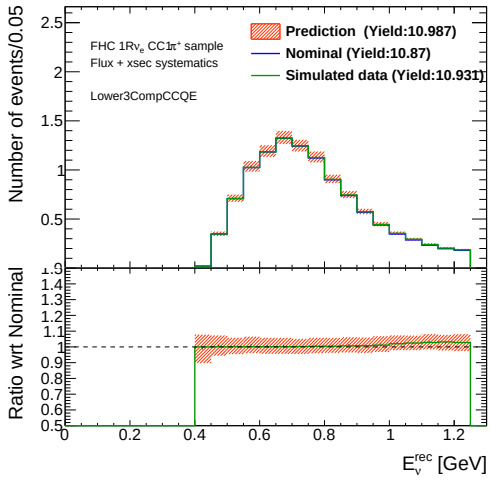

(e) ν mode 1Re1de

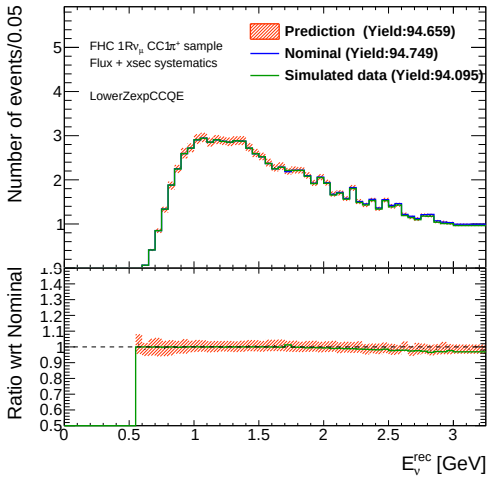

(f) ν mode CC1π multi-ring

Figure A.31: Comparison plots of the number of events between the nominal far detector sample (blue solid line), the simulated data of the alternative model (green solid line) and the prediction from the near detector fit (red band) as a function of the reconstructed neutrino energy. The bottom insets show the ratio of data to simulation.

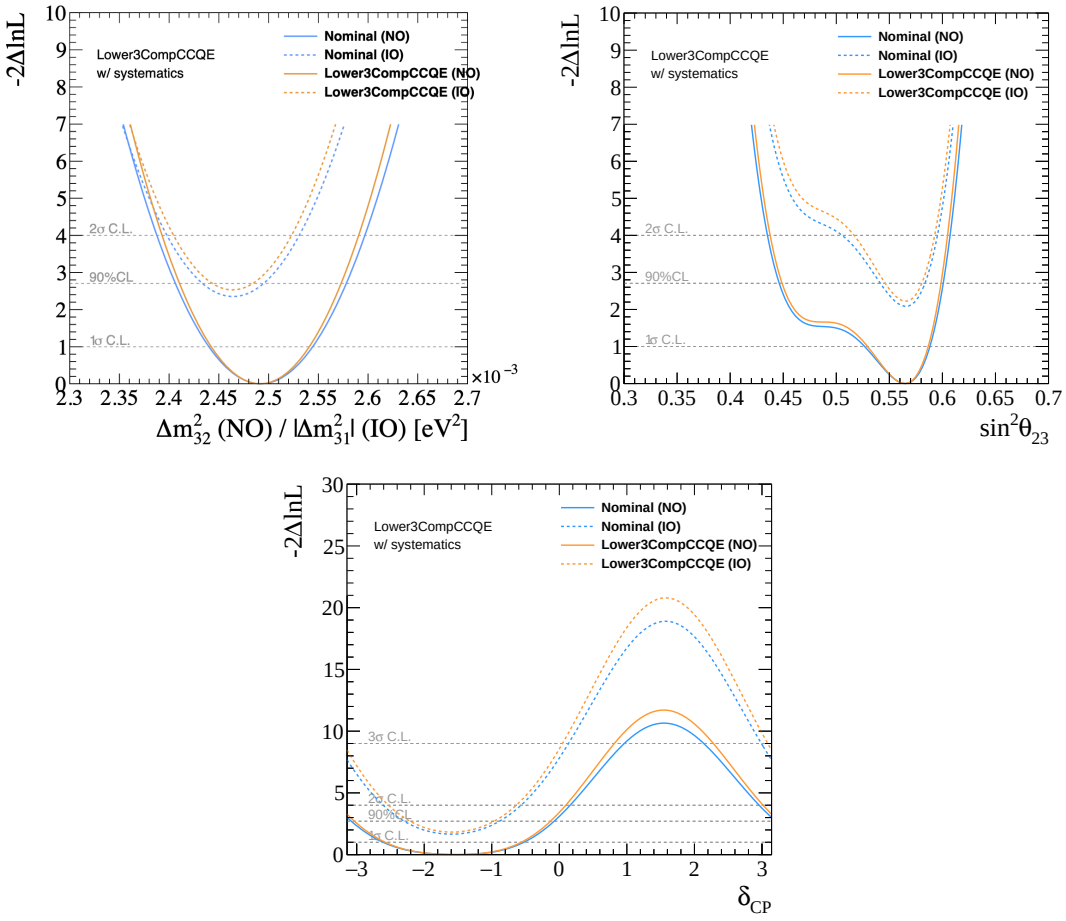

Figure A.32: Comparison of likelihood surface for Δm^2_{32}, $\sin^2\theta_{23}$ and δ_{CP}. Orange lines show those from -1σ 3Component robustness studies and blue lines show those of nominal MC for the normal and inverted mass orderings.

A.5 Martini Model

This model is related to the single pion production process as discussed in Sec. 3.4.3. Figures A.33 and A.34 show fitting results of the cross section and flux parameters using this alternative model. Several parameters which is related to the single pion production process move slightly as expected. Using the covariance matrices which are based on that near detector fit, we made the reconstructed neutrino energy prediction at the far detector as shown in Fig. A.35. The near detector fit predictions cover the simulated data lines well.

Figure A.36 shows the fit results for three oscillation parameters. There is no large bias which should be considered as the systematic errors following the criteria discussed in Sec. 6.3.

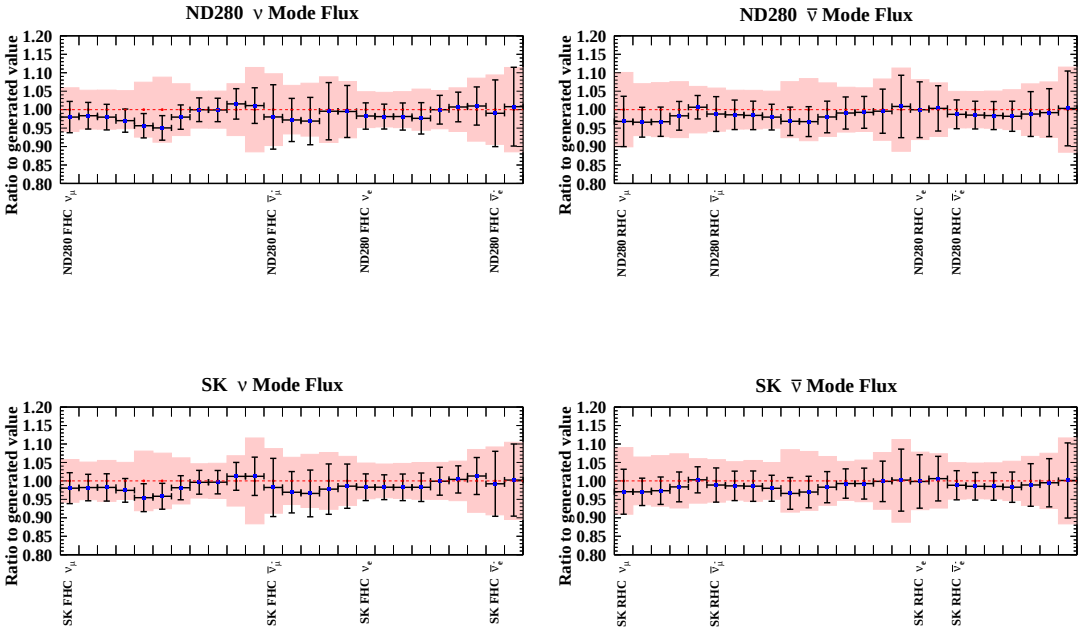

Figure A.33: Pre- (red band) and post-fit (blue dots and black error bands), flux parameters for the ν mode (left) and the $\bar{\nu}$ mode (right), and for the ND280 (top) and SK (bottom) from the near detector fit to the simulated data set of Martini model.

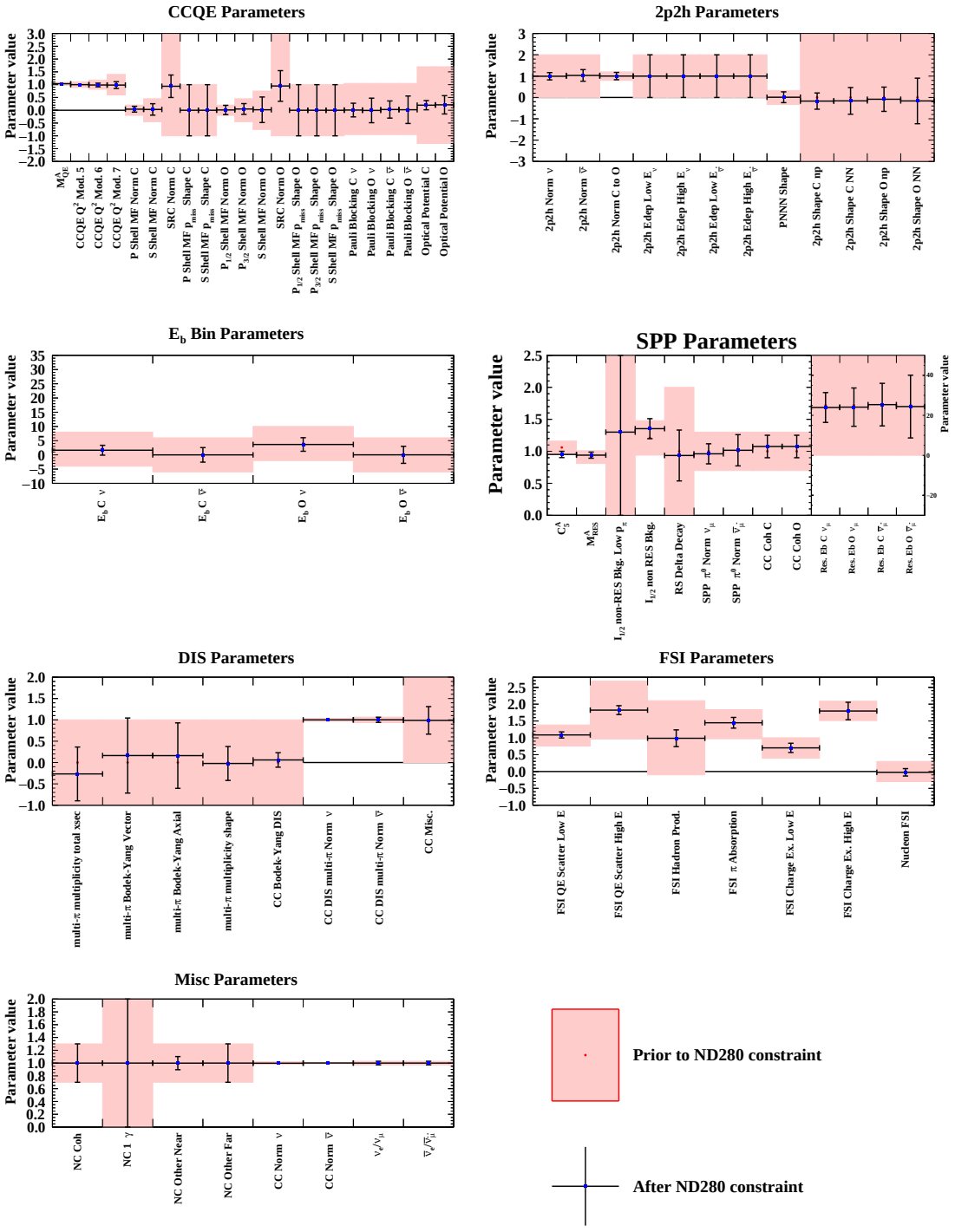

Figure A.34: Pre-(red band) and post-fit (blue dots and black error bands), cross-section parameters for CCQE, 2p2h, E_b, Single Pion Production (SPP), FSI, DIS, and misc from the near detector fit to the simulated data set of Martini model.

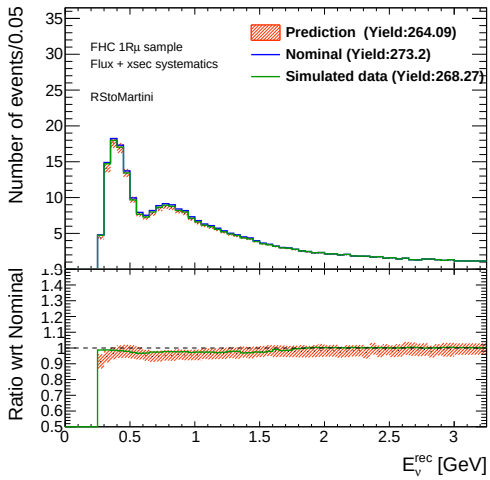

(a) ν mode 1Rμ

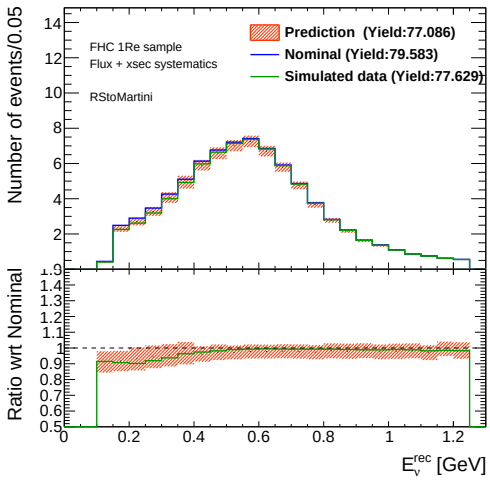

(b) ν mode 1Re

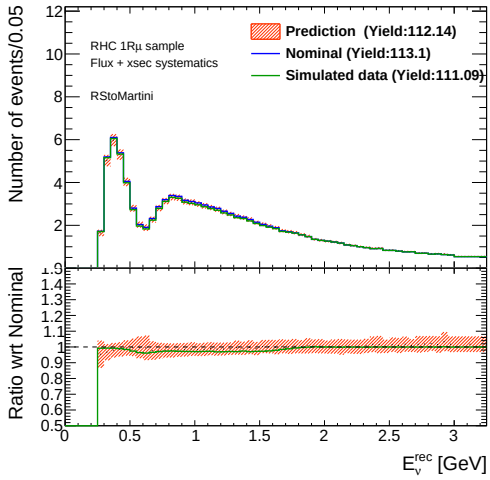

(c) $\bar{\nu}$ mode 1Rμ

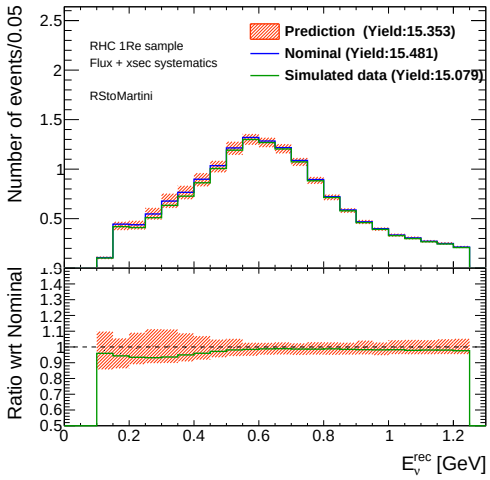

(d) $\bar{\nu}$ mode 1Re

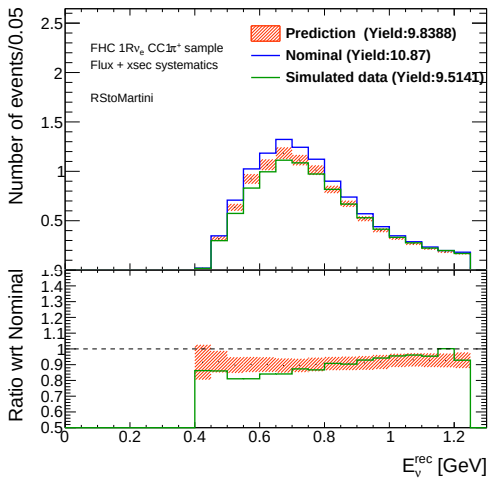

(e) ν mode 1Re1de

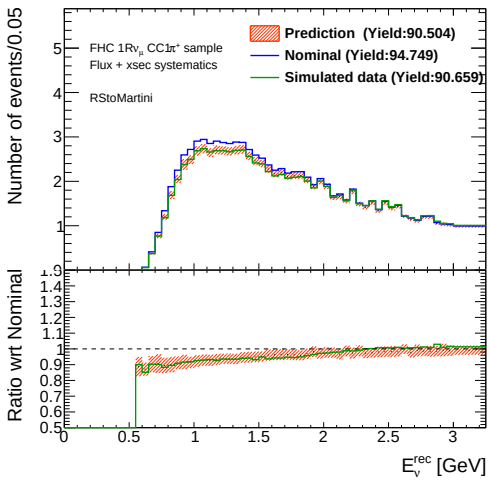

(f) ν mode CC1π multi-ring

Figure A.35: Comparison plots of the number of events between the nominal far detector sample (blue solid line), the simulated data of the alternative model (green solid line) and the prediction from the near detector fit (red band) as a function of the reconstructed neutrino energy. The bottom insets show the ratio of data to simulation.

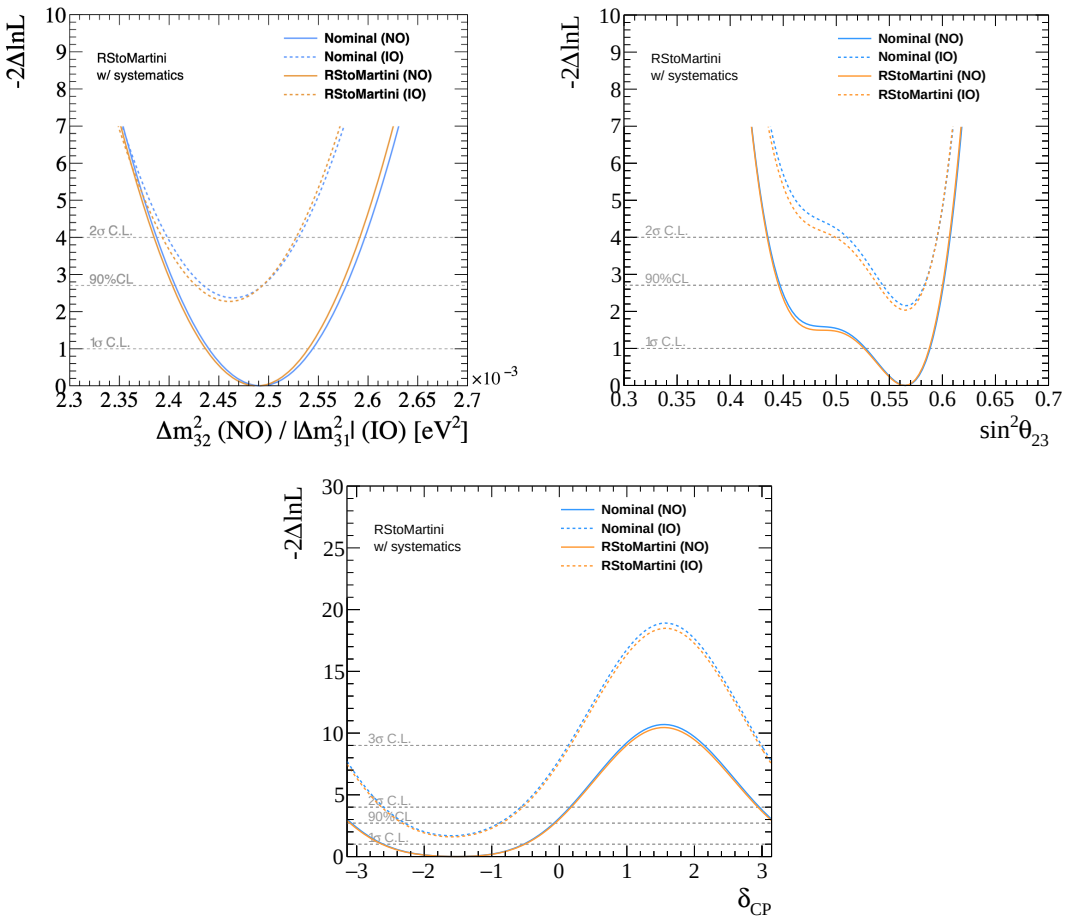

Figure A.36: Comparison of likelihood surface for Δm^2_{32}, $\sin^2\theta_{23}$ and δ_{CP}. Orange lines show those from Martini robustness studies and blue lines show those of nominal MC for the normal and inverted mass orderings.

A.6 Data-driven Model Focusing on Pion Kinematics

This model is related to the difficulties of the predictions for the pion kinematics distributions in the current near detector fit as discussed in Sec. 6.1.3. Figures A.37 and A.38 show fitting results of the cross section and flux parameters using this alternative model. Several parameters which is related to the single pion production process move slightly as expected as with the Martini model. Using the covariance matrices which are based on that near detector fit, we made the reconstructed neutrino energy prediction at the far detector as shown in Fig. A.39. The near detector fit predictions cover the simulated data lines well.

Figure A.40 shows the fit results for three oscillation parameters. There is no large bias which should be considered as the systematic errors following the criteria discussed in Sec. 6.3.

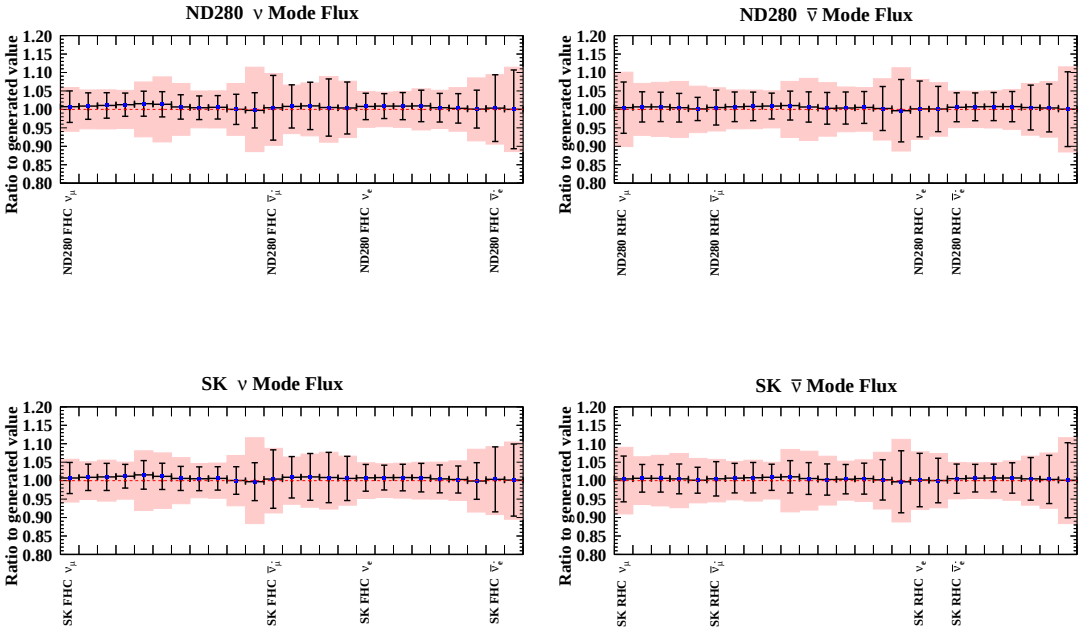

Figure A.37: Pre- (red band) and post-fit (blue dots and black error bands), flux parameters for the ν mode (left) and the $\bar{\nu}$ mode (right), and for the ND280 (top) and SK (bottom) from the near detector fit to the simulated data set of data-driven model focusing on pion kinematics.

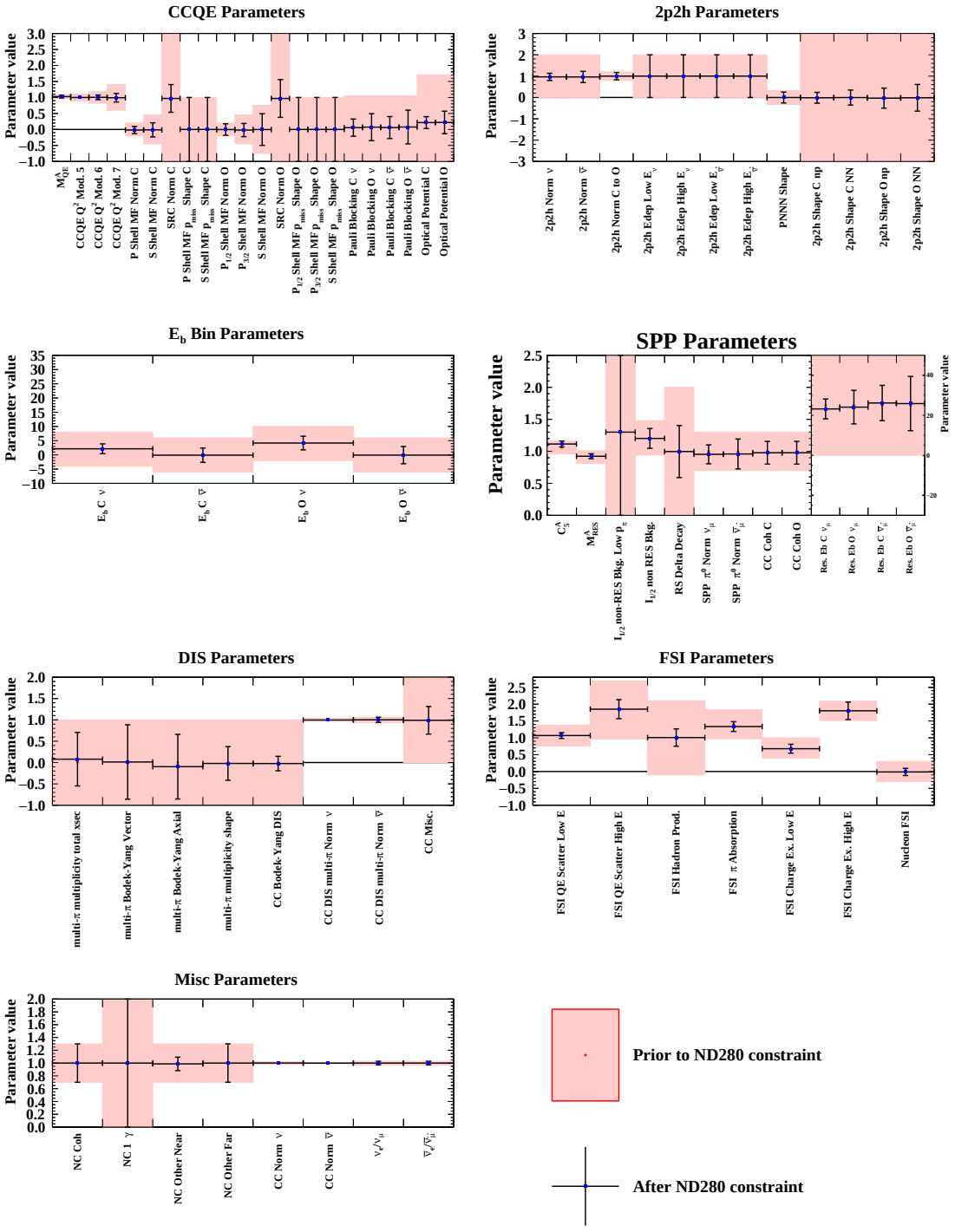

Figure A.38: Pre-(red band) and post-fit (blue dots and black error bands), cross-section parameters for CCQE, 2p2h, E_b, Single Pion Production (SPP), FSI, DIS, and misc from the near detector fit to the simulated data set of data-driven model focusing on pion kinematics.

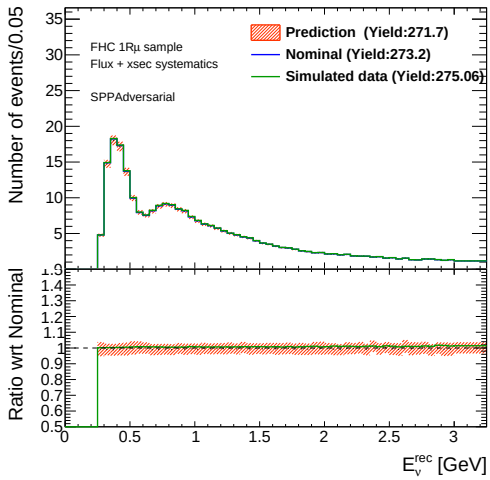

(a) ν mode 1Rμ

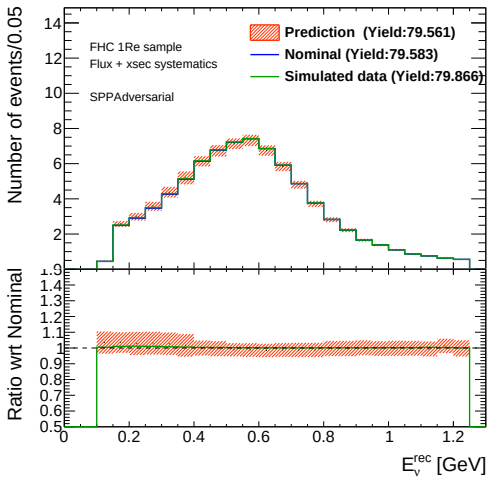

(b) ν mode 1Re

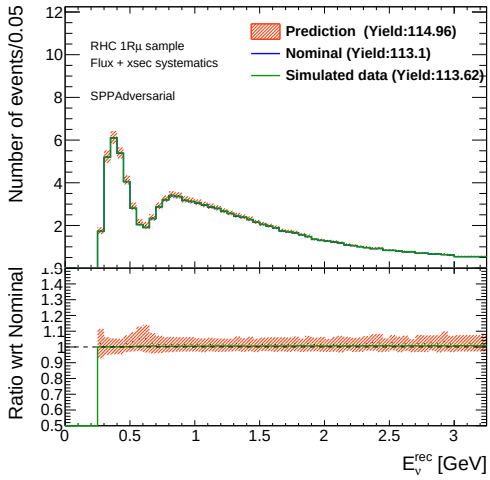

(c) $\bar{\nu}$ mode 1Rμ

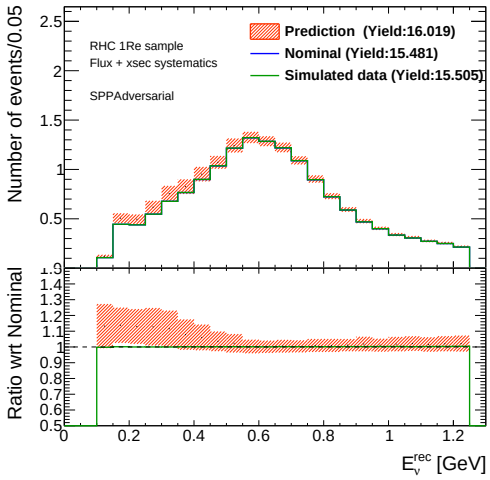

(d) $\bar{\nu}$ mode 1Re

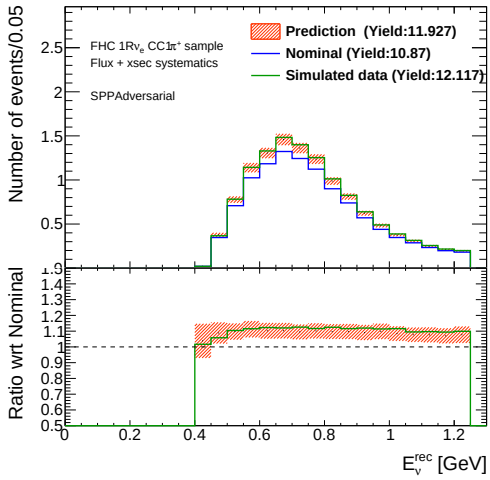

(e) ν mode 1Re1de

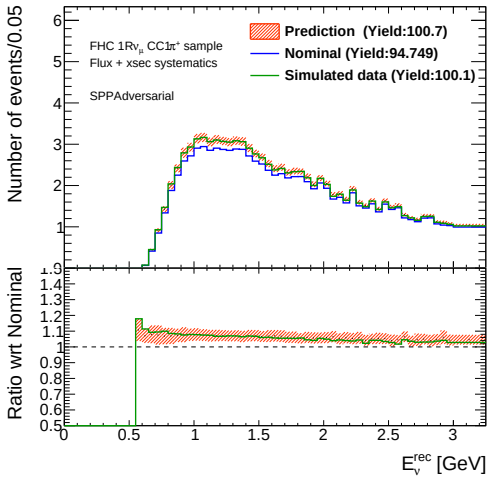

(f) ν mode CC1π multi-ring

Figure A.39: Comparison plots of the number of events between the nominal far detector sample (blue solid line), the simulated data of the alternative model (green solid line) and the prediction from the near detector fit (red band) as a function of the reconstructed neutrino energy. The bottom insets show the ratio of data to simulation.

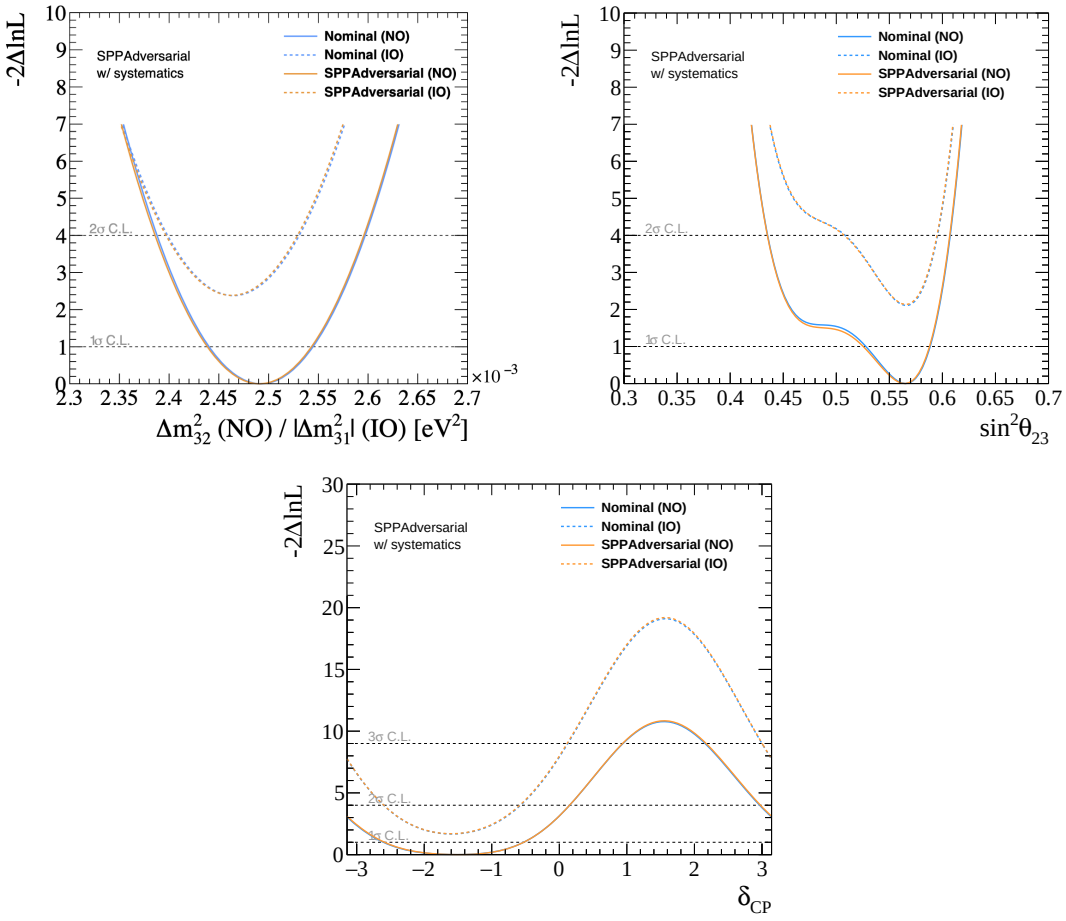

Figure A.40: Comparison of likelihood surface for Δm^2_{32}, $\sin^2\theta_{23}$ and δ_{CP}. Orange lines show those from robustness studies of data-driven model focusing on pion kinematics alternation and blue lines show those of nominal MC for the normal and inverted mass orderings.

A.7 Pion Kinematics Alternation Related to $\Delta(1232)$ Resonance

This section summarize the results of the fit to the simulated datasets with the pion kinematics alternation discussed in Sec. 3.4.3. We produced the two simulated data sets ($\pm 1\sigma$) based on the variation due to the theoretical analysis. Figures A.41, A.42, A.45 and A.46 show fitting results of the cross section and flux parameters using this alternative model. We could see the shifts of the high Q^2 parameters as expected. Using the covariance matrices which are based on that near detector fit, we made the reconstructed neutrino energy prediction at the far detector as shown in Figs. A.43 and A.47. The near detector fit predictions cover the simulated data lines well.

Figures A.44 and A.48 show the fit results for three oscillation parameters. There is no large bias which should be considered as the systematic errors following the criteria discussed in Sec. 6.3.

A.7.1 Pion Kinematics Alternation Related to $\Delta(1232)$ Resonance $+1\sigma$

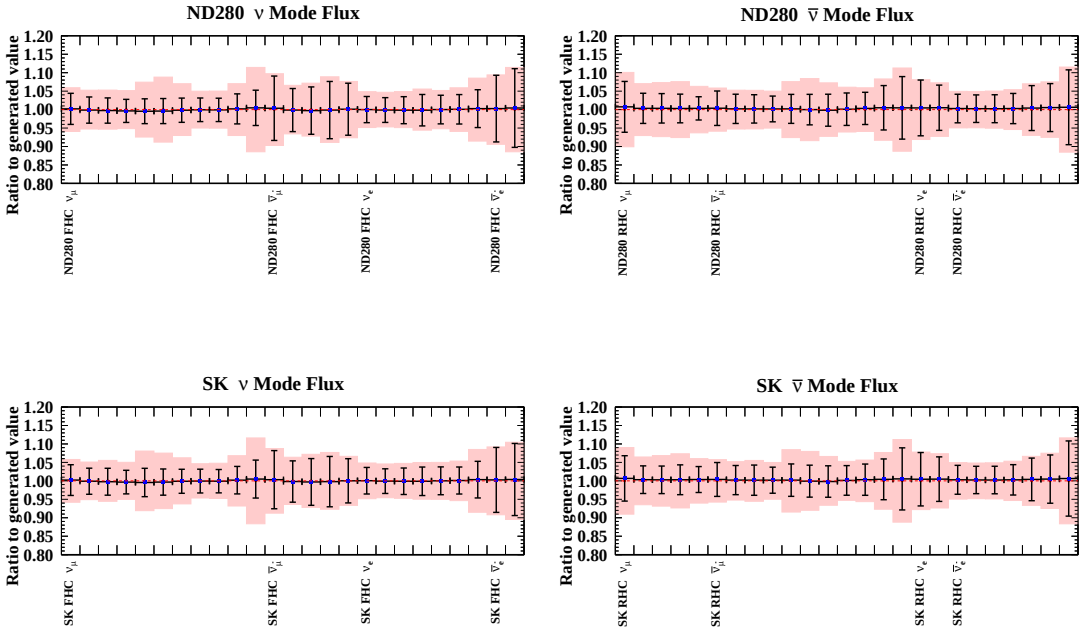

Figure A.41: Pre- (red band) and post-fit (blue dots and black error bands), flux parameters for the ν mode (left) and the $\bar{\nu}$ mode (right), and for the ND280 (top) and SK (bottom) from the near detector fit to the simulated data set of $+1\sigma$ pion kinematics alternation.

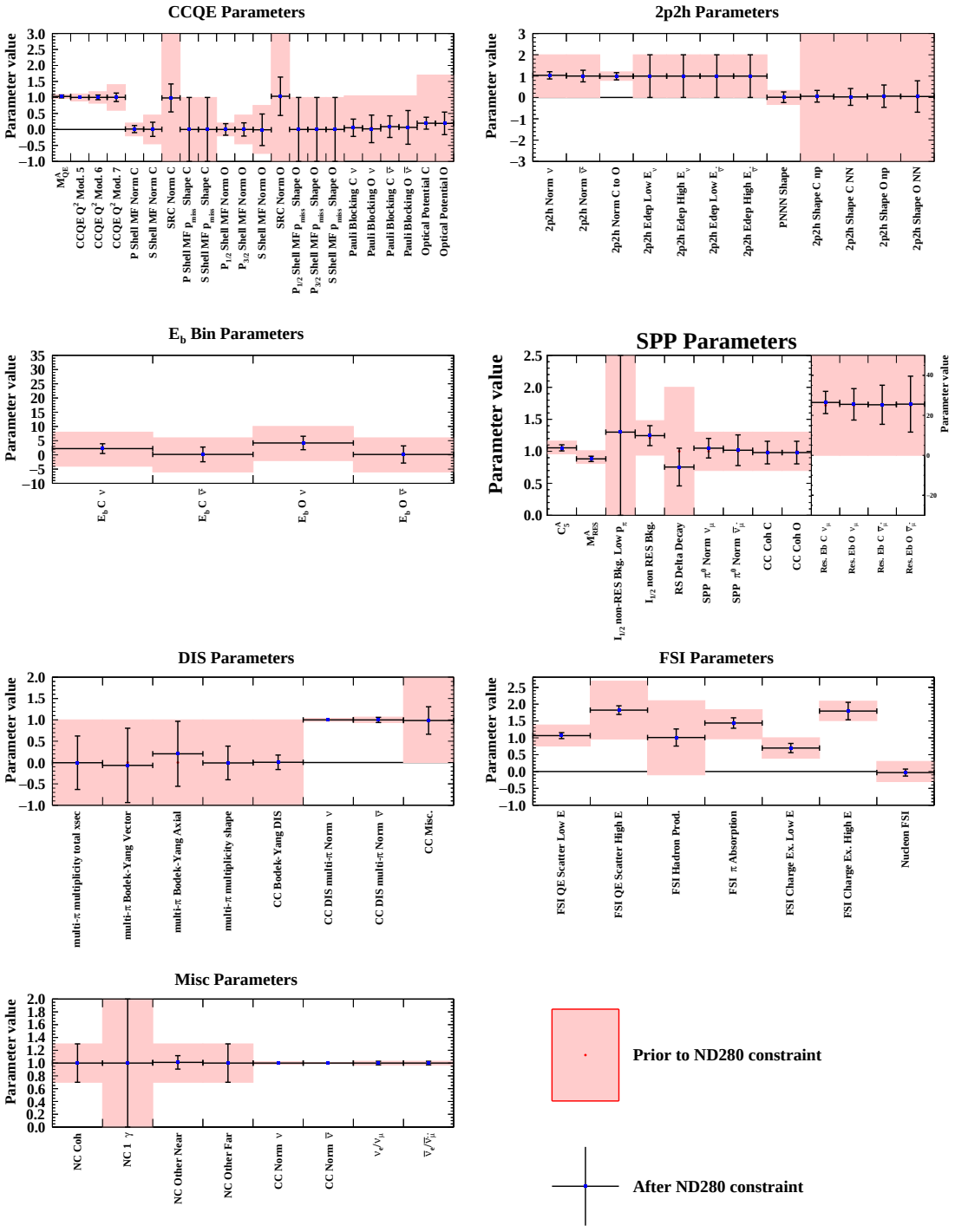

Figure A.42: Pre-(red band) and post-fit (blue dots and black error bands), cross-section parameters for CCQE, 2p2h, E_b, Single Pion Production (SPP), FSI, DIS, and misc from the near detector fit to the simulated data set of $+1\sigma$ pion kinematics alternation.

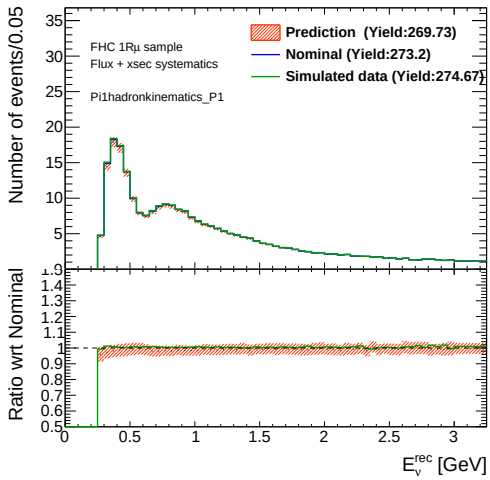

(a) ν mode 1Rμ

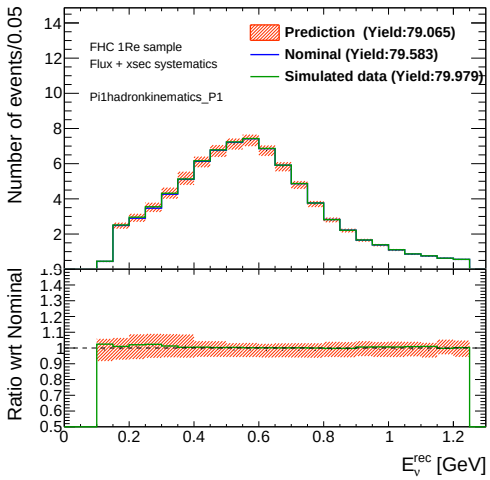

(b) ν mode 1Re

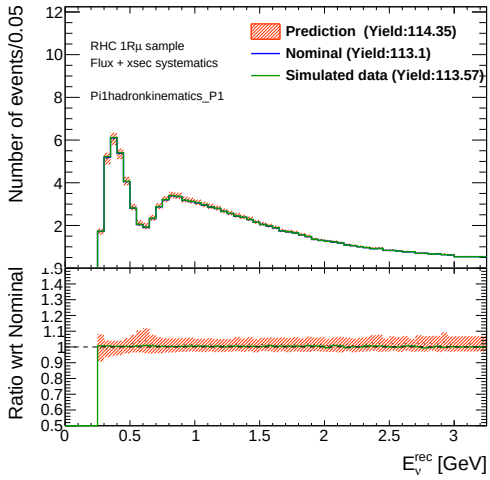

(c) $\bar{\nu}$ mode 1Rμ

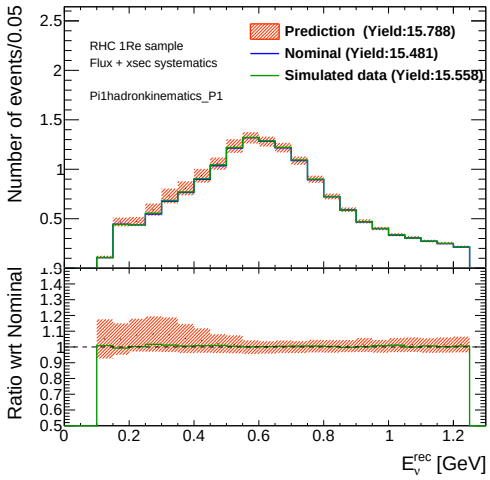

(d) $\bar{\nu}$ mode 1Re

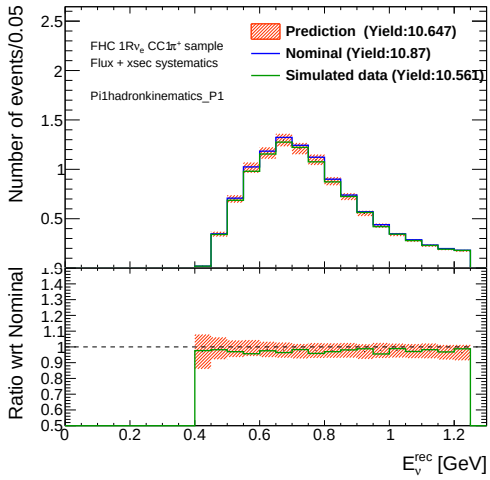

(e) ν mode 1Re1de

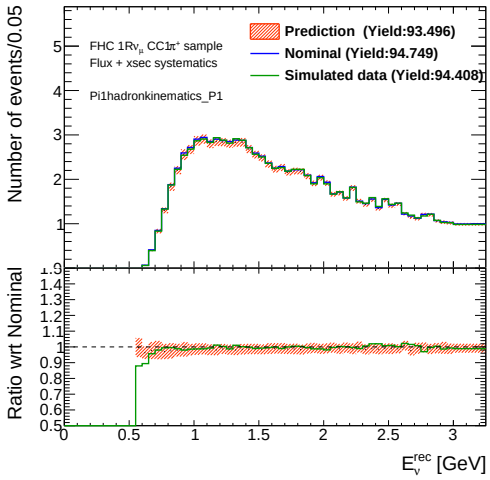

(f) ν mode CC1π multi-ring

Figure A.43: Comparison plots of the number of events between the nominal far detector sample (blue solid line), the simulated data of the alternative model (green solid line) and the prediction from the near detector fit (red band) as a function of the reconstructed neutrino energy. The bottom insets show the ratio of data to simulation.

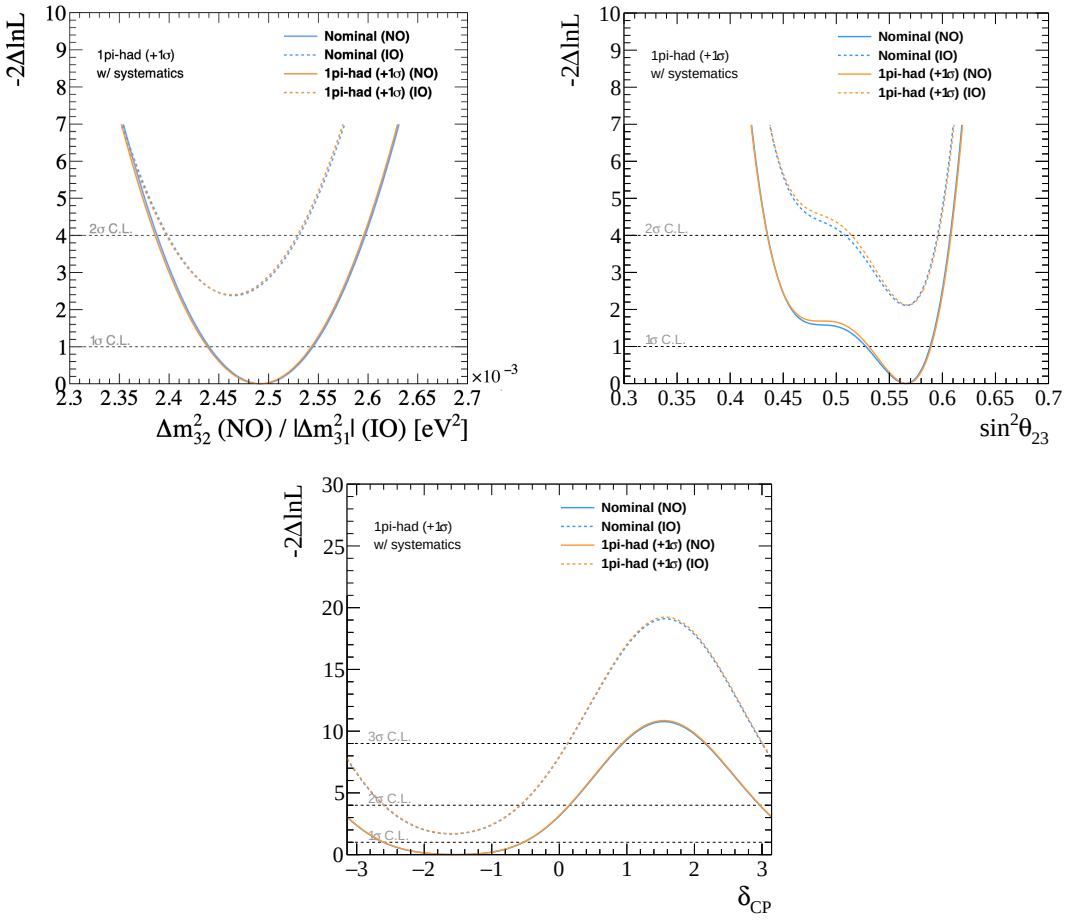

Figure A.44: Comparison of likelihood surface for Δm^2_{32}, $\sin^2\theta_{23}$ and δ_{CP}. Orange lines show those from $+1\sigma$ pion hadron kinematics alternation robustness studies and blue lines show those of nominal MC for the normal and inverted mass orderings.

A.7.2 Pion Kinematics Alternation Related to $\Delta(1232)$ Resonance -1σ

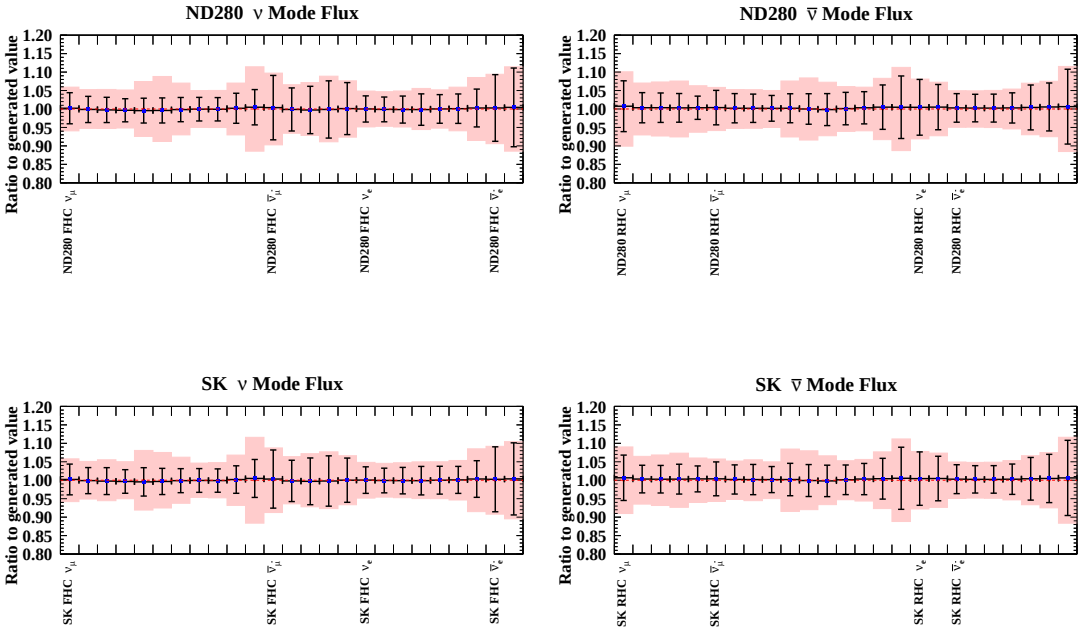

Figure A.45: Pre- (red band) and post-fit (blue dots and black error bands), flux parameters for the ν mode (left) and the $\bar{\nu}$ mode (right), and for the ND280 (top) and SK (bottom) from the near detector fit to the simulated data set of -1σ pion kinematics alternation.

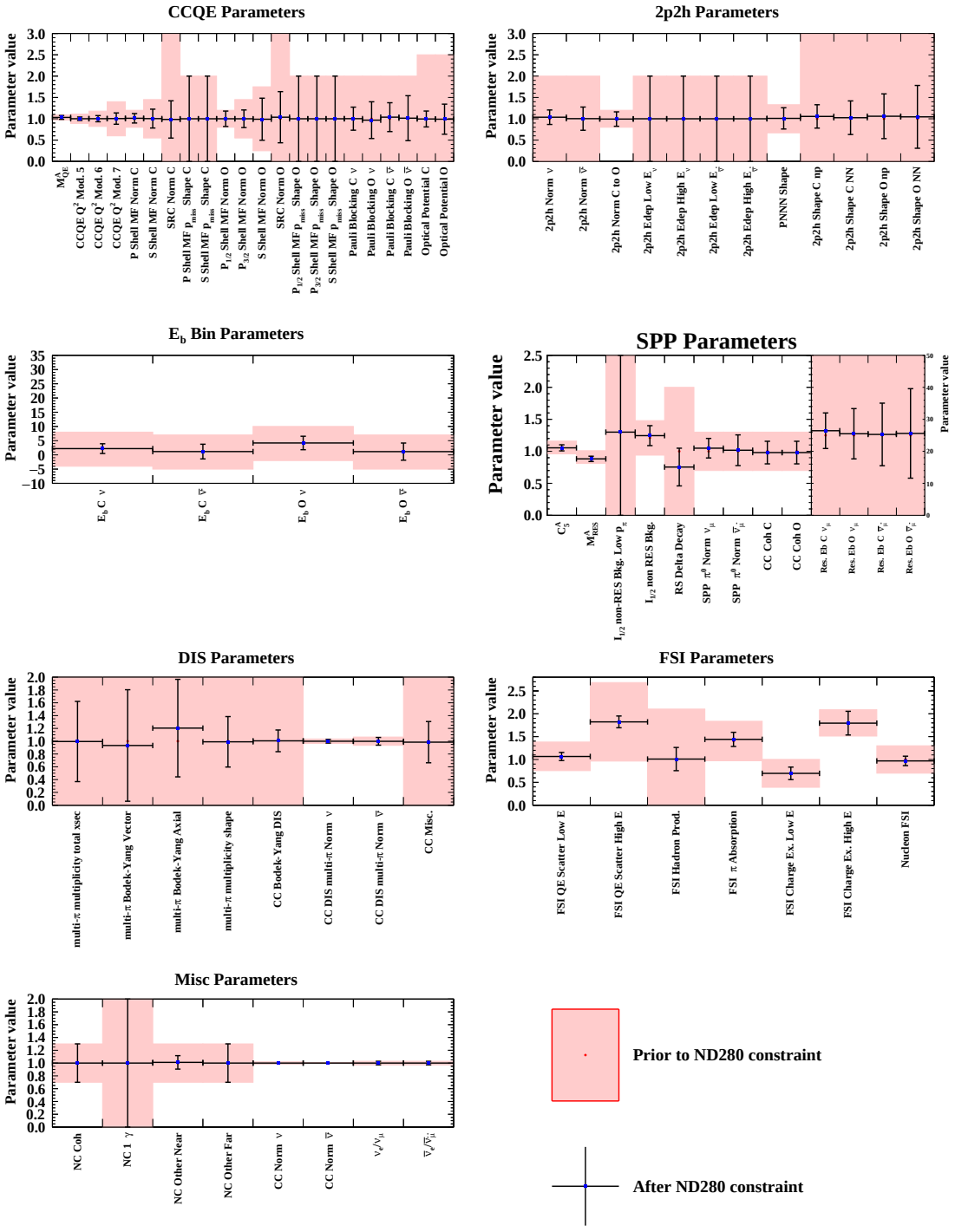

Figure A.46: Pre-(red band) and post-fit (blue dots and black error bands), cross-section parameters for CCQE, 2p2h, E_b, Single Pion Production (SPP), FSI, DIS, and misc from the near detector fit to the simulated data set of -1σ pion kinematics alternation.

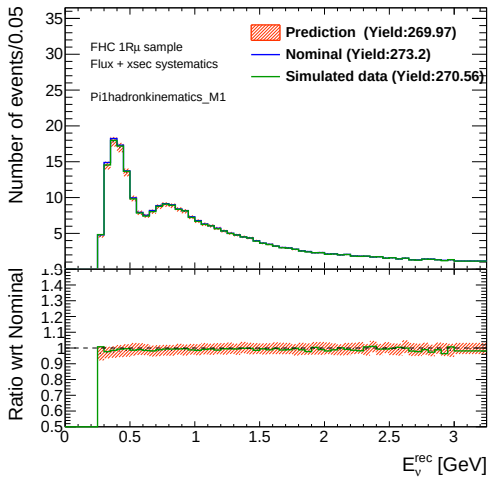

(a) ν mode 1Rμ

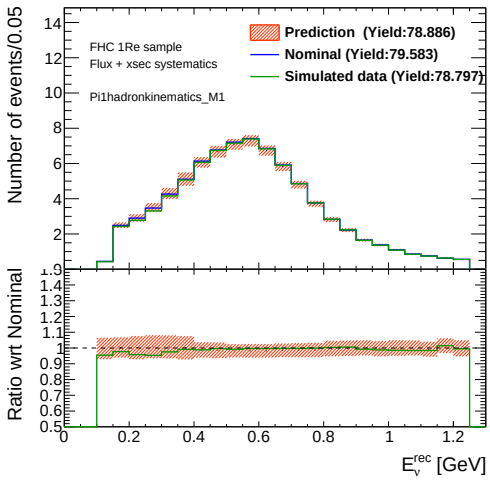

(b) ν mode 1Re

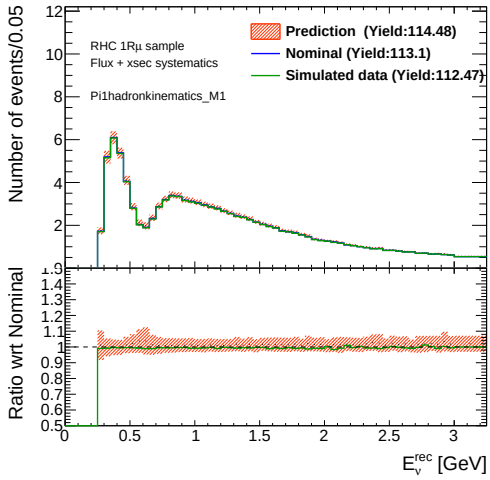

(c) $\bar{\nu}$ mode 1Rμ

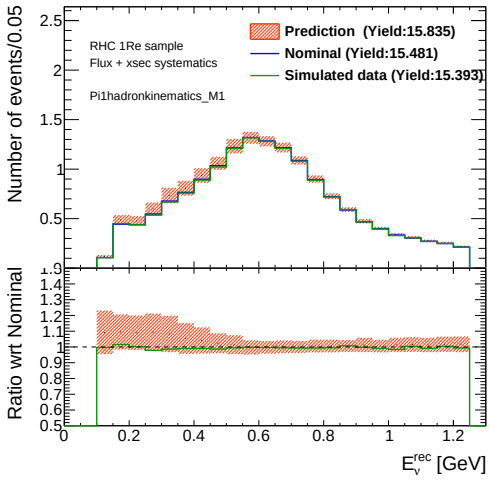

(d) $\bar{\nu}$ mode 1Re

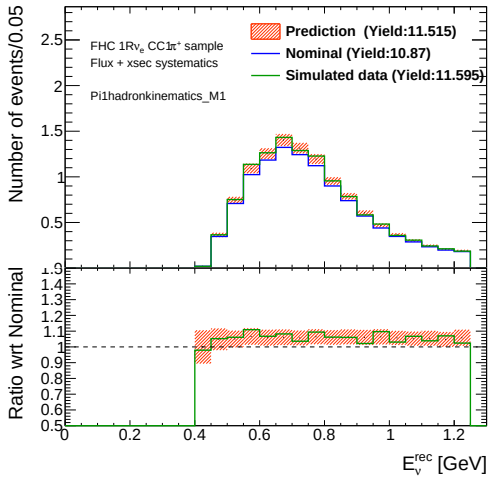

(e) ν mode 1Re1de

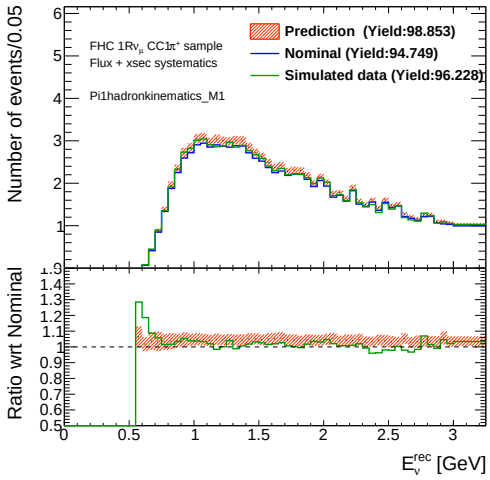

(f) ν mode CC1π multi-ring

Figure A.47: Comparison plots of the number of events between the nominal far detector sample (blue solid line), the simulated data of the alternative model (green solid line) and the prediction from the near detector fit (red band) as a function of the reconstructed neutrino energy. The bottom insets show the ratio of data to simulation.

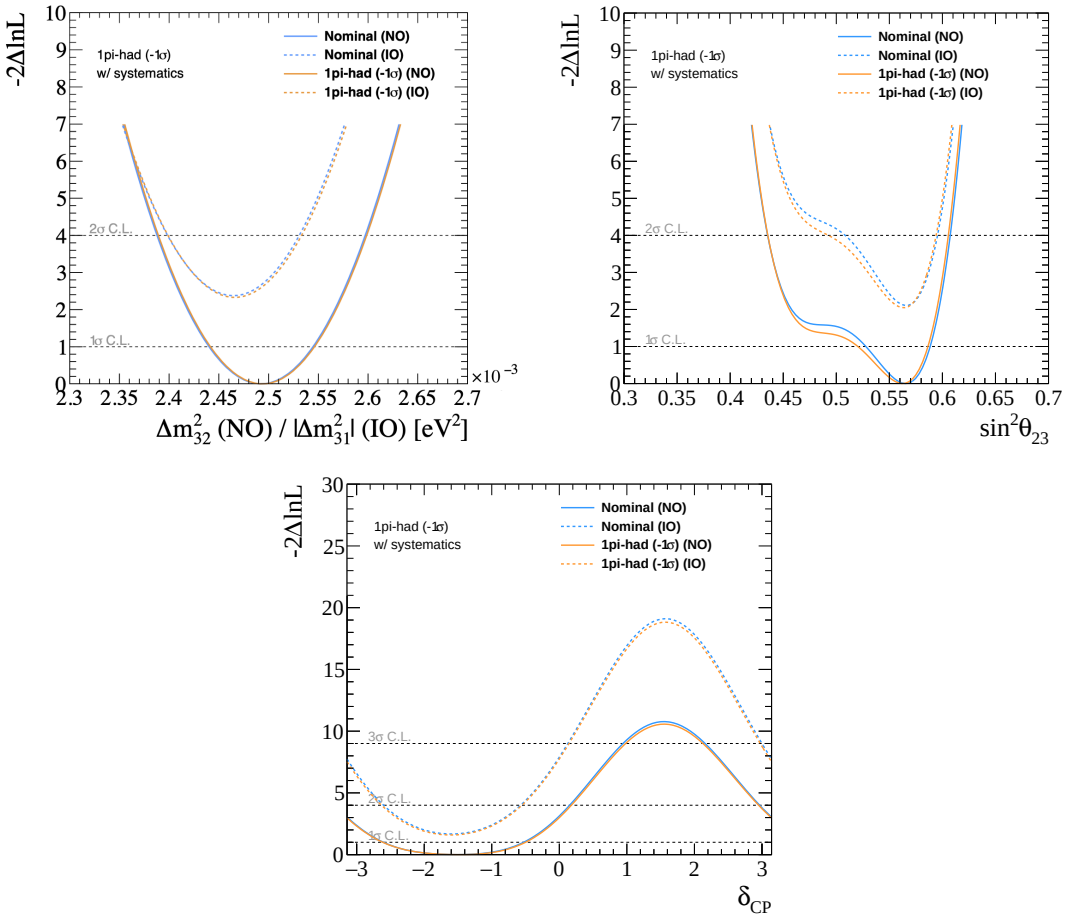

Figure A.48: Comparison of likelihood surface for Δm^2_{32}, $\sin^2\theta_{23}$ and δ_{CP}. Orange lines show those from -1σ pion hadron kinematics alternation robustness studies and blue lines show those of nominal MC for the normal and inverted mass orderings.

A.8 Low Q^2 Suppression Derived from MINERνA Experiment

This model is motivated by the discrepancy between our nominal model and the MINERνA experiment data as discussed in Sec. 3.4.3. Figures A.49 and A.50 show fitting results of the cross section and flux parameters using this alternative model. Several parameters which is related to the single pion production process move in order to compensate the difference between our nominal model and this simulated data. Using the covariance matrices which are based on that near detector fit, we made the reconstructed neutrino energy prediction at the far detector as shown in Fig. A.51. The near detector fit predictions cover the simulated data lines well.

Figure A.52 shows the fit results for three oscillation parameters. There is no large bias which should be considered as the systematic errors following the criteria discussed in Sec. 6.3.

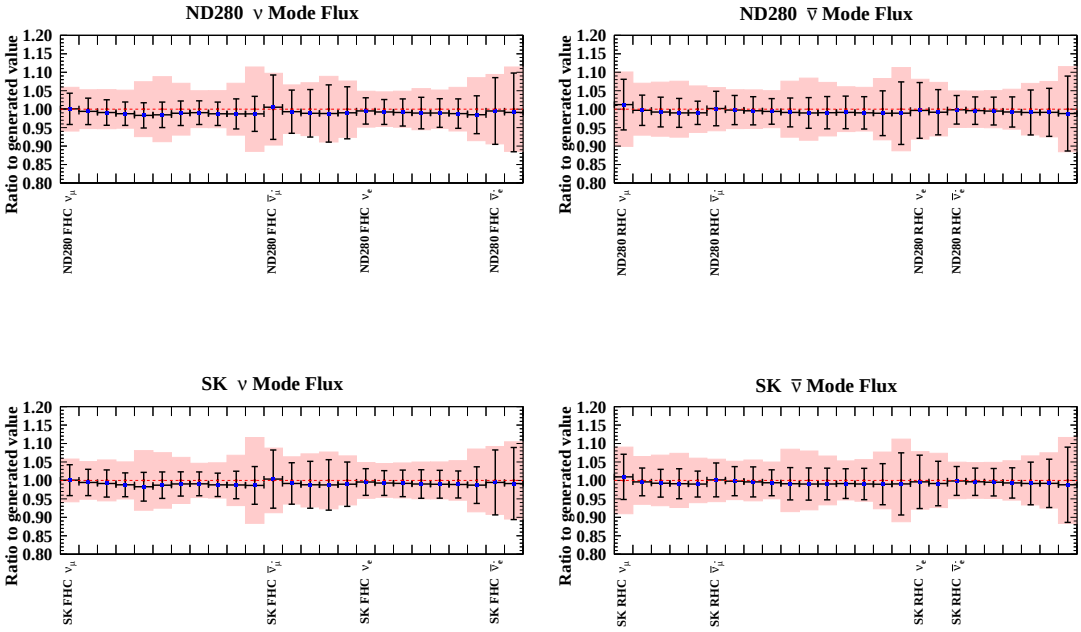

Figure A.49: Pre- (red band) and post-fit (blue dots and black error bands), flux parameters for the ν mode (left) and the $\bar{\nu}$ mode (right), and for the ND280 (top) and SK (bottom) from the near detector fit to the simulated data set of data-driven model derived from the MINERνA experiment.

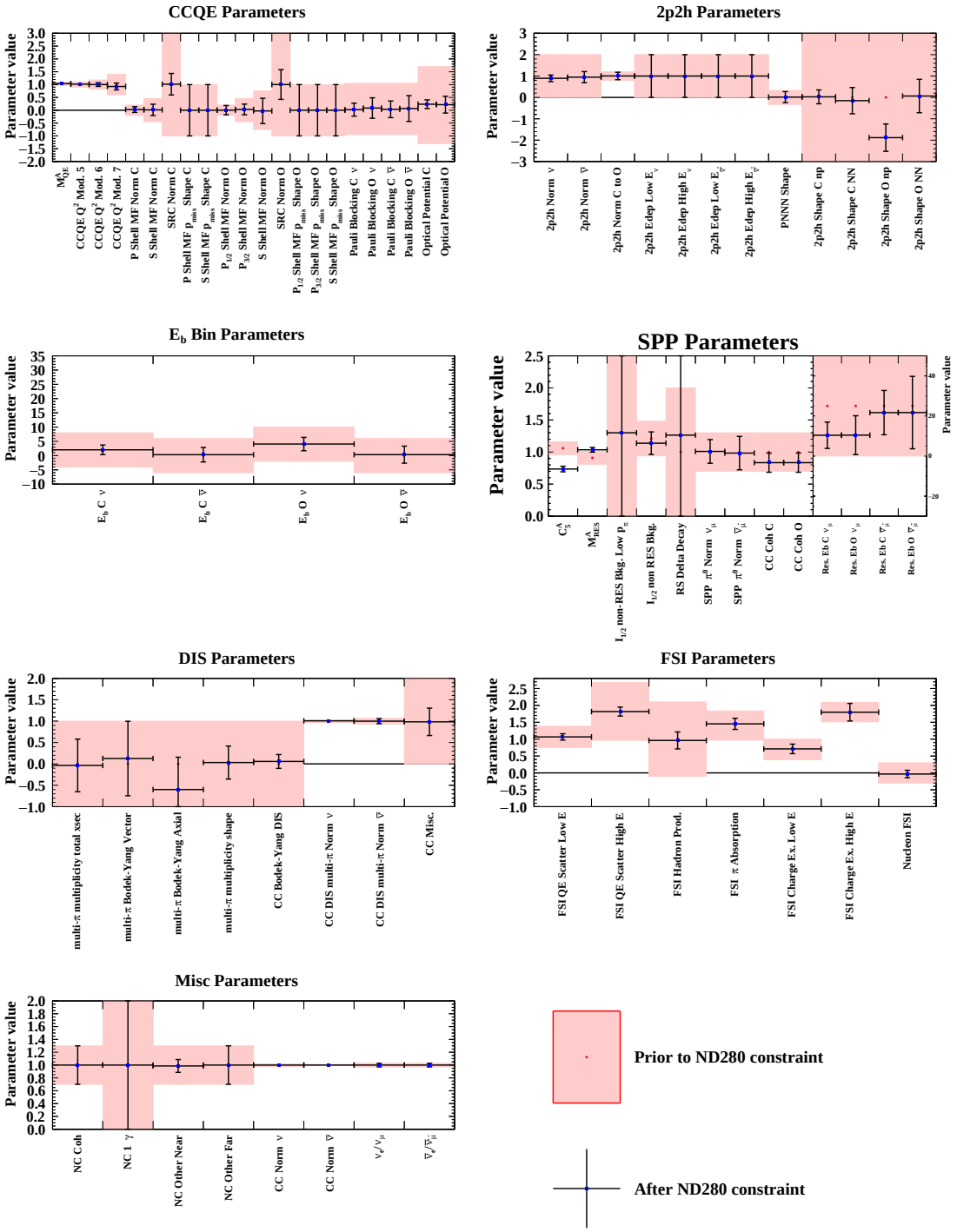

Figure A.50: Pre-(red band) and post-fit (blue dots and black error bands), cross-section parameters for CCQE, 2p2h, E_b, Single Pion Production (SPP), FSI, DIS, and misc from the near detector fit to the simulated data set of data-driven model derived from the MINERνA experiment.

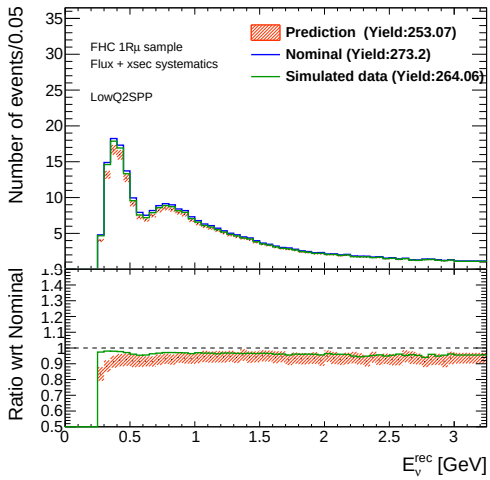

(a) ν mode 1Rμ

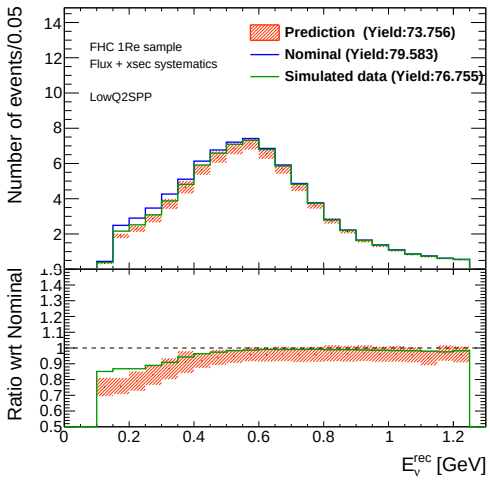

(b) ν mode 1Re

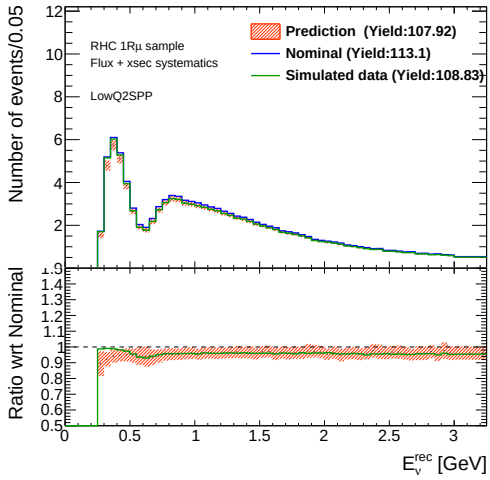

(c) $\bar{\nu}$ mode 1Rμ

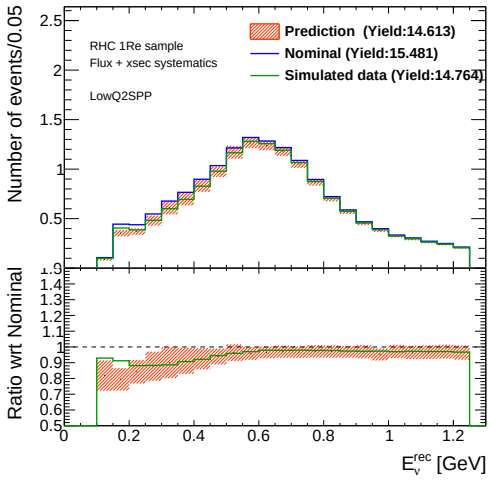

(d) $\bar{\nu}$ mode 1Re

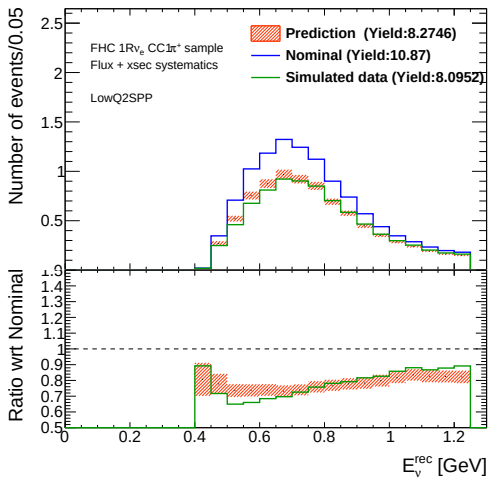

(e) ν mode 1Re1de

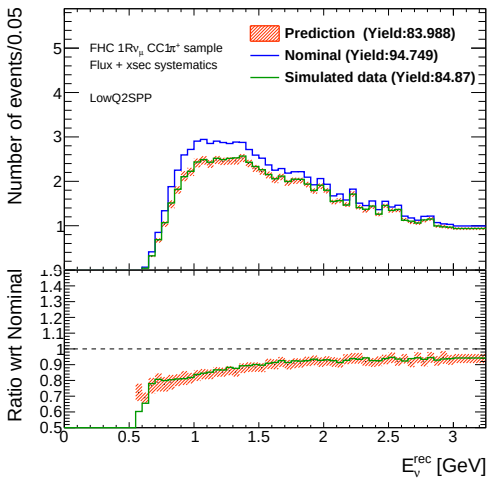

(f) ν mode CC1π multi-ring

Figure A.51: Comparison plots of the number of events between the nominal far detector sample (blue solid line), the simulated data of the alternative model (green solid line) and the prediction from the near detector fit (red band) as a function of the reconstructed neutrino energy. The bottom insets show the ratio of data to simulation.

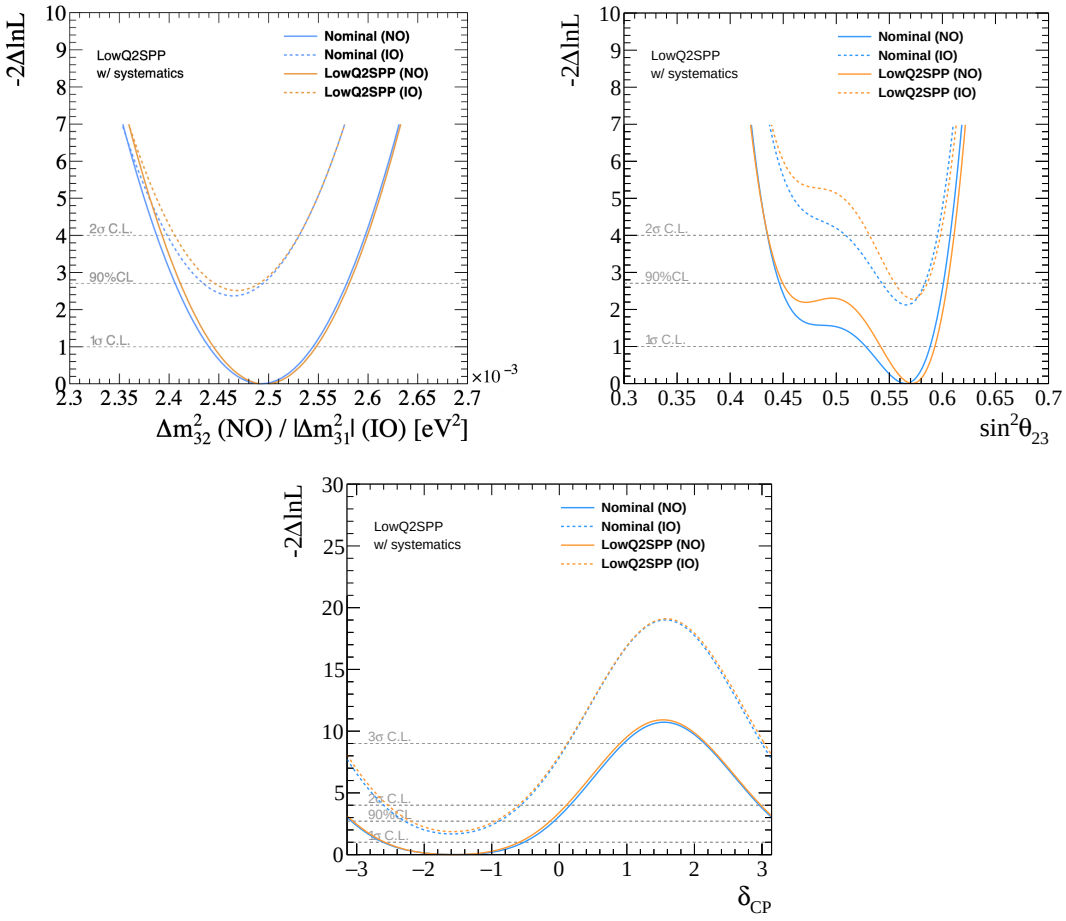

Figure A.52: Comparison of likelihood surface for Δm^2_{32}, $\sin^2\theta_{23}$ and δ_{CP}. Orange lines show those from this robustness studies of data-driven from the MINERνA and blue lines show those of nominal MC for the normal and inverted mass orderings.

A.9 Radiative Correction

This study is related to the real photon emission as discussed in Sec. 6.1.2. We made this simulated data set only for the far detector since the effects on the far detector selection is the motivation for this study. In the near future, we will also make the simulated data for the near detector in order to investigate of the effects on the near detector selection.

Figure A.53 shows the fit results for three oscillation parameters. There is no large bias which should be considered as the systematic errors following the criteria discussed in Sec. 6.3.

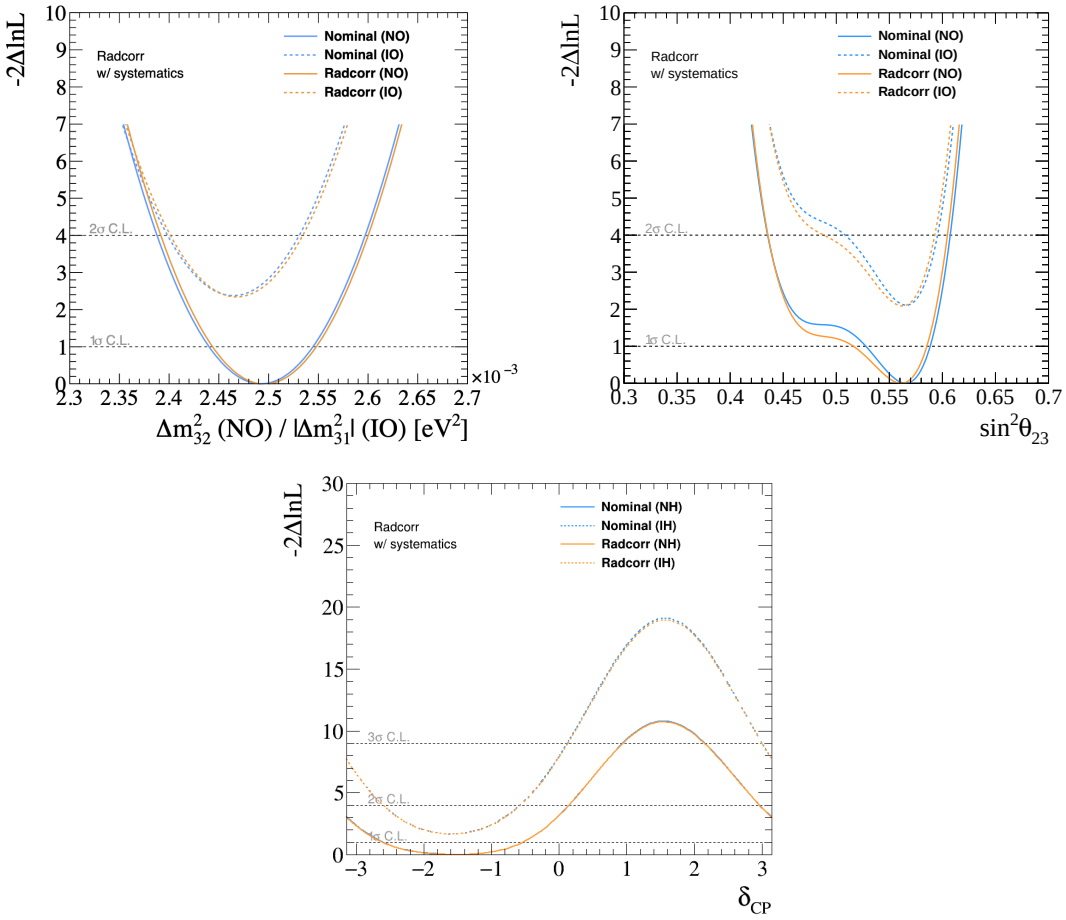

Figure A.53: Comparison of likelihood surface for Δm^2_{32}, $\sin^2\theta_{23}$ and δ_{CP}. Orange lines show those from radiative correction robustness studies and blue lines show those of nominal MC for the normal and inverted mass orderings.

Bibliography

[1] W. Pauli, Phys. Today **31N9**, 27 (1978).

[2] F. Reines, C. L. Cowan, F. B. Harrison, A. D. McGuire, and H. W. Kruse, Phys. Rev. **117**, 159 (1960).

[3] G. Danby, J.-M. Gaillard, K. Goulianos, L. M. Lederman, N. Mistry, M. Schwartz, and J. Steinberger, Phys. Rev. Lett. **9**, 36 (1962).

[4] A. collaboration, D. collaboration, L. Collaboration, O. collaboration, S. collaboration, and L. E. W. G. *et al.*, arXiv preprint hep-ex/0509008 (2005).

[5] K. *et al.*. Kodama (DONUT), Phys. Lett. B **504**, 218 (2001), arXiv:hep-ex/0012035 .

[6] Z. Maki, M. Nakagawa, and S. Sakata, Prog. Theor. Phys. **28**, 870 (1962).

[7] E. Majorana, Nuovo Cim **14**, 50 (1937).

[8] L. Wolfenstein, Phys. Rev. D **17**, 2369 (1978).

[9] S. P. Mikheev and A. Y. Smirnov, Nuovo Cim. C **9**, 17 (1986).

[10] R. Davis, Jr., D. S. Harmer, and K. C. Hoffman, Phys. Rev. Lett. **20**, 1205 (1968).

[11] K. S. *et al.*. Hirata (Kamiokande-II), Phys. Rev. Lett. **63**, 16 (1989).

[12] M. Cribier (GALLEX), Nucl. Phys. B Proc. Suppl. **70**, 284 (1999).

[13] M. *et al.*. Altmann (GNO), Phys. Lett. B **490**, 16 (2000), arXiv:hep-ex/0006034 .

[14] J. N. *et al.*. Abdurashitov (SAGE), J. Exp. Theor. Phys. **95**, 181 (2002), arXiv:astro-ph/0204245 .

[15] Y. *et al.*. Fukuda (Super-Kamiokande), Phys. Rev. Lett. **81**, 1562 (1998), arXiv:hep-ex/9807003 .

[16] K. *et al.*. Abe (Super-Kamiokande), Phys. Rev. D **97**, 072001 (2018), arXiv:1710.09126 [hep-ex] .

[17] M. G. *et al.*. Aartsen (IceCube), Phys. Rev. Lett. **120**, 071801 (2018), arXiv:1707.07081 [hep-ex] .

[18] K. *et al.*. Abe (T2K), Phys. Rev. Lett. **107**, 041801 (2011), arXiv:1106.2822 [hep-ex] .

[19] D. *et al.*. Adey (Daya Bay), Phys. Rev. Lett. **121**, 241805 (2018), arXiv:1809.02261 [hep-ex] .

[20] G. *et al.*. Bak (RENO), Phys. Rev. Lett. **121**, 201801 (2018), arXiv:1806.00248 [hep-ex] .

[21] H. *et al.*. de Kerret (Double Chooz), Nature Phys. **16**, 558 (2020), arXiv:1901.09445 [hep-ex] .

[22] K. *et al.*. Abe (Super-Kamiokande), Phys. Rev. D **94**, 052010 (2016), arXiv:1606.07538 [hep-ex] .

[23] B. *et al.*. Aharmim (SNO), Phys. Rev. C **87**, 015502 (2013), arXiv:1107.2901 [nucl-ex] .

[24] G. *et al.*. Bellini, Phys. Rev. Lett. **107**, 141302 (2011), arXiv:1104.1816 [hep-ex] .

[25] S. *et al.*. Abe (KamLAND), Phys. Rev. Lett. **100**, 221803 (2008), arXiv:0801.4589 [hep-ex] .

[26] M. A. *et al.*. Acero (NOvA), Phys. Rev. D **106**, 032004 (2022), arXiv:2108.08219 [hep-ex] .

[27] I. Esteban, M. C. Gonzalez-Garcia, M. Maltoni, T. Schwetz, and A. Zhou, JHEP **09**, 178, arXiv:2007.14792 [hep-ph] .

[28] I. Esteban, M. C. Gonzalez-Garcia, M. Maltoni, T. Schwetz, and A. Zhou, NuFIT 5.1 (2021), www.nu-fit.org.

[29] A. D. Sakharov, Pisma Zh. Eksp. Teor. Fiz. **5**, 32 (1967).

[30] J. H. Christenson, J. W. Cronin, V. L. Fitch, and R. Turlay, Phys. Rev. Lett. **13**, 138 (1964).

[31] B. *et al.*. Aubert (BaBar), Phys. Rev. Lett. **86**, 2515 (2001), arXiv:hep-ex/0102030 .

[32] K. *et al.*. Abe (Belle), Phys. Rev. Lett. **87**, 091802 (2001), arXiv:hep-ex/0107061 .

[33] M. Yoshimura, Phys. Rev. Lett. **41**, 281 (1978), [Erratum: Phys.Rev.Lett. 42, 746 (1979)].

[34] M. Fukugita and T. Yanagida, Phys. Lett. B **174**, 45 (1986).

[35] N. Cabibbo, Phys. Rev. Lett. **10**, 531 (1963).

[36] M. Kobayashi and T. Maskawa, Prog. Theor. Phys. **49**, 652 (1973).

[37] F. Plentinger, G. Seidl, and W. Winter, Nucl. Phys. B **791**, 60 (2008), arXiv:hep-ph/0612169 .

[38] F. *et al.*. An (JUNO), J. Phys. G **43**, 030401 (2016), arXiv:1507.05613 [physics.ins-det] .

[39] K. *et al.*. Abe (Hyper-Kamiokande), (2018), arXiv:1805.04163 [physics.ins-det] .

[40] K. *et al.*. Abe (T2K), Nature **580**, 339 (2020), [Erratum: Nature 583, E16 (2020)], arXiv:1910.03887 [hep-ex] .

[41] Y. Hayato and L. Pickering, The European Physical Journal Special Topics **230**, 4469 (2021).

[42] K. *et al.*. Abe (T2K), Nucl. Instrum. Meth. A **659**, 106 (2011), arXiv:1106.1238 [physics.ins-det] .

[43] A. K. Ichikawa, Nucl. Instrum. Meth. A **690**, 27 (2012).

[44] K. Matsuoka, A. Ichikawa, H. Kubo, T. Maruyama, A. Murakami, T. Nakaya, and M. Yokoyama, Nucl. Instrum. Meth. A **623**, 385 (2010).

[45] K. *et al.*. Matsuoka, Nucl. Instrum. Meth. A **624**, 591 (2010), arXiv:1008.4077 [physics.ins-det] .

[46] D. *et al.*. Beavis (E899) (1995).

[47] M. *et al.*. Barranco-Luque (UA1), Nucl. Instrum. Meth. **176**, 175 (1980).

[48] P. A. *et al.*. Amaudruz (T2K ND280 FGD), Nucl. Instrum. Meth. A **696**, 1 (2012), arXiv:1204.3666 [physics.ins-det] .

[49] N. *et al.*. Abgrall (T2K ND280 TPC), Nucl. Instrum. Meth. A **637**, 25 (2011), arXiv:1012.0865 [physics.ins-det] .

[50] I. Giomataris, R. De Oliveira, S. Andriamonje, S. Aune, G. Charpak, P. Colas, A. Giganon, P. Rebourgeard, and P. Salin, Nucl. Instrum. Meth. A **560**, 405 (2006), arXiv:physics/0501003 .

[51] Y. *et al.*. Itow (T2K), in 3rd Workshop on Neutrino Oscillations and Their Origin (NOON 2001) (2001) pp. 239–248, arXiv:hep-ex/0106019 .

[52] C. *et al.*. Andreopoulos, Nucl. Instrum. Meth. A **614**, 87 (2010), arXiv:0905.2517 [hep-ph] .

[53] T. Golan, C. Juszczak, and J. T. Sobczyk, Phys. Rev. C **86**, 015505 (2012), arXiv:1202.4197 [nucl-th] .

[54] D. Casper, Nucl. Phys. B Proc. Suppl. **112**, 161 (2002), arXiv:hep-ph/0208030 .

[55] O. Buss, T. Gaitanos, K. Gallmeister, H. van Hees, M. Kaskulov, O. Lalakulich, A. B. Larionov, T. Leitner, J. Weil, and U. Mosel, Phys. Rept. **512**, 1 (2012), arXiv:1106.1344 [hep-ph] .

[56] C. L. Smith, Nuclear Physics B **228**, 205 (1983).

[57] D. Mund, B. Märkisch, M. Deissenroth, J. Krempel, M. Schumann, H. Abele, A. Petoukhov, and T. Soldner, Physical review letters **110**, 172502 (2013).

[58] P. Stowell, C. Wret, C. Wilkinson, L. Pickering, S. Cartwright, Y. Hayato, K. Mahn, K. McFarland, J. Sobczyk, and R. *et al.*. Terri, Journal of Instrumentation **12** (01), P01016.

[59] K. Miller, S. Barish, A. Engler, R. Kraemer, B. Stacey, M. Derrick, E. Fernandez, L. Hyman, G. Levman, and D. *et al.*. Koetke, Physical Review D **26**, 537 (1982).

[60] B. Bourguille, J. Nieves, and F. Sanchez, Journal of High Energy Physics **2021**, 1 (2021).

[61] N. Baker, A. Cnops, P. Connolly, S. Kahn, H. Kirk, M. Murtagh, R. Palmer, N. Samios, and M. Tanaka, Physical Review D **23**, 2499 (1981).

[62] D. Allasia, C. Angelini, G. van Apeldoorn, A. Baldini, S. Barlag, L. Bertanza, F. Bobisut, P. Capiluppi, P. van Dam, and M. *et al.*. Faccini-Turluer, Nuclear Physics B **343**, 285 (1990).

[63] T. Kitagaki, S. Tanaka, H. Yuta, K. Abe, K. Hasegawa, A. Yamaguchi, K. Tamai, T. Hayashino, Y. Otani, and H. *et al.*. Hayano, Physical Review D **28**, 436 (1983).

[64] A. A. *et al.*. Aguilar-Arevalo (MiniBooNE), Phys. Rev. D **81**, 092005 (2010), arXiv:1002.2680 [hep-ex] .

[65] R. *et al.*. Gran (K2K), Phys. Rev. D **74**, 052002 (2006), arXiv:hep-ex/0603034 .

[66] V. Bernard, L. Elouadrhiri, and U.-G. Meißner, Journal of Physics G: Nuclear and Particle Physics **28**, R1 (2001).

[67] D. Rein and L. M. Sehgal, Annals Phys. **133**, 79 (1981).

[68] K. M. Graczyk and J. T. Sobczyk, Phys. Rev. D **77**, 053003 (2008), arXiv:0709.4634 [hep-ph] .

[69] K. M. Graczyk and J. T. Sobczyk, Phys. Rev. D **77**, 053001 (2008), [Erratum: Phys.Rev.D 79, 079903 (2009)], arXiv:0707.3561 [hep-ph] .

[70] R. P. Feynman, M. Kislinger, and F. Ravndal, Phys. Rev. D **3**, 2706 (1971).

[71] D. Rein and L. M. Sehgal, Nucl. Phys. B **223**, 29 (1983).

[72] D. Rein and L. M. Sehgal, Phys. Lett. B **657**, 207 (2007), arXiv:hep-ph/0606185 .

[73] S. L. Adler, Phys. Rev. **135**, B963 (1964).

[74] C. Berger and L. M. Sehgal, Phys. Rev. D **79**, 053003 (2009), arXiv:0812.2653 [hep-ph] .

[75] A. *et al.*. Higuera (MINERvA), Phys. Rev. Lett. **113**, 261802 (2014), arXiv:1409.3835 [hep-ex] .

[76] T. Sjostrand, Comput. Phys. Commun. **82**, 74 (1994).

[77] A. Bodek and U. K. Yang, AIP Conf. Proc. **670**, 110 (2003), arXiv:hep-ex/0301036 .

[78] R. A. Smith and E. J. Moniz, Nucl. Phys. B **43**, 605 (1972), [Erratum: Nucl.Phys.B 101, 547 (1975)].

[79] J. Nieves, I. Ruiz Simo, and M. J. Vicente Vacas, Phys. Rev. C **83**, 045501 (2011), arXiv:1102.2777 [hep-ph] .

[80] O. Benhar, A. Fabrocini, S. Fantoni, and I. Sick, Nuclear Physics A **579**, 493 (1994).

[81] J. Nieves, I. R. Simo, and M. V. Vacas, Physics Letters B **707**, 72 (2012).

[82] M. Martini, M. Ericson, G. Chanfray, and J. Marteau, Phys. Rev. C **80**, 065501 (2009).

[83] G. D. Megias, J. E. Amaro, M. B. Barbaro, J. A. Caballero, and T. W. Donnelly, Phys. Rev. D **94**, 013012 (2016), arXiv:1603.08396 [nucl-th] .

[84] K. *et al.*. Abe (T2K), Eur. Phys. J. C **83**, 782 (2023), arXiv:2303.03222 [hep-ex] .

[85] L. L. Salcedo, E. Oset, M. J. Vicente-Vacas, and C. Garcia-Recio, Nucl. Phys. A **484**, 557 (1988).

[86] E. P. Guerra, C. Wilkinson, S. Bhadra, S. Bolognesi, J. Calcutt, P. De Perio, S. Dolan, T. Feusels, G. Fiorentini, and Y. *et al.*. Hayato, Physical Review D **99**, 052007 (2019).

[87] P. *et al.*. Gueye, Phys. Rev. C **60**, 044308 (1999).

[88] B. Bhattacharya, R. J. Hill, and G. Paz, Phys. Rev. D **84**, 073006 (2011), arXiv:1108.0423 [hep-ph] .

[89] C. Adamuščín, E. Tomasi-Gustafsson, E. Santopinto, and R. Bijker, Physical Review C **78**, 035201 (2008).

[90] N. Jachowicz, K. Heyde, J. Ryckebusch, and S. Rombouts, Physical Review C **65**, 025501 (2002).

[91] M. Martini, G. Chanfray, M. Ericson, and J. Marteau, AIP Conf. Proc. **1189**, 323 (2009), arXiv:0909.0642 [nucl-th] .

[92] T. Bohlen, F. Cerutti, M. Chin, A. Fasso, A. Ferrari, P. Ortega, A. Mairani, P. Sala, G. Smirnov, and V. Vlachoudis, Nuclear Data Sheets **120**, 211 (2014).

[93] N. *et al.*. Abgrall (NA61/SHINE), Eur. Phys. J. C **76**, 617 (2016), arXiv:1603.06774 [hep-ex] .

[94] K. Abe, N. Abgrall, H. Aihara, T. Akiri, J. Albert, C. Andreopoulos, S. Aoki, A. Ariga, T. Ariga, and S. *et al.*. Assylbekov, Physical Review D **87**, 012001 (2013).

[95] N. *et al.*. Abgrall (NA61/SHINE), Eur. Phys. J. C **76**, 84 (2016), arXiv:1510.02703 [hep-ex] .

[96] A. Bodek and T. Cai, Eur. Phys. J. C **79**, 293 (2019), arXiv:1801.07975 [nucl-th] .

[97] G. M. *et al.*. Radecky, Phys. Rev. D **25**, 1161 (1982), [Erratum: Phys.Rev.D 26, 3297 (1982)].

[98] M. *et al.*. Derrick, Phys. Rev. D **23**, 569 (1981).

[99] T. *et al.*. Kitagaki, Phys. Rev. D **34**, 2554 (1986).

[100] N. J. Baker, A. M. Cnops, P. L. Connolly, S. A. Kahn, M. J. Murtagh, R. B. Palmer, N. P. Samios, and M. Tanaka, Phys. Rev. D **23**, 2495 (1981).

[101] T. Yang, C. Andreopoulos, H. Gallagher, K. Hoffmann, and P. Kehayias, Eur. Phys. J. C **63**, 1 (2009), arXiv:0904.4043 [hep-ph] .

[102] M. *et al.*. Tanabashi (Particle Data Group), Phys. Rev. D **98**, 030001 (2018).

[103] K. S. Kim and M. K. Cheoun, AIP Conf. Proc. **1189**, 163 (2009).

[104] J. Engel, Phys. Rev. C **57**, 2004 (1998), arXiv:nucl-th/9711045 .

[105] R. Barlow and C. Beeston, Computer Physics Communications **77**, 219 (1993).

[106] R. Brun and F. Rademakers, Nucl. Instrum. Meth. A **389**, 81 (1997).

[107] S. S. Wilks, The annals of mathematical statistics **9**, 60 (1938).

[108] R. B. Patterson, E. M. Laird, Y. Liu, P. D. Meyers, I. Stancu, and H. A. Tanaka, Nucl. Instrum. Meth. A **608**, 206 (2009), arXiv:0902.2222 [hep-ex] .

[109] G. J. Feldman and R. D. Cousins, Phys. Rev. D **57**, 3873 (1998), arXiv:physics/9711021 .

[110] N. *et al.*. Abgrall (NA61/SHINE), Eur. Phys. J. C **79**, 100 (2019), arXiv:1808.04927 [hep-ex] .

[111] K. *et al.*. Abe (T2K), Phys. Rev. D **101**, 112004 (2020), arXiv:2004.05434 [hep-ex] .

[112] A. Bodek and U.-k. Yang (2010) arXiv:1011.6592 [hep-ph] .

[113] P. A. *et al.*. Zyla (Particle Data Group), PTEP **2020**, 083C01 (2020).

[114] L. Wan, Atmospheric neutrino_super-k (2022).

[115] T. Stuttard, Atmospheric Neutrino_Particle physics with atmospheric neutrinos at IceCube (2022).

[116] P. *et al.*. Adamson (MINOS+), Phys. Rev. Lett. **125**, 131802 (2020), arXiv:2006.15208 [hep-ex] .

[117] K. *et al.*. Abe (T2K, J-PARC Neutrino Facility Group), (2019), arXiv:1908.05141 [physics.ins-det] .

[118] K. *et al.*. Abe (T2K), (2019), arXiv:1901.03750 [physics.ins-det] .

[119] X. G. Lu, L. Pickering, S. Dolan, G. Barr, D. Coplowe, Y. Uchida, D. Wark, M. O. Wascko, A. Weber, and T. Yuan, Phys. Rev. C **94**, 015503 (2016), arXiv:1512.05748 [nucl-th] .

[120] S. *et al.*. Dolan, Phys. Rev. D **105**, 032010 (2022), arXiv:2108.11779 [hep-ex] .

List of Tables

List of Figures